Energy Research and Development Division
FINAL PROJECT REPORT

DEVELOPMENT AND EVALUATION OF GAS FUEL INTERCHANGEABILITY CRITERIA AND METHODOLOGIES

Prepared for: California Energy Commission
Prepared by: University of California, Irvine

MAY 2014
CEC-500-2015-063

PREPARED BY:

Primary Author(s):
Vince McDonell
Brendan Shaffer
Amin Akbari
David Page
Zhixuan Duan
David Beerer
Andrés Colorado

UCI Combustion Laboratory
University of California, Irvine
131 Engineering Laboratory Facility
Irvine, California 92697-3550
Tel: (949) 824-5950 x121
Fax: (949) 824-7423
www.ucicl.uci.edu

Contract Number: 500-08-034

Prepared for:

California Energy Commission

Marla Mueller
Contract Manager

Aleecia Gutierrez
Office Manager
Energy Generation Research Office

Laurie ten Hope
Deputy Director
ENERGY RESEARCH AND DEVELOPMENT DIVISION

Robert P. Oglesby
Executive Director

DISCLAIMER

This report was prepared as the result of work sponsored by the California Energy Commission. It does not necessarily represent the views of the Energy Commission, its employees or the State of California. The Energy Commission, the State of California, its employees, contractors and subcontractors make no warranty, express or implied, and assume no legal liability for the information in this report; nor does any party represent that the uses of this information will not infringe upon privately owned rights. This report has not been approved or disapproved by the California Energy Commission nor has the California Energy Commission passed upon the accuracy or adequacy of the information in this report.

ACKNOWLEDGEMENTS

Boyd Fackler, Megan Karulus, Igor Novolevsky, Professor John Kramlich, and Professor Phil Malte contributed substantially to the material within this report; in particular, the material associated with the Jet-Stirred Reactor description, experimental results, and analyses of the these results. Additional details of their contributions are contained in Appendix D: Flame Structure and Interpretation Detailed Flame Structure and Appendix E: Reduced Order Kinetic Mechanisms for Alternative Fuels. As a result of their efforts on this project, Drs. Fackler and Karulus obtained PhD degrees.

Andrew Marshall, Dr. Prabhakar Venkateswaran, and Professor Tim Lieuwen contributed substantially to the overall program and were able to provide a novel consideration for turbulent flame speed, which is described in detail in Appendix B: Flame Speed Test Results and Analysis.

It is noted that the work of Amin Akbari, Dr. David Beerer, and Zhixuan Duan on the content of this report contributed substantially to their advanced degrees from the University of California, Irvine.

In addition to the technical contribution of the university partners, the participation of the advisory board for the project is also acknowledged. Those who participated and provided critical feedback in the direction and reporting of the project include:

Ajay Agrawal
- University of Alabama

Luke Cowell
- Solar Turbines, Incorporated

Leonard Angello
- EPRI

Don Ferguson
- National Energy Technology Laboratory

Al Baez
- South Coast Air Quality Management District

Kim Kemp
- Pacific Gas & Electric

Les Bamburg
- Sempra Energy

Ray Laster
- Siemens Energy

Chuck Baukal
- John Zink Co., LLC

Steve Moore
- San Diego Air Quality Management District

Robert Cheng
- Lawrence Berkeley National Laboratory

Floyd Vergara
- California Air Resources Board

Med Colkett
- United Technologies Research Center

Dave Warner
- San Joaquin Valley Quality Management District

PREFACE

The California Energy Commission Energy Research and Development Division supports public interest energy research and development that will help improve the quality of life in California by bringing environmentally safe, affordable, and reliable energy services and products to the marketplace.

The Energy Research and Development Division conducts public interest research, development, and demonstration (RD&D) projects to benefit California.

The Energy Research and Development Division strives to conduct the most promising public interest energy research by partnering with RD&D entities, including individuals, businesses, utilities, and public or private research institutions.

Energy Research and Development Division funding efforts are focused on the following RD&D program areas:

- Buildings End-Use Energy Efficiency
- Energy Innovations Small Grants
- Energy-Related Environmental Research
- Energy Systems Integration
- Environmentally Preferred Advanced Generation
- Industrial/Agricultural/Water End-Use Energy Efficiency
- Renewable Energy Technologies
- Transportation

Development and Evaluation of Gas Fuel Interchange Criteria and Methodologies is the final report for the California Energy Commission project project (contract CEC-08-034) conducted by The University of California, Irvine; University of Washington; and Georgia Tech. The information from this project contributes to Energy Research and Development Division's Energy-Related Environmental Research Program.

For more information about the Energy Research and Development Division, please visit the Energy Commission's website at www.energy.ca.gov/research/ or contact the Energy Commission at 916-327-1551.

ABSTRACT

Using alternative gaseous fuels such as those derived from biomass or waste streams is an important strategy to help meet California's greenhouse gas reduction targets. The majority of fuel-using power generation systems have been developed and optimized to use natural gas. To meet important pollutant emission regulations, many of these devices operate at conditions that promote relatively low combustion temperatures. The natural gas combustion temperatures when nitrogen oxide (NOx) formation is the highest can be avoided by operating the burner in lean (high excess air) conditions with a good mix of fuel and air. However, while this offers the potential for low NOx emissions, lean combustion systems are prone to operating issues, including autoignition, blowoff and flashback. For these systems, pollutant emission levels are also an issue. If these devices are to operate on alternative fuels, it is important to predict how fuel composition affects operability and pollutant emissions. This report provides an overview of strategies to predict the impact of fuel composition on these performance parameters. The researchers evaluated these strategies and provided recommendations for predicting fuel composition impacts for various combustion device configurations, including jet burners, low-swirl burners, and high-swirl burners. Methodologies to predict blowoff and autoignition for various fuels are promising. Predicting flashback, while demonstrated for certain configurations, remains a challenge. Several operability methods use models of reaction rates to determine some of the quantities. Although these packages are becoming increasingly user friendly, some experience and background knowledge is required. To predict emissions behavior reliably, additional information about the system is required. That information may be determined from photographic images of the reaction, detailed measurements, or information from computational fluid dynamic simulations; however, computational fluid dynamics also requires experience to apply.

Keywords: flashback, emissions, blowoff, autoignition, correlations, chemical reactor network, experimental research, flame speed.

Please use the following citation for this report:

McDonell, Vincent, Brendan Shaffer, Amin Akbari, David Page, Zhixuan Duan, David Beerer, and Andrés Colorado (University of California, Irvine). 2014 ***Development and Evaluation of Gas Fuel Interchangeability Criteria and Methodologies.*** California Energy Commission. Publication number: CEC-500-2015-063.

TABLE OF CONTENTS

Acknowledgements i

PREFACE ii

ABSTRACT iii

TABLE OF CONTENTS iv

LIST OF FIGURES vi

LIST OF TABLES xii

EXECUTIVE SUMMARY 1

Introduction 1

Project Purpose 1

Project Results 2

Benefits to California 3

CHAPTER 1: Introduction 5

1.1 Rationale for Lean Combustion 5

1.2 Challenges with Lean Premixed Combustion 6

1.3 Scope of current Effort 7

CHAPTER 2: Fuel Selection 8

CHAPTER 3: Existing Interchanges Parameters and Methodologies 11

CHAPTER 4: Interchangeability 13

4.1 Evaluation of Autoignition Prediction 13

4.1.1 Review of Key Factors 13

4.1.2 Ignition Delay Experimental Test Bed 15

4.1.3 Results for Alkane Based Fuels 17

4.1.4 Results for Hydrogen Containing Fuels 28

4.1.5 Comprehensive Modeling of Autoignition 30

4.1.6 Summary 43

4.2 Evaluation of Blowoff/Flashback Prediction 46

4.2.1 Review of Key Factors 46

4.2.2 Test Beds for Blowoff/Flashback Expirements 46
4.2.3 Results for Jet Flame Flashback 59
4.2.4 Results for Jet Stireed Reactor Blowoff 70
4.2.5 Results for Low Swirl Burner Flashback 73
4.2.6 Results for a High Swirl Burner 80
4.2.7 Results for Capstone Engine 92
4.2.8 Summary 93
CHAPTER 5: 95
5.1 Review of Key Factors 95
5.2 Evaluation of Emissions Predictions Preformance 95
5.2.1 Results for Stirred Reactor 95
5.2.2 Results for High-Swirl Burner 123
5.2.3 Results for Capstone Engine 148
5.3 Comments Regarding NOx "Entitlement" Levels 159
5.4 Summary 161
CHAPTER 6: Summary of Recommended Interchangeability Methodologies 163
6.1 Autoignition 163
6.2 Blowoff 164
6.3 Flashback 165
6.4 Emission 166
REFERENCES 176
APPENDIX A: Review of Fuel Composition .....
APPENDIX B: Review of Existing Interchange Parameters and Methodologies .....
APPENDIX C: Alkane Ignition Delay Correlations .....
APPENDIX D: Details and Heat Transfer Analysis of JSR .....
APPENDIX E: Topical Report – Flame Speed Test Results and Analysis .....
APPENDIX F: Topical Report – Diffusion Transport Porperty Calculator .....
APPENDIX G: Topical Report – Flame Structure Tests and Interpretation .....

LIST OF FIGURES

Figure 1: Pollutant Concentration and Temperature Dependency Upon Relative Amounts of Air and Fuel (Methane/Air). 6

Figure 2: Illustration of Combustion Operability Issues for Gas Turbine Combustor at Fixed Inlet Temperature and Pressure. 7

Figure 3: Illustration of Ignition Delay Plotted in an Arrhenius Plot 14

Figure 4: Flow Reactor Schematic. Photodiodes are used to detect flame front. 17

Figure 5: Ignition Delay Times of Alkanes. All results are at 9 atm and □.=.0.6. 18

Figure 6: Ignition Delay Times of Binary Methane/Ethane Blends 20

Figure 7: Ignition Delay Trends for Binary Methane/Blends as Ethane Content Is Increased 21

Figure 8: Ignition Delay Times of Binary Methane/Propane Blends 22

Figure 9: Ignition Delay Times (Correlations) for Binary Blends of Methane with Ethane or Propane. Correlations calculated for 9 atm pressure. 23

Figure 10: Ignition Delay Times of Blends of 70 percent Methane with the Remaining 30 percent Being Composed of Higher Hydrocarbons. All points are at 9 atm. 23

Figure 11: Ignition Delay Times of Natural Gas in Comparison to Binary Blends and Pure Fuels 24

Figure 12: Comparison of Ignition Delay Time and Methane Number 26

Figure 13: Ignition Delay Times of a Methane/Hydrocarbon Blend at 7, 9, and 15 atm 27

Figure 14: Ignition Delay Times Conducted at Various Pressures Collapsed onto a Single Line 28

Figure 15: Comparison of Flow Reactor Results from the Current Study to the Flow Reactor 29

Figure 16: Comparison between Current Study (Points) and Kinetic Simulations (Curves) at 9 atm, 820 K–920 K. 31

Figure 17: Ignition Delay Simulations of Various Mechanisms in Comparison to Experimental Data 32

Figure 18: Simulations of Methane/Ethane/Propane Blend at Varying Pressures 33

Figure 19: Simulated and Experimental Ignition Delay Times of Methane/Ethane Blends 34

Figure 20: Simulated and Experimental Ignition Delay Times of Methane/Propane Blends 34

Figure 21: Ignition Delay Times of Mixtures of CH4 and CO2 at 5 atm. The legend indicates percent CO2 in fuel by mole/volume. 36

Figure 22: Normalized Ignition Delay of 40 Percent/60 Percent CH4/CO2 as a Function of Pressure 37

Figure 23: Comparison of Experimental Hydrogen/Air Ignition Delay Measurements to Homogenous Simulations Using the Kinetic Mechanism from the Galway Group 39

Figure 24: Hydrogen-Oxygen Explosion Limit Chart with Experimental Test Conditions Identified. The shaded region represents typical gas turbine combustor inlet temperature and pressures 41

Figure 25: Schematic of the Axisymmetric Single Injector Rig and Associated Supporting Hardware 47

Figure 26: Schematic of the Enclosure Holder 48

Figure 27: Schematic of the Thermocouple Alignment 49

Figure 28: Diagram of the Experimental Setup 50

Figure 29: Sampling Locations within the JSR 51

Figure 30: Schematic of the Model Combustor 52

Figure 31: Blowoff Stages for 20/80 Mixture of NG/H2 with 500 K Preheat and 81 kg/hr Air Flow Rate 53

Figure 32: Schematic of Flashback and Temperature Jump in Thermocouples 54

Figure 33: Low-Swirl Injector, Upstream Face (left) and Downstream Face (right) 55

Figure 34: Schematic of the LSI within the Premixer and Sudden Expansion Nozzle 55

Figure 35: Aerodynamics of a Low-Swirl Flame 56

Figure 36: High-Pressure Vessel and Facility 57

Figure 37: Cross-Sectional Image of Pressure Vessel and Combustor Test Section 57

Figure 38: C65 Combustor Schematic with Two Sections Illustrating the Two Planes of Tangential Injectors 58

Figure 39: Predicted vs. Measured Values of gc Using Equation 29 and Equation 30 61

Figure 40: Predicted (Equation 31) 62

Figure41: AFT vs. Re vs. Measured gc 62

Figure42: Model Predicting gc without Consideration of Material Effects 65

Figure 43: Models Predicting gc: Quartz Tube (Blue Diamonds) and Stainless Tube (Red Triangles) 65

Figure 44: Models Predicting gc with Tip Temperature Instead of Inlet Temperature 66

Figure 45: Models Predicting gc with Tip Temperature for Non-Preheated Cases 67

Figure 46: Comparison of Actual Values vs. Predicted Values by Multi-Parameter Model (Equation 37) 68

Figure 47: Comparison of Actual Values vs. Predicted Values by Multi-Parameter Model (Equation 39) 69

Figure 48: Experimentally Determined Blowout Temperature for Fuel Compositions Outlined in Table 11 72

Figure 49: Experimentally Determined Blowout Temperature for CH4 Mixed with Increasing Levels of H2 and C2H6. Blowout for pure C3H8 is shown for reference. 73

Figure 50: Flashback Limits with the Aero-Vane LSI and Sudden Expansion Nozzle with 90/10 Hydrogen/Methane Blend at Various Pre-Heats, Pressures and Velocities 74

Figure51: Flashback Limits Normalized by Pressure 76

Figure 52: Flashback Data Correlated as a Function of ϕ, PO, and TO 77

Figure 53: Combustor Inlet Temperature as a Function of Pressure Ratio Assuming 87 Percent Compression Efficiency. Inlet temperature is 294 K. 77

Figure 54: Calculated Primary Zone Firing Temperature 78

Figure 55: AFT and Equivalence Ratio vs. Fuel Composition for Ultimate Blowoff 81

Figure 56: Modeled Phi vs. Measured Phi Using the Residence Time Approach for Ultimate Blowoff 82

Figure 57: Calculated Variables for Different Fuel Compositions for All the Cases for Ultimate Blowoff 84

Figure 58: Measured Phi vs. Adjusted Model Phi Based on Local Equivalence Ratio for Ultimate Blowoff 85

Figure 59: Modeled Phi vs. Measured Phi Using the Residence Time Approach for Initiation of Blowoff 86

Figure 60: Measured vs. Adjusted Model Phi Based on Local Equivalence Ratio for the Beginning of Blowoff 87

Figure 61: Equivalence Ratios vs. Cq and Cq* at Flashback 89

Figure 62: Predicted vs. Measured Equivalence Ratios Using the Cq* Constant Method 90

Figure 63: Predicted Phi vs. Modeled Phi Based on the Adjusted Equivalence Ratio Method 91

Figure 64: Temperature Ratio at Flashback for Different Fuel Compositions..... 91

Figure 65: Three-Element CRN Used for Chemical Kinetic Modeling of the Experimental JSR.. 96

Figure 66: Comparison of NOx Prediction Obtained by the Baseline Three-Element CRN Using Five Different Chemical Kinetic Mechanisms..... 97

Figure 67: Net NOX Production Rate for LPM CH4 Combustion, Showing Both Experimental and Modeling Results..... 98

Figure 68: NOX Production for LPM CH4 Combustion from Each of the Four Pathways Calculated for a Series of Temperatures from two Different Methods 101

Figure 69: NOX Rate of Production from Each of the Four Pathways in the Recirculation Zone and Turbulent Flame Brush Elements of the CRN Model 102

Figure 70: Oxygen Concentration in the Recirculation Zone and CH Concentration in the Flame Brush for the Modeling Results Shown in Figure 69 103

Figure 71: Measured NOX as EI versus Mass Fraction of N2 or CO2 Diluent in Fuel Stream. Temperature is maintained constant at 1,800 K..... 105

Figure 72: Measured NO..... 105

Figure 73: Measured NOX as (ppm, dry) versus Exit Gas O2 (mole %, dry). Temperature is maintained constant at 1,800 K. 106

Figure 74: NOX Emission Index Predicted by CRN Model: Total and by Four Pathways. CH4 diluted with N2. 107

Figure 75: NOX Emission Index Predicted by CRN Model: Total and by Four Pathways. CH4 diluted with CO2..... 107

Figure 76: NOX Production Reported as Emission Index for Each of the Four Mechanisms in Each of the Three Reactor Elements of the CRN model. The O2 concentration is 3.6 percent (dry mole fraction)..... 108

Figure 77: O Atom Concentration in the Recirculation Zone and PSB for both Diluted Fuels... 109

Figure 78: H-atom Concentration in the Recirculation Zone and Turbulent Flame Brush for both Diluted Fuels..... 110

Figure 79: CH Concentration within the Flame Brush for CH4 Diluted with both N2 and CO2 110

Figure 80: The Volumes Computed for the PSB as a Function of C2H6 Concentration in the Fuel Stream for a Fuel Mixture of CH4 and C2H6 from both GRI-Mech 3.0 and C2 NOx. Temperature in the recirculation zone is kept constant at 1,800 K 112

Figure 81: NOX Concentration as a Function of C2H6 Concentration in the Fuel Stream for a Fuel Mixture of CH4 and C2H6 from Experiment and the Three-Element CRN. Temperature in the recirculation zone is kept constant at 1,800 K. 112

Figure 82: NOX Concentration as a Function of H2 Concentration in the Fuel Stream for a Fuel Mixture of CH4 and H2. Combustion temperature is kept constant at 1,800 K. 114

Figure 83: Volume of Turbulent Flame Brush as a Function of H2 Concentration in the Fuel Stream. Combustion temperature is kept constant at 1,800 K. 115

Figure 84: NOX Rate of Production from Each of the Four Pathways in the Recirculation Zone. 116

Figure 85: CH and NNH Concentration in the Turbulent Flame Brush for H2 Mixed with CH4. Combustion temperature is kept constant at 1,800 K. 116

Figure 86: CH, NNH, and N2O Concentration in the Recirculation Zone for H2 Mixed with CH4. Combustion temperature is kept constant at 1,800 K 117

Figure 87: O and H Concentration in the Recirculation Zone for H2 Mixed with CH4. Combustion temperature is kept constant at 1,800 K. 118

Figure 88: NOX Concentration as a Function of H2 Concentration in the Fuel Stream for a Fuel Mixture of H2 and CO. Combustion temperature is kept constant at 1,800 K. 119

Figure 89: NOX Production Reported as a Function of H2 Concentration in the Fuel Stream. 120

Figure 90: NOX Production Reported as a Function of H2 Concentration in the Fuel Stream for Each NOX Formation Pathway. 120

Figure 91: Radical Concentrations in the Recirculation Zone Reported as a Function of H2 Concentration. 121

Figure 92: Measured NOx Levels for Different Fuel Compositions 124

Figure 93: CRN NOx Prediction for the Described Conditions in Table 14 125

Figure 94: Comparison between CRN and Measured Values for Cases in Table 14 125

Figure 95: CRN Prediction of NOx for Alkane Cases 127

Figure 96: CRN Prediction of CO for Alkane Cases 128

Figure 97: CRN Prediction of NOx for Diluted Fuels along with Alkanes Cases 129

Figure 98: CRN Prediction of CO for Landfill Gas Cases along with Alkanes Cases 130

Figure 99: Details of NOx Formation Pathway for CH4 130

Figure 100: Details of NOx Formation Pathway for CO2/CH4 20/80 131

Figure 101: Details of NOx Formation Pathway for CO2/CH4 50/50 131

Figure 102: Formaldehyde Emission for Hydrocarbon Fuels at 1,800, 1,900, and 2,000 K 132

Figure 104: Impact of Fuel Composition in NG/H2 Blend on NOx, 1,800 K AFT, 500 K Tp, 20 ms Residence Time 134

Figure 105: Details of NOx Formation Pathways, 1,800 K AFT, 500 K Tp, 20 ms Residence time 135

Figure 106: CRN and Measured NOx and CO, 1,800 K AFT, 500 K Tp, Natural Gas 136

Figure 107: Details of NOx Formation Pathways, 1,800 K AFT, 500 K Tp, Natural Gas 137

Figure 108: CRN and Measured NOx and CO, 1,800 K AFT, 500 K Tp, 50/50 NG/H2 138

Figure 109: Details of NOx Formation Pathways, 1,800 K AFT, 500 K Tp, 50/50 NG/H2 139

Figure 110: Impact of Fuel Composition in NG/H2 Blend on NOx, 1,900 K AFT, 500 K Tp, 20 ms Residence Time 140

Figure 111: Details of NOx Formation Pathways, 1,900 K AFT, 500 K Tp, 20 ms Residence Time 141

Figure 112: CRN and Measured NOx and CO, 1,900 K AFT, 500 K Tp, Natural Gas/ 142

Figure 113: NOx Formation Pathways, 1,900 K AFT, 500 K Tp, Natural Gas. 143

Figure 114: NOx Formation Pathways, 1,900 K AFT, 500 K Tp, 50/50 NG/H2 143

Figure 115: CRN and Measured NOx and CO, 1,900 K AFT, 500 K Tp, 50/50 NG/H2 144

Figure 116: CRN and Measured NOx and CO, 500 K Tp, 50/50 NG/H2, 20 ms residence time . 146

Figure 117: NOx Formation Pathways, 500 K Tp, 50/50 NG/H2, 20 ms residence time 147

Figure 118: Temperature Contours of a Turbine Combustion Chamber. 149

Figure 119: Example of a Combustion System Divided into Several Chemical Reactors 151

Figure 120: Comparison of NOx Emissions (CRN and Experimental) at Constant Adiabatic Flame Temperature and Preheated Combustion Air Temperature (AFT = 1,850 K, preheated air temperature = 835 K) 152

Figure 121: Influence of the Different NOx Pathways to the Total NOx Emissions 152

Figure 122: Influence of the Different NOx Pathways to the Total NOx Emissions for Mixtures Methane-Carbon Dioxide 154

Figure 123: NO Emissions as a Function of the Concentration of CO2 in the Fuel (Experimental Results and CRN) 155

Figure 124: NO2 Emissions as a Function of the Concentration of Carbon Dioxide in the Fuel 156

Figure 125: NO Emissions for Early Radial Injectors Operated on a Mixture of Hydrogen and Natural Gas 157

Figure 126: Influence of the Different NOx Pathways to the Total NOx Emissions for Mixtures Methane-Hydrogen 157

Figure 127: NO2 Emissions as a Function of the Concentration of Hydrogen in the Fuel 159

Figure 128: Natural Gas NOx Emission Results Compared with "Entitlement" Levels 160

LIST OF TABLES

Table 1: Fuels to Be Studied: Dry, Clean Nominal Compositions (Volumetric Basis*) 9

Table 2: Recommended Gases and Ranges for Study 10

Table 3: Composition of Test Fuels from this Study 19

Table 4: List of Current Commercial Engines with their Approximate Combustor Inlet Pressure and Temperature, along with Estimations of Ignition Delay Times for Pure Methane, Ethane, and Propane at Specific Inlet Conditions 45

Table 5: Test Matrix for Alkane Fuels 60

Table 6: Units for Correlated Parameters 60

Table7: Estimated gc Values and Re Number 63

Table 8: Fuel Compositions for Synthesis Gas Flashback. 63

Table 9: Units for Parameters Correlated 64

Table 10: Definition of Reference Values 68

Table 11: Fuel Composition for the 16 cc Reactor Blowout Studies 71

Table 12: Parameters and Ranges Evaluated 80

Table 13: Major Reactions of NOX Formation 100

Table 14: Experimental Conditions for High-Swirl Burner Emissions 124

Table 15: Wider Fuel Composition Range Study for High-Swirl Burner Emissions 126

Table 16: Equilibrium Products of Combustion (Volume Fraction) for 1,850 K Flame Temperature for Room Temperature Reactants 161

Table 17: Definition of Reference Values for Equation 51 166

EXECUTIVE SUMMARY

Introduction

Natural gas is burned in many industrial and commercial burners, appliances, and vehicles. Burning natural gas produces oxides of nitrogen (NOx) emissions, which contribute to ground-level ozone formation and its associated health risks. NOx emissions are regulated in California. The natural gas combustion temperatures when NOx formation is the highest can be avoided by operating the burner in lean (high excess air) conditions with a good mix of fuel and air. However, while this offers the potential for low NOx emissions, lean combustion systems are prone to operatability issues, including autoignition (premature ignition of the fuel-air mixture), blowoff (the reaction cannot be sustained for various reasons), and flashback (the reaction moves rapidly into an upstream region of the fuel-air mixer). It is difficult to predict how burners will perform in these operability issues. In addition to these issues it is essential to understand and predict how different fuel composition will impact operability and emissions.

California market and regulatory pressures to reduce greenhouse gas emissions are increasing interest in renewable fuels such as landfill and digester gases, synthetic natural gas, and hydrogen, either to substitute for or mix with natural gas. Any increased fuel flexibility benefits, however, will be offset if these fuels result in reduced combustion system efficiency, increased maintenance costs, or degraded air quality. Since the current performance measures developed for natural gas were not designed for use with alternative fuel composition, it is important to learn how switching to alternative fuels would affect burner performance and NOx emissions.

Project Purpose

This project developed and validated parameters, methodologies, and criteria to help combustion system operators, manufacturers, and regulatory agencies predict the impact of varying fuel composition (fuel interchangeability) on operability and emissions from power generation systems. These methods focus on autoignition, flashback, lean blowout, and emissions of combustion systems operated on different types of fuels. The project measured combustion performance using potential alternative fuels in three burner configurations. Attention was given to systems that currently address requirements for low-emission performance but were not specifically designed for alternative fuels. The researchers assumed burner performance was directly related to fuel composition, which allowed a better understanding of the effects from using alternative fuels. Even though these fuels can potentially reduce carbon emissions, the impact on safety and air quality can now be assessed.

This project was coordinated with existing Public Interest Energy Research Program research looking at natural gas interchangeability for industrial and commercial burners, appliances, and vehicles. The gas fuel interchangeability methods resulting from this project are distinct from and complementary to already established methods. Project Results

Project Results

Traditional interchange parameters and methodologies were developed for laminar (uncontrolled burners) that were not optimized to minimize emissions. A new look at fuel interchangeability is necessary for current systems that generally (1) have control systems to maintain heat input or firing temperatures, (2) are highly turbulent, and (3) are optimized for minimum emissions.

Historic interchange parameters are limited and were designed considering simple flames and only variations in natural gas (e.g., generally the fuel was mostly methane) and renewable gaseous fuels. These burner systems are complex and different methodologies or design tools were required for different classes and configurations of burners including jet burners, jet-stirred reactors, low-swirl burners, and high-swirl burners.

Additionally, to have the broadest impact, several general "fuel classes" based on fuels that may play a role in both the near and long term within California, such as landfill and digester gases, synthetic natural gas, and hydrogen were identified to study.

Autoignition, Blowoff, Flashback, and Emissions

To be able to use different fuels, it is necessary to know how a given combustion device will respond to non-conventional fuels. The researchers conducted several experiments and, based on the results, developed predictive guidance.

To predict autoignition of hydrogen-containing fuels, using detailed chemistry calculations appear to be problematic because hydrogen, unlike the alkanes, tends to ignite at low temperature. It is recommended that correlations based on measured data be utilized for the low-temperature regimes. At high temperatures (generally above 1,000 kelvin), detailed kinetic calculations can be used reliably, which requires some experience with the use of kinetic solvers such as Cantera or CHEMKIN. Again, appropriate chemistry mechanisms are needed, and several that are available in the literature appear to work well. In addition, simple EXCEL type correlations can also be used reliably, but only for high temperatures.

For prediction of blowoff, concepts based on the ratio of physical (e.g., time of mixing of air with fuels) to chemical timescales (e.g., time for a given chemical reaction) are generally recommended. The principal challenge with this approach is associated with the appropriate value for the chemical time. This value can be determined in a number of ways (e.g., chemical kinetics software, literature correlations).

For flashback, the situation is significantly more complex than for ignition and blowoff, due in part to the several distinct modes of flashback that can occur. The configurations studied allowed evaluation of three flashback modes: (1) into the core flow, (2) along the wall, and (3) that induced by combustion vortex breakdown at the centerline of the burner. The research provides specific recommendations on how to predict flashback in the main body of this report.

Relative to emissions, the concept of "entitlement" (minimum physically possible emission levels) as a performance target is important, as it can help establish a basis for technology

improvement. In this context, entitlement is taken to mean the minimum possible emissions levels that can be expected for a given combustion condition. As a result, it can be used to establish how the emissions performance of a given system is to the best performance expected.

To predict emissions, it appears that some concepts based on simple correlations can capture some of the trends within a given fuel class. This is true for very-low-emission systems that are approaching "entitlement" levels of NOx. Likewise, the C/H ratio also appears to capture trends for very well-mixed alkane-fueled systems.

When examining hydrogen-containing fuels, conventional concepts cannot be applied. As a result, an alternative strategy is required. The methodology recommended from the present work is the use of advanced computational tools (i.e., chemical reactor networks) to predict emission behavior.

Benefits to California

Desire to reduce greenhouse gas emissions are leading to increased consideration of renewable fuels such as landfill and digester gases, synthetic natural gas, and hydrogen either to substitute for or to be interchanged with natural gas. While these fuels offer the potential for lower carbon signatures, and increased energy security, these benefits could be offset if adopting these fuels leads to an increase in pollutant emissions or a decrease in combustion efficiency. By developing fuel interchangeability methods, these benefits of alternative fuels can be gained, while still curtailing pollutant emissions. With the methodologies presented, it is possible to predict fuel composition effects on ignition delay times, blowoff, and certain types of flashback.

CHAPTER 1: Introduction

This project evaluated and/or developed parameters, methodologies, and criteria for the performance of lean premixed combustion systems as operated on a range of potential gaseous fuels. This collection of parameters, methodologies, and criteria are referred to as "gas fuel interchange criteria." This definition expands beyond the typical notion of fuel interchange criteria and therefore involves numerous potential factors. Generally, the more widely used fuel interchange criteria have focused on the supply. This is important because fuel systems and burner fuel port (hole) sizes will be affected by changes in the fuel heating value.

As a result, parameters like Wobbe Index are commonly used in the context of interchange. The context of interchange criteria was expanded in this project in order to capture how fuel composition affects burner operability (i.e., autoignition, flashback, blowoff) and emissions. Recognizing that these criteria may vary for different types of burners, it is expected that classes of criteria specific to configuration will likely be needed. This report first presents a discussion regarding burner configurations, followed by a general summary of the physics associated with operability and emissions. That is followed by discussions of specific burner configurations, with a summary of criteria considered for each type of burner.

This project was coordinated with, and expands on, the existing Public Interest Energy Research (PIER) Program looking at natural gas interchangeability for industrial and commercial burners, appliances, and vehicles. It is anticipated that the gas fuel interchangeability criteria resulting from this project will be distinct, yet complementary to already established interchangeability indices such as the Wobbe Index, which generally do not capture details regarding operability (i.e., flashback, blowoff) or emissions dependency upon fuel composition. The traditional interchange parameters and methodologies were developed for laminar, uncontrolled burners, which were not particularly optimized to minimize emissions. A new look at fuel interchangeability is warranted, with respect to current systems, which generally (1) have control systems to maintain heat input or firing temperatures, (2) are highly turbulent, and (3) are optimized for minimum emissions. One particular area of interest was predicting how variation in fuel composition impacts operability and emissions.

1.1 Rationale for Lean Combustion

Figure 1 illustrates the motivation for operating combustion systems under lean conditions. Lean strategies are being incorporated in both industrial combustion systems and advanced natural-gas-fired reciprocating engines in order to mitigate nitrogen oxide (NOx) formation. By operating lean, the combustion temperatures at which oxides of nitrogen (NO) formation rates start to accelerate can be avoided. Furthermore, the conditions desirable to oxidize unburned hydrocarbons (HCs) and carbon monoxide (CO) are also attainable. As a result, operating lean provides some obvious benefits from an emissions standpoint. Additional details are available elsewhere (e.g., Dunn-Rankin 2008). To achieve optimal conditions, the fuel and air must be

very well mixed prior to combustion. This generally poses other challenges, which are discussed in the next section.

Figure 1: Pollutant Concentration and Temperature Dependency Upon Relative Amounts of Air and Fuel (Methane/Air).

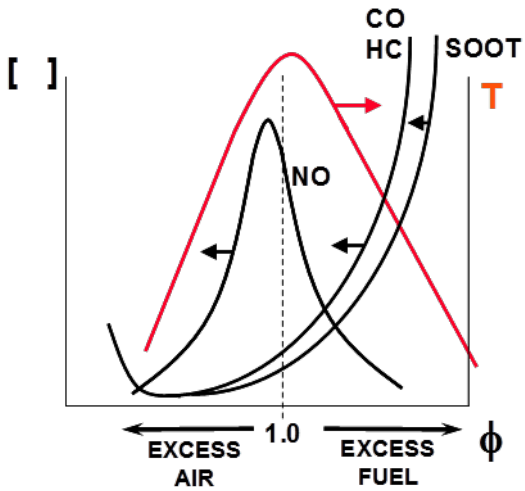

1.2 Challenges with Lean Premixed Combustion

The need to premix also leads to additional operability issues, which are discussed below. The barriers that must be overcome to achieve success with lean combustion in gas turbines can be associated with operability and emissions. Since emissions reduction is a principal driver for using lean combustion, the challenges are associated with achieving low emissions while maintaining stability, avoiding autoignition and flashback, and achieving sufficient turndown to cover the range of conditions needed to fulfill the engine's operating map. In addition to this report, consult other recent reviews of this subject (Richards et al. 2001; Lieuwen et al. 2008). Figure 2 illustrates the challenges associated with lean combustion in the context of a typical combustor "stability loop." For a given inlet pressure and temperature, the fuel-to-air ratio for a given mass flow through the combustor can be increased or decreased to a point where the combustor can no longer sustain the reaction. Limits in fuel-to-air ratio are found on both rich and lean sides of stoichiometric, at which point the reaction will no longer be stable. This locus of conditions at which the reactions are no longer sustained is shown as the "static stability limit" in Figure 2. This loop may change as temperature, pressure, or fuel composition change. Figure 2 also illustrates the presence of flashback, which can be an issue as the velocities in the fuel injector/premixer become relatively low.

Finally, discrete points often along the static stability limits are shown. These points correspond to operating conditions where combustion oscillations are problematic. Each of these operability issues is discussed in upcoming sections.

Figure 2: Illustration of Combustion Operability Issues for Gas Turbine Combustor at Fixed Inlet Temperature and Pressure.

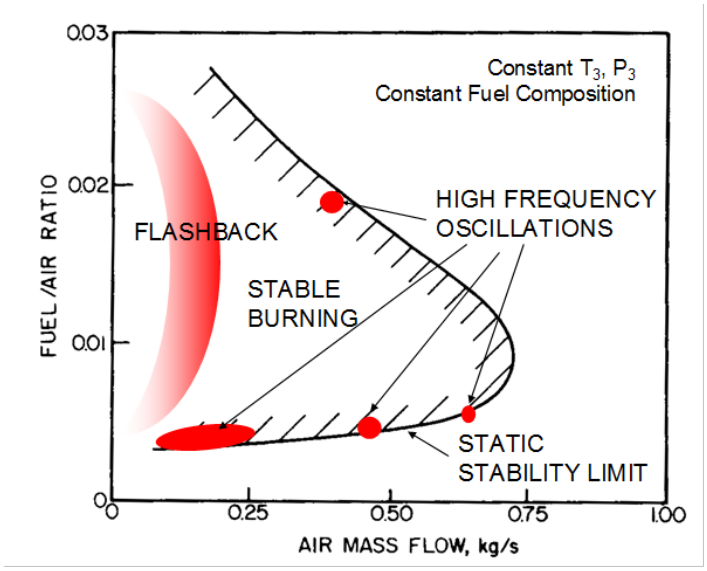

Source: Adapted from Lieuwen et al. 2008

1.3 Scope of current Effort

Predicting the details of the loop in Figure 2 is not straightforward, as it is a function of many factors. In the grand scheme, the ultimate goal for combustion engineers is to be able to predict all the aspects of this loop, including the location of combustion oscillations. However, this was beyond the scope of this project's effort. Instead, the goal was to establish design guidelines to predict how, for a given class of burner geometries, changing fuel type might affect performance in terms of blowoff, flashback, and emissions. As a result, this presumes to a large extent that experience with a given combustion system/burner has been attained, and that some knowledge of these parameters for a given base fuel is available. This is not unreasonable; most combustion systems in production or in the field have been developed and optimized for performance using natural gas. Hence the question is: if the fuel composition is changed from natural gas to another fuel type for a given system, how will operability and emissions be affected? While much of the science underlying the combustion aspect can be applied to a wide variety of combustion devices, the main emphasis is on turbulent continuous combustion systems. In terms of operability, this leads to a focus on gas turbines and industrial combustion devices. However, the methodologies associated with emissions dependency upon fuel type can also be applied to general combustion systems, including reciprocating engines. The fact that most of these systems operate under turbulent conditions is a significant factor that causes issues for application of traditionally developed interchange criteria, which were developed largely for laminar systems. Under laminar conditions, many of the key properties such as flame speed are intrinsic properties of the fuel-to-air mixture. Under turbulent conditions, these properties may depend more upon the flowfield than on the chemistry. As a result, large variations between properties under turbulent conditions and those under laminar conditions will be found.

CHAPTER 2:
Fuel Selection

Diversification of fuel choices for combustion systems can help mitigate cost fluctuations from supply and demand factors. Coupled with costs are impending regulatory pressures to consider renewable fuels and/or mitigate greenhouse gas emissions. As a result of these market and regulatory forces, the use of unprocessed natural gas, coal bed methane, landfill and digester gases, biomass and coal-derived gases (e.g., synthetic natural gas), and hydrogen is expected to increase if these fuels are readily available and economical. Benefits of increased fuel flexibility will be offset if these fuels result in reduced combustion system efficiency, increased maintenance costs, or degraded air quality.

It is difficult to determine which fuels will have the greatest impact/utilization in the future, yet it seems clear that a "poly fuel future" is important to consider. Extremes range from pure hydrogen in a "hydrogen economy scenario" to variations on natural gas either derived from fossil fuels or from renewable sources. Scenarios also exist in which blends of fuels (e.g., natural gas and biogas blends) may be used. Regardless, the sensitivity of combustion devices to variation in fuel composition, whether from local generation of fuel or from natural gas pipeline infrastructure, will need to be considered because many of these devices have been optimized in recent years to minimize pollutant emissions. This optimization generally leads to a reduction in the tolerance of the system to large variation in fuel composition.

It is not clear how gas fuel infrastructure will evolve to encompass such a future, and this is a critical question moving forward relative to how fuels might evolve. With the potential for local power generation to use fuels generated locally, it is reasonable to consider scenarios where a wide variety of fuels can be used to generate electricity and/or heat near the source of the fuel. Examples include use of agricultural waste or municipal waste as a fuel source. Wastewater treatment plants are a specific application, where the methane generated from anaerobic digestion of wastes can be used to produce both electricity and heat, which can be used entirely to operate the plant. If the feedstock capacity is large enough, such a plant could also be configured to provide fuels for transportation, such as hydrogen. An alternative to the local use of various fuels is the local cleanup/conditioning of fuels and their use in the existing natural gas infrastructure. This may seem attractive in the near term, but the cost of gas cleanup and possible pressurization requirements will affect the relative cost/benefit of pipeline injection. However, compared to other renewable options (such as wind and solar, which are intermittent), even relatively high costs may still lead gas injection to be a more economic approach to meeting renewable portfolio standard goals. Also, if pipeline insertion is used, the overall efficiency of the downstream use must be compared to the use of that gas on the site producing it. It may be possible that the site producing the gas has a large thermal need which could be met with high efficiency using a combined heat and power system It is likely that both strategies can be employed.

The use of fuels with varying composition, coupled with the sensitivity of the most advanced combustion devices to fuel composition, leads to a potentially serious combustion performance

and operability problems. Already, these problems have resulted in litigation among utilities and original equipment manufacturers (OEMs). The reasons for this sensitivity have been outlined in several articles (Richards et al. 2001; Lieuwen et al. 2008) and motivated this project, as advanced combustion systems are expected to operate robustly on various fuels and maintain low pollutant emissions.

Additional details regarding potential future fuels are provided in Appendix A.

As is evident from the discussion above, the potential fuel compositions that combustion systems could operate on are vast. However, examination of the compositions that seem most likely for California applications yields a subset of possibilities. Table 1 outlines the set of recommended fuels.

Table 1: Fuels to Be Studied: Dry, Clean Nominal Compositions (Volumetric Basis*)

SOURCE	H_2	CO	CH_4	CO_2	N_2	C_{2+}	LHV (Btu/ft^3)	Wobbe Index
High H_2	100	0	0	0	0	0	265	1,006
Process and Refinery Gas	29	11	65	5	0	0	398	603
Gasified Coal/Petcoke (O_2-blown)	37	46	1	14	2	0	247	289
Gasified Biomass (air-blown)	17	17	5	13	48	0	142	152
Gasification w/N_2 Dilution	23	31	1	10	35	0	165	183
Landfill and Digester	0	0	~65	~25	~10	0	~650	650
Higher Hydrocarbon	0	0	75	0	0	25	~1,150+	1,385+

*Nominal compositions. For purpose of this study, variations about the representative values will be examined

As noted, each nominal fuel will require some variation about the nominal composition, to reflect variation expected from the processes and feedstocks used. Note that the air-blown and O2-blown sources with nitrogen dilution appear to overlap substantially when ranges are examined, and thus they can be treated as the same general class of gas. Given the assessment presented herein, Table 2 presents the recommend "fuel classes" and the ranges of composition variation for study.

Table 2: Recommended Gases and Ranges for Study

SOURCE	H_2	CO	CH_4	CO_2	N_2	C_{2+}
High H_2	90–100	0	0–10	0	0	0
Process and Refinery Gas	25–55	10	30–65	5	0	0
Gasified Coal/Petcoke (O_2-blown)	35–40	45–50	0–1	10–15	2	0
Gasified Biomass (air blown) and Gasification w/N_2 Dilution	15–25	15–35	0–5	5–15	30–50	0
Landfill and Digester	0	0	35–65	35–55	0–20	0
Higher Hydrocarbon	0	0	75–95	0	0	5–25

While this fuel space is broad, it is also evident that it could be viewed as consisting of (1) natural gas and it variants (e.g., with higher hydrocarbons), (2) dilute natural gas fuels (e.g., digester gases), and (3) hydrogen-containing fuels (e.g., gasified biomass). The high reactively of hydrogen often creates a situation where hydrogen dominates most of the behavior of these fuels

CHAPTER 3:
Existing Interchanges Parameters and Methodologies

A detailed overview of interchange parameters and methodologies is provided in Appendix B. Generally speaking, indices established in the 1940s and 1950s for fuel interchangeability focused on laminar systems. These parameters were mainly developed for operation of things like stove flames or water heater flames which might experience modest variation in fuel composition. They are not designed for situations where pressure drop, air flow, or preheat temperature change, which is the case for many practical generation systems. For advanced turbulent low-emission systems relying on generally lean operation, these parameters are likely to not capture the overall behavior, although some concepts may be useful relative to concepts for characterizing things like blowoff (i.e., flame liftoff) and flashback. These indices may work for simple atmospheric burners for which they were developed, but it is not reasonable to expect them to work for devices such as boilers, furnaces, gas turbines, or reciprocating engines.

Many other parameters are available to predict phenomena like autoignition, blowoff, and flashback, but comprehensive consideration of fuel compositional effects is somewhat lacking. For autoignition, data covering key regions of high-pressure, low-temperature regimes is lacking. Also, the distinct nature of hydrogen ignition compared to alkanes causes a number of issues for hydrogen-containing fuels. Most correlations, or even complex kinetic calculations, rely upon assumptions like homogeneous behavior. Hydrogen does not act this way, and thus even complex kinetic calculations can provide results that are in strong disagreement with experimental results in the low-temperature, high-pressure range. Thus more work is needed in this area.

For blowoff, concepts like Damköhler number have a strong physics basis for applicability, and this seems likely to be able to predict fuel composition effects. Thus it is expected that correlations based on Damköhler number are likely to be successful. That said, correctly capturing the chemical time scale requires care. For fuel mixtures, some of the quantities needed, such as diffusivity, may not be readily available.

For flashback, different mechanisms will be present for different burner types. As a result, classification is necessary. For core flashback, concepts related to flame propagation rate are needed, but for practical systems, turbulence levels and local conditions may be difficult to know. Hence it is likely that some additional information from either experiments or simulation may be needed. For boundary layer flashback, the framework established in the 1940s has been relied upon. However, a lack of systematic variation in fuel composition is evident. It is possible, with suitable additional data that the framework can still work.

In terms of emissions, “entitlement levels” is an important concept in terms of evolving system performance. Entitlement levels have been shown as a function of adiabatic flame temperature. However, no fuel compositional variation has been considered. For a given flame temperature, concepts like C/H ratio have shown reasonable correlation with measured effects of added higher hydrocarbons. The situation for hydrogen-containing fuels is less complete. No concept

of entitlement NOx levels exists for these fuels. Also, C/H ratio cannot capture NOx trends. As a result, simple correlations are not available for hydrogen-containing fuel emission levels. The concept of chemical reactor networks appears to have promise relative to predicting emission performance.

CHAPTER 4: Interchangeability

4.1 Evaluation of Autoignition Prediction

As shown in Appendix B, considerable variation in the prediction of autoignition is evident in the literature. Particularly concerning is the disagreement between models and measured values in the high-pressure, low-temperature regime, which is where many low-emissions systems that rely upon premixing operate. As a result, this project obtained additional data to fill in missing information. Modeling approaches for predicting ignition delay in these regions are shown and validated using the data obtained.

4.1.1 Review of Key Factors

The mechanism behind autoignition is a complex overlapping series of chemical reactions and physical processes. Initially the fuel and oxidizer mixture must mix to form a homogenous mixture. If the fuel is initially in a liquid form, atomization and vaporization of the fuel must occur prior to mixing. Contact of the fuel and oxidizer initiates chemical reactions leading to formation of radical species, which consume the fuel and produce even more radicals. This self accelerating process eventually reaches a critical point where fuel is rapidly consumed, producing a great deal of heat leading to a rapid rise in temperature. This is the moment of autoignition.

The chemistry involved in autoignition can be quite complex and includes tens to hundreds of reactions, depending upon the fuel complexity. Comprehensive chemical kinetic mechanisms can describe the reaction process in detail. However, from an engineering point of view, the details of the individual reactions are less important than knowing the overall rate of the process. Therefore it has been common practice in the past to use a simple global reaction rate of the form: Fuel + Air ☐ Products, to d
obey the Arrhenius rate form shown in Equation 1:

$$RR = k[fuel]^m[oxidizer]^n \qquad \text{Equation 1}$$

k is the rate constant which is function of an activation energy and temperature:

$$k = \mathcal{B}\, exp\left(-\frac{E}{RT}\right)$$

Where:

- B is the pre-exponential factor or coefficient
- R is the universal gas constant
- E is the activation energy of the overall process

The exponential dependence of the temperature indicates that temperature is by far the most dominant parameter on the rate of reaction. The importance of the fuel and oxidizer quantity is manifested in the reaction orders m and n.

The ignition delay time of a mixture is inversely proportional to the reaction rate. In other words, a fast reaction leads to a short ignition delay, while a slow reaction leads to a long ignition delay. As a result, ignition delay is commonly correlated in the form in Equation 2:

$$\tau \, \alpha \frac{1}{RR} = \mathcal{B}^{-1} \, exp\left(\frac{E}{RT}\right)[fuel]^{-m}[oxidizer]^{-n} \qquad \text{Equation 2}$$

Dividing Equation by the fuel and oxidizer concentration, followed by taking the logarithm of both sides, gives Equation 3:

$$log(\tau[fuel]^{m}[oxidizer]^{n}) = -\log(\mathcal{A}) + \frac{E}{R} \cdot \frac{1}{T} \qquad \text{Equation 3}$$

This equation is useful when plotting ignition delay data, as will be seen later on. Plots of ignition delay data of the form (log □) vs. (1/T) will yield a s proportional to the activation energy, E. Also, the intercept of the line with the ordinate axis can be used to determine the pre-exponential factor A, as seen in Figure 3.

Figure 3: Illustration of Ignition Delay Plotted in an Arrhenius Plot

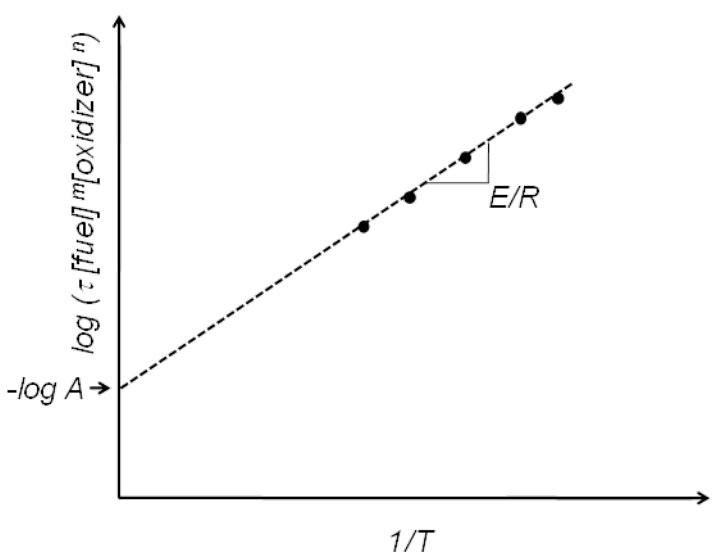

The ignition delay data (dots) form a straight line whose slope is proportional to the activation energy (E) and intercept is proportional to the constant (A). Note that higher temperatures are to the left.

The volumetric molar concentration fuel and oxidizer (typically with units [mol/cc]) can be determined using the ideal gas law shown in Equation 4:

$$[\ \ ]_i = \frac{X_i P}{RT} \qquad \text{Equation 4}$$

In many engineering applications, flow rates, pressures and equivalence ratios are more commonly reported than mixture fractions or molar concentrations. Also the oxidizer is typically air. Therefore, the Arrhenius ignition delay equation can be modified into a more manageable form for industrial use as shown in Equation 5:

$$\tau = \mathcal{A}\ exp\left(\frac{E}{RT}\right) P^b \phi^{\,e} \qquad \text{Equation 5}$$

Here A, b, and e are the pre-exponential factor, pressure exponent, and equivalence ratio exponent respectively. These are not necessarily the same values as B-1, m, and n. Expressions in this form should be most useful to a burner engineer who would like to know the ignition delay time for a given equivalence ratio, burner inlet pressure, and temperature. In this report, expressions for ignition delay time for fuel air will often be given in the form of Equation 5. When these equations are used, the ordinate of the Arrhenius plot is typically the product of the delay times and the pressure, τ•P^(-b), instead of the fuel and air molar concentrations as seen Figure 3. This approach allows for comparison between results obtained at different pressures. In most studies the pressure dependency, b, is usually found to be near unity.

4.1.2 Ignition Delay Experimental Test Bed

For the present work, a turbulent flow reactor was used to gather data because it is well suited to reach the low-temperature, high-pressure conditions encountered in many lean premixed systems within the premixing device.

In a flow reactor, a heated carrier gas (normally air) flows down a straight circular or square duct. Fuel is injected near the beginning of the duct, where it is rapidly mixed with the carrier gas. The mixture chemically reacts as it flows downstream until it reaches the end of the duct where the reactions are quenched (from injection of dilution air or water). Figure 4 shows a schematic of a flow reactor. Ideally, the flow is steady and in one direction only. This is commonly referred to in chemical engineering as a plug flow. Plug flows are also radially uniform in their velocity profile and species concentrations. Axial dispersion of products (diffusion/mixing) is rendered negligible by maintaining a sufficiently high axial (convective)

velocity, while eliminating any recirculation zones. Because of the similarity between a continuous flow reactor and a gas turbine premixer in terms of geometry and function, a number of previous studies have measured ignition delay times in flow reactors in order to access the autoignition propensity of gas turbine premixers.

The ignition delay time can be measured in different ways in a flow reactor. One method flows fuel and air under steady conditions and allows the mixture to autoignite and establishes a flame some distance downstream. The distance between the flame front and fuel injection point, L, is measured, and this value is divided by the average velocity of the flow, Uavg to obtain an ignition delay time, as shown in Equation 6:

$$\tau = \frac{L}{U_{avg}} \qquad \text{Equation 6}$$

The average velocity can be determined based on the volumetric flow rate of the gases and the cross-section area of the flow reactor, as shown in Equation 7:

$$\mathrm{U_{avg}} = \frac{Volumetric\ Flow\ Rate}{Area} = \frac{\dot{m}_{mix} R_{mix} T_{mix}}{PA} \qquad \text{Equation 7}$$

Where $\dot{m}$ is the mass flow rate, R is the gas constant and T is the temperature. Another method is to first establish a steady air flow inside the flow reactor, then inject fuel at a specific time, (t injection), and measure time when the mixture ignites, (t ignition). The difference in time between these two events is the ignition delay time, shown in Equation 8:

$$\tau = t_{ignition} - t_{injection} \qquad \text{Equation 8}$$

The time or location of the autoignition flame can be detected by means of photodiodes or photomultiplier tubes, mounted at various positions and orientations along the test section, which monitor the light emission. Data from the devices can be recorded at high speed on a computer. The readings of photodiodes can be seen in Figure 4. The photodiodes upstream of the flame do not detect light emission, whereas the photodiodes downstream do.

The first technique is referred to as the steady fuel flow method because while using this technique both the fuel and air flow are in a steady state. The latter technique is referred to as the transient flow method, as the fuel is flowing only for a brief moment during a test. An evaluation of the two methods found that measurements from either technique are usually within 20 percent of each other (Beerer and McDonell 2008).

Figure 4: Flow Reactor Schematic. Photodiodes are used to detect flame front.

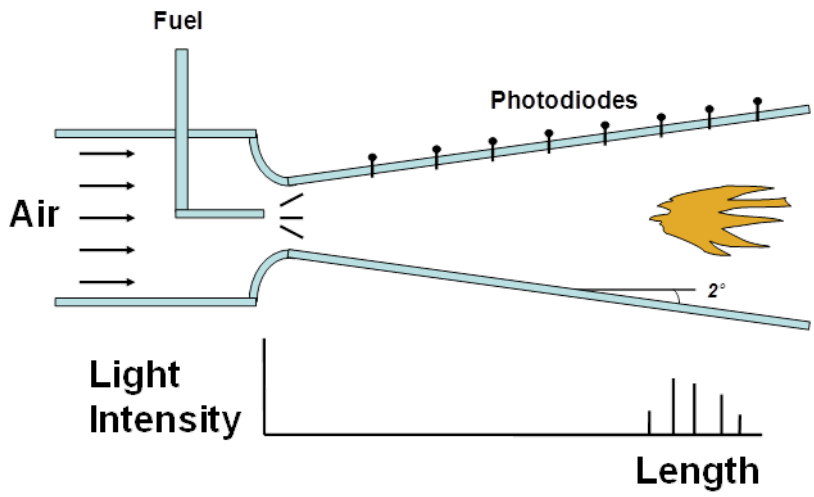

4.1.3 Results for Alkane Based Fuels

4.1.3.1 Individual Alkane Fuels

To help address the gap in data for the low-temperature, high-pressure regime, the flow reactor test bed was used to first measure the ignition properties of the individual alkane fuels that make up the majority of natural gas; that is methane, ethane, and propane. The ignition delay times of the three alkanes are presented in Figure 5. Methane has the longest delay time, ethane has an intermediate delay, and propane has the shortest delay at these conditions. Methane has the lowest activation energy in this temperature region, at only 18 kcal/mol. Ethane has the largest activation energy of the alkanes tested, at 33 kcal/mol, while propane's activation energy is in between the other two, at 30 kcal/mol. The larger activation energies for ethane and propane mean that the ignition delay times of these alkanes are more sensitive to temperature variation than is methane. At a temperature of 860 K, the propane ignition delay time is roughly 30 percent that of methane; while ethane's delay time is roughly 50 percent as long as methane's. At a temperature of 915 K, ethane's ignition delay time reduced to only 30 percent that of methane's.

Qualitatively, Figure 5 is similar to the shock tube data for the same fuels but at high temperatures (Burcat et al. 1971). Some distinct differences do exist between the two data sets. For one, the ignition delay times at the higher temperatures range from tens to hundreds of microseconds, while the delay times recorded in this study at intermediate temperatures ranged from tens to hundreds of milliseconds. Second the activation energies for these fuels at higher temperatures are larger, ranging from 37 to 50 kcal/mol, compared to 18 to 33 kcal/mol at lower temperatures. In both studies, methane is observed to have the longest ignition delay time. However, at higher temperatures, methane's ignition delay time is nearly a factor of 5 to 10 longer than the other alkanes, while at intermediate temperatures the methane's ignition delay time is only 2 to 3 times as long. Finally one other significant difference is that at intermediate temperatures, propane is observed to have a shorter delay time than ethane; while at higher temperatures, ethane is observed to have the shortest delay time. These differences indicate that the chemical kinetics responsible for autoignition in the two temperature regimes is different

and underscores the need for the data gathered in this project to help guide design in these lower-temperature regimes relevant to premixed conditions prior to combustion.

Figure 5: Ignition Delay Times of Alkanes. All results are at 9 atm and $\square = 0.6$.

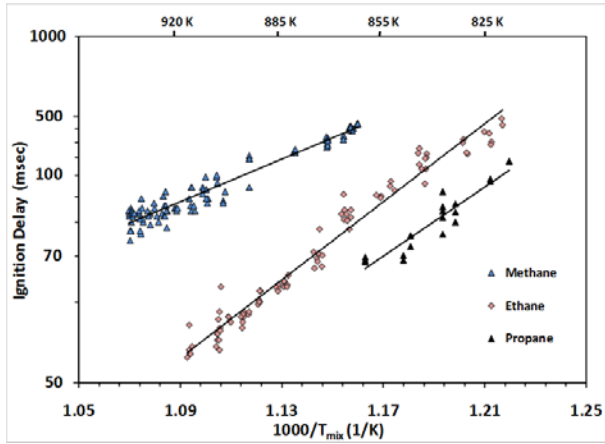

Based on the data presented in Figure 5, correlations were derived for each alkane fuel. The expressions are in the Arrhenius form, as shown in Equation 5. Because no significant equivalence ratio dependency was found, the value for the equivalence ratio exponent is zero, (i.e., e = 0). The delay time was found to be inversely proportional to the pressure (i.e., b = -1) and the activation energy, E, (see Equation 5) is presumed to be independent of pressure and temperature for each fuel.

The expressions for the three alkanes are shown in equations 9, 10, and 11:

$$\text{Methane: } \tau = 9.08 \times 10^{-5} \exp\left(\frac{18.425}{RT_{mix}}\right) P^{-1.0} \qquad \text{Equation 9}$$

$$\text{Ethane: } \tau = 5.71 \times 10^{-9} \exp\left(\frac{33.540}{RT_{mix}}\right) P^{-1.0} \qquad \text{Equation 10}$$

$$\text{Propane: } \tau = 3.29 \times 10^{-8} \exp\left(\frac{29.765}{RT_{mix}}\right) P^{-1.0} \qquad \text{Equation 11}$$

In each correlation, Tmix is the mixture temperature of the fuel and air (in Kelvin), and not the inlet temperature of the air alone. P is the absolute pressure (in atm) and $\square$ is the ignition delay time (in seconds). The activation energy, E, is in units of kcal/mol. The universal gas constant, R, is 1.987 $\square^{-3}$ kcal/mol-K.

These correlations are valid over the range of temperature between 820 and 930 K. Extrapolation to temperature outside this range may be possible, but some caution should be taken because the chemical reactions responsible for ignition may change from one temperature regime. The pressures studied in this work were between 7 and 15 atm. The inverse pressure relation held for all the fuels reasonably well over the entire temperature range studied. The chemical kinetics responsible for ignition are less likely to change with pressure as they are with

temperature, so it is likely these correlations can be extrapolated to higher pressures (up to 40 atm) without much loss of accuracy.

4.1.3.2 Alkane Blends

After verifying that the flow reactor could produce repeatable and accurate measurements for pure alkanes, the effect of fuel composition on ignition-delay, natural gas type-fuels was conducted next. A total of twelve different fuels were studied. The composition of each fuel is listed in Table 3. Fuels 1 through 3 consisted of pure alkanes; methane, ethane, and propane. Fuels 4 through 6 consisted of binary blends between methane and ethane. Fuels 7 through 9 consisted of binary blends between methane and propane. Fuel 10 is a ternary blend of methane, ethane, and propane. Fuel 11 and 12 consist of blends that simulate natural gas in the United States with smaller fractions of larger hydrocarbons (compared to mixtures 4-10) along with some diluents (nitrogen and carbon dioxide). In fact, Fuel 12 is actually Irvine natural gas taken from the local pipeline at the laboratory.

Table 3: Composition of Test Fuels from this Study

Fuel # / Volume %	**1**	**2**	**3**	**4**	**5**	**6**	**7**	**8**	**9**	**10**	**11**	**12**
Methane	100			90	85	70	95	90	70	70	89.6	96.45
Ethane		100		10	15	30				15	5.0	1.34
Propane			100				5	10	30	15	1.0	0.5
n-Butane											0.3	0.04
i-Butane											0.3	0.04
Pentane											0.3	0.01
Hexane											0.03	
Nitrogen											1.0	0.45
Carbon Dioxide											2.4	1.34

The quantity of ethane and propane chosen for the binary blends in Fuels 4 through 9 were made to approximately the fraction of these species reflected in the fuels selected in Table 2.

Testing for each fuel was conducted at standard test conditions inside the flow reactor: air flow 34 grams per second (g/s), pressure 9 atm, and equivalence ratio 0.6. These conditions could be achieved readily in the flow reactor and maintained over a course of a test. Because the conditions in the flow reactor were the same for each fuel, the difference in ignition delay time between each fuel could be confidently attributed to chemical kinetics.

The effect on the ignition delay time by adding 10, 15, and 30 percent ethane to methane (Fuels 4–6) is seen in Figure 6. All the testing shown in this figure was performed at the standard conditions of 9 atm pressure, 34 g/s mass air flow rate, and equivalence ratio of 0.6. The ignition delay times of pure methane and ethane are displayed as well. Adding ethane to the fuel is seen to reduce the ignition delay time in comparison to pure methane. The ignition delay times of all the mixtures are in between the delay time of the two constituent fuels. Also interesting to note is that the activation energy of the mixture monotonically increases as the ethane fraction increases. Correlations developed for the binary blend fuels can be found in Table C-1 in Appendix C.

Figure 6: Ignition Delay Times of Binary Methane/Ethane Blends

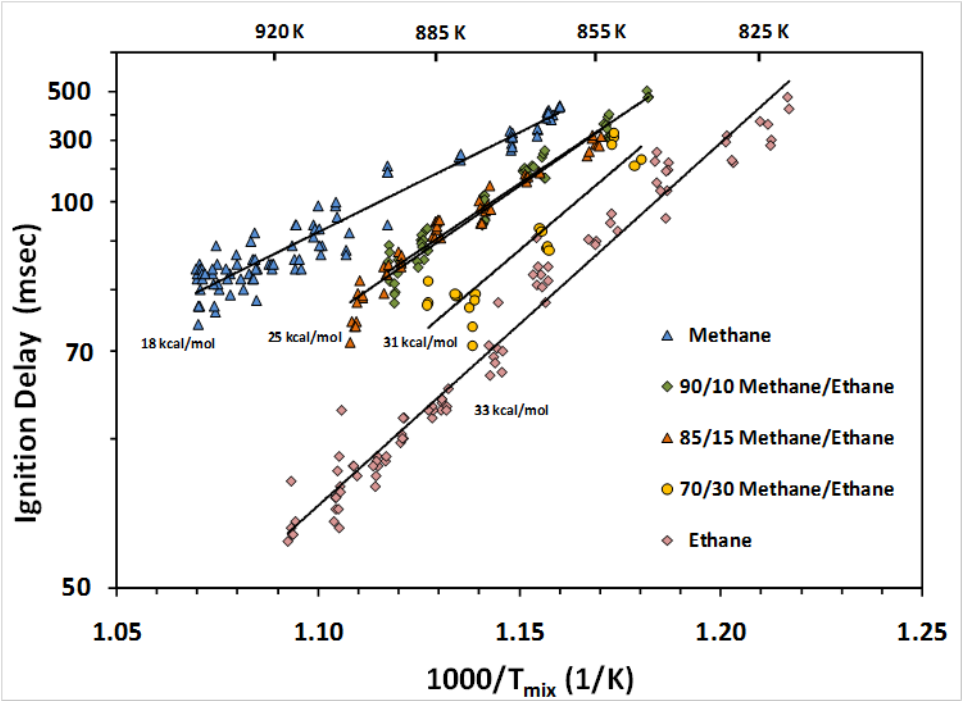

In Figure 7, the ignition delay time is plotted as a function of ethane fraction for a variety of temperatures. The curves for 850 and 950 K were obtained through the correlations developed from this study's data. The ignition delay times are also compared to binary methane/ethane mixtures at high temperatures. The curves for 1,400, 1,500, and 1,600 K were taken from kinetic simulations in the literature Westbrook (1979). Notice that mixtures with even small percentages of ethane have significantly shorter delay time than that of pure methane. As the ethane content of the fuel increases, the delay time monotonically decreases, but at a diminishing rate. The reducing effect that ethane appears to have on the ignition delay time is greater at higher temperatures than at intermediate temperatures. This is not surprising since the delay time of ethane is much shorter than methane at intermediate temperatures.

Figure 7: Ignition Delay Trends for Binary Methane/Blends as Ethane Content Is Increased

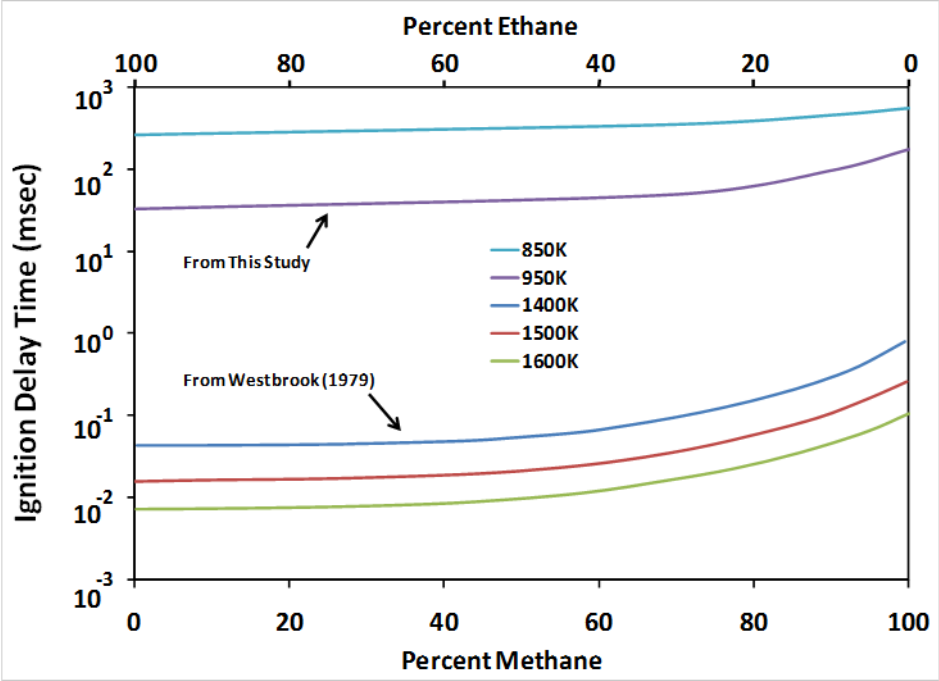

The curves from 850 and 950 K are based on data from this study, while the other curves are based on high-temperature kinetic simulations of Westbrook (1979).

Binary blends of methane and propane (Fuels 7–9) are presented in Figure 8. Mixtures with 5, 10, and 30 percent propane with methane were studied. The ignition delay times of the pure methane and pure propane are shown in the figure as well. Qualitatively adding propane is similar to adding ethane to methane. In each case, larger fractions of propane in the fuel led to shorter delay times. The delay times of the 5 percent and 10 percent propane in methane blends fall in between the delay times of the pure fuels; however, the delay times of the 30 percent propane-in-methane blend is nearly identical to that of pure propane. It appears that once the propane content approaches 30 percent, the methane kinetics have little to no influence on the ignition properties of the fuel.

Figure 8: Ignition Delay Times of Binary Methane/Propane Blends

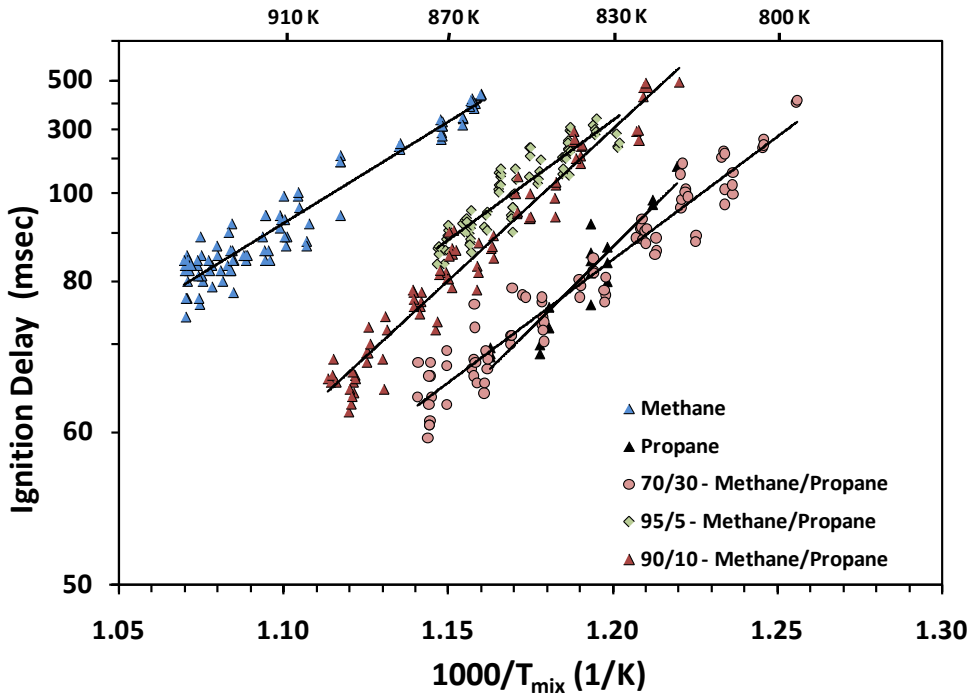

The correlations shown in Appendix C for each of the binary blends and pure fuels are presented in graph form in Figure 9 for 9 atm pressure. It is seen that the ignition delay time for the 5 percent propane-in-methane blend is shorter than the 10 percent ethane-in-methane blend. Also the delay time of the 10 percent propane blend is roughly the same as that of the 30 percent ethane blend. Propane has a greater reducing effect on the ignition delay time than ethane. That is, smaller portions of propane addition to the fuel are required in comparison to ethane to reduce the ignition delay time by the same amount. This is an important find, because while propane is usually found in smaller quantities than ethane in natural gas, its effect on the delay time can still be quite significant.

One ternary mixture (Fuel 10) was tested. The composition of this fuel was 70 percent methane, 15 percent ethane, and 15 percent propane. Figure 10 shows the ignition delay times of this fuel, along with the binary blends of 70/30 methane/ethane and 70/30 methane/propane. Notice that, for each fuel, methane makes up 70 percent of the composition by mole, and the remaining 30 percent is composed of higher hydrocarbons. The ignition delay time of the mixture with 30 percent propane content is shorter than the mixture with 30 percent ethane. Likewise, the delay time of the mixture with a 15 percent ethane, 15 percent propane split is in between the delay time of the other two. Again this trend is consistent with the finding above that propane reduces the delay time compared to ethane.

Figure 9: Ignition Delay Times (Correlations) for Binary Blends of Methane with Ethane or Propane. Correlations calculated for 9 atm pressure.

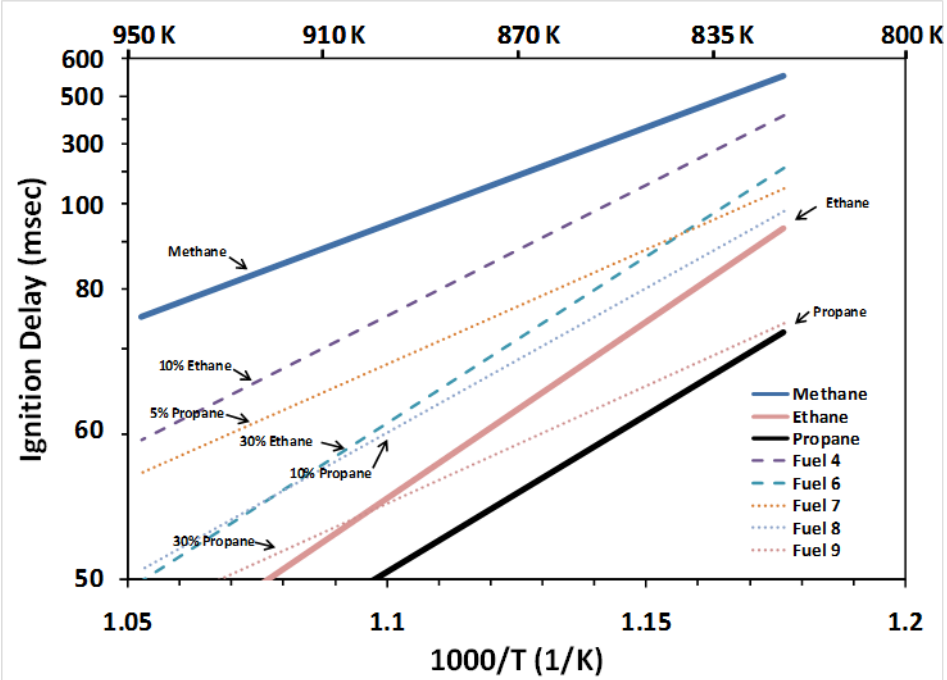

Figure 10: Ignition Delay Times of Blends of 70 percent Methane with the Remaining 30 percent Being Composed of Higher Hydrocarbons. All points are at 9 atm.

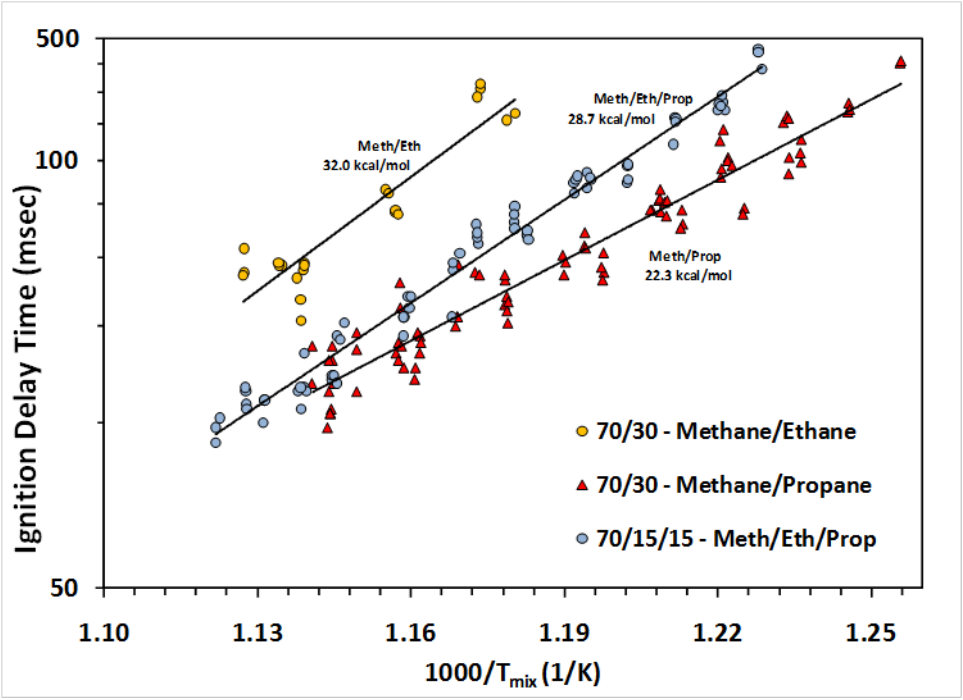

The ignition delay times of the two natural gas blends (Fuels 11 and 12) were the last to be studied. These fuels contain primarily methane, with a few percentages of ethane, propane, and diluents (carbon dioxide and nitrogen). Even larger hydrocarbons also exist in trace amounts. Figure 11 presents the ignition delay times of these fuels (at 9 atm) in comparison to the individual alkanes and the binary blend of 10 percent ethane with methane. The delay times of both natural gases are shorter than the 10 percent ethane binary blend, albeit by only a small amount at lower temperatures. Both natural gases contain less than 10 percent ethane, but have a small portion of higher hydrocarbons up through hexane. These higher hydrocarbons accelerate the ignition process significantly.

The ignition delay time of a fuel at these conditions is heavily dependent on the fuel's composition. Mixtures with as little as 5 percent propane had noticeably shorter ignition delay times than those of pure methane. This observation is in complete contrast to the shock tube study from Goy et al. (2001). Another significant difference between the shock tube results and the work from the flow reactor is the order of magnitude of the delay times. This study measured delay times from 60 to 600 milliseconds for all the fuels, consistent with the previous flow reactor results from Cowell and Lefebvre (1986) and Wagner(1990). These delay times are a factor of 10 times longer than those measured in the shock tube study of Goy et al. (2001). These discrepancies are believed to be a result of delay time being device dependent. Again, because of the similarity between a flow reactor and premixer, the results obtained in this study are much more likely to represent the delay times that will be observed in actual gas turbine premixers with these fuels at elevated pressures and intermediate temperatures.

Figure 11: Ignition Delay Times of Natural Gas in Comparison to Binary Blends and Pure Fuels

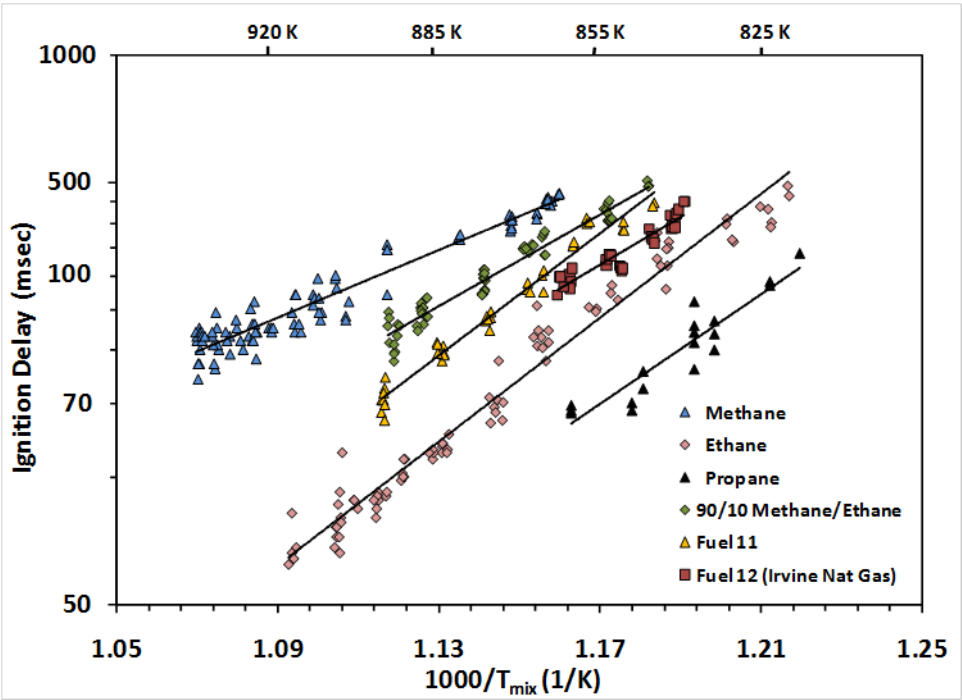

As indicated in Section 3.2.3.2, it may also be possible to correlate results using knock indices from automotive engines. Octane or cetane numbers are used to describe the relative resistance or relative ease with which gasoline or diesel fuels will autoignite. Conceptually this has been extended to gaseous fuels in the form of methane number (MN).

The MN is therefore somewhat related to the combustion properties of the fuel, such as reaction rate. It is analogous to the "motor octane number" (MON) defined for gasoline. While defined in the context of internal combustion engines for transportation, MN may also affect the performance of power generation devices located in the same distribution region.

The MON equivalent for natural gas is also related to the reactive hydrogen-to-carbon ratio of the fuel, as shown in Equation 12:[1]

$$MON = -406.14 + 508.04\left(\frac{H}{C}\right) - 173.55\left(\frac{H}{C}\right)^2 + 20.17\left(\frac{H}{C}\right)^3 \qquad \text{Equation 12}$$

Further, empirical correlations are available to relate MN to a MON "equivalent" of the gas as a measure of knock resistance according to Equation 13:

$$MN = 1.624 * MON - 119.1 \qquad \text{Equation 13}$$

Because knock (i.e., pre-ignition in a spark ignited reciprocating engine) and ignition delay are likely related, it is possible that MN or MON can be used as an indicator of relative ignition times for alkane fuel mixtures.

As shown in Figure 12, it appears that MN can be used to predict ignition delay times on a relative basis.

[1] California Air Resources Board. "Proposed Amendments to the California Alternative Fuels for Motor Vehicles Regulations." Appendix D

Figure 12: Comparison of Ignition Delay Time and Methane Number

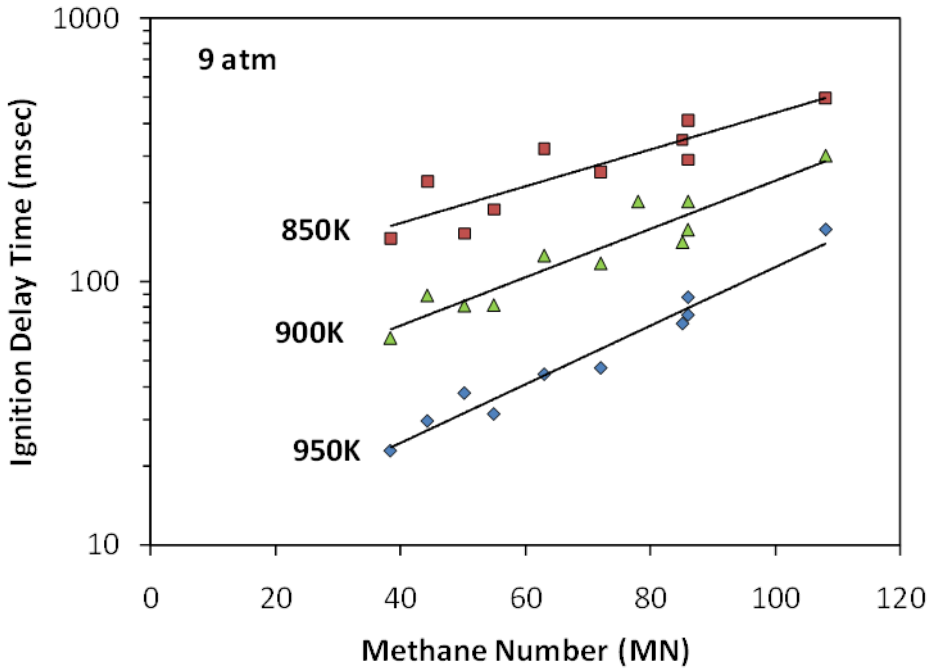

4.1.3.3 Effect of Pressure

The large difference in pressure ratio between gas turbine engines makes it important to know how the ignition delay will be affected by different inlet pressure conditions. To study this effect, ignition delay times were obtained in the flow reactor at different pressures while keeping the overall mass flow rate of the fuel and air fixed.

Figure 13 presents the ignition delay time of a methane/ethane/propane mixture (70/15/15 by volume) as a function of pressure. Overall the ignition delay time is seen to decrease with increasing pressure. For example, the ignition delay times at 9 atm are roughly 20 percent shorter than at 7 atm. The activation energy of the 7, 9, and 15 atm tests were found to be 30.7 □ 2 kcal/mol, 28.7 9□ 2 kcal/mol, and 25. □ 2 kcal/mol, re that the activation energy may be weakly pressure dependent. However given the relative uncertainty in the measurement and closeness of these values, it is difficult to truly assess this. For most of the correlations developed in this work, the activation energy is assumed to be constant over the range of pressure and temperatures studied.

Figure 13: Ignition Delay Times of a Methane/Hydrocarbon Blend at 7, 9, and 15 atm

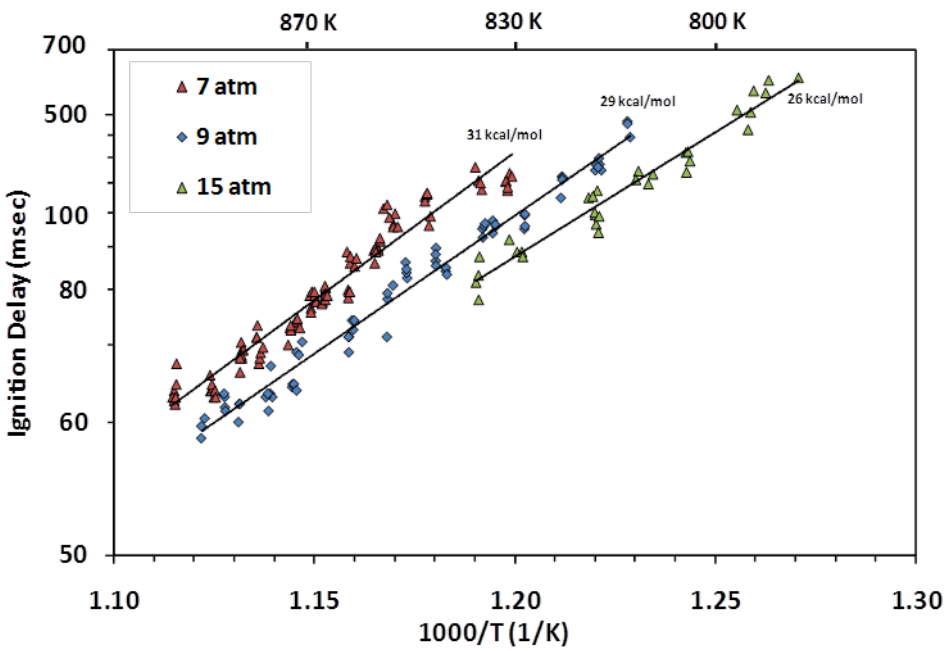

Given that the delay time is commonly proportional to temperature and pressure through the Arrhenius expression, τ ~ exp(E/RT) 〖•P〗^b, the product of the delay time and pressure Pb were plotted against the inverse of the temperature (i.e., τ P^(-b) vs. exp(E/RT)), in order to find the pressure dependency, b. The pressure exponent, b, was then systematically varied until the ignition delay points from the two tests collapsed onto a single line. As seen in Figure 1Figure 14, the value of b = -1.0 [illegible] In other words the ignition delay time is inversely proportional to the pressure.

This value is consistent with literature values. Cowell and Lefebvre (1986) found the delay times of methane and propane to be proportional to P-1.0 and P-1.2, respectively, at intermediate temperatures in their flow reactor. At higher temperatures, Spadaccini and Colket (1994) found the ignition delay of natural gas to be proportional to P-0.75. Based on the observations from this and previous studies, it was assumed that an inverse pressure dependency holds for all the fuels in this study when correlating ignition delay results. This also justifies using the P-1 scaling power to normalize the propane ignition delay data presented earlier.

Figure 14: Ignition Delay Times Conducted at Various Pressures Collapsed onto a Single Line

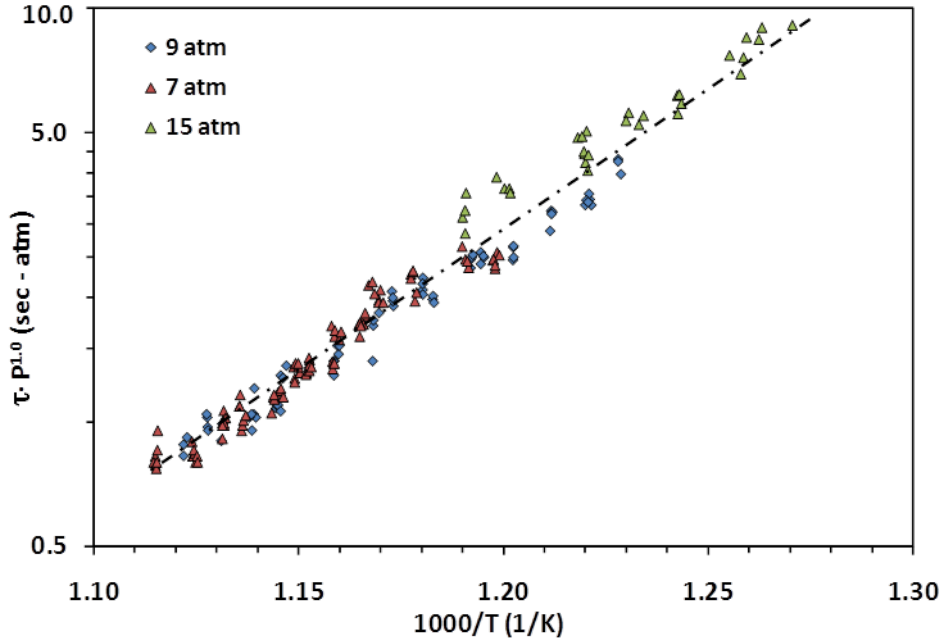

4.1.4 Results for Hydrogen Containing Fuels

The ignition delay times for the hydrogen/air ignition events are presented in Figure 15, along with shock tube and flow reactor results of other investigations (Snyder et al. 1965; Blumenthal et al. 1996; Wang et al. 2003; Peschke and Spadaccini 1985; Santoro 2009). Peschke and Spadaccini, as well as Santoro, used flow reactors, while the other investigations used shock tubes. The temperature dependency of hydrogen is quite unique. At the highest temperatures (above 1,200 K), the activation energy is very low (16 kcal/mol) but gradually rises as the temperature drops below 1,000 K. In the lower-temperature region below 900 K, the activation once again reduces. This would suggest a complex interaction between many factors (chemical or physical) unlike the alkane work, which generally exhibited constant activation energy throughout the entire temperature range studied. The current study was conducted at lower pressures than the work of Peschke and Spadaccini (1985), which may explain the relatively longer ignition delay times observed. The flow reactor work of Santoro (2009) was performed at pressures only slightly higher than the current study, and the agreement between the two studies is very good. Interestingly, all three flow reactor studies show activation energies as little as 3 to 8 kcal/mol, indicating a very small temperature dependency. Noteworthy is that Peschke and Spadaccini observed autoignition as low at 660 K, while the current study and Santoro et al. only observed autoignition at temperatures above, roughly, 750 K. Unfortunately no explanation for these differences could be determined.

Figure 15: Comparison of Flow Reactor Results from the Current Study to the Flow Reactor

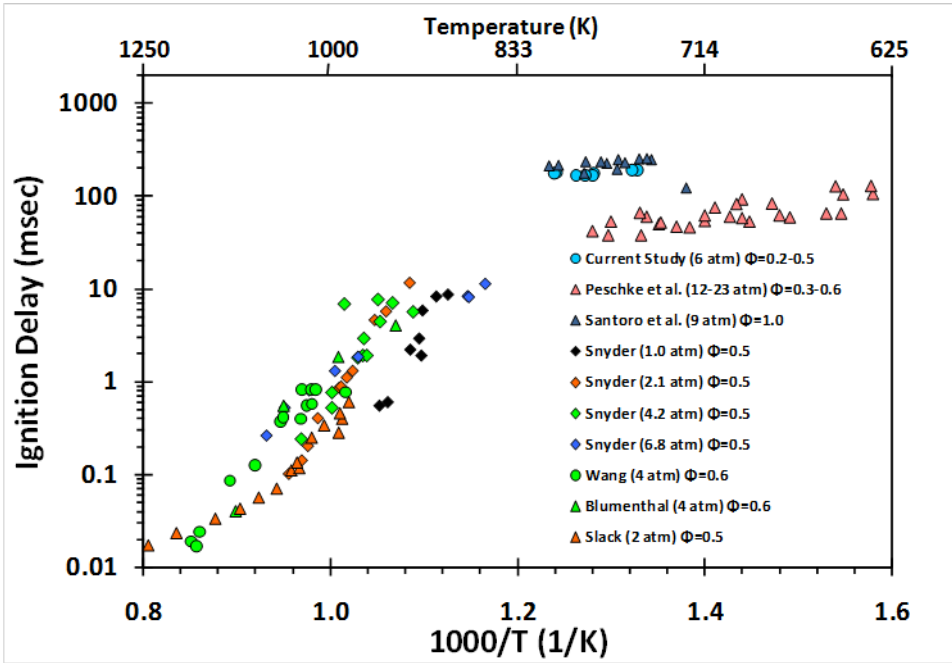

Results of Peschke and Spadaccini (1985) and Santoro et al. (2009), and the Shock Tube Results of Snyder et al. (1965), Blumenthal et al. (1996), Slack (1977), and Wang (2003).

For the low-temperature, high-pressure conditions typical of premixed conditions for reciprocating engines or gas turbines, the behavior of the ignition delay time appears to be relatively insensitive to temperature. Data obtained recently agrees well with the flow reactor work from Peschke and Spadaccini (1985), thus it appears the correlation from that work is appropriate in these regimes (i.e., 600 to 800 K up to 23 atm). For convenience, this correlation is provided in Equation 14:

$$\tau(s) \cdot [O_2]^{0.50}[F]^{0.25} = 1.29 \times 10^{-7} \exp(\frac{3985}{T}) \qquad \text{Equation 14}$$

In Appendix B, a correlation by Donato and Petersen (2008) was discussed which could presumably be applied to calculate ignition delay times. When this correlation is used to evaluate the ignition delay time for the results presented in Figure 15, it is observed that the calculated times are two to three orders of magnitude longer than the measured times. Hence the correlations provided by Donato and Petersen (2008) are not recommended for the low-temperature regime. The reason for the disparity in the low-temperature regime has to do with the sporadic nature of hydrogen autoignition, which is explored in further detail in the following sections.

4.1.5 Comprehensive Modeling of Autoignition

With advancements in combustion modeling in recent years, a modeling effort was undertaken to assess the ability of modern chemical kinetic simulations using commercially available software to predict the trends observed in the experiments from this study. The software CHEMKIN v4.0 by Reaction Design and DARS v2.0 by CD-Adapco were used to model the ignition delay inside a plug flow. The reaction between fuel and air was modeled as an isolated isobaric adiabatic reaction with only gas phase chemistry. The ignition delay time is defined in the model as the time of maximum OH radical concentration. This time also corresponds to the time of maximum temperature rise in the system.

There are a number of chemical kinetic mechanisms in the literature, and three were chosen to be used in this study. The first mechanism was GRI-Mech 3.0 (Smith et al. 2000) because of its popularity in the natural gas combustion community; however, the authors of the mechanism do warn that it was only validated for temperatures above 1,200 K. The two other mechanisms came from the combustion groups at the Lawrence Livermore Lab (LLNL) (Ribocour et al. [2000] and Galway Combustion Chemistry Centre [Petersen et al. 2007b]).

Each mechanism was developed in a hierarchical manner (Westbrook and Dryer 1984); that is, each mechanism contains elementary reactions for not only the main component fuel but smaller fuels as well. In other words, a propane kinetic mechanism also contains reactions for C2 and C1 species along with H2 and CO reactions. Therefore, these mechanisms are suitable for simulating ethane, methane, and hydrogen as well.

4.1.5.1 Modeling Autoignition of Alkane Mixtures

The Galway mechanism (Petersen et al. 2007b) was first used to simulate the ignition delay of methane, ethane, and propane at same conditions found in the ethane experiments; that is, from roughly 825 to 950 K at 9 atm with an equivalence ratio of 0.6. The simulations and experimental data are presented in Figure 16. The simulation predicts methane to have the longest ignition delay. Propane is predicted to have the shortest delay time, while ethane's delay time is in between methane and propane. This is the same trend observed experimentally.

Figure 16: Comparison between Current Study (Points) and Kinetic Simulations (Curves) at 9 atm, 820 K–920 K.

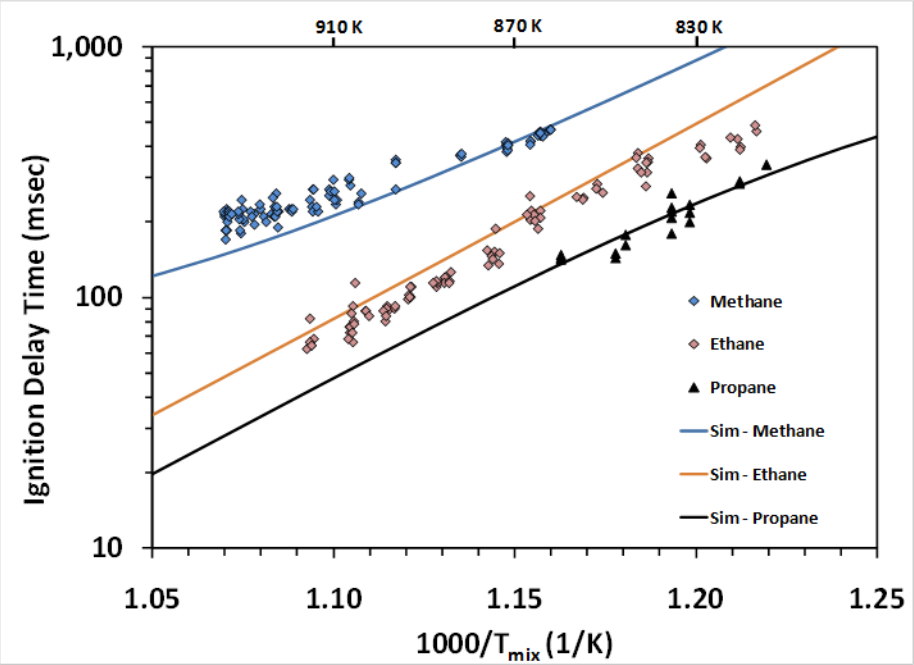

Simulations were performed using a single isobaric, homogenous reactor with an equivalence ratio of 0.6.

The simulation under-predicts the ignition delay time for methane by roughly 50 percent above 910 K, but the two agree quite well below 900 K. Between 860 and 950 K the simulation predicts the activation energy for methane to be 25.7 kcal/mol. This value is roughly 8 kcal/mol higher than that observed experimentally in this study, but is not too far off the 25.0 kcal/mol value observed by Cowell and Lefebvre (1986). The ethane simulation slightly overpredicts the ethane delay times by roughly 10 to 20 percent over most of the temperature range. The activation energy for each fuel was measured from 800 to 925 K for all the simulations. The simulation predicted ethane's activation energy to be 35.6 kcal/mol, which is quite close to the 33.5 kcal/mol measured experimentally. The propane simulation and experimental points match very well. The simulation found propane to have an activation energy of 29.8 kcal/mol from 820 to 860 K. This value is in good agreement with the measured 30 ☐ 2 kcal/mol v
at the same conditions.

Simulations were next carried out with the mechanisms from Ribacour et al. (2000) and GRI-Mech 3.0. The results of the simulations are presented in Figure 17. The GRI mechanism (dotted lines), as expected, did not perform well at these conditions. The mechanism overpredicted the ignition delay time of all three fuels (especially ethane) severely. On the other hand, the Ribacour mechanism (dashed lines) performed well. It predicts accurately that methane has the longest delay time, ethane an intermediate delay time, and propane the shortest delay time of the three fuels. In fact, the Ribacour mechanism's predictions for methane ignition delay times are within 20 percent on average of the experimental points, which is better than the Galway mechanism. However the Ribacour mechanism appears to overpredict the measured ethane ignition delay values by roughly 40 percent over the entire temperature range. The simulated

propane delay times from the Ribacour mechanism and Galway mechanism are both within 10 percent of the measurements.

In summary, the GRI mechanism is not recommended for use in ignition delay at these intermediate to low temperatures; rather such simulations should use a mechanism which specifically includes low-temperature chemistry such as the Galway or Ribacour mechanism. The remaining simulations in this report will use the Galway mechanism.

Figure 18 compares the experimental and simulated ignition delay times of the methane/ethane/propane blend at pressures between 7 and 9 atm. The simulations also found methane and propane to have an inverse pressure dependency, P-1. It is difficult to determine whether the slight disagreement is a result of uncertainties in the kinetic mechanism, experimental error, or due to the simplified modeling effort (using a single homogenous reactor). However, the overall qualitative and quantitative agreement over most of the test conditions is very encouraging.

Figure 17: Ignition Delay Simulations of Various Mechanisms in Comparison to Experimental Data

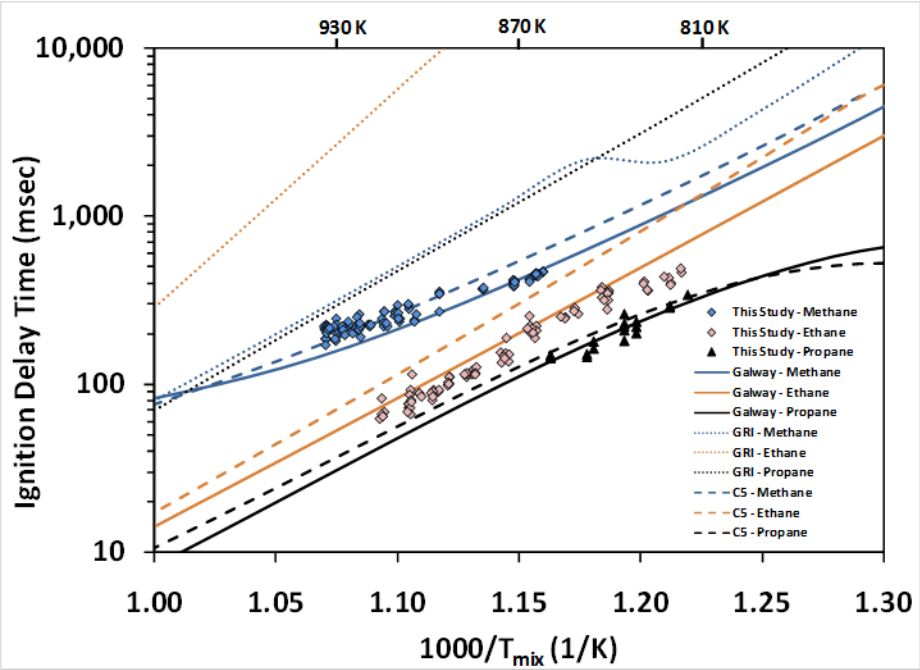

Figure 18: Simulations of Methane/Ethane/Propane Blend at Varying Pressures

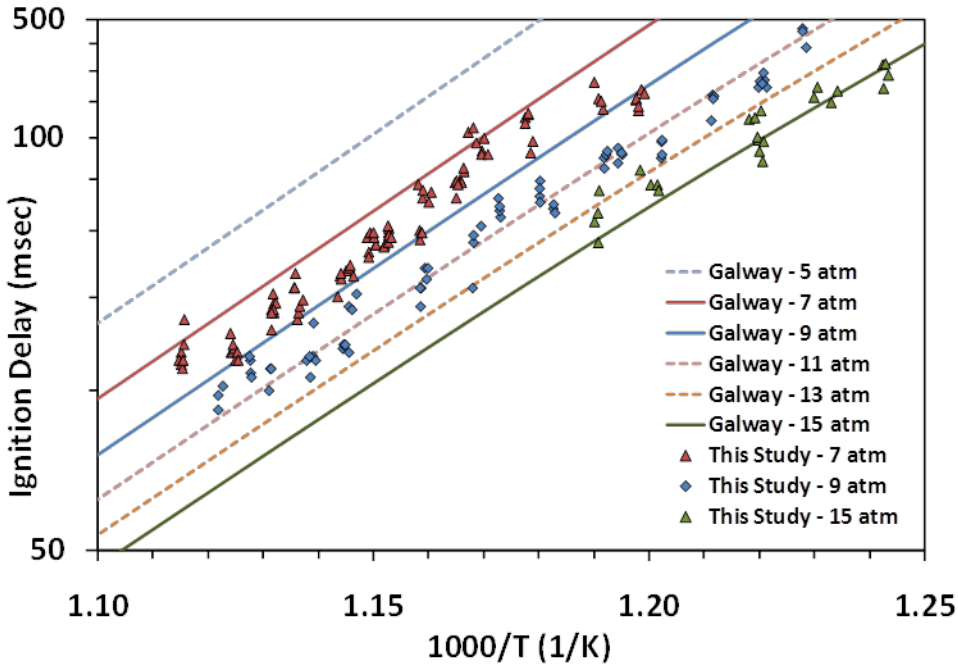

The effect of ethane and propane addition to methane was studied next in the simulation. Figure 19 presents the simulated ignition delay times of methane with 10 percent and 30 percent ethane addition (mole fraction). The experimental ignition delay measurements from this study for pure methane, ethane, and the 90/10 and 70/30 methane/ethane blend are included as well. Figure 20 presents the simulated delay time of methane with 5, 10 and 30 percent propane, along with experimental results. In both sets of simulations, ignition delay decreases monotonically as the higher hydrocarbon content is increased. The reducing effect that the higher hydrocarbons have on the ignition delay is most significant at the lower quantities. Qualitatively, these observations are the same as was observed experimentally. Additionally, the simulation predicts the delay times from this study's blends are within 30 percent on average. Also noteworthy is that the simulation predicts that for ethane quantities above 20 percent, the activation energy of the mixtures are roughly that of pure ethane. This coincides with the observation that the 70/30 methane/ethane blend has an activation energy of 32 kcal/mol which is close to the 33.5 kcal/mol measurement for pure ethane.

Overall, the kinetic simulation appears to be able to predict not only the ignition delay times of the pure fuels, but also the mixtures as well. The general agreement over the entire range of pressures and temperature studied for each fuel species suggest that the chemistry involved in the autoignition process is well understood. The incorporation of a chemical model into a CFD code that includes one of the low-temperature mechanisms should likely be able to predict the ignition delay time and position of any autoignition flame accurately.

Figure 19: Simulated and Experimental Ignition Delay Times of Methane/Ethane Blends

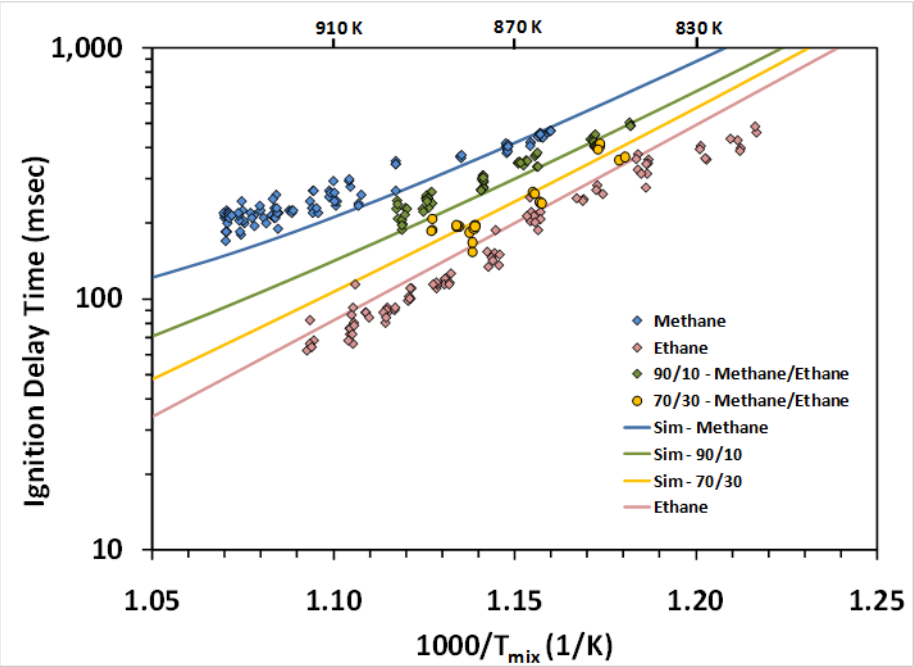

Figure 20: Simulated and Experimental Ignition Delay Times of Methane/Propane Blends

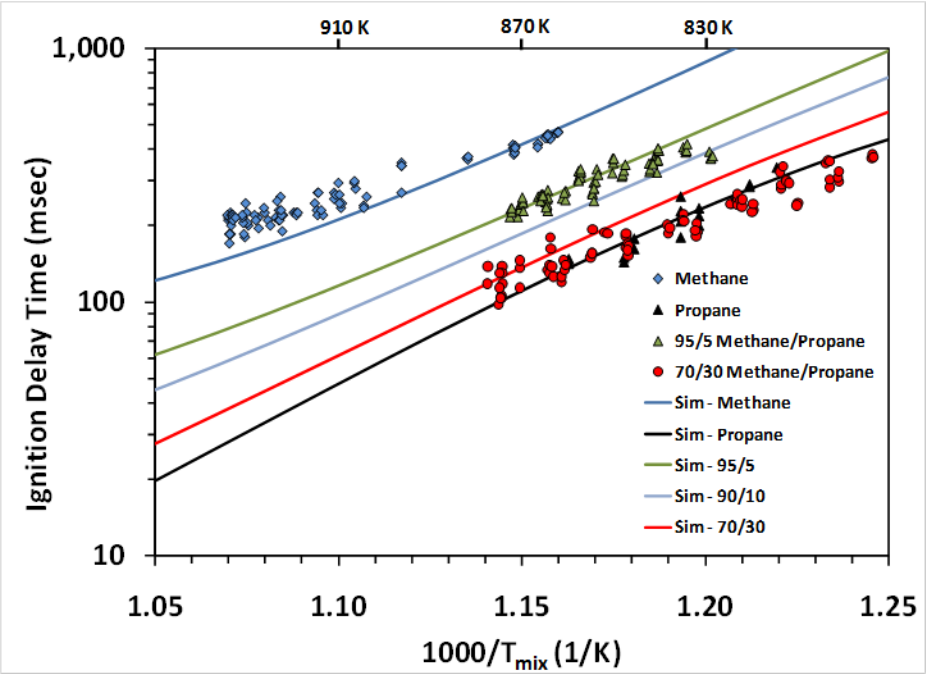

In summary, the elementary reactions that are responsible for the oxidation of the fuel and ignition vary and depend heavily upon the system's initial pressure and temperature. As a result, the autoignition behavior of each of the fuels studied can vary drastically, which explains the observed reversal of relative ignition delay time of propane and ethane at lower temperatures (seen in the current study) and higher temperatures (seen in Burcat et al.'s study), along with the smaller activation energies at lower temperatures. In spite of the complex and sometimes non-intuitive behavior, more recent chemical kinetic mechanisms are able to capture all of these autoignition features, which suggest that the chemistry is well understood at these relatively low-temperature and high-pressure combustion systems.

The work here indicated either correlations or detailed kinetic simulations (e.g., CHEMKIN, Cantera) can properly be used to estimate ignition delay times for alkane mixtures over a wide range of conditions and compositions.

4.1.5.2 Modeling Autoignition of Dilute Alkanes

Ignition delay times of mixtures of methane and carbon dioxide were simulated in the reactor model at similar inlet conditions. These fuels are intended to simulate the biogas produced at landfills or from industrial processes involving decomposition organic matter. Figure 21 shows the calculated ignition delay times of mixtures at 5 atm at an equivalence ratio of 0.6 for temperatures between 833 and 1,000 K ($1.2 < 1{,}000/T < 1$). The concentration of CO2 in the fuel ranged from 0 to 60 percent in increments of 20 percent, with the balance being methane. As with pure methane, the ignition delay decreases with higher temperatures. When CO2 is added, the ignition delay is lengthened. At all temperatures, increasing CO2 concentration monotonically increased the ignition delay time, but only by a small amount. At 1,000 K the 40/60 CH4/CO2 blend has an ignition delay time 20 percent longer than the pure methane; at 833 K, the blend's delay time is only 5 percent longer.

Figure 21: Ignition Delay Times of Mixtures of CH4 and CO2 at 5 atm. The legend indicates percent CO2 in fuel by mole/volume.

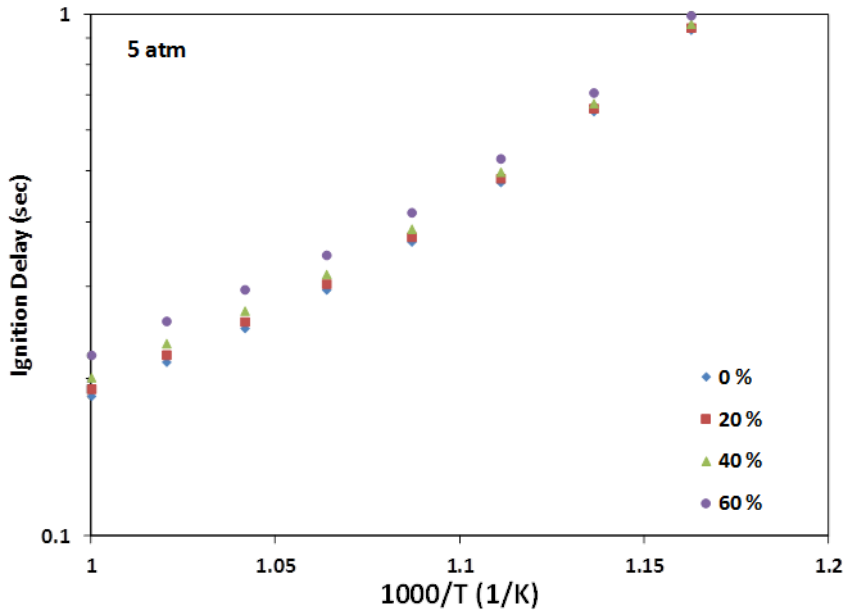

To more clearly see the effect of the diluent on ignition delay time and also pressure effect, Figure 22 shows the ignition delay of the 40/60 CH4/CO2 blend normalized by the ignition delay time of pure methane for the same inlet/initial conditions, that is, . In all cases, the value is greater than 1, which indicates that CO2 always increases the ignition delay time. At 1 atm, as the temperature increases, the delay time ratio initially increases, peaks near 930 K (1,000/T = 1.07) and then decreases slightly. At 23 atm, the ratio increases monotonically with higher temperatures. At most, CO2 addition increases the ignition delay time by 20 percent; at lower temperatures, the increase is not more than 10 percent. This dependency is of the same order as that of the pressure and temperature dependency.

Rather than carrying out additional ignition delay measurements for dilute alkanes, a review of the literature identified existing data. For example, Holton (2008) observed a 2 percent and 3 percent increase in ignition delay when he added 5 percent and 10 percent CO2 to CH4, respectively, at atmospheric pressures and inlet temperatures from 1,020 to 1,150 K. Calculations in the reactor model for 10 percent CO2 addition at atmospheric pressures showed an increase in the delay time by about 1 percent over the pure methane case. These results, along with the overall success of the model with alkane blends, validates the use of detailed kinetic calculations to determine the ignition delay time for these diluted alkanes.

Figure 22: Normalized Ignition Delay of 40 Percent/60 Percent CH4/CO2 as a Function of Pressure

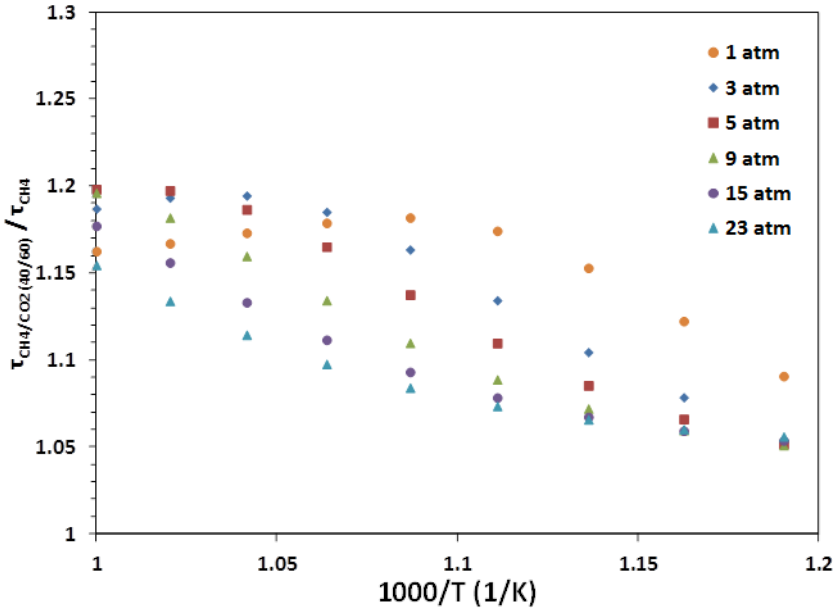

A sensitivity analysis was performed to understand how the CO2 addition affects the ignition delay time. The addition of CO2 to the mixture lowers the adiabatic flame temperature; this reduction in temperature during the ignition process ultimately reduces the reaction rate and extends the ignition delay time. The relative delay time is not uniformly extended over the range of pressures and temperatures (i.e., a 20 percent increase is seen at 1,000 K and only a 5 percent increase at 833 K) because of the changes in dominant elementary reactions involved in ignition process. At lower temperatures the chain branching from the decomposition of hydrogen peroxide via a third body, M,

$$H_2O_2 + M \rightarrow OH + OH + M \qquad \text{Equation 15}$$

will slow down. Without the H2O2 decomposition, the ignition process becomes dominated by the peroxy radical (compound involving molecules containing O2—CH3O2 in Equation 16) reactions. For methane, the reaction

$$CH_3 + O_2 + M \rightarrow CH_3O_2 + M \qquad \text{Equation 16}$$

will influence the delay time. Nitrogen has the highest concentrations, but has fairly low third-body (i.e., "M"--a molecule which does not change composition in the reaction) efficiency relative to influencing the reaction. Carbon dioxide has an efficiency that is an order of magnitude higher. Holton (2008) reports that the reaction

$$CH_3 + O_2 + CO_2 \rightarrow CH_3O_2 + CO_2 \qquad \text{Equation 17}$$

is 10 times faster than

$$CH_3 + O_2 + N_2 \rightarrow CH_3O_2 + N_2. \qquad \text{Equation 18}$$

As a result, as the CO2 concentration is increased the augmentation of the reaction by CO2 counterbalances the overall reaction rate (due to the lower reaction temperature) such that the overall increase in ignition delay time is moderated. At higher pressures, the temperatures where peroxy (R-O2) reactions become dominate increases such that the overall increase of the ignition delay time at higher pressures is less than at lower pressures. For instance for the 40/60 CH4/CO2 mixtures at 920 K, the delay time is 18 percent longer at 1 atm and only 8 percent longer at 23 atm versus their corresponding methane delay times. However, even when the concentrations are as high as 60 percent CO2, the relative concentration of N2 to CO2 is still eight times higher, for an equivalence ratio of 0.6. Therefore the relative changes are still fairly small, and thus manifest themselves in changes of only a few percentage of the overall ignition delay time.

As a result, while it would appear that diluents might dramatically increase ignition delay times, for practical purpose it appears that using results and models for alkane mixtures would be appropriate, considering that some safety margin will generally be desired. Generally speaking, fuels diluted with inerts will pose much less of an autoignition risk than undiluted fuels.

4.1.5.3 Modeling Hydrogen Autoignition

Hydrogen autoignition was modeled using the same Galway mechanism and plug flow reactor used in the alkane simulations. The simulated ignition delay curves for pressures between 1 and 10 atm are shown in Figure 23. Hydrogen's ignition delay times are seen to be highly dependent upon both the pressure and temperature. At higher temperatures (above 1,100 K), the overall activation energy for all pressures is roughly 17 kcal/mol. When the temperature is lowered to around 1,000 K, the activation energy increases to roughly 100 kcal/mol, while below approximately 900 K the activation energy reduces to 45 kcal/mol. The activation energy for each region is labeled in Figure 23. The transition from one region to another is pressure dependent. The simulation predicts that the transition from one activation energy region to another will shift to high temperatures with increasing pressure. At higher temperatures, the delay times decrease monotonically with increasing pressure. But in the 100 kcal/mol region the reverse is true. In the 45 kcal/mol region, the ignition delay times are seen to once again monotonically decrease with increasing pressure.

The shock tube data obtained by Snyder et al. (1965), Bhaskaran et al. (1973), Slack (1977), Blumenthal et al. (1996), and Wang et al. (2003), also exhibit an activation energy transition as a

function of pressure and temperature. Quantitatively, the shock tube data and simulation are in agreement in the high-temperature (17 kcal/mol activation energy) region. However, the shock tube ignition delay times at lower temperatures, after the transition from the 100 kcal/mol activation energy region, are several times shorter than the simulation. Also perplexing is that all of the flow reactor work (the current work; Santoro et al. 2009; Peschke and Spadaccini 1985) report ignition delay times orders of magnitudes shorter than the simulation's. The activation energy of the flow reactor data is roughly 3 to 8 kcal/mol—much less than the simulation's 45 kcal/mol.

Figure 23: Comparison of Experimental Hydrogen/Air Ignition Delay Measurements to Homogenous Simulations Using the Kinetic Mechanism from the Galway Group

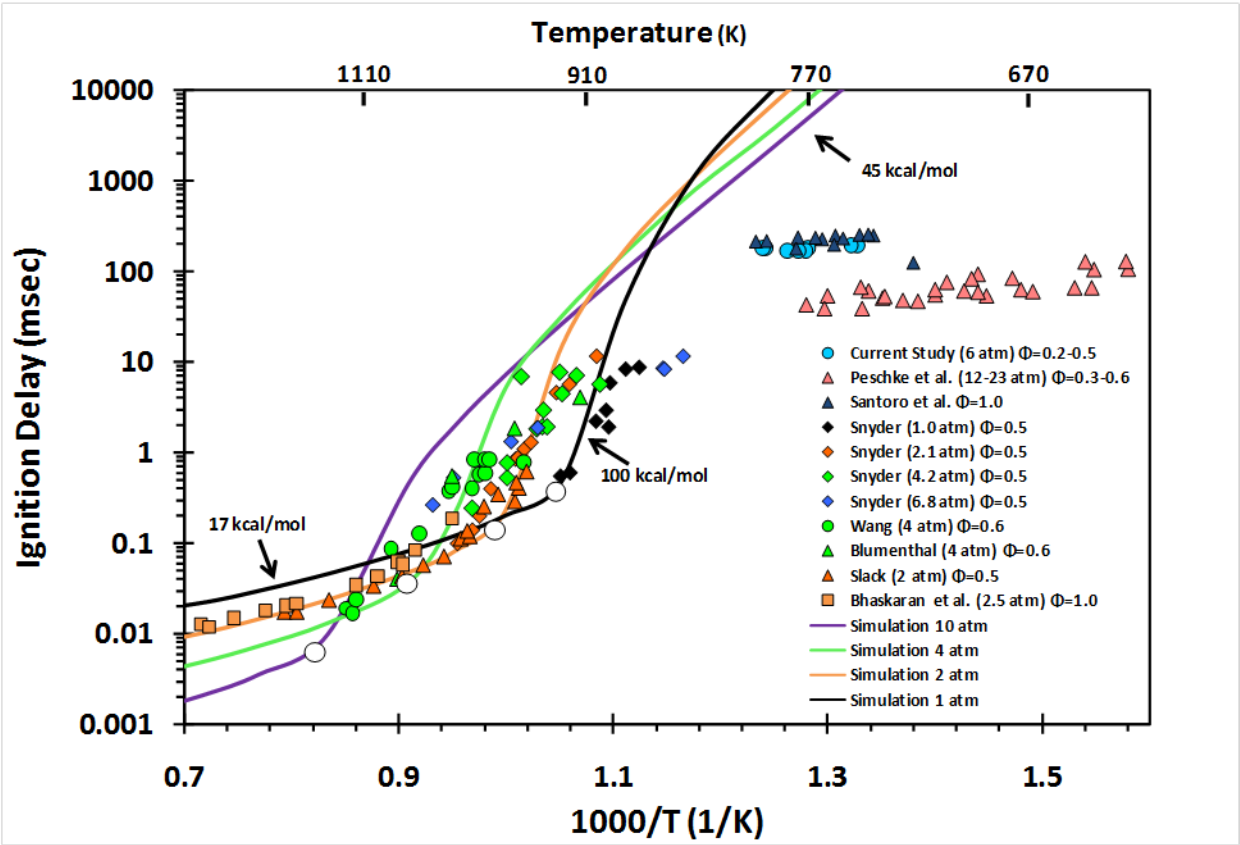

The reason for these discrepancies is not known with any confidence and is still an open question. The short ignition delay times for the shock tube at intermediate temperatures are reminiscent of the methane results from de Vries and Petersen (2007) and Huang et al. (2004). One could possibly argue that the non-idealities present in low-temperature shock tube data from hydrocarbons fuel experiments also effect hydrogen (Dryer and Chaos 2008). However this does not explain why the flow reactor results disagree with the simulation. In spite of this, the dominant chemistry involved in hydrogen autoignition is believed to be well understood and can explain some of the trends observed in the simulation and experimental data (Yetter et al. 1991, 1992).

At high temperatures, the chain branching of the system is dominated by the elementary reaction: H + O2 □ OH + O. This re
(Mueller 2000), which is similar to the overall activation energy of the hydrogen simulation at high temperatures (17 kcal/mol). The O and OH radicals formed from this step react with the following branching reactions (Equation 19 and Equation 21) to further increase the radical pool:

$$O + H_2 \rightarrow H + OH \qquad \text{Equation 19}$$

$$OH + H_2 \rightarrow H + H_2O \qquad \text{Equation 20}$$

$$O + H_2O \rightarrow OH + OH \qquad \text{Equation 21}$$

The fast radical formation from these reactions results in very short ignition delay times for mixtures in the branched chain explosive region. Upon crossing into the thermal/chain explosive region, the recombination reaction H + O2 + M □ HO2 radicals for H2 radicals competes
and produces the HO2. The HO2 radicals formed react with themselves or with molecular hydrogen to form H2O2, which decomposes into two reactive OH radicals (Equation 22 through Equation 24):

$$H_2 + HO_2 \rightarrow H_2O_2 + H \qquad \text{Equation 22}$$

$$HO_2 + HO_2 \rightarrow H_2O_2 + O_2 \qquad \text{Equation 23}$$

$$H_2O_2 + M \rightarrow OH + OH + M \qquad \text{Equation 24}$$

The radicals formed from this sequence can combine with the previous reaction steps to increase the radical pool. However the addition of this latter reaction sequence reduces the overall rate of reaction. These reactions are, however, highly exothermic, which can increase the system's temperature to the point that the system passes back into the branched chain explosive region (Yetter et al. 1991, 1992). This exothermic process provides the name for this region's name; that is "thermal/chain" explosive region.

The activation energy of the hydrogen peroxide decomposition reaction is 45.5 kcal/mol, which is quite close to the overall ignition delay activation energy in the lower temperature range (45 kcal/mol). The similarity of the dominant elementary reactions in the branched chain explosive region and thermal explosive region to the overall activation energy of the hydrogen ignition delay at high and low temperature, respectively, suggest a relationship between them. To demonstrate this relationship, the pressures and temperatures where the transition from the 17 to 100 kcal/mol occurs in Figure 23 (marked as white circles) are also plotted on the hydrogen/oxygen explosive limits chart in Figure 24 (again marked as white circles). The

pressure and temperature of this transition region fall on the extended second-limit boundary, as seen in Figure 24. Hence the transition from the 17 to 100 kcal/mol region is a result of crossing the extended second limit. It is curious that the overall activation energy does not transition directly from 17 to 45 kcal/mol. No definitive reasons as to why the system temporally exhibits a region of 100 kcal/mol could be found.

Figure 24: Hydrogen-Oxygen Explosion Limit Chart with Experimental Test Conditions Identified. The shaded region represents typical gas turbine combustor inlet temperature and pressures.

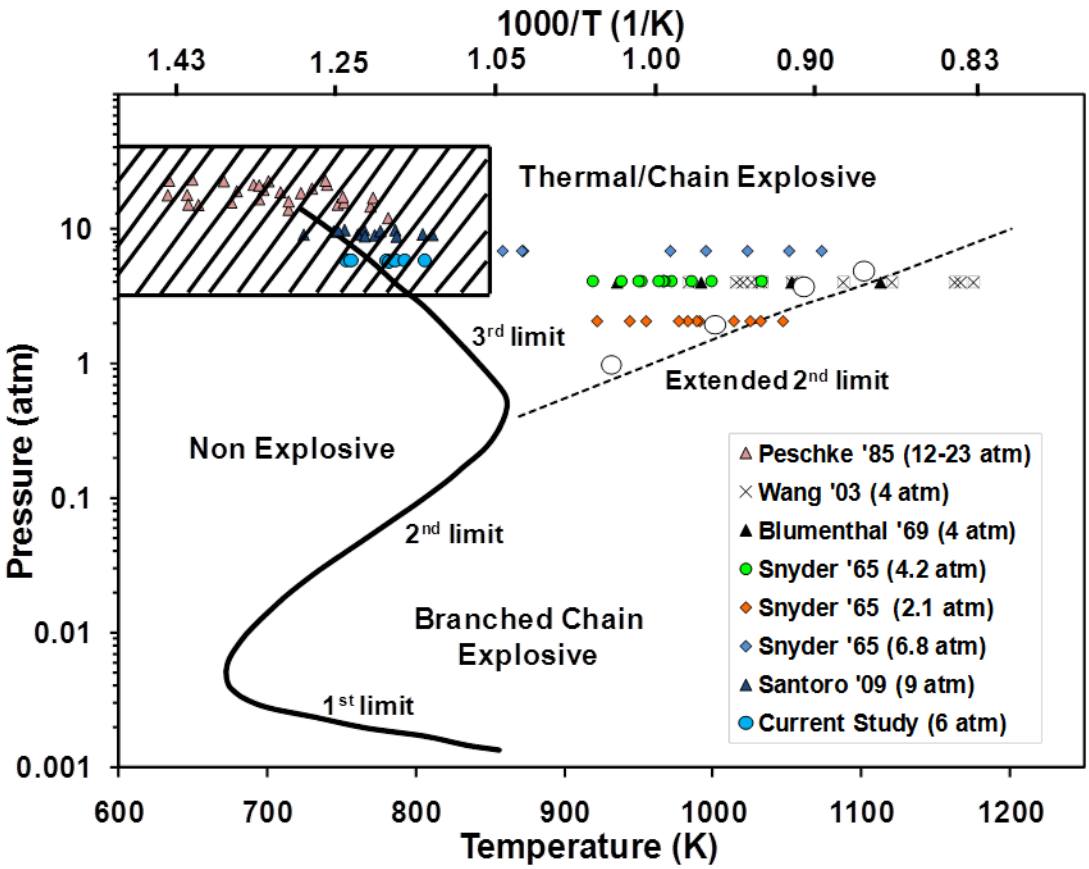

Identifying the dominant reaction steps helps explain some of the trends seen in Figure 23. At high temperatures, where ignition delay times are inversely proportional to pressure, all the simulated initial conditions of the fuel/air mixture are within the branched chain region. On the other hand, around 1,000 K the ignition delay time is seen to be shorter at 1 atm than at higher pressures (2, 4, 10 atm, etc.) which is a result of the 1 atm event starting in the relatively fast branched chain region, while the other events start in the slower thermal/chain explosive route. Once all the simulations are all within the thermal/chain explosive region (about 800 K), the ignition delay is once again seen to be inversely proportional to pressure. The pressure relation is a result of the hydrogen-peroxide decomposition step itself being directly proportional to pressure. This complex behavior should make one wary of extrapolating hydrogen correlations

to pressures and temperatures well outside the region in which they were derived, as the dependency can change rather dramatically.

All flow reactor testing was performed in the region close to the third limit, which divides the thermal/chain explosive region from the non-explosive region in Figure 24. The shock tube data span both the thermal/chain explosive region and the branched chain region. Like the simulation, the experimental data points also show a large increase in the activation energy upon crossing the extended second limit. The high temperature shock tube data (in the branched chain explosive region) both qualitatively and quantitatively agree with the simulation. However, the shock tube and flow reactor ignition data (for mixtures of fuel and air with initial conditions within the thermal/chain explosive region) are overpredicted by simulation.

The model's ability to reproduce the alkane ignition points at intermediate temperatures would hint that similar agreement could be obtained with hydrogen. However, this clearly is not true. Because the disagreement only occurs in the thermal/chain region where HO2 and H2O2 is dominant, one may draw the conclusion that the discrepancy could be due to uncertainties in these specific elementary reaction rates. However, Sabia et al. (2006) analyzed these reactions using sensitivity analysis and concluded that unrealistic modifications to the rate constants would be required in order to better match the experimental work of Snyder et al. (1965). Also any large modification to the reaction rates would almost certainly affect the simulation's ability to predict alkane ignition delay as well. Dryer and Chaos (2008) agree with this conclusion and argue that the short measurement ignition delay times are an experimental artifacts. For the case of low-temperature shock tube experiments, they cite Voevodski and Soloukhin (1965) along with Meyer and Oppenheim (1971). Both studies observed, through high-speed photography, that hydrogen ignition features randomly spaced ignition kernals in the end gas at these intermediate temperature regions, rather than a clean spatially uniform homogenous event behind the shock. They believed that the inhomogeneous ignition at intermediate temperatures (in the thermal explosive region) were due not purely to chemical kinetics but also to small mixture inhomogeneity in species concentration or temperature. Pang et al. (2009) have also suggested that boundary layer build up or bifurcation of the shock could also create these inhomogeneous regions in shock tube that could lead to early ignition events.

High-speed photography was not available in the current study, so no definite conclusions can be made as the source of the very short ignition delay times in flow reactors. The low activation energy of the flow reactor data from all three works, (the current study; Santoro 2009; Peschke and Spadaccini 1985) is low and is rather suspicious. The repeatability of hydrogen ignition delay times has been reported to be poor in comparison to alkane fuels. It is possible that some unknown mechanism could be initiating the autoignition event in hydrogen; say perhaps static electricity build up or possible catalytic effect with the wall. Dryer and Chaos (2008) also suggest that the finite time for mixing in the venturi could alter the rate the radical pool grows during the induction period. The CFD and flow measurements on the rig did find that a small separation zone existed in the venturi. However this appears to have not an effect on the alkane measurements, as their experimental values agreed well with the simulation. Hydrogen is

perhaps much more sensitive to any small perturbations in the plug flow. Further work is still definitely warranted in this region, as many questions still remain unanswered.

In terms of commercial application, the hatched region in Figure 24 represents the inlet temperature and pressure conditions where most gas turbine premixer currently operate. Unfortunately this hatched region falls in the area where all these hydrogen autoignition discrepancies occur. The ramifications of these results for hydrogen and alkane on commercial application are discussed in the next section.

4.1.6 Summary

Both a flow reactor and premixing chambers contain a turbulent air stream in a cylindrical duct in which fuel is injected, mixed, and convected downstream at a high velocity before the mixture autoignites. The similarity between the two devices would suggest that the ignition delay times that will be encountered in gas turbine premixers will likely be quite similar to those observed and measured in a flow reactor experiment. While the disagreement between measurements in flow reactors and shock tubes may be of much academic interest and still unresolved, for the gas turbine engineer, what matters most is a reliable method for predicting the ignition delay time inside his or her premixer. For this reason, ignition delay correlations developed in the flow reactor experiments are a useful design tool for predicting autoignition in premixers. It is noteworthy that the experimental results obtained in the present work are well predicated using homogeneous chemical kinetic simulations. It is equally noteworthy that only if appropriate kinetic mechanisms are used is such agreement realized. Specifically, GRI-Mech 3.0 was found to significantly overpredict the delay times at the conditions of interest.

To provide an efficient means of applying the results from the present work, simple ignition delay correlations were developed for each of the twelve alkane mixtures studied in the form:

$$\tau = \mathcal{A}\ exp\left(\frac{E}{RT}\right) P^{b} \phi^{e} \qquad \text{Equation 25}$$

These correlations can be found in **Table C-1** in Appendix C. In addition to just these correlations, general expressions for the pre-exponential factor, A, and the activation energy, *E*, have were empirically derived as a function of fuel composition. These expressions can be found in **Table C-2** in Appendix C.

Unlike the ignition delay correlation developed by Spadaccini and Colket (1994) for natural gas, results from the current work found that at gas turbine conditions, grouping all the higher hydrocarbon content in a single term, (HC), would be inadequate to describe the ignition delay time because each higher hydrocarbon affects the ignition delay time differently. Additionally, the activation energy was found to vary as a function of the fuel composition, something which was not observed at higher temperatures. For this reason, the correlation expression derived in Table C-2 in Appendix C are based on activation energies, E, and pre-exponential factors, A, that are functions of the specific fuel composition.

When the fuel contains hydrogen, it dominates the ignition process. The correlation provided in Equation 14 is appropriate for estimating the autoignition delay time for fuels with hydrogen.

In order to demonstrate their applicability, the correlations for pure methane, ethane, propane, and hydrogen were used to evaluate the ignition delay time at premixer inlet conditions for a number of gas turbines in commercial use today. These delay times indicate how long of a mixing time can be tolerated before autoignition occurs if one of these engines were to hypothetically use one of these fuels in operation.

As an example, the Solar Mercury 50 has a premixer inlet temperature and pressure of 880 K and 9.9 atm. The correlations estimate the ignition delay of methane, ethane, and propane at these conditions to be 266 ms, 123 ms, and 82 ms, respectively. Therefore the premixing time for the Mercury 50 should not exceed the delay time calculated here for each fuel. In most engines the mixing time is typically 1–5 ms (Lieuwen et al. 2008), so the delay times calculated here suggest that autoignition does not pose a significant problem in most cases. However, this simple analysis involves numerous assumptions. As stated by Lieuwen et al. (2008):

> *"The time scales associated with physical mixing in the current low emissions is on the order of 1 to 5 milliseconds, based on the bulk velocities and premixer volumes. However, it should be recognized that the complex aerodynamics associated with swirl, separation, and strong gradients can make it difficult to assign a single time scale to represent the physical premixing time in a given system. Even if a very small fraction of the mixture has a longer residence time, spontaneous ignition of that mixture can lead to ignition of the entire mixture within the premixer."*

The engine application analysis illustrated in Table 4 implies that the premixer design has aerodynamically "smooth" passages without any large recirculation zones or wake regions. Given these assumptions, this study finds that such fuels (assuming they are clean, dry, in the gaseous phase, and contaminant free) should not pose a significant hazard in terms of premixer autoignition for future gas turbines.

Table 4: List of Current Commercial Engines with their Approximate Combustor Inlet Pressure and Temperature, along with Estimations of Ignition Delay Times for Pure Methane, Ethane, and Propane at Specific Inlet Conditions

Engine	Pressure	Inlet Temp	τ (msec)	τ (msec)	τ (msec)	τ (msec)
	atm	K	CH_4	C_2H_6	C_3H_8	H_2
GE 9H *	23	705	2,036	6,213	2,421	85
Solar Taurus 65	15	670	6,205	33,277	11,264	153
Solar Taurus 60	12.3	644	13,232	112,220	33,876	221
Solar Mercury 50 **	9.9	880	346	123	82	59
GE LM 6000	35	798	289	251	134	35
Siemens V-94.3A*	17.7	665	5,835	34,082	11,293	141
Siemens V-94.2*	12	600	38,988	786,278	191,174	336
Capstone C60 **	4.2	833	1,477	859	506	140
Alstom G24/26 EV Burner *	30	815	264	188	105	35
Alstom G24/26 SEV Burner ***	15	1,300	1.65	0.07	0.104	0.003

* Inlet estimated from ideal gas isentropic compression

** Recuperated Engine Cycle

*** Re-heat burner, used CHEMKIN and Galway Mechanism to calculate τ with φ = 0.6

τ for alkanes calculated from correlations in Beerer et al. (2011)

τ for hydrogen calculated from correlations in Peschke and Spadaccini (1985)

4.2 Evaluation of Blowoff/Flashback Prediction

4.2.1 Review of Key Factors

4.2.1.1 Blowoff

Blowoff is a significant operability issue, especially for low-emission systems that tend to operate close to the lean stability limit to keep reaction temperatures low. From review of the literature and the candidate parameters, a Damköhler number approach is recommended as a strategy to predict fuel interchange in this regard. As a result, this ratio of chemical to physical time scales is evaluated for several burner configurations and conditions to explore the general applicability of this concept for predicting blowoff.

4.2.1.2 Flashback

Flashback (FB) issues for current combustion systems have proven to be highly problematic, but mainly for high-hydrogen-content fuels. As a result, emphasis in the flashback prediction evaluation is given to fuels with hydrogen. By way of example, in the testing involving the Capstone microturbine generator, tests with mixtures of natural gas and ethane were carried out, varying the amount of ethane up to 100 percent. Under no operating conditions was flashback observed with ethane in any amount. In contrast, flashback was observed with as little as 10 percent hydrogen by volume in natural gas for certain conditions. Similarly, for the simple jet flame it was difficult to attain flashback with pure alkanes unless very low injection velocities were considered. These velocities were so low as to become outside of the range of typical operating conditions. Hydrogen-containing fuels, on the other hand, were found to flash back even under turbulent high-velocity conditions. Flashback through the boundary layer appears to be the most likely mechanism. This is typically characterized by the critical velocity gradient, hence this parameter is adopted as the preferred means of characterizing flashback propensity. It is thus evaluated herein for its ability to capture the fuel compositional effects summarized here.

4.2.2 Test Beds for Blowoff/Flashback Expirements

Flashback and/or blowoff experiments were obtained in three test beds and used to evaluate the ability of the preferred blowoff and flashback interchange parameters to account for variation in fuel composition. The test beds used for these experiments are described in this section, followed by the results and parameter evaluation.

4.2.2.1 Jet Flame

The overall experimental system consisted of gas and air supply and mixing, an axisymmetric injector, FB detection, and the data acquisition (DAQ) and control system. The schematic of the setup is shown in Figure 25.

For this test bed, an inline air heater (4 kW Sylvania heater PN 038823) was installed to allow variation in the inlet air temperature to the injector. Insulation was also added to the long stainless steel tube that allows for premixing and flow conditioning below the injector. The control of the heater outlet temperature is accomplished by proportional integral derivative (PID) control of the power supplied to the heater via a silicon-controlled rectifier SCR power

controller. The installation of this heater is capable of supplying air at temperatures of 810 K at a flow rate of 470 standard liter per minute (SLPM).

The enclosure holder was also modified for better temperature measurement (Figure 26). Several grooves were introduced on the face of the enclosure holder plate. The radial grooves allow for the placement of thermocouples on the outer wall of the injector tip. The thermocouples placed in these grooves were set in place using epoxy, which also helped with thermal contact to the outer wall of the injector tip. The enclosure grooves allow for three enclosure diameters to be evaluated. However, only the results from the mid-diameter size (ID = 63.5 mm) will be discussed here.

Figure 25: Schematic of the Axisymmetric Single Injector Rig and Associated Supporting Hardware

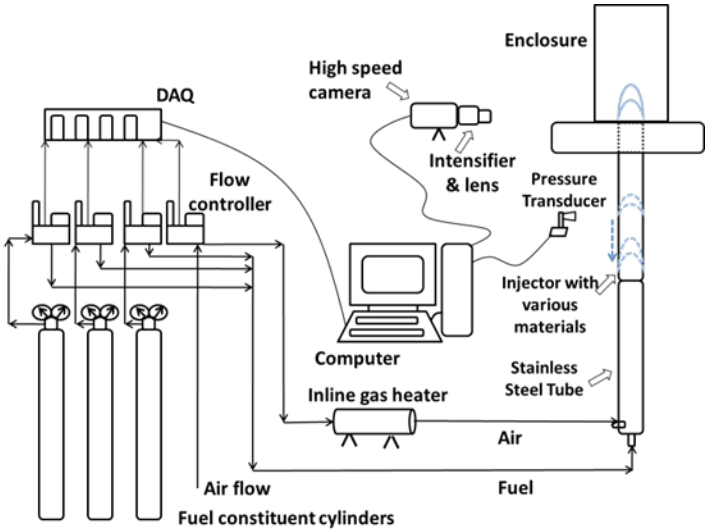

To detect the FB events, a pressure transducer was installed to provide reliable FB monitoring. More thermocouples (TCs) were also added onto the injector. Figure 27 shows the alignment of thermocouples. The injector was notched on outer walls to allow the thermocouple position to be as close to the tip as possible. The thermocouples were fixed to the injector using the same methods as those on the enclosure holder. The tip temperature was calculated by averaging the values measured by TC1 and TC3. TC2 was used along with the pressure transducer to detect the FB event. TC4–TC7 was used to measure the temperature distribution on the plate surface.

Test Protocol

Two protocols were used to approach FB.

- **Protocol I:** Constant adiabatic flame temperature (AFT). Air and fuel flow rates are decreased once thermal equilibrium had been fully achieved on the burner rim. The AFT is held constant in each FB experiment at 1,700 K or 1,900 K.
- **Protocol II:** Constant air flow rate. For some tests, FB occurred at flow rates low enough to compromise safe operation of the preheater. In these cases, the minimum flow rate for safe operation of the heater was kept constant while the fuel was increased (i.e., AFT was increased) to approach FB events. Thermal equilibrium was still ensured with this test procedure.

Figure 26: Schematic of the Enclosure Holder

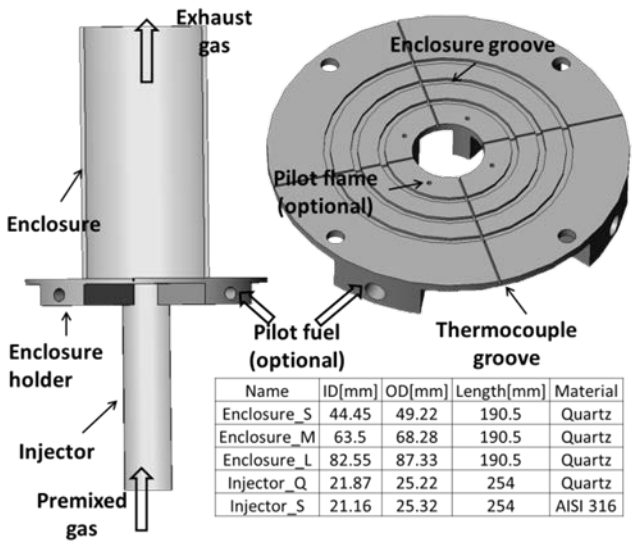

Name	ID[mm]	OD[mm]	Length[mm]	Material
Enclosure_S	44.45	49.22	190.5	Quartz
Enclosure_M	63.5	68.28	190.5	Quartz
Enclosure_L	82.55	87.33	190.5	Quartz
Injector_Q	21.87	25.22	254	Quartz
Injector_S	21.16	25.32	254	AISI 316

Figure 27: Schematic of the Thermocouple Alignment

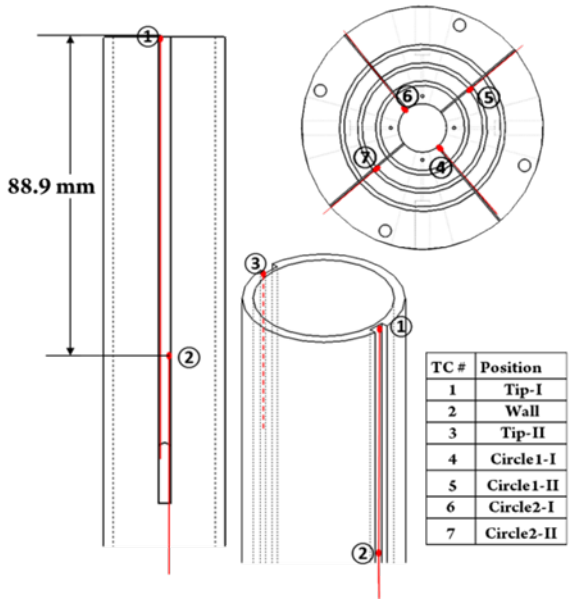

4.2.2.2 Jet Stirred Reacrot (JSR)

The well-stirred reactor (WSR) has been used since the mid-twentieth century to study many aspects of premixed turbulent combustion, including global reaction rates, pollutant formation, and turbulent flame stability near blowout (Turns 2012). A jet-stirred reactor (JSR) approaches the idealized situation regarding the isolation of combustion chemistry from mixing. Appendix D provides details regarding the JSR, and key features are summarized here.

The JSR used in the present work is shown in Figure 28. Both fuel and air enter the reactor through the premixer. The air is preheated to 573 K. Neglecting back heating from the reactor cavity; the fuel-and-air mixture has a nominal temperature of about 550 K as it enters the reactor. The stagnation pressure of the premixed fuel/air mixture is measured 5 centimeters (cm) upstream of the reactor cavity and is typically about 21 pounds per square inch, gage (psig). The premixed reactants enter the cast alumina reactor cavity through a 2 mm nozzle, resulting in a sonic jet velocity of approximately 450 meters per second (m/s). The total volume of the reactor is 15.8 cubic centimeters (cc), the mass flow rate of air is 1.08E-3 kg/s, and nominal combustion temperature is held constant at 1,800 K. This results in a mean fluid residence time of 2.7 ± 0.3 ms.

Figure 28: Diagram of the Experimental Setup

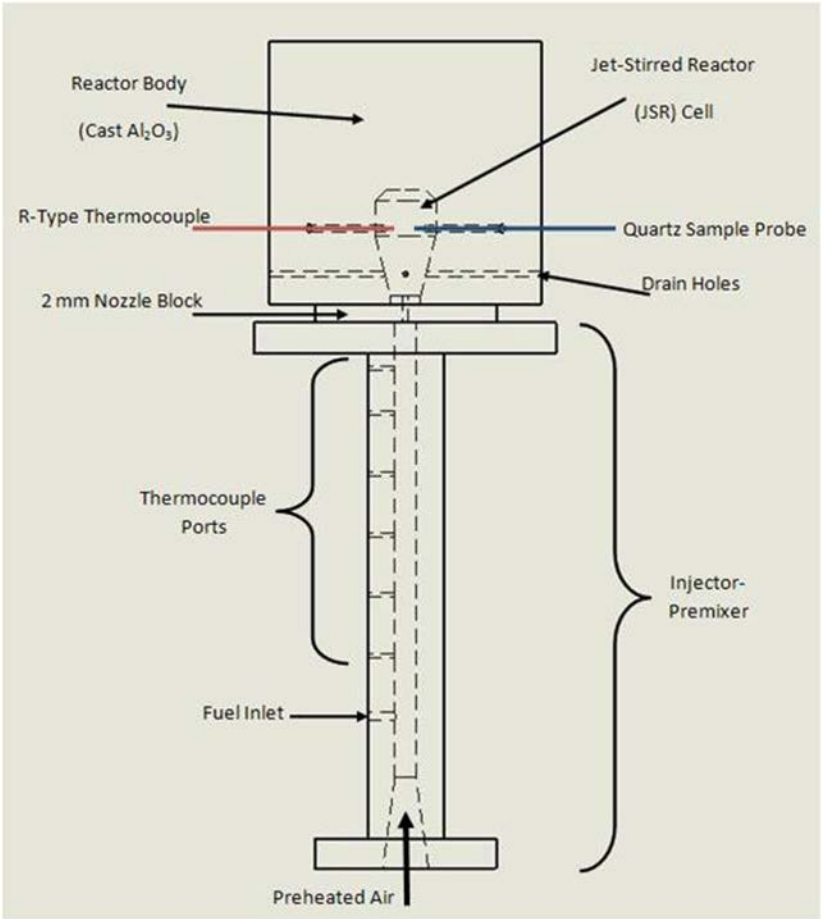

As shown in Figure 29, both temperature and species concentrations are measured at two-thirds of the reactor height, with the nominal sampling location being 2 mm inside the reactor wall. This sampling location is far enough into the reactor to avoid thermal and fluid boundary layer effects, but not so far as to experience the effects of the jet. In addition to collecting data at the standard sampling location, detailed reactor spatial probing is conducted in order to gain insight of flame structure within the reactor. Both temperature and species measurements are taken radially between the reactor wall and centerline at two-thirds of the total reactor height.

Figure 29: Sampling Locations within the JSR

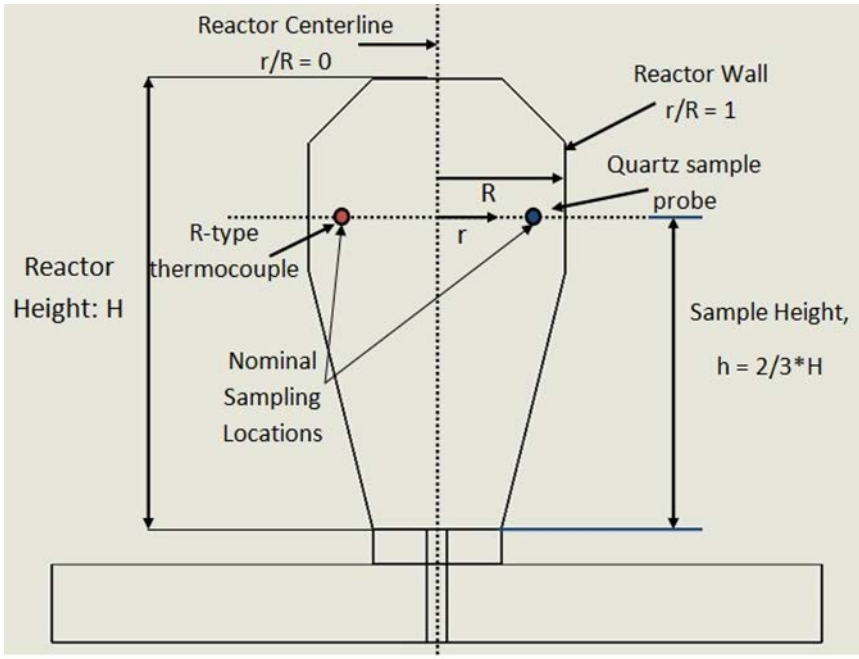

The combustion gas temperature is measured with a type-R thermocouple that is coated with alumina to prevent catalytic effects. The measured temperature on the coated thermocouple bead is affected by a balance between convection from the hot gases to the bead and losses from the bead radiating to the colder reactor wall and conduction through the thermocouple wires, as shown in Equation 26.

$$Q_{conv} = Q_{rad} + Q_{cond} \qquad \text{Equation 26}$$

Other researchers have shown that using sufficiently thin thermocouple wire reduces the conduction to a negligible amount (Lee 2000; Singh 1978).

Neglecting conduction in the wire, the measured combustion temperature is between 50 and 70 K below the reported temperature, which is obtained by correcting the measured thermocouple temperature for radiation to the colder reactor wall (Steele 1995). The hot combustion gases are sampled through a warm-water-cooled, quartz sample probe. The sample gas is drawn by a metal bellows pump into a heated Teflon tube (to prevent condensation). The sample is then drawn through an ice bath, where the H2O in the sample is removed, and the dried gas is sent to a three-gas (CO2, CO, and O2) analyzer (Horiba VA-3000) and a NOX analyzer (Thermo Electron Model 10) in parallel. The CO2 and CO analyzers operate on the non-dispersive infrared (NDIR) principle, while the O2 and NOX analyzers are paramagnetic and chemiluminescent instruments, respectively.

4.2.2.3 High-Swirl Burner

Figure 30 shows the model high-swirl-stabilized lean premixed combustor validation test bed. The swirl number (calculated per the method of Gupta et al. 1984) for this burner is 0.98. Generally, values above 0.7 result in recirculation and are thus considered high swirl. This is in contrast with the low-swirl test bed described in Section 4.2.2.4, which has a swirl number below 0.6.

Figure 30: Schematic of the Model Combustor

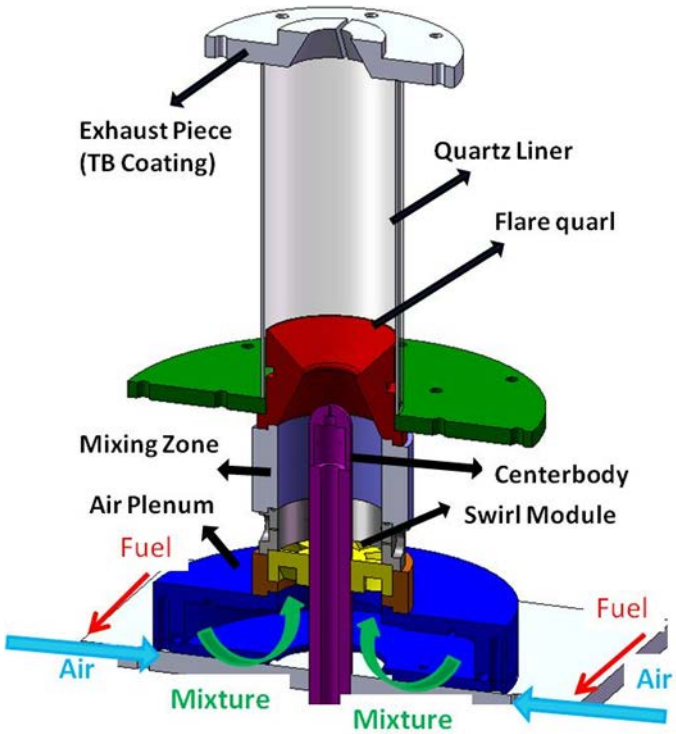

In the high-swirl burner used in the present study, the mixing zone allows any wakes and flow structures from the swirler to decay prior to the combustion zone. The quarl accelerates the flow and increases the resistance to flashback into the mixing zone. The centerbody contributes to formation of center recirculation zone and enhances the stability of the reaction. A quartz cylinder 80 mm in diameter and 175 mm in length serves as a transparent liner to allow optical access to the reaction zone. A contracting piece at the exit prevents any backflow of gases under either reacting or non-reacting conditions, thus providing a clear boundary condition for application of CFD.

Air, at temperatures up to 700 K, is fed to the combustor through two circuits via sonic orifices and pressure regulators to control the flow rate. Fuel flows are introduced to the test rig through Brooks Instruments® mass flow controllers (MFC) and master control units. A Labview®-based data acquisition system was developed to record and monitor air and fuel flow rates, as well as temperatures of interest. More details are available in Akbari (2013).

To identify the stages of blowoff, OH* chemiluminescence was imaged by a 16-bit intensified 384 × 576 pixel charge-coupled device (CCD) camera (Princeton Instruments® model 375-E; with Micro Max intensifier controller, Win View 32 v. 2.5.21.0 operating and analysis software). An ultraviolet transmissive lens with an appropriate band pass filter (centered at 308 nanometers [nm]) was used to isolate the OH* emission. Combinations of aperture size, intensifier gain, and exposure time were adjusted for each case to achieve reasonable intensity images. This technique is especially effective for high-hydrogen-content fuel cases where the reaction emission in the visible range is very low. Below shows an example of different stages of blowoff for a 20/80 composition of NG/H2 mixture. The contours correspond to OH* intensity. A "rope shaped flame" was observed in this study for "ultimate" blowoff.

Figure 31: Blowoff Stages for 20/80 Mixture of NG/H2 with 500 K Preheat and 81 kg/hr Air Flow Rate

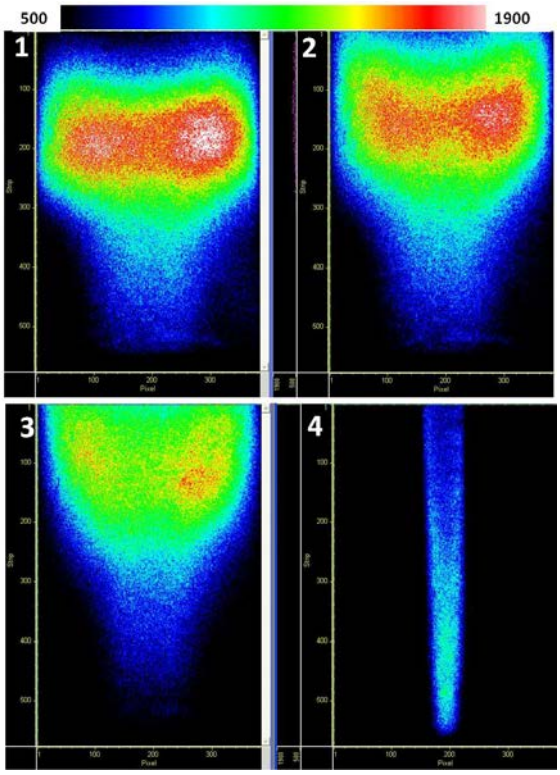

As both blowoff and flashback are spontaneous events, care is required in documenting the observed behavior. For blowoff, the final or ultimate blowoff point is generally reported in the literature. However, it is the initiation of blowoff that has physical correlation with chemical and flow residence time. Thus, in the present study, in addition to noting the ultimate blowoff, the initiation of blowoff was also documented via OH* imaging as described above.

For flashback, the signal from the temperature rise for thermocouples in the premixer was logged to document the event and to trigger shutoff of the fuel. An example of thermocouple readings upon flashback is shown in Figure 32. As a quartz liner was used for this study, a limit

of 2,100 K was imposed for the present effort. As a result, during the testing, the equivalence ratio was incrementally increased until flashback occurred or the adiabatic flame temperature (AFT) reached 2,100 K. As this study focused on low-emission applications, AFTs below 2,100 K were generally desired.

Figure 32: Schematic of Flashback and Temperature Jump in Thermocouples

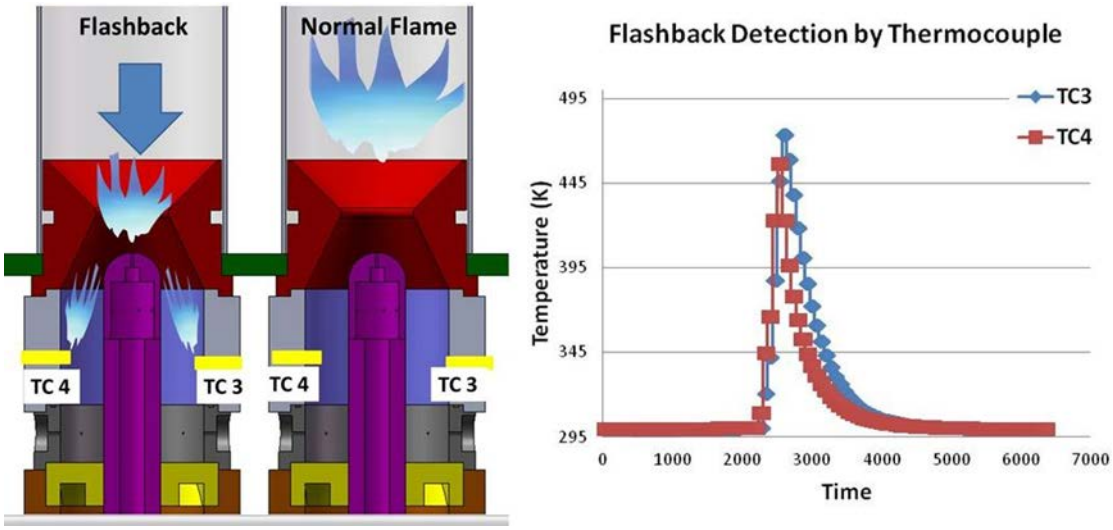

4.2.2.4 Low-Swirl Burner

In contrast to the high-swirl burner described above, a low-swirl burner operates without recirculation and thus avoids large reaction zones (Chan et al. 1992). Stabilization is achieved through a detached or lifted flame that is freely propagating into a divergent turbulent flow field. The flow of premixed reactants exiting the nozzle is divided into two regions. The outer region contains a swirling flow, while the inner region is unswirled. Figure 33 is a photograph of one such low-swirl injector (LSI). It consists of an inner channel with a perforated plate and an annulus containing multiple swirl vanes. Figure 34 illustrates that the premixed reactants that pass through the annulus form the swirling outer region, while the reactants passing through the inner channel form the non-swirling inner region. The perforated plate imparts a certain degree of turbulence on the inner flow and also sets the flow splits between the two regions. As illustrated in Figure 35, upon exiting the nozzle, the swirling region expands radially outward through a centrifugal action. This induces the inner non-swirling region to similarly diverge. Through the principle of conservation of mass, this divergence leads to a linearly decreasing mean axial velocity within the inner flow field. This mean axial velocity gradient in the inner region of the flow is analogous the stagnation flows in the laminar opposed-jet burner or turbulent stagnation burner. Also note that this flow does not contain any vortex breakdown or recirculation zones within the central region, as are present in high-swirl flows.

Figure 33: Low-Swirl Injector, Upstream Face (left) and Downstream Face (right)

Figure 34: Schematic of the LSI within the Premixer and Sudden Expansion Nozzle

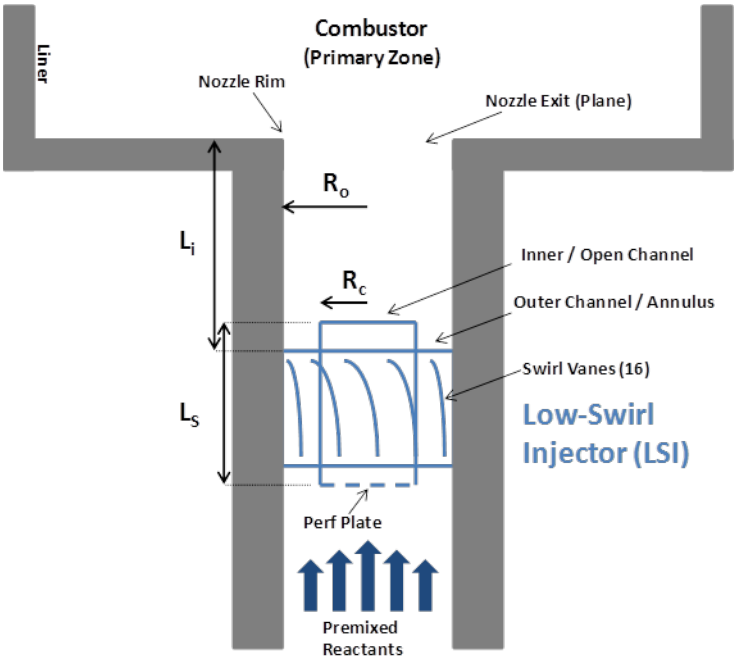

Figure 35: Aerodynamics of a Low-Swirl Flame

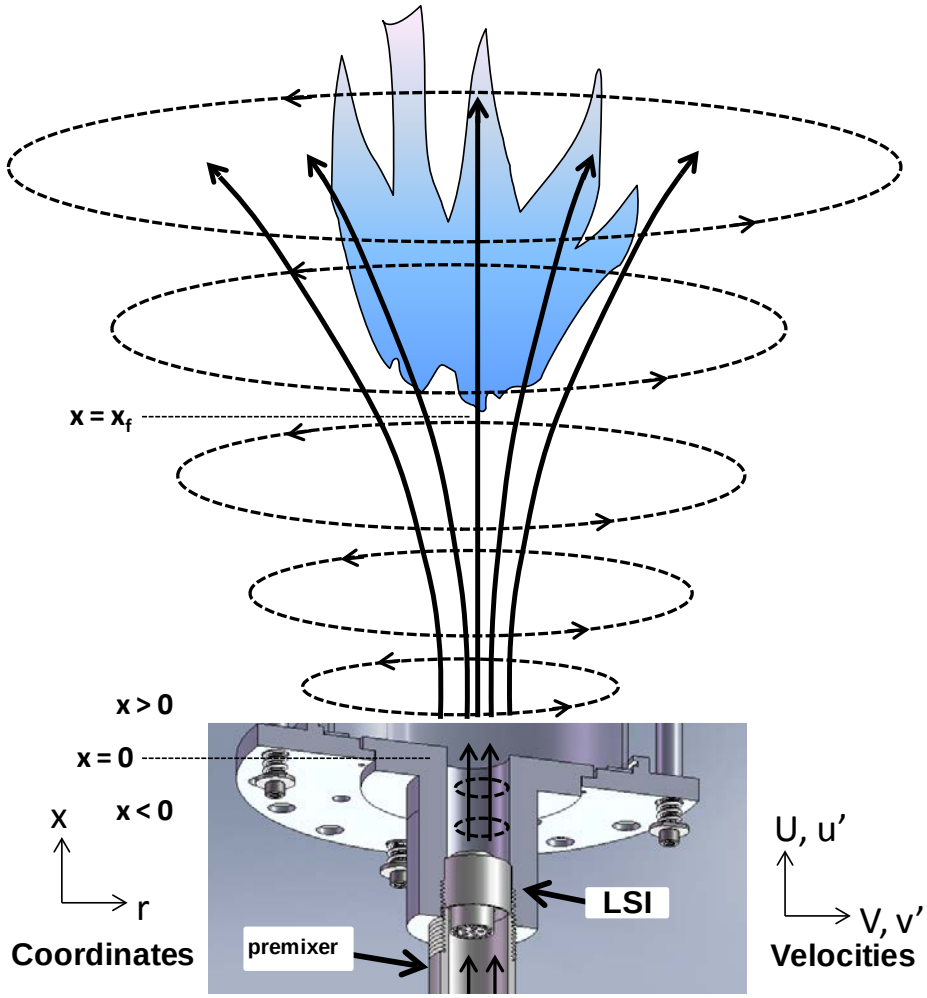

The LSI experiments in this study were performed in the optically accessible pressure vessel shown in Figure 36. The facility is fed by three air compressors, and electric resistance heaters raise the temperature of the air. The pressure, inlet temperature, and air and fuel flows all can be independently adjusted and controlled through PID feedback control loops. A cross-sectional image of the high-pressure vessel can be seen in Figure 37. The vessel itself is made from a 16″ schedule-40 chrome-moly steel pipe with 16″-300 lb. flange ends. The vessel contains two pairs of window ports. One window pair is 15.3 cm (6″) in diameter, and the other pair is 20 cm by 15.5 cm (8″ x 6″). Each window is made from 5 cm (2″) thick fused quartz.

Within the pressure vessel is a single nozzle combustor. The test section consists of a quartz tube 15 cm (6″) in diameter, 3 mm thick, and 23 cm (9″) in length that is compressed between two stainless steel plates that are rigidly held into place with four posts. Graphite gaskets are used to produce an air-tight fit between the quartz tube and the metal even at high flame temperatures. Springs are located at the end of each post to allow the combustor to grow from

thermal expansion. Fuel injection is done well before the LSI to ensure good mixing of fuel and air prior to combustion. Addition details are available in Beerer (2013) and Beerer et al. (2014).

Figure 36: High-Pressure Vessel and Facility

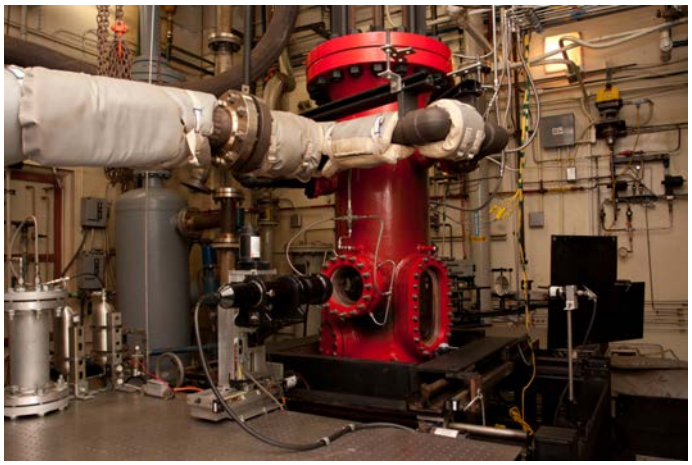

Figure 37: Cross-Sectional Image of Pressure Vessel and Combustor Test Section

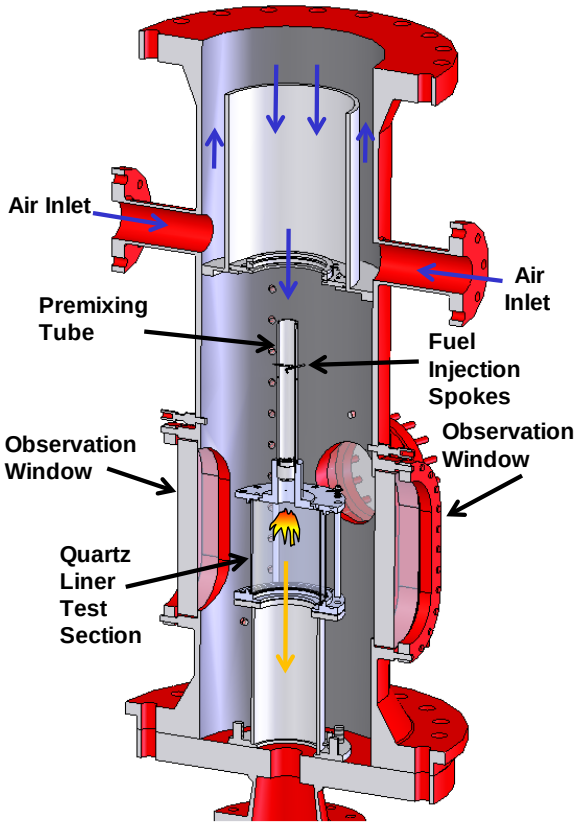

4.2.2.5 Capstone Engine

The final evaluation platform is the Capstone C65 microturbine (65 kW recuperated Brayton cycle). The C65 combustor has an annular configuration and consists of a primary zone that is fed by six tangential injectors in two planes (see Figure 38). The fueling of these injectors is staged according to the load set point while the primary air is fed to each injector over the entire load profile, which leads to quenching at certain loads. The fuel and air mix along the length of the injectors before entering the primary zone. The dilution air enters the dilution zone through two sets of holes. The air splits across the primary zone and dilution holes are proprietary. The engine power demand is controlled by varying the engine shaft speed while maintaining a constant turbine exit temperature.

The focus of these engine tests was to determine the limits to which the baseline combustor design could withstand increasing hydrogen content in the fuel with only modifications to the injector hardware. Modifications to the baseline C65 combustor liner may be required to allow operation on a 50/50 mixture of hydrogen and carbon monoxide, but these tests focused only on the baseline injector design and one modified injector design.

Figure 38: C65 Combustor Schematic with Two Sections Illustrating the Two Planes of Tangential Injectors

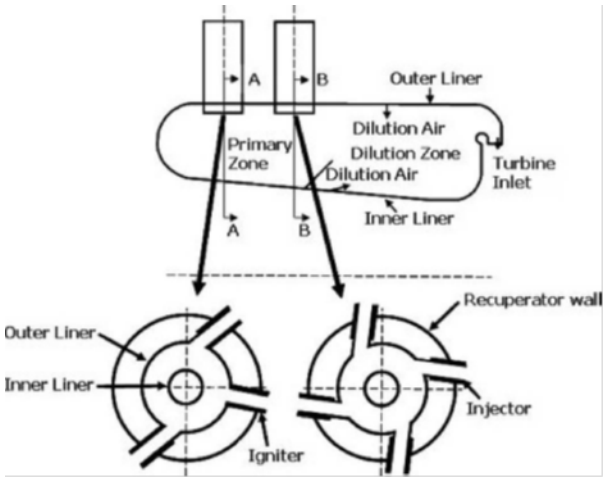

The baseline injector design was tested first with the new modified injector design tested after these initial tests. These engine scale tests consisted of setting the engine power level for a given anchor fuel (carbon monoxide or natural gas) and then gradually blending in hydrogen to this anchor fuel at the mixing station until flashback in the engine resulted. The procedures for the H2/CO fuel mixtures versus the H2/NG fuel mixtures were much more difficult because of the need to run the engine on pure carbon monoxide for these H2/CO tests. Running the engine on only CO required different engine settings for some power levels because of the very different Wobbe numbers of carbon monoxide compared to those of natural gas (330 Btu/scf for CO vs. 1,370 Btu/scf for natural gas). However, these engine setting changes could not be made while the engine was operating; therefore, to start and warm up the engine without using large amounts of expensive CO, the engine would be started on a sufficiently low Btu mixture of

natural gas/carbon dioxide (55/45 NG/CO2). Once engine warm up was achieved, the fuel switch to CO could be accomplished, and then the doping of hydrogen into the CO anchor fuel could begin.

In contrast, the H2/NG tests consisted simply of starting and warming the engine up on natural gas and then proceeding to blend hydrogen into the natural gas anchor, with no need for making changes to the engine settings. It must also be noted here that the fuel composition was changed in time intervals such that the variation in fuel composition had time to reach the engine before the next change in fuel composition was made. This is an important concern because of the physical distance between the engine and the mixing station.

The criterion for flashback relies on the measurement of temperatures at three different injector locations. In the engine tests, flashback is defined as that point when the injector temperatures near the tip of the injector begin increasing.

4.2.3 Results for Jet Flame Flashback

As discussed in Section 3.2.2.2, the critical velocity gradient gc is the classical way to assess boundary layer flashback and is defined in Equation 27:

$$g = \frac{0.03955 Re^{0.75} \bar{u}}{D} = \frac{0.03955 \bar{u}^{1.75} \rho^{0.75}}{\mu^{0.75} D^{0.25}} \qquad \text{Equation 27}$$

The role of fuel composition is apparently captured through viscosity and density. However, the quenching distance is also significant in the determination of whether boundary layer FB will occur. The criterion for the situation in which a flame is quenched by a cold wall was further defined as when the rate of heat release by chemical reactions inside the slab is less than the rate of heat loss through the slab by conduction. A concept described by Turns (2012) is used to capture the quenching distance (Equation 28):

$$d_q = \frac{2\alpha\sqrt{b}}{S_L} \sqrt{\frac{AFT - T_{tip}}{AFT - T_{inlet}}} \qquad \text{Equation 28}$$

The thermophysical properties of the fuel mixture, □, and the flame spe
influence of fuel composition. The term b is an arbitrary constant introduced by Turns (2012). It is defined as the ratio of local temperature gradient near the wall to that averaged through thermal boundary layer. In the current research, the constant 2 √ b is assumed to be 1 for convenience.

4.2.3.1 Alkane-Based Fuels

The flashback propensity of mixtures of methane, ethane, and hydrogen were measured in terms of the critical velocity gradient and used to develop an expression for prediction of flashback as a function of fuel composition. Single-component fuels were tested as a reference. Binary mixtures of hydrogen-alkane were examined to mimic more practical conditions and survey the fuel interaction effects. The matrix used is shown in Table 5.

Table 5: Test Matrix for Alkane Fuels

Composition	mix1	mix2	mix3	mix4	mix5	mix6
CH_4 [%]	100	75	50	0	0	0
C_2H_6 [%]	0	0	0	50	75	100
H_2 [%]	0	25	50	50	25	0
Legend in related figures	◇	△	○	●	▲	◆

The measured results were correlated using analysis of variance (ANOVA) with EQ or AFT, and fuel composition. The final selection of terms is based on the ANOVA results, with terms having a p-value less than 0.0001 retained. Equation 29 and Equation 30 show the equations generated from the model using EQ and AFT, respectively. The tip temperature-based gc correlates the data better than the inlet temperature-based gc and is thus the preferred expression. Units used in the correlation are presented in the models. Both of these two models yield high R2 values (0.9020 and 0.9015, respectively) and Figure 3 presents the comparison between predicted and measured values.

Table 6: Units for Correlated Parameters

Parameter	Unit	Parameter	Unit
Fuel Composition	[-]	EQ	[-]
Temperature	[K]	S_L	[cm/s]
Thermal Diffusivity	[cm^2/s]	d_q	cm

In addition to the statistics-based correlations, a model based on key physical parameters was developed, shown by Equation 31.This correlation provides good predictive capability (R2 of 0.9203), as indicated in Figure 40. As sketched by the red straight line, those data points cover the whole range of tested mixtures and yield approximately the same gc. Based on these conditions, the predicted values are calculated using the models in Equation 109–Equation 111. Table 7 summarizes the predicted values using the three models. Generally the models perform

quite well in predicting the measurement results, but the error grows as hydrogen composition increases.

$$g_c = (46.48H_2 + 23.08CH_4 + 21.77C_2H_6 - 64.13EQ + 49.78H_2 \cdot C_2H_6 - 102.44H_2 \cdot EQ)^2 \quad \text{Equation 29}$$

$$g_c = (50.76H_2 + 108.88CH_4 + 105.82C_2H_6 - 0.069AFT + 56.29H_2 \cdot C_2H_6 + 3631.54CH_4 \cdot C_2H_6)^2 \quad \text{Equation 30}$$

$$g_c = \left(-5571.78 + 302.12S_L + 819.63\alpha - 0.61T_{tip} + 450479d_q - 12262.8S_L \cdot d_q - 68827.3\alpha \cdot d_q - 3.998{S_L}^2 - 7180478{d_q}^2\right)^2 \quad \text{Equation 31}$$

Figure 39: Predicted vs. Measured Values of gc Using Equation 29 and Equation 30

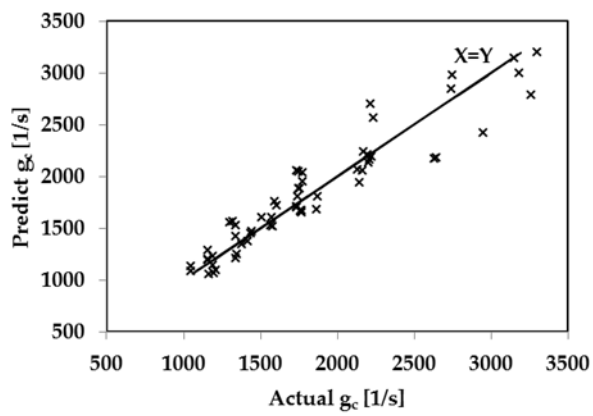

(a) Equation 29

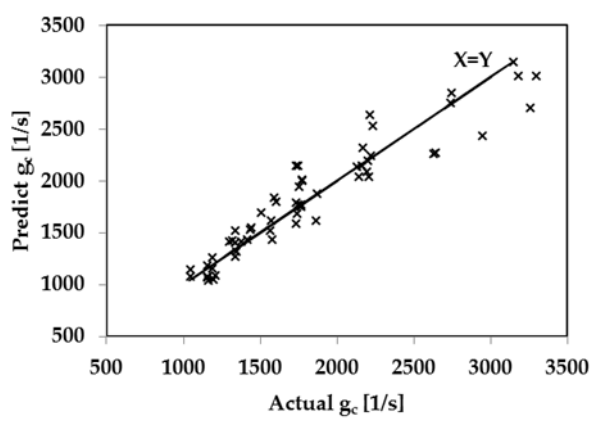

(b) Equation 30

Figure 40: Predicted (Equation 31)

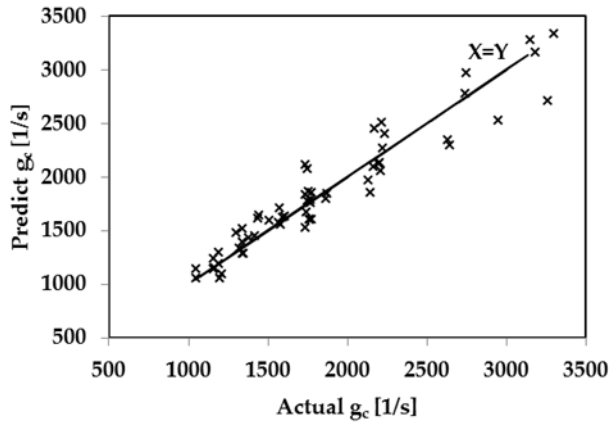

Figure41: AFT vs. Re vs. Measured gc

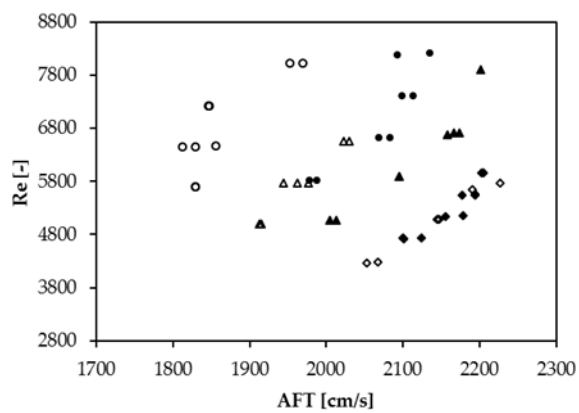

Table7: Estimated gc Values and Re Number

Composition	mix1	mix2	mix3	mix4	mix5	mix6
CH_4 [%]	100	75	50	0	0	0
C_2H_6 [%]	0	0	0	50	75	100
H_2 [%]	0	25	50	50	25	0
AFT real [K]	2,209	1,961	1,829	1,983	2,095	2,204
g_c real [1/s]	1,758	1,741	1,743	1,763	1,762	1,769
g_c (Equation 29) [1/s]**	1,868	1,800	2,048	1,912	1,664	1,661
g_c (Equation 30) [1/s]**	1,892	1,673	2,140	1,969	1,753	1,755
g_c (Equation 31) [1/s]**	1,715	1,653	2,091	1,857	1,601	1,768
Re [-]***	867	2,243	4,693	1,529	1,150	243

Notes: ** predicted values using models based on the same conditions as measured; *** estimation of Re number with AFT = 1,700 K)

The results confirm that the critical velocity gradient concept is able to capture the flashback propensity of a wide range of fuels. Because testing was done only under limited conditions, the generality of the results is somewhat limited. However, the utility of these expressions is that the relative flashback propensity of a given fuel versus a baseline fuel can be established. For example, if flashback has been noted for methane for a given condition, the correlations can be used to estimate the change in flow rate or quenching distance needed to prevent flashback with hydrogen content.

4.2.3.2 Hydrpgen-Containing Fuels

In this section, results and analyses are presented for hydrogen-containing fuels. Table 8 shows the seven fuel mixtures that will be studied.

To further enhance understanding of the thermal effects on FB, inlet temperature, injector material, and reaction AFT were also studied. The effect of the injector material was also investigated, as flame propagation behavior was observed to be affected by tube material (Bollinger and Edse 1956; Kedia and Ghoniem 2012). Most tests were conducted with an AFT of either 1,700 or 1,900 K

Table 8: Fuel Compositions for Synthesis Gas Flashback.

H_2	25	50	75	25	50	75	100
CO	75	50	25	0	0	0	0
CH_4	0	0	0	75	50	25	0

The following describes the conditions for these experiments:

- Preheat temperatures of 300, 450, 588, and 810 K for each fuel composition in Table 8
- An AFT of 1,700 and 1,900 K with both injector materials (quartz and stainless steel 316).

Statristical Model

The first statistical model (Equation 112) expresses gc in terms of fuel composition, inlet temperature, and AFT. The model does not account for material effects and yields an R2 value of 0.7901. Units are shown in Table 9.

Table 9: Units for Parameters Correlated

	Unit		Unit
Fuel Composition	[-]	EQ	[-]
Temperature	[K]	S_L	[cm/s]
Thermal Diffusivity	[cm^2/s]	d_q	cm

Figure 42 compares the predicted values (Equation 32) with the measured values. It is noted that the data from the stainless steel and quartz tube experiments diverge, indicating that material effects are significant. With this model, the quartz data are underestimated, while the stainless steel tube data are overestimated. This reveals that quartz injectors result in higher FB propensity than in stainless steel injectors.

To further quantify material effects, an ANOVA was performed separately for quartz (Equation 33) and stainless steel tubes (Equation 34). The correlations are significant with an R2 of 0.9702 and 0.9485 for quartz and stainless steel, respectively. As seen in Figure 43, the prediction of the statistical model is much better than without accounting for the injector material.

$$g_c = (283.12H_2 + 23.07CO - 51.50CH_4 + 314.13H_2 \cdot CH_4 + 0.076H_2 \cdot T_{inlet} - 0.277H_2 \cdot AFT)^2 \quad \text{Equation 32}$$

$$g_{c_quartz} = (324.45H_2 + 31.91CO - 75.43CH_4 + 416.75H_2 \cdot CH_4 + 0.07H_2 \cdot T_{inlet} - 0.32H_2 \cdot AFT)^2 \quad \text{Equation 33}$$

$$g_{c_stainless} = (224.18H_2 + 9.36CO - 45CH_4 + 232.63H_2 \cdot CH_4 + 0.0331H_2 \cdot T_{inlet} - 0.213H_2 \cdot AFT)^2 \quad \text{Equation 34}$$

Figure42: Model Predicting gc without Consideration of Material Effects

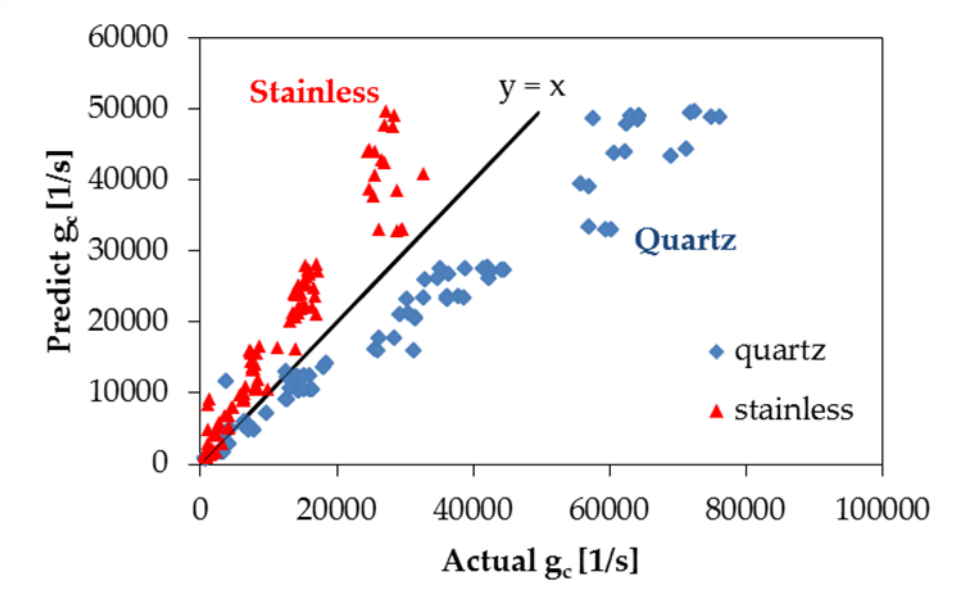

It was noted that the tip temperature for the quartz injector was higher than that for the stainless steel injector, all other parameters being equal. This difference between the two injector materials is a result of the different thermal properties of the two materials. Therefore, as a strategy to incorporate the effects of materials, the injector tip temperature is selected as a parameter for inclusion in the ANOVA. Equation 35 is the resulting model when incorporating the factor of tip temperature for various inlet temperatures. Equation 36 represents a simplification for only non-preheated cases.

Figure 43: Models Predicting gc: Quartz Tube (Blue Diamonds) and Stainless Tube (Red Triangles)

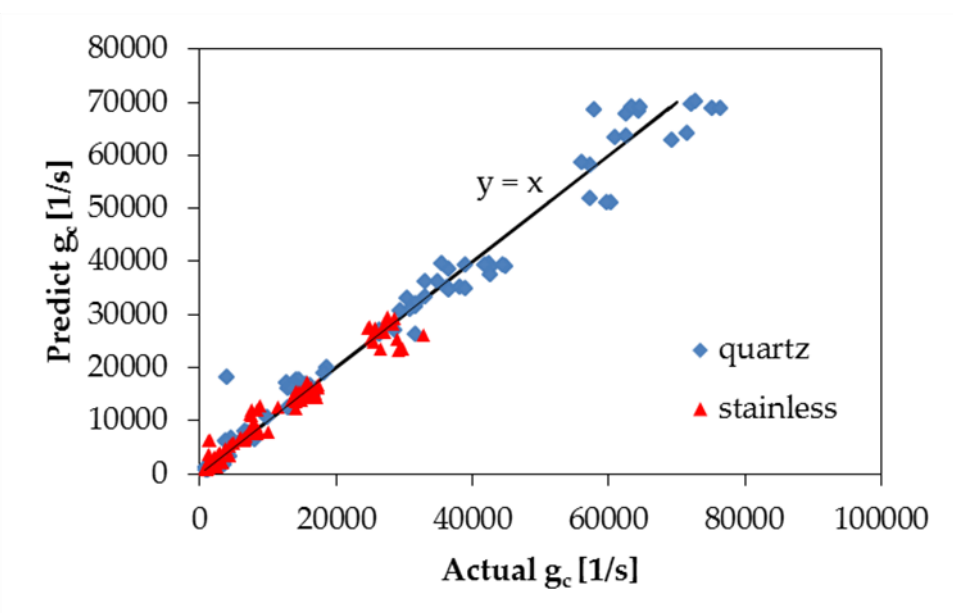

Figure 44 and Figure 45 show that the correlations of Equation 35 and Equation 36 better predict the critical velocity gradient compared to Equation 32, as shown in Figure 42. The R2 values are 0.9108 and 0.9717 for Equation 35 and Equation 36, respectively. It is also noted that AFT was not found to be significant and is thus not included in the correlations. Thus, introducing the tip temperature as a factor reasonably captures the material effect. However, the correlation predictive power is improved when only non-preheated cases are analyzed suggests that some phenomena are still missed in this model.

$$g_c = (210.25H_2 - 35.23CO - 149.97CH_4 + 0.135H_2 \cdot T_{inlet} - 0.783H_2 \cdot T_{tip} + 0.315CH_4 \cdot T_{tip})^2 \quad \text{Equation 35}$$

$$g_c = (261.74H_2 - 30.69CO - 188.38CH_4 - 0.8H_2 \cdot T_{tip} + 0.424CH_4 \cdot T_{tip})^2 \quad \text{Equation 36}$$

Figure 44: Models Predicting gc with Tip Temperature Instead of Inlet Temperature

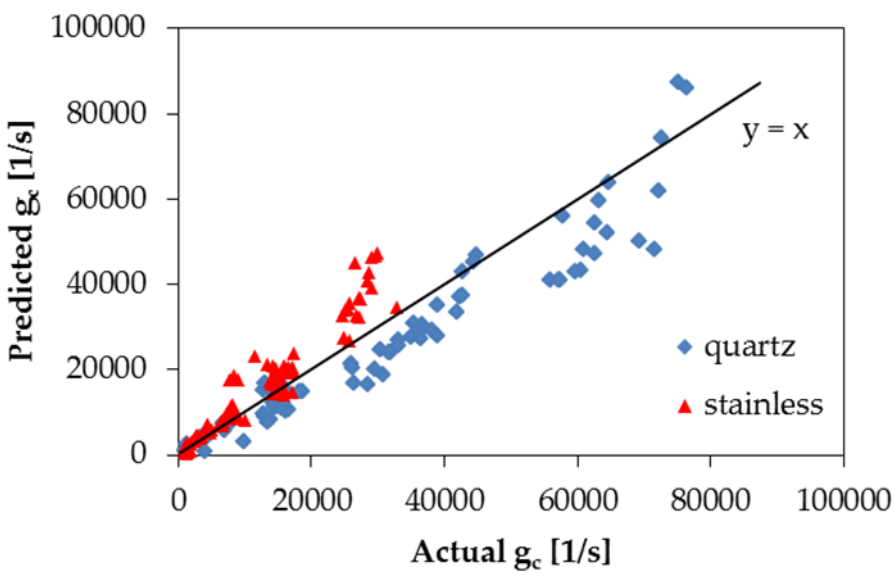

Figure 45: Models Predicting gc with Tip Temperature for Non-Preheated Cases

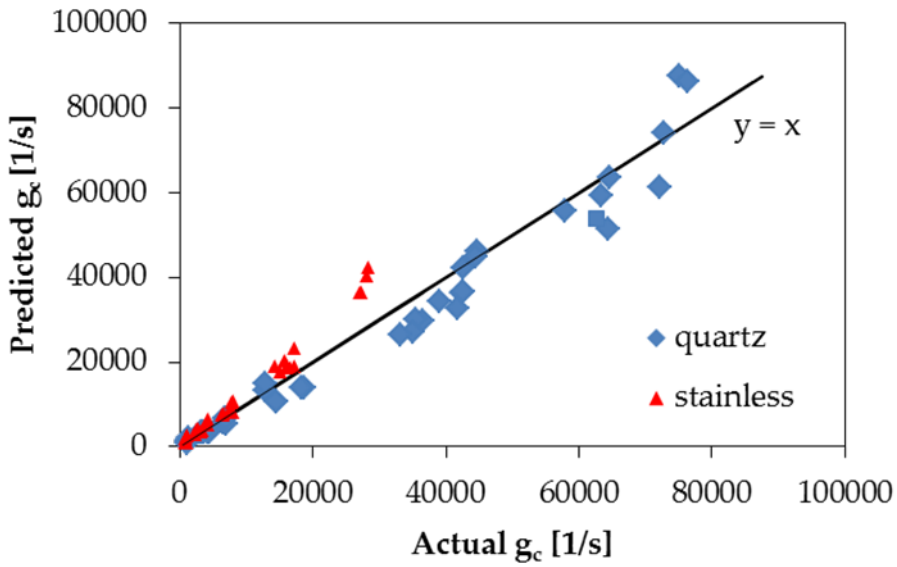

The statistical models developed correlate the FB propensity, gc, with operational inputs (i.e., fuel compositions, inlet temperature, tip temperature, and AFT) well. The tip temperature is found to effectively capture the injector material effect, which verifies the connection between thermophysical properties and FB propensity. However, the statistical model is limited with respect to providing insight into the physical natural of FB. Therefore, a deeper physical analysis is necessary and is addressed in the following section.

Physical Model

While the previous correlations are useful as an indicator of how the factors studied affect FB, they do not yield a physical interpretation. To capture these effects, physical parameters were introduced as inputs (i.e., thermal diffusivity and quenching distance), and an ANOVA was again performed. Additionally, all parameters included in the analysis were both based on tip temperature and inlet temperature. All terms that yielded p values greater than 0.0001 were eliminated. The parameter elimination process revealed that only terms that were calculated using tip temperature were statistically significant. This reaffirms the significance of the tip temperature.

Equation 37 presents the resulting correlation, which has an R2 value of 0.9367. All parameters are normalized by reference values shown in Table 10. Figure 46 illustrates the superior performance of the new model compared to those presented above.

$$g_{c_tip} = (155 + 122.9\frac{\alpha_{tip}}{\alpha_0} + 1340.8\frac{d_{q_{tip}}}{d_{q0}} - 212\frac{T_{tip}}{T_0} - 49\frac{S_{L_{tip}}}{S_{L0}} + 74\frac{\alpha_{tip}T_{tip}}{\alpha_0 T_0} - 8549\frac{d_{q_{tip}}S_{L_{tip}}}{d_{q0}S_{L0}} - 31.1\frac{T_{tip}S_{L_tip}}{T_0 S_{L0}})^2 \qquad \text{Equation 37}$$

Table 10: Definition of Reference Values

	Definition	Value
S_{L0}	Maximum laminar flame speed of methane	44.8 cm/s (Glassman 1996)
d_{q0}	Quenching distance of CH_4/Air at EQ=1	0.25 cm (Barnett and Hibbard 1957)
α_0	Thermal diffusivity of air at 1 atm and 300 K	22.5E-6 m^2/s (Incropera and DeWitt 2007)
T_0	Ambient temperature	300 K

Figure 46: Comparison of Actual Values vs. Predicted Values by Multi-Parameter Model (Equation 37)

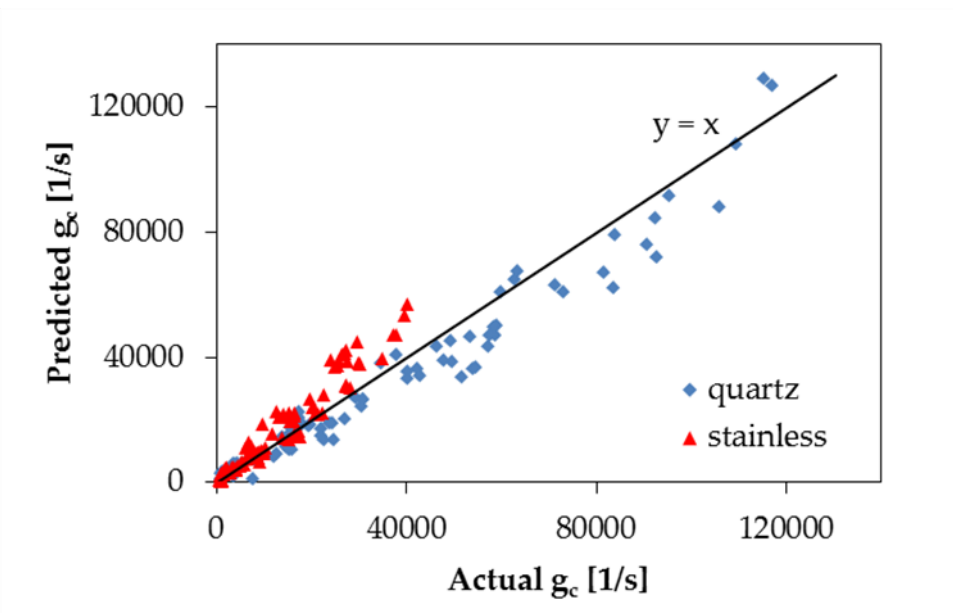

The model in Equation 37 correlates the data well using physics-based parameters. However, the physical meaning of the correlation itself is not obvious. As a result, additional parameter analysis was carried out to refine the model in a manner that allows more straightforward interpretation.

Given the relationship (see Equation 38) between the critical velocity gradient, the laminar flame speed:

$$g_c \equiv \frac{V_0}{d_p} \sim \frac{S_L}{d_q} \qquad \text{Equation 38}$$

and the quenching distance as proposed by Lewis and von Elbe (1943), another form of a physics-based model was developed. The laminar flame speed and quenching distance are combined, generating the model with an R2 value of 0.895, shown by Equation 39.

$$g_{c_tip} = 92.28\left(\frac{\alpha_{tip}}{\alpha_0}\right)^{2.04}\left(\frac{S_{L_tip}d_{q0}}{S_{L0}d_{q_tip}}\right)^{0.328} \qquad \text{Equation 39}$$

The predicted and actual gc values are shown in Figure 47.

Figure 47: Comparison of Actual Values vs. Predicted Values by Multi-Parameter Model (Equation 39)

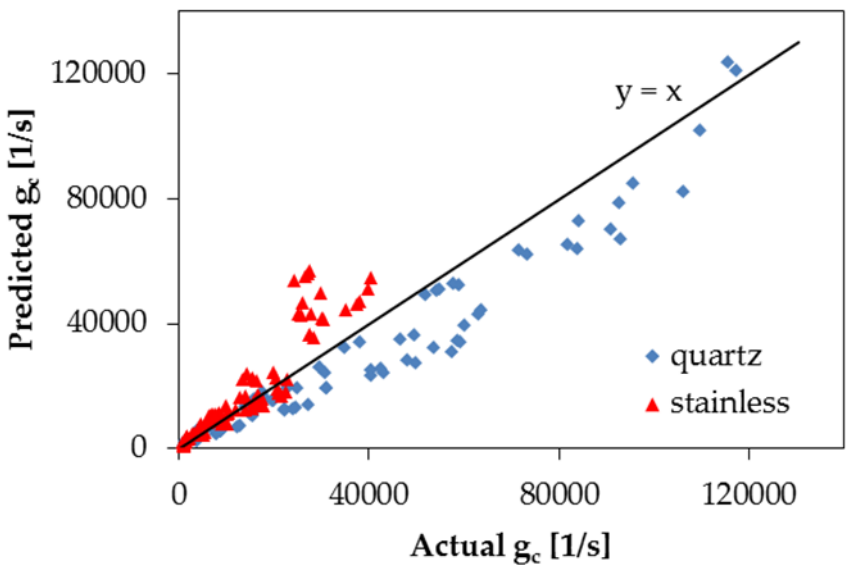

Equation 39 indicates similar performance as Equation 37. However, evidence of material effects can still be seen from the scatter in the results. This leads to the conclusion that the large difference in flashback propensity between steel and quartz may not be explained by tip temperature alone. Another effect originating from the material itself may be present, e.g., a third-body or catalytic effect.

The expression in Equation 39 allows interpretation that is consistent with intuition and previous understanding of FB. For example, smaller quenching distances indicate higher FB propensity. Mixtures with higher diffusivity will be more prone to FB, and mixtures with higher flame speeds will be more prone to FB. Again, it is emphasized that use of the correct mixture temperatures for assessing these properties is very important. For practical systems, ascertaining the burner tip temperature may be difficult. However it could be estimated from CFD, inlet temperatures, or other means. It also provides an insight that FB prevention may be achieved by cooling the burner rim. To help explore this, the next section presents a heat

transfer model that may allow a mechanism for ascertaining the tip temperature based on other known boundary conditions.

Finally, it should be pointed out that the above correlations were developed based on the data collected from the specific burner setup, thus they may not be universally applicable. However, they can be used to establish relative flashback propensity for a given fuel composition.

Summary

For the jet burner configuration, extensive data were obtained to survey the various parameter effects on FB propensity, including fuel composition, AFT, inlet temperature, and injector material. Statistical analysis of the results led to correlations based on the historically used critical velocity gradient. It was found that better correlations can be obtained if material temperatures are incorporated. Flashback propensity is also influenced by the laminar flame speed as expected. But if the flame speed is calculated based on injector tip temperature (versus gas inlet temperature), performance is much better. A key observation is that, for practical systems, where the injector tip temperature can be significantly higher than the ambient temperature, incorporation of this effect on the quenching distance is vital for getting reasonable predictive ability. This work has produced correlations for alkane- and hydrogen-containing fuels that can be used to establish relative fuel composition impacts on flashback propensity of jet burners that can assist the designer.

4.2.4 Results for Jet Stireed Reactor Blowoff

The connection between turbulent flame speed and flow velocity controls the combustion stability under LPM combustion. Flame stability depends both on (1) how well hot recirculating products mix with fresh reactants, and (2) the ability to sustain a large-enough flame speed relative to the fluid velocity. Lean blowout occurs when the heat release from the primary combustion zone is not high enough to raise the temperature of the reactants to an adequate level to sustain reaction (Lefebvre and Ballal 2010).

Blowout tests were conducted for a selected number of the fuel compositions outlined in Chapter 2, with the addition of pure CH4 for reference. A blowout test can be achieved through a number of different methods: (1) hold the fuel flow constant while increasing the airflow until the flame blows out, (2) increase both the fuel and air flow rate at constant equivalence ratio until the flame blows out, and (3) hold the air flow rate constant while decreasing the fuel flow until a blowout event occurs. The goal of this study was to investigate the difference between a wide variety of fuel blends, so it was decided that Method 3 was the best experiment to conduct, since the fluid dynamics would remain relatively constant for each fuel tested. For the blowout experiments conducted, the air flow rate was held constant at 1.08E-3 kg/s, and the air inlet temperature was kept at 573 K. The fuel flow rate was gradually decreased until a blowout event occurred.

Procedurally, the blowout temperature is found by starting at 1,800 K and reducing the fuel flow rate so that the reactor temperature decreases by approximately 50 K. This flow rate is then held for 15 minutes, and the fuel flow rate is again adjusted to decrease the combustion temperature another 50 K. Eventually the reactor will undergo blowout; however, due to the

thermal hysteresis in the system this temperature will be somewhat lower than the actual blowout temperature. That is, the reactor can run at a reduced gas temperature because of the thermal inertia of the reactor solid material. Next, the reactor is heated up to 50 K above the blowout temperature found in the previous test. The fuel flow rate is then adjusted to achieve a combustion temperature that is 10 K lower than the initial temperature. This flow rate is held for 30 minutes and the process repeated. In between times when the fuel is being adjusted, the temperature in the reactor is falling due to the falling temperature of the solid material; however, it was determined that 30 minutes is sufficiently long enough to overcome the JSR's thermal inertia, and the temperature within the reactor stabilizes. Once the new blowout temperature is determined, the test is conducted once more by preheating the reactor to 20 K hotter than the newly determined blowout temperature. The temperature is then decreased in 5 K increments, separated by 30 minutes, to determine a more refined blowout temperature. The composition of fuels tested is shown in Table 11, and the results are shown in Figure 48.

Table 11: Fuel Composition for the 16 cc Reactor Blowout Studies

	Composition (vol %)						
Mix	**H_2**	**CO**	**CH_4**	**CO_2**	**N_2**	**C_2H_6**	**C_3H_8**
1	100	0	0	0	0	0	0
2-A	25	0	50	0	0	25	0
2-B	55	0	35	0	0	10	0
3	40	50	0	10	0	0	0
4	0	0	50	35	15	0	0
5	0	0	75	0	0	25	0
CH_4	0	0	100	0	0	0	0

Figure 48: Experimentally Determined Blowout Temperature for Fuel Compositions Outlined in Table 11

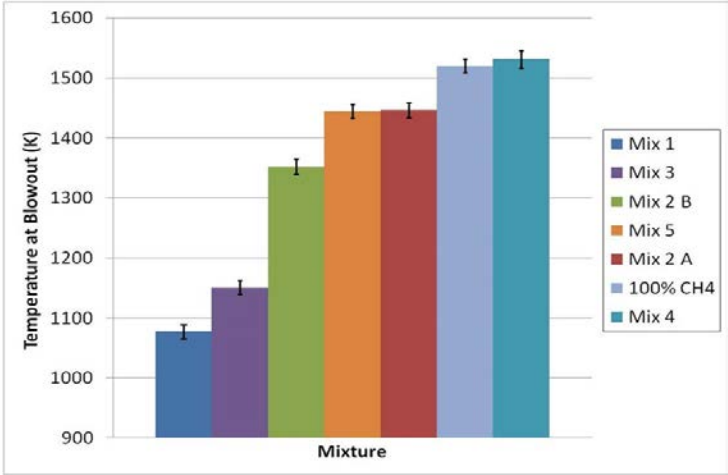

The results of Figure 48 lend themselves to a number of conclusions. First, H2 blows out about 500 K cooler than pure CH4 does. This is not surprising since H2 is far more reactive than CH4. When diluent is added to pure CH4, as in Mix 4, the blowout temperature is somewhat increased, most likely due to the lower reactivity and flame speed due to dilution effects. Mixes 2A and 5 blow out approximately 75 K cooler than pure CH4 does. Due to the large C-H bond energy and lack of carbon-to-carbon (C-C) bonds, CH4 has a relatively high ignition temperature and in general is less reactive than higher-order hydrocarbons such as C2H6 (Turns 2012). While Mix 5 is composed of 75 percent/25 percent CH4/C2H6, Mix 2A contains 25 percent H2 in place of some CH4. It is interesting to note that the H2 addition does not significantly affect the blowout temperature. Blowout behavior appears to be best represented by the least reactive fuel component in the mixture. This point is further illustrated by comparing blowout temperature between Mixes 3 and 2B. Both mixtures contain about 50 percent H2; however, Mix 2B contains hydrocarbon species, while the balance of Mix 3 is composed mainly of CO. The difference in blowout temperature is significant (about 200 K). This is thought to be related to the high C-H bond energy of CH4.

Although this study's goal was to determine the emissions and blowout characteristics of actual fuel compositions found in nature and from industrial by-products, we can learn valuable information by expanding the compositional parameter space beyond that presented by the fuels alone. Figure 49 shows that the addition of small amounts H2 to CH4 has a relatively small effect, and this effect increases as the H2 mixture fraction gets above 50 percent. In contrast, the blowout temperature for the CH4/C2H6 follows the CH4/H2 mixture up to a 50 percent mixture fraction and then levels off.

Figure 49: Experimentally Determined Blowout Temperature for CH4 Mixed with Increasing Levels of H2 and C2H6. Blowout for pure C3H8 is shown for reference.

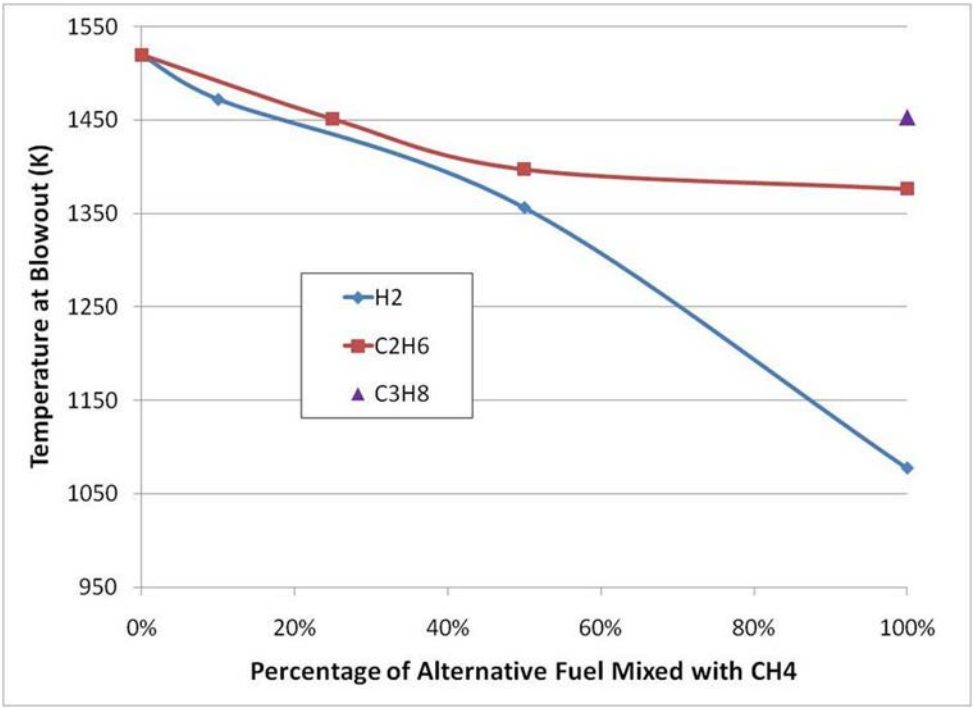

4.2.5 Results for Low Swirl Burner Flashback

The flashback limits for the low-swirl burner configuration were measured with the 90/10 H2/CH4 blend using the aero-vane LSI and sudden expansion nozzle for pressures ranging from 3 to 8 atm, inlet mixtures temperatures from 294 to 600 K, and velocities from 20 to 60 m/s. The flashback limits are plotted in Figure 50 as a function of versus at flashback. The inlet temperature is constant in each plot, and the data points are grouped by pressure. In general, a clear trend is seen that the firing temperature at flashback increases at higher velocities, but decreases with increasing pressure.

Figure 50: Flashback Limits with the Aero-Vane LSI and Sudden Expansion Nozzle with 90/10 Hydrogen/Methane Blend at Various Pre-Heats, Pressures and Velocities

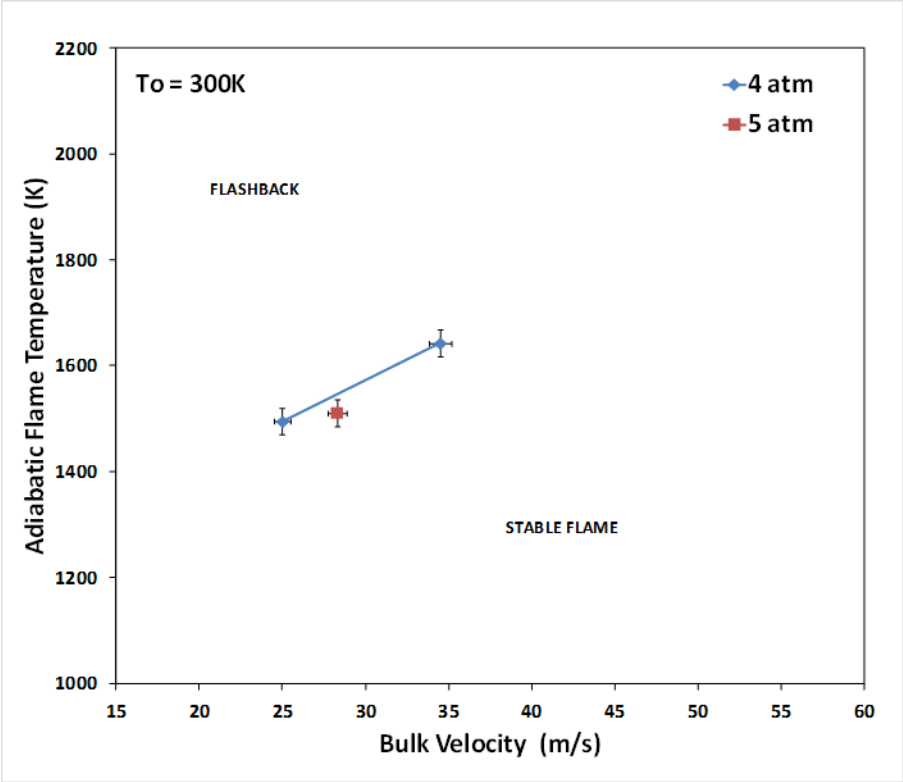

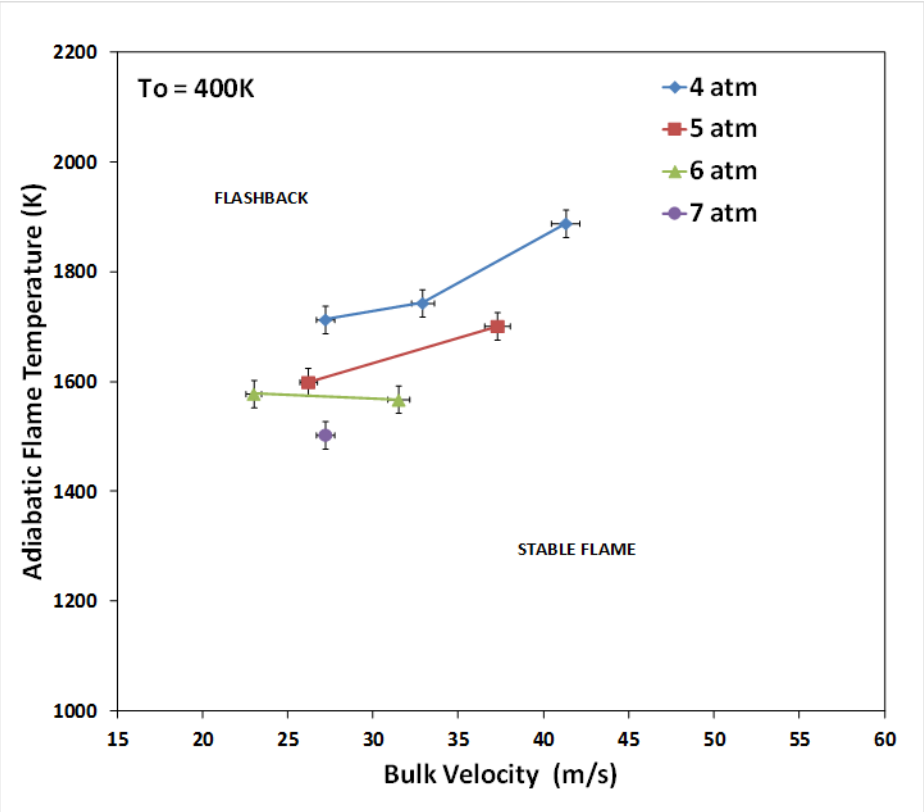

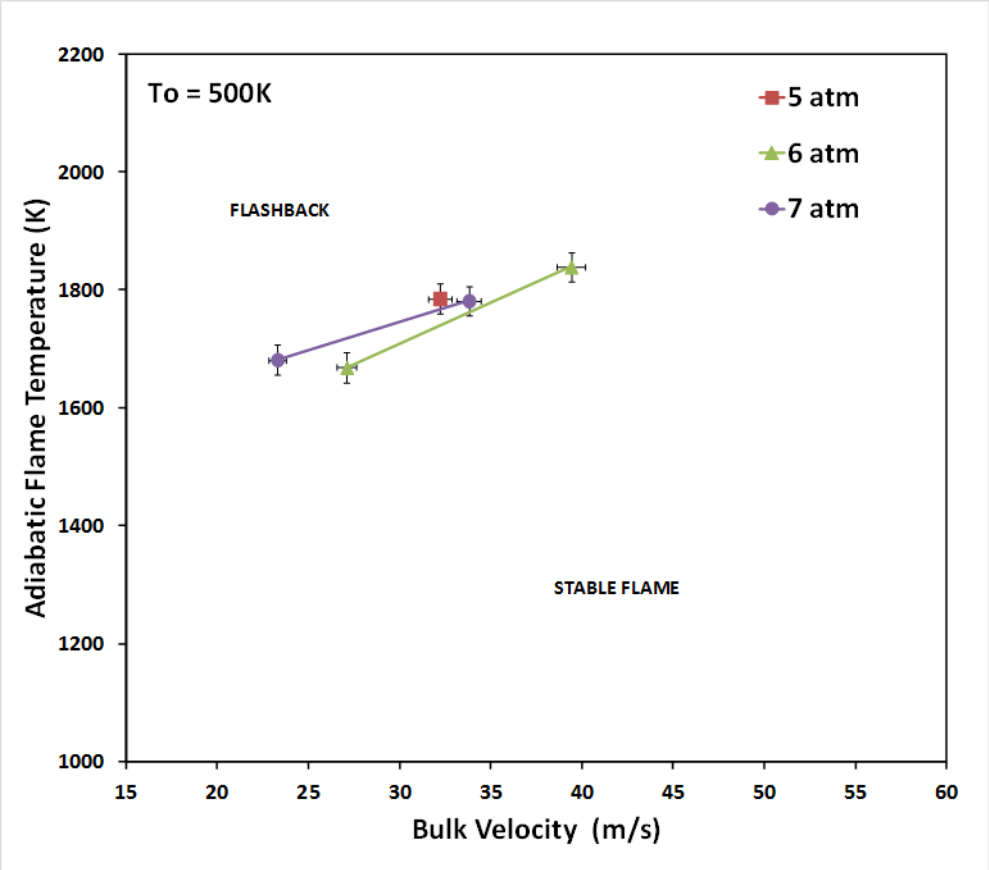
To = 500K
5 atm
6 atm
7 atm
FLASHBACK
STABLE FLAME
Adiabatic Flame Temperature (K)
Bulk Velocity (m/s)
2200
2000
1800
1600
1400
1200
1000
15
20
25
30
35
40
45
50
55
60

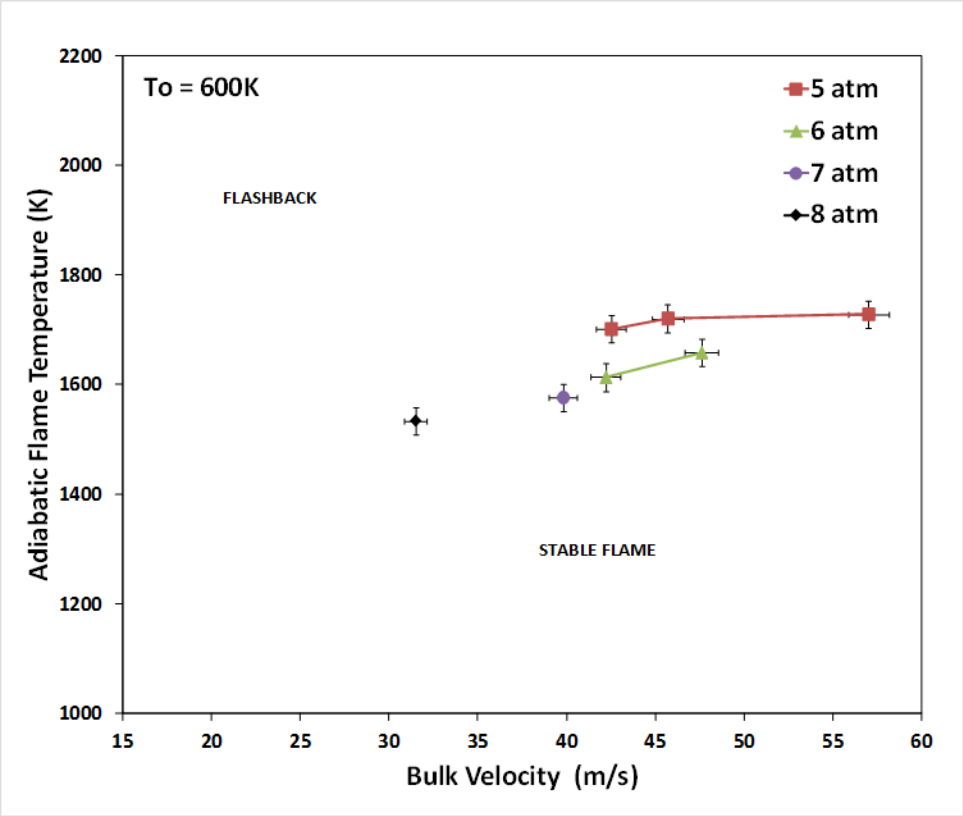
To = 600K
5 atm
6 atm
7 atm
8 atm
FLASHBACK
STABLE FLAME
Adiabatic Flame Temperature (K)
Bulk Velocity (m/s)
2200
2000
1800
1600
1400
1200
1000
15
20
25
30
35
40
45
50
55
60

Figure 51 plots all the data normalized by an inverse pressure dependence P-1, which allows for the effect of temperature to be seen more clearly. Increasing the inlet temperature from 300 to 500 K increases the flashback firing temperature. This trend is rather surprising because jet flames from Danielle et al. (2010) and high-swirl flames from Noble et al. (2006) have generally found that increasing temperatures decreases the operating window. The flashback data was regressed into an expression for Φ as function of , shown in Equation 40:

$$\phi_{flashback} = 6.51 \cdot 10^{-5} \cdot \left(\frac{U_O^{[m/s]} T_O^{[K]}}{P_O^{[atm]}} \right) + 0.336 \qquad \text{Equation 40}$$

Figure 52 shows that the flashback results collapse quite well with the correlation. The average error between the actual and predicted value from the correlation is ± 3 percent. However, it should be noted that this expression only holds for the specific LSI design used in the present study. For another LSI, the values for , , or the flame lift-off height, , may be different and could affect the LSI's propensity for flashback. How it changes, though, were beyond the scope of this study.

Figure51: Flashback Limits Normalized by Pressure

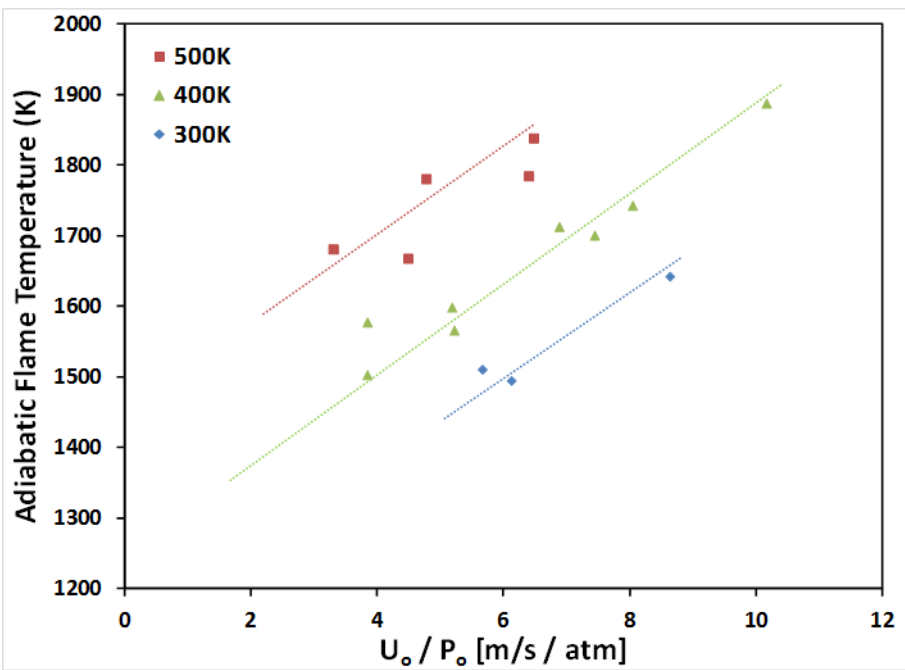

Figure 52: Flashback Data Correlated as a Function of ϕ, PO, and TO

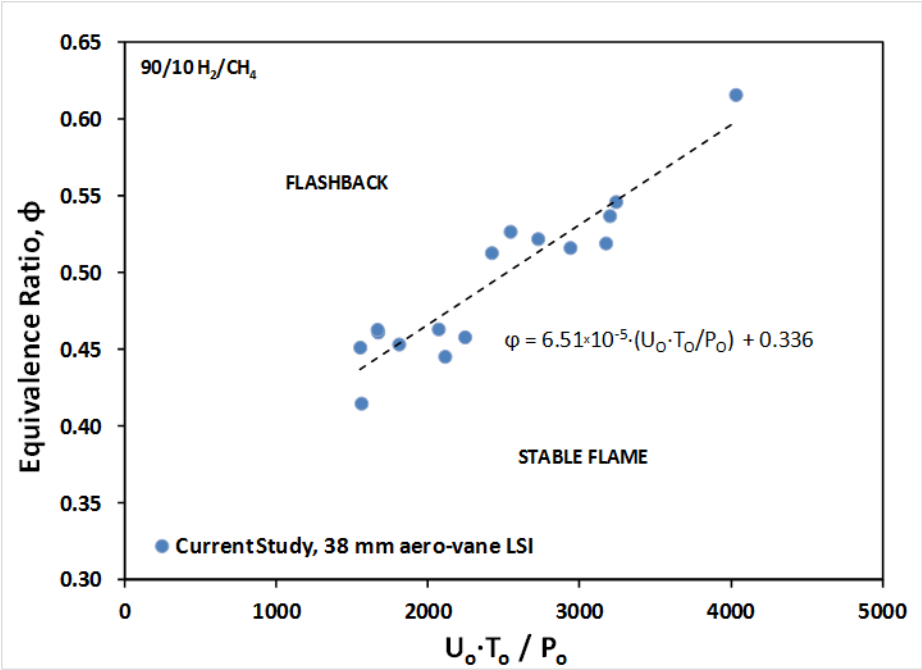

Figure 53: Combustor Inlet Temperature as a Function of Pressure Ratio Assuming 87 Percent Compression Efficiency. Inlet temperature is 294 K.

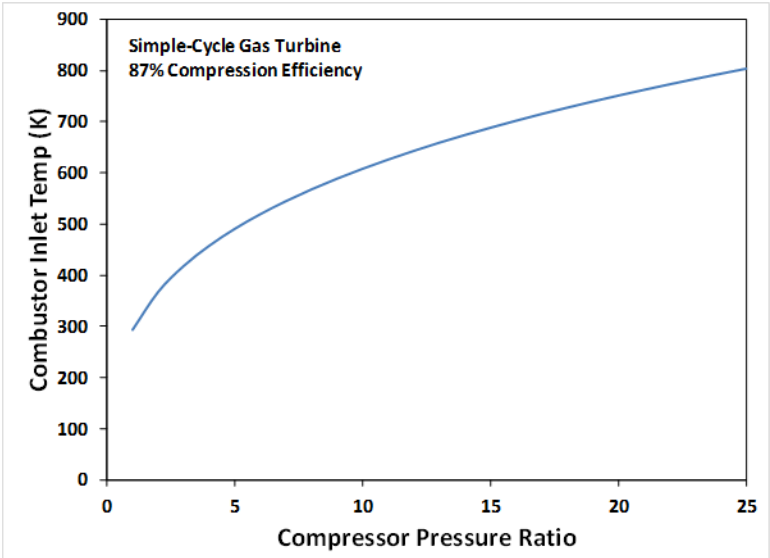

Given this information, the equivalence ratio at flashback, $\phi_{flashback}$ was calculated using the correlation for a range of velocities and pressure ratios. The pressure and temperature for each pressure ratio were taken from the curve in Figure 53. Using $\phi_{flashback}$ along with the combustor inlet pressure, PO, and temperature, TO, the corresponding adiabatic flame temperature $AFT_{flashback}$ at flashback was calculated in CHEMKIN. The results are shown in Figure 54. For a given pressure ratio, the $AFT_{flashback}$ increases with bulk velocities, U_O as expected. The plot reveals that for all velocities, $AFT_{flashback}$ initially decreases with increasing pressure ratio, but reaches a minimum and then steadily increases with pressure ratio thereafter. For U_O = 30, the minimum occurs for a pressure ratio of 10. For higher velocities, the minimum occurs at higher pressure ratios

Figure 54: Calculated Primary Zone Firing Temperature

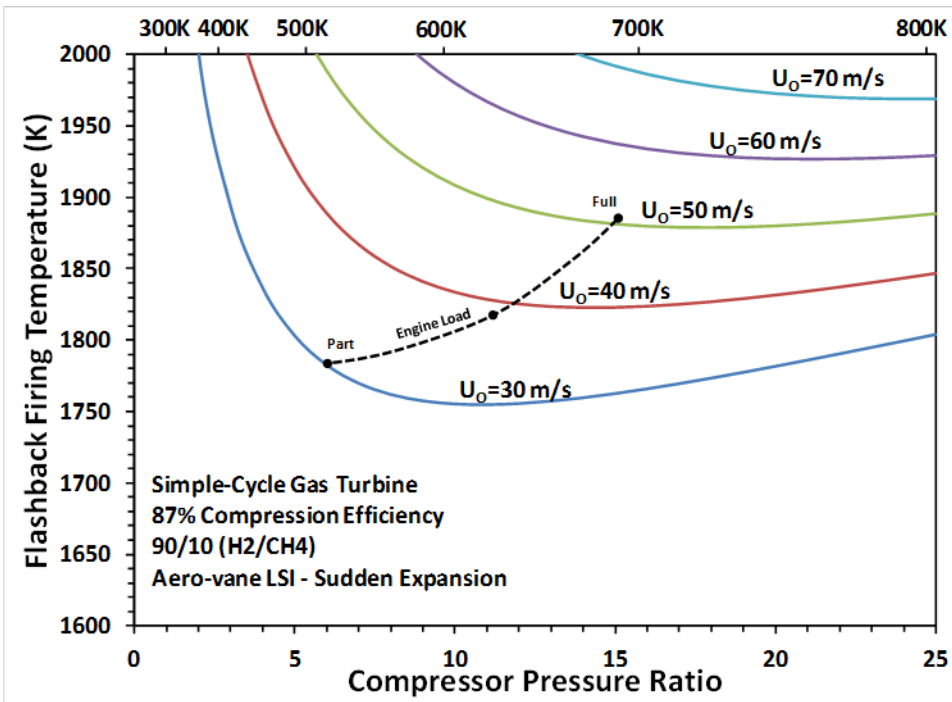

The non-monotonic behavior is the result of the competing effects between pressure and temperature on $\phi_{flashback}$ and $AFT_{flashback}$. The experiments from this study demonstrated that increasing the pressure (for fixed T_O) decreases the $AFT_{flashback}$, and increasing inlet temperature (with constant P_O) increases the $AFT_{flashback}$. For the simple-cycle gas turbine, the combustor inlet pressure and temperature will increase simultaneously as the pressure ratio is raised. As seen in Figure 53, initially increasing the pressure ratio will lead to a larger increase in the compressor exit pressure than in the exit temperature. But because of the roll-off, further increases in pressure ratio will lead to larger increases in exit temperature versus exit pressure. The net result is that at lower pressure ratios, the pressure term in the flashback correlation is

dominate, and increasing pressure ratio will lead to a decrease in $AFT_{flashback}$. But at higher pressure ratios, the increase in exit temperature more than offsets the increase in pressure, leading to an overall increasing $AFT_{flashback}$ with pressure ratio.

In reviewing the flashback dependency on inlet conditions, several other types of burners, such as the jet-burner and high-swirl burner, indicate a reduction in $AFT_{flashback}$ with increasing inlet temperature— opposite to what is observed with the LSI. This feature is very important, because in the case of the high-swirl or jet burners the doubly detrimental effect of increased inlet temperature and pressure would result in the curves in Figure 54 to monotonically decrease with pressure ratio. In fact, Daniele et al. (2010) observed that their jet burner could not be operated at pressures above 12 atm with fuels in excess of 50 percent hydrogen (by volume) because the flashback limit would intercept the blow out limit. The LSI results in the inlet temperature counterbalancing the pressure, allowing it to operate under a much wider range of pressure ratios.

To further illustrate the utility of the flashback chart in Figure 54, the nominal operating conditions for the Solar® Taurus 70 engine are shown as black dashed line. The Taurus 70 is a simple-cycle, medium-sized gas turbine with an output power of 7.7 MW. The full load combustor inlet pressure, temperature, and velocity are roughly 16 atm, 700 K, and 50 m/s, respectively. Johnson et al. (2005) and Nazeer et al. (2006) reported results of rig-testing at Solar's facilities with a single nozzle LSI operating with natural gas at both part- and full-load Taurus conditions. The dots on the dashed line in Figure 54 represent the inlet conditions for runs 1, 3, and 5, and are representative of full- and part-load operation, respectively. At full load condition (pressure ratio of 15), the LSI combustor can operate at a firing temperature of up to 1,885 K before flashback. At the part-load condition with a pressure ratio of 6, the combustor $AFT_{flashback}$ is around 1,785 K. The lower $AFT_{flashback}$ is due primarily to the large drop in the flow rate, or U_O, with load. The primary zone firing temperature for the Taurus at full load conditions according to Cheng et al. (2008) is around 1,866 K (2,900°F), which is just below the 1,885 K calculated flashback limit. Nazeer et al. (2006) reports testing at firing temperatures as low as 1,700 K, if this represents the primary zone firing temperature at the lowest pressure ratio tests, then this would indicate that even at part load the $AFT_{flashback}$ still appears to be slightly above the nominal operating temperature.

To increase the safety margin, the LSI nozzle could be decreased in diameter, which would increase U_O for a fixed mass flow rate. Another approach would be to change the LSI geometry (e.g., the perforated plate) slightly to increase the lift-off height and improve flashback resistance. Of course, other factors would need to be considered that take into account the overall engine design. For instance, changing the nozzle diameter will affect the pressure drop across the burner. By reducing the diameter, it would increase velocity and flashback resistance, but it would come at the cost of slightly higher pressure drops and decreased efficiency. Such details would need to be analyzed by the manufacture. Overall, the analysis in

the present study indicates that operation of a gas turbine with hydrogen fuel concentrations upwards of 90 percent appears quite feasible with an LSI-stabilized combustor at all pressure ratios. It would, therefore, be worthwhile in future efforts to pursue further development of the LSI for gas turbine operation.

4.2.6 Results for a High Swirl Burner

The effect of preheat air temperature; air velocity, and fuel composition on flashback and blowoff in the high-swirl burner configuration were evaluated, under the conditions outlined in Table 12.

Table 12: Parameters and Ranges Evaluated

Reference V (m/s)	Preheat T (K)	NG/H_2 %
4.9	300	0/100
9.8	400	20/80
	500	50/50
		80/20
		100/0

The reference velocity is defined as the bulk axial velocity in the premixing zone annulus. It was kept constant for each preheat temperature by adjusting air flow rates.

The test matrix resulting from the parameters outlined in Table 12 leads to thirty tests for blowoff and flashback data points. In addition, thirty tests were conducted to establish differences between the initiation of blowoff and ultimate blowoff. Many test points were repeated several times to establish uncertainty.

4.2.6.1 Blowoff

The test protocol documented both the ultimate blowoff condition and the condition at initiation of blowoff. Results are presented first for the ultimate blowoff conditions.

Figure 55 shows the equivalence ratio and AFT at the ultimate blowoff condition for all the cases. It is apparent that the AFT at ultimate blowoff significantly depends on hydrogen concentration in fuel mixture. Interestingly, although the equivalence ratio at ultimate blowoff varies significantly among the cases studied, the AFT at ultimate blowoff is very similar for a given fuel composition at both reference velocities and preheat temperatures. This illustrates that the flame temperature and fuel composition are the dominant drivers relative to ultimate blowoff.

Figure 55: AFT and Equivalence Ratio vs. Fuel Composition for Ultimate Blowoff

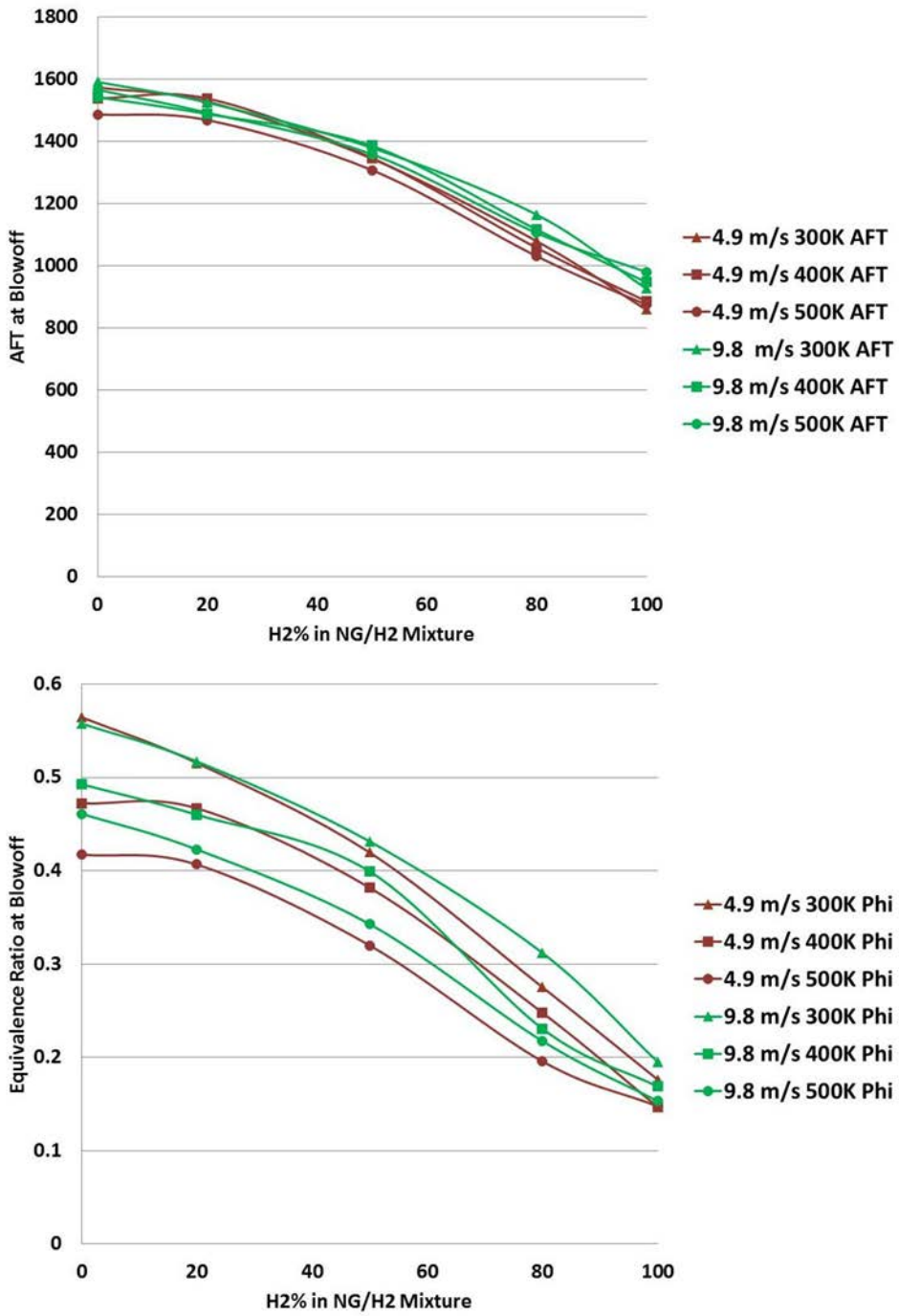

With the results in Figure 55, the ability of the "constant residence time" approach to predict the ultimate blowoff behavior can be evaluated (Strakey et al. 2007). CHEMKIN Pro was used to calculate the residence time corresponding to the blowoff equivalence ratio for 100 percent natural gas. This time is then used to predict the blowoff equivalence ratios of different fuel compositions. Six different residence times are necessary for the three preheat temperatures and two reference velocities. Figure 56 shows the predicted equivalence ratio (phi) versus the measured equivalence ratios at blowoff. As shown, reasonable agreement is demonstrated at lower hydrogen concentrations, but departure is noted at high hydrogen content fuel mixtures.

This result suggests that using a constant residence time for PSR simulations does not allow one to predict the impact of hydrogen addition on the ultimate blowoff for the current combustor. Note that the residence times for the conditions studied span more than an order of magnitude. Therefore, it may not be surprising that using a constant residence time based on 100 percent natural gas cannot predict blowoff for high hydrogen content fuel mixtures.

Figure 56: Modeled Phi vs. Measured Phi Using the Residence Time Approach for Ultimate Blowoff

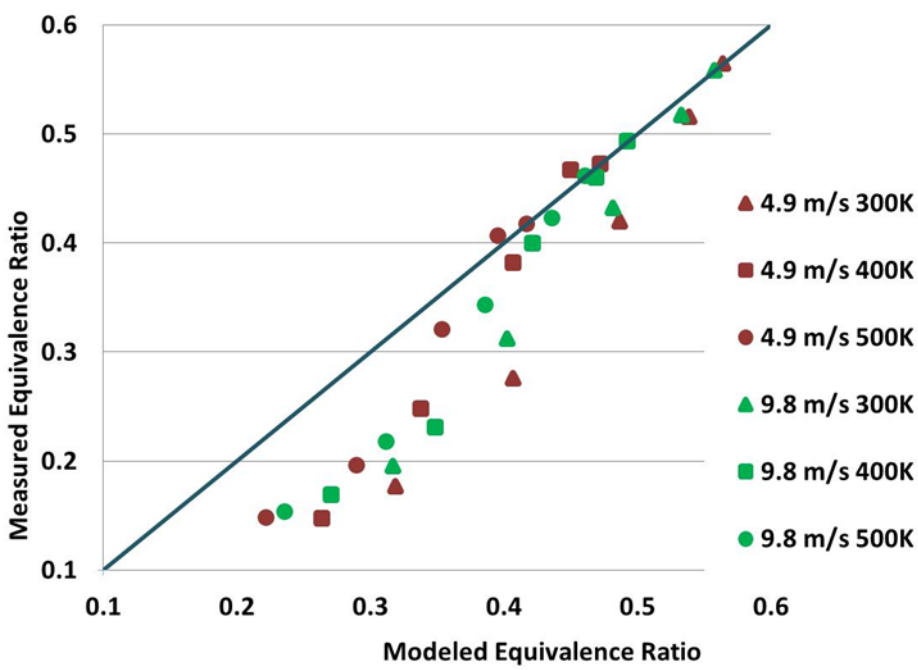

Next, the "local equivalence ratio" (Noble et al. 2006) approach is evaluated. The local equivalence ratio approach can, in principle, account for variation in mass diffusivities of mixtures of different fuels. It was suggested that adjusting the PSR equivalence ratio in a manner accounting for variation in mass diffusivity, the modeled equivalence ratios for constant residence time can capture the impact of fuel composition (Noble et al. 2006). The effect of fuel diffusivity is thus expressed in Equation 41:

$$\varphi_{adjusted} = \varphi_{Local} = \varphi_{measured} + \Delta\varphi \qquad \text{Equation 41}$$

Where

$$\Delta\varphi = C \times ln\left(\frac{D_F}{D_{OX}}\right) \qquad \text{Equation 42}$$

Where

= the fuel mass diffusivity,

= the oxygen diffusivity, and

C is a constant.

Alternatively, 1/LeF (inverse fuel Lewis number) can be used in place of the DF/DOX ratio (Equation 43):

$$Le_F = \frac{\alpha_m}{D_{Fm}} \qquad \text{Equation 43}$$

Where

α_m = the thermal diffusivity of the mixture.

As Lewis number is a dimensionless number, it is a more general way of expressing the ratio of mass diffusivities of fuel and oxygen. Using either 1/LeF or DF/DOX leads to the same result in this study. Thus, the analysis is shown only for the Lewis number.

Correlations for D_F and D_{OX} are presented in Kroner et al. (2003). Note that these calculations require values of $D_{H_2CH_4}$, $D_{H_2O_2}$, $D_{H_2N_2}$, $D_{CH_4H_2}$, $D_{CH_4O_2}$, $D_{CH_4N_2}$, $D_{O_2H_2}$, $D_{O_2CH_4}$, $D_{O_2N_2}$, that are the binary mass diffusion, and X_{H_2}, X_{CH_4}, X_{O_2}, and X_{N_2} that are the molar fraction of species of reactants. The binary diffusion coefficients are calculated using an in-house code (see Appendix F: Mixture Property Calculator). Figure 57 illustrates that, although D_F, D_{OX}, and α_m have different values for a given hydrogen concentrations at different velocities and preheat temperatures, ln(1/Le_F) and ln(D_F/D_{OX}) are very similar. It implies that those variables can provide physical insights into the impact of mass diffusion of high hydrogen content fuels on blowoff limits.

Figure 58 shows that the modeled equivalence ratio at blowoff, incorporating an adjustment for diffusivity, matches the measured value shown in Figure 56. The adjustment to the measured results here is obtained using $\Delta\phi = C \times Ln(\frac{1}{Le_F})$, where $C = 0.058$. It is also confirmed that using $\Delta\phi = C \times Ln(\frac{D_F}{D_{OX}})$ will give similar improvement in the results, with $C = 0.051$. It shows that all fuel compositions with the adjusted equivalence ratio have similar residence times at blowoff.

Figure 57: Calculated Variables for Different Fuel Compositions for All the Cases for Ultimate Blowoff

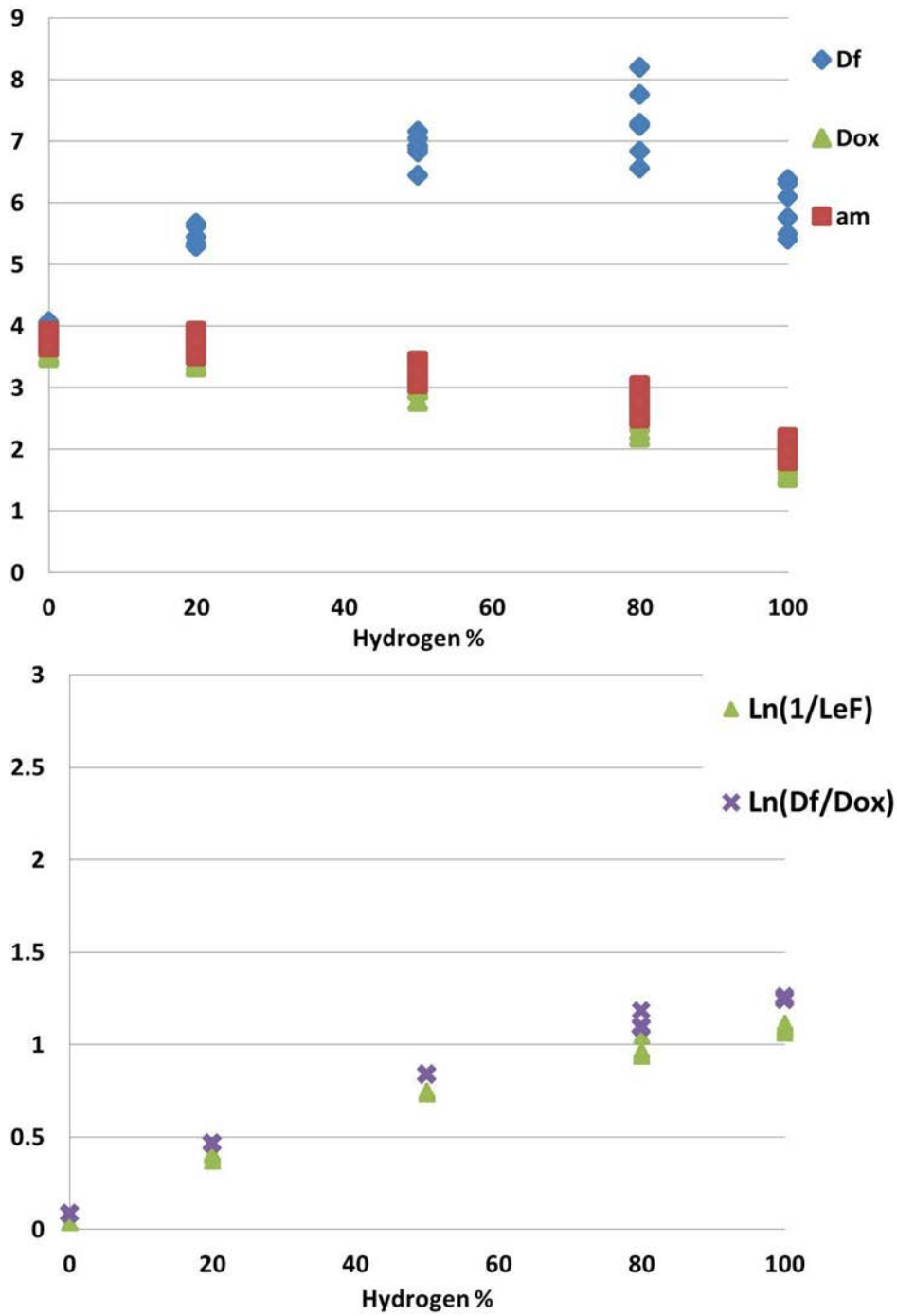

Figure 58: Measured Phi vs. Adjusted Model Phi Based on Local Equivalence Ratio for Ultimate Blowoff

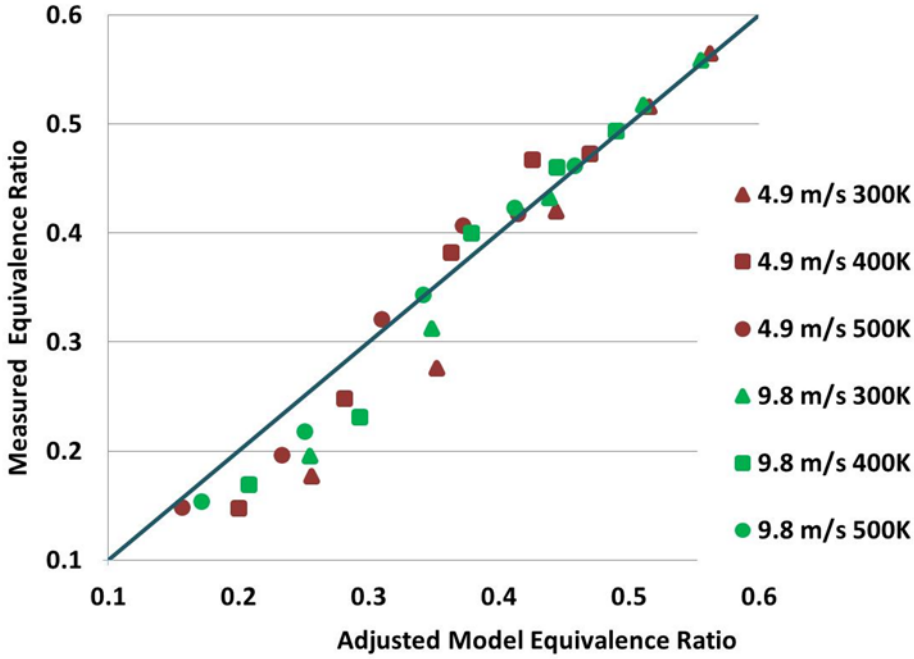

This result is significant because if the equivalence ratio at blowoff for one fuel composition is known, the equivalence ratios for other compositions and conditions can then be estimated by using convenient chemical kinetics simulations anchored to that single composition residence time.

In principle, a constant Da should apply for each set of test with the same air bulk velocity and preheat temperature. A constant value of Da implies that, for different fuel compositions with constant air flow rates and preheated temperatures, the chemical residence time is constant, since the flow residence time which is $\tau_{res}=L_C/U_c$ is constant for a fixed bulk velocity U_c and characteristic length, L_C. However, Figure 58 shows some data points that still fall away from the linear correlation. It could be because the constant Da approach for detecting flashback is actually correlated to the beginning (i.e., the initiation) of blow off events. As the hydrogen concentration in fuel increases, the difference in equivalence ratio at which the initiation of blowoff and ultimate blowoff occurs increases. This is due to ability of hydrogen to withstand stretch and corrugation in the flame near blowoff.

To explore this further, an evaluation of the constant residence time and local equivalence ratio approaches evaluated above to predict initiation of blowoff is undertaken. As explained earlier (Figure 31), OH* chemiluminescence is used to identify the beginning of blowoff. Figure 59 presents the measured equivalence ratios at initiation of blowoff versus the modeled equivalence ratios using the constant residence time approach. The results in Figure 59 are closer to the line of unity compared to Figure 56, but the accuracy again degrades for a higher hydrogen concentration.

Figure 59: Modeled Phi vs. Measured Phi Using the Residence Time Approach for Initiation of Blowoff

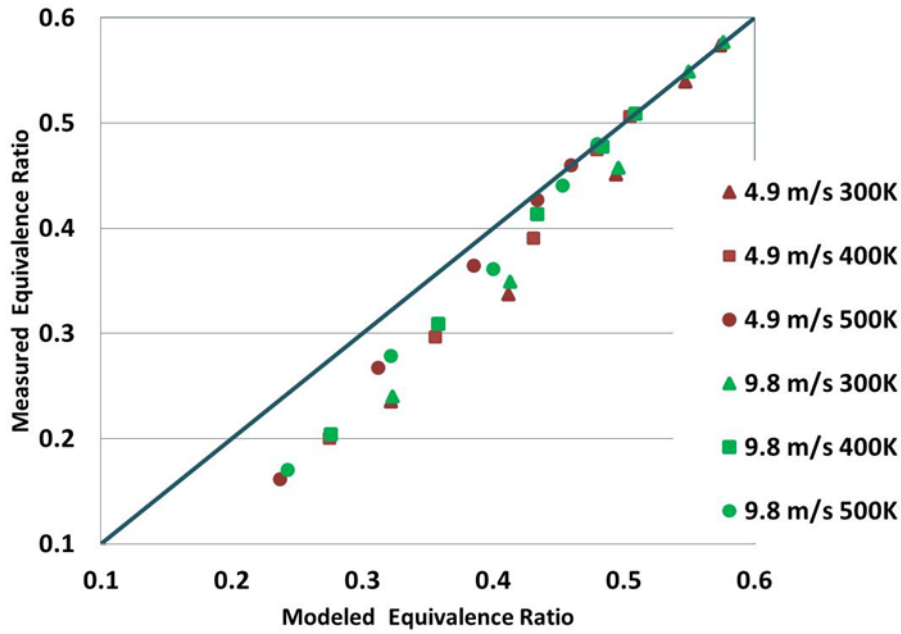

The alternative approach, adjusting the predicted equivalence ratio using Δϕ (Equation 41 and Equation 42), produces much better results, as shown in Figure 60. Furthermore, the prediction of the blowoff initiation condition correlates much better than does the ultimate blowoff behavior, as shown inFigure 58. Hence, the results obtained in the present work support the physical arguments about blowoff provided previously Shanbhogue et al. 2010).

Thus, to predict the equivalence ratio at initiation of blowoff for a range of mixtures of natural gas and hydrogen, it is sufficient to know (or measure) the equivalence ratio for one composition. Then, using chemical kinetics simulations, the residence time for a PSR near extinction can be calculated. This residence time can be used to determine an equivalence ratio for other fuel mixtures, which, when adjusted by $\Delta\phi = C \times Ln(\frac{1}{Le_F})$ provide a predicted blowoff result for the fuel mixture of interest. Although works well for the present work, the value could be different for other applications.

Figure 60: Measured vs. Adjusted Model Phi Based on Local Equivalence Ratio for the Beginning of Blowoff

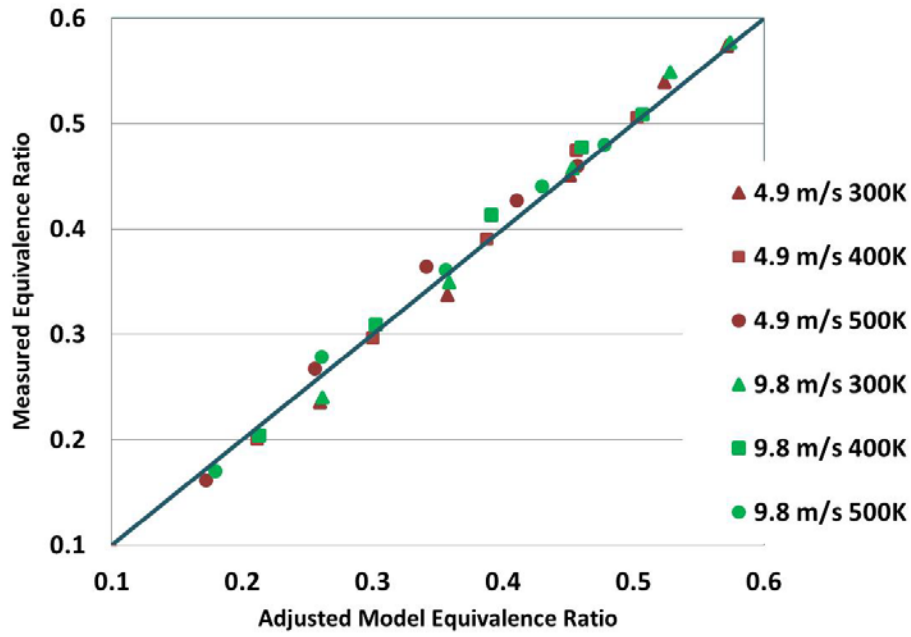

4.2.6.2 Flashback

Flashback was studied for cases with AFT below 2,100 K in order to prevent damage to the quartz combustor liner that was used.

For the high-swirl burner, a prominent mechanism for flashback is associated with combustion induced vortex breakdown (CIVB). Appendix B provides details in Section B.2.2. The parameters associated with CIVB flashback are C_{quench} and C^*_{quench} which must are calculated for all cases to evaluate if they can predict flashback. To do this, τ_PSR is calculated for the measured equivalence ratio at blowoff, and u¯ and d are calculated based on air flow rates and dimensions. The 〖Le〗_F calculation is described in Appendix B, Section B.2.2.4. Figure 61 shows Cq and Cq* for all the cases where flashback occurred. It is noted that one data point (C_q = ~18; C_q* = 6.5) is not included, as it was significantly different than the other values. As shown, no single value of C_q or C_q* was able to predict flashback. C_q* does improve the results compared to C_q, though again a single value is unable to predict flashback for all cases. The reason for this could be that the chemical residence times from PSR simulations are orders of magnitude different for different fuel compositions. Thus, values of C_q or C_q* based on the chemical residence time may have an order-of-magnitude difference for different fuel composition. This is particularly evident for the cases without preheat.

To further assess the constant C_q * method, equivalence ratios at flashback for different fuel compositions were determined. In this case, the equivalence ratio at flashback for one case is measured, and the constant C_q * determined. Then, for this constant C_q* value, the equivalence ratios corresponding to this fixed value for each set of cases with same bulk velocity and

preheat temperature were determined using a PSR simulation. For instance, taking the first case as a reference, the following calculations are carried out using Equation 44:

$$C^*_{quench\text{-}1} = C^*_{quench\text{-}2} \quad \text{so}$$

$$Le_{F_1} \times \tau_{PSR_1} \times \frac{\bar{u}_1}{d_1} = Le_{F_2} \times \tau_{PSR_2} \times \frac{\bar{u}_2}{d_2} \qquad \text{Equation 44}$$

Since the characteristic length and velocity is the same for each set of cases, it implies that

$$Le_{F_1} \times \tau_{PSR_1} = Le_{F_2} \times \tau_{PSR_2} \qquad \text{Equation 45}$$

Therefore, if C_q* is constant through the cases, $\tau_{PSR_2} \times = \frac{Le_{F_1}}{Le_{F_2}} \times \tau_{PSR_1}$

If τ_{PSR_1} is known, and C_q* is a constant, by calculating τ _(〖PSR〗_2), the equivalence ratio of the second case can be calculated by PSR simulation at blowoff. The predicted equivalence ratios using this method are shown versus the measured equivalence ratios in Figure 62, which illustrates that the constant C_q* method is unable to predict how conditions and fuel composition affect flashback in the current high-swirl burner.

The CIVB flashback mechanism and blowoff mechanism both suggest a competition between cold flow quenching the flame and the reaction zone heat release sustaining the flame. Given that the local equivalence ratio approach improved the correlation for blowoff, this method is now applied as well to the flashback results.

Again, the residence time at blowoff is calculated for measured equivalence ratio of one case using PSR simulations. Then that residence time was used to predict the equivalence ratio at blowoff for the other cases. The equivalence ratios are adjusted using the same approach described above in the discussion of Equation 41 and 42. For this case, C = 0.1 gives good results for some cases. The results obtained from this method are presented in Figure 63. Significant improvement is noted for the cases with no preheat compared to results shown in Figure 62, which were based on constant C_q*. However, with preheat, the predictions are still poor. As discussed above, the behavior of flashback for cases with preheated air is different from the ones without preheating. For cases where flashback occurs because the premixer zone cannot quench the flame, using the local equivalence ratio method can predict flashback for a range of fuel composition. However, for other cases, this method does not appear to work. It could be that, for these cases, another mechanism is controlling flashback, and flashback is not only governed by ability of premixer to quench the flame.

Figure 61: Equivalence Ratios vs. Cq and Cq* at Flashback

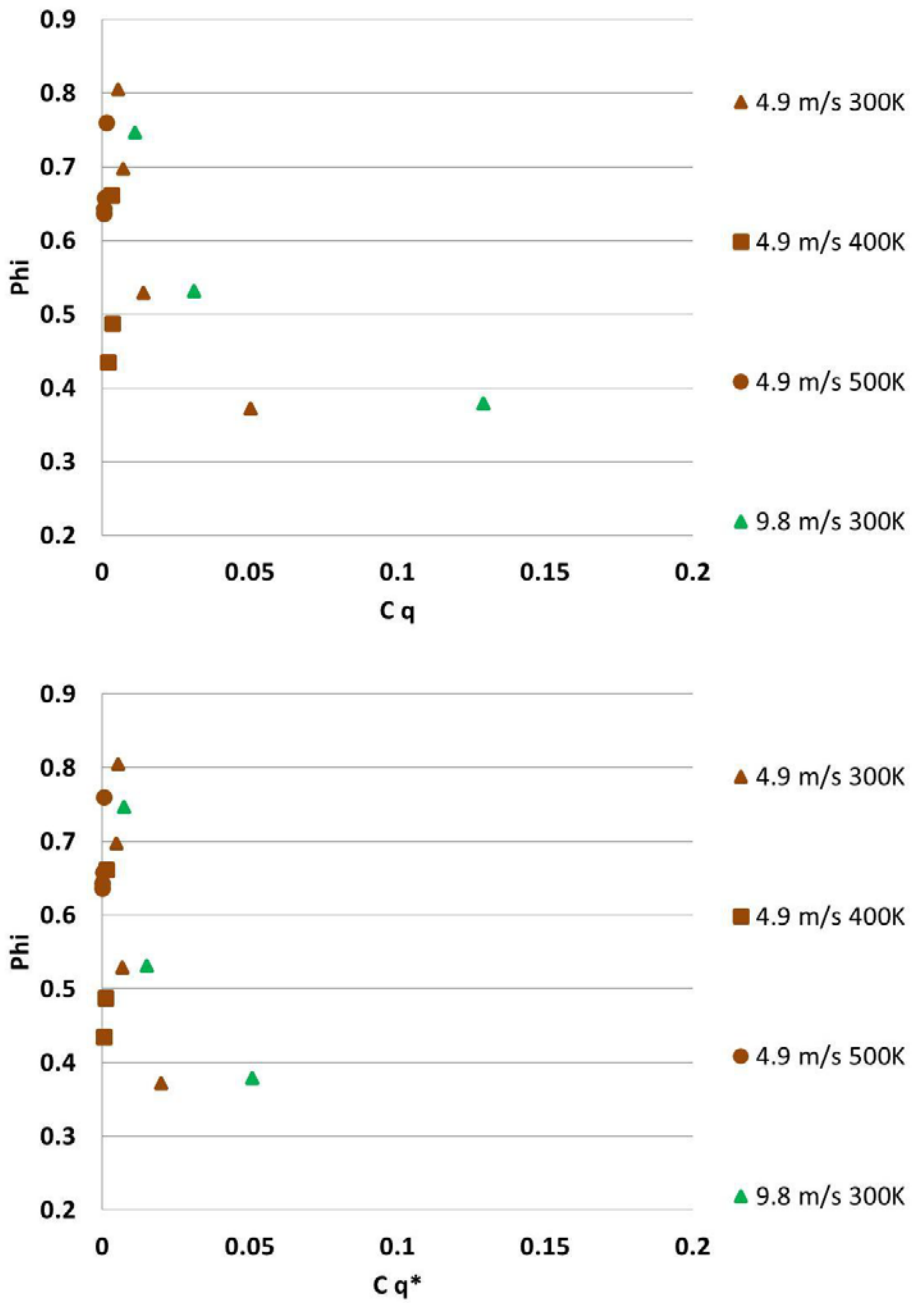

Figure 62: Predicted vs. Measured Equivalence Ratios Using the Cq* Constant Method

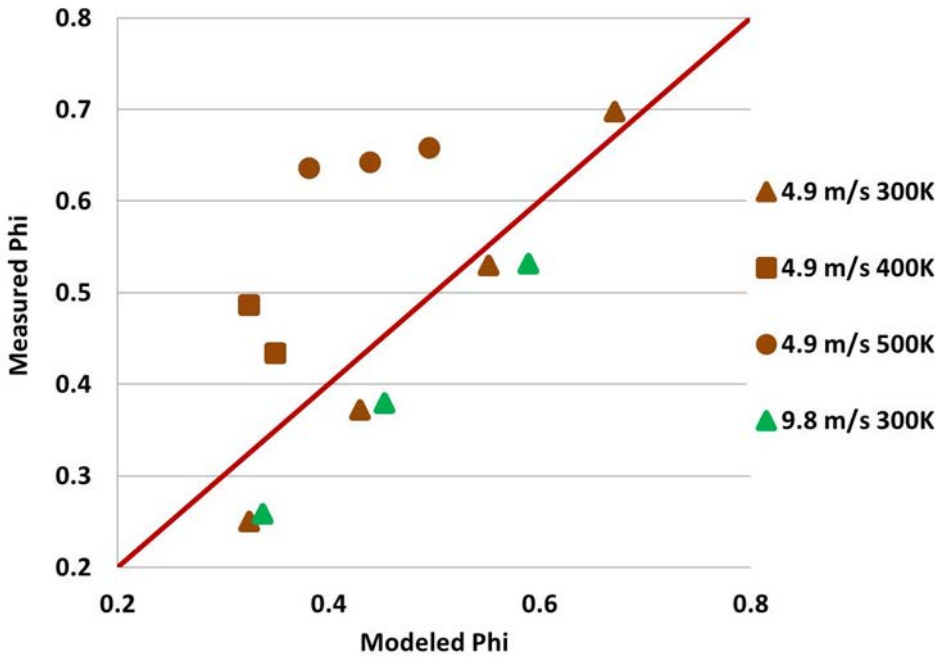

Note that, for the preheated cases, the temperature jump at flashback (ratio of burned and unburned temperatures) is very similar. Density changes across the reaction front, which are reversely correlated to temperature jumps, can generate baroclinic vorticity and thus contribute to formation of a vortex breakdown flashback mechanism. The temperature jump is shown in Figure 64 for all the cases.

For the cases without preheat, the temperature ratio decreases as hydrogen concentration in the fuel mixture increases. For 400 K preheating temperature, the rate of change in temperature ratio decreases in comparison. For 500 K preheat, the temperature jump is fairly constant over the fuel composition range. For both preheat cases, the measured equivalence ratios at flashback are higher than modeled ones based on local equivalence ratio approach. It indicates that for these cases, the flowfield is resistant to flashback until the temperature reaches a specific value. Flashback at constant temperature for different fuel compositions are also reported elsewhere (Noble et al. 2006).

Figure 63: Predicted Phi vs. Modeled Phi Based on the Adjusted Equivalence Ratio Method

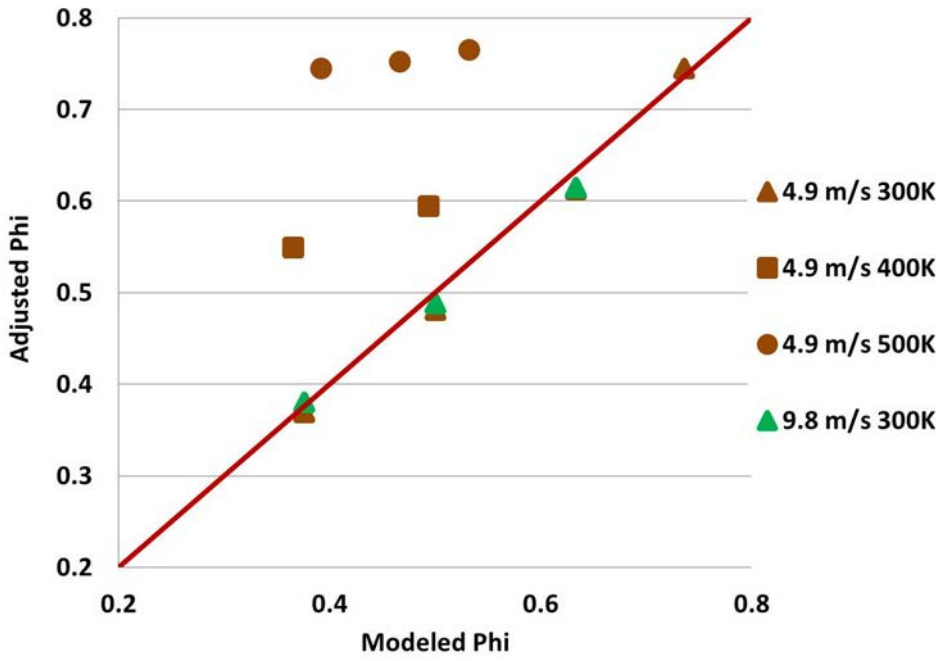

Figure 64: Temperature Ratio at Flashback for Different Fuel Compositions

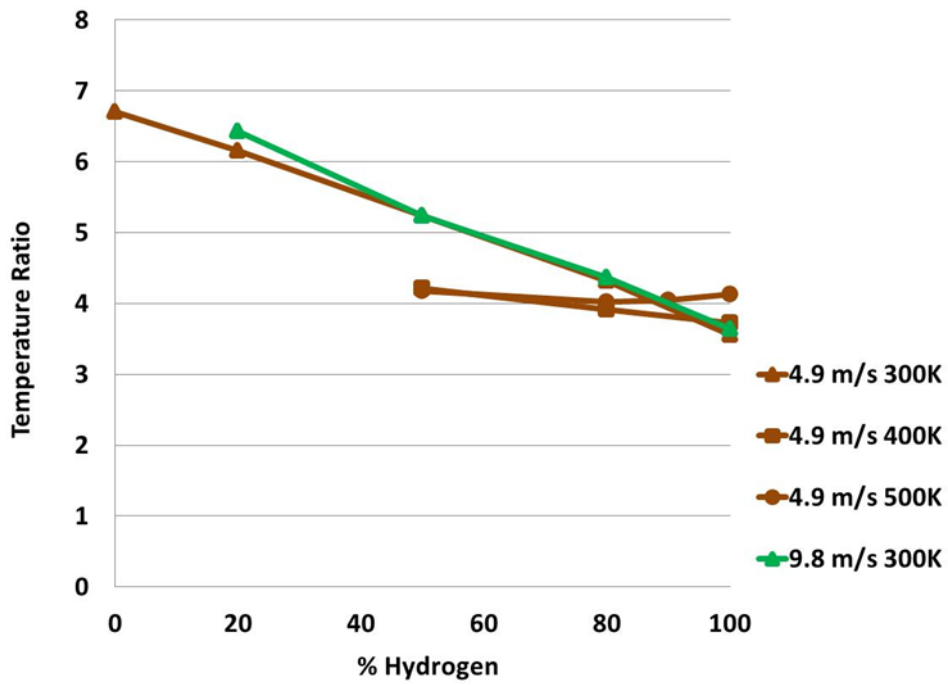

4.2.6.3 Summary

In this section, blowoff and flashback events for a mixture of natural gas and hydrogen operated in a high-swirl burner are correlated using different methodologies proposed in the literature. For the case of blowoff, fuel Lewis number was identified as a strong parameter in correlating the equivalence ratios at blowoff for different fuel compositions. It was also concluded that the "beginning of blowoff" can be better correlated with proposed interchangeability index compared to ultimate blowoff.

For the case of flashback, experimental measurements were used to validate existing parameter based on quenching correlation proposed by other researchers for CIVB flashback. Results showed that the quenching approach failed to predict the flashback events in general. A modification to that correlation was suggested which improved the predictive ability for some flashback cases. It could be that the CIVB flashback mode is not the dominant mode for this particular high-swirl burner.

4.2.7 Results for Capstone Engine

Operability studies on the Capstone engine test platform proved to be very challenging. For blowoff studies, modification to the engine operating system was required to reduce the target firing temperature on the turbine. Due to the recuperated engine, significant thermal inertia is present. Thus, systematically reducing the target firing temperature until blowoff took significant time, to the extent that large quantities of fuel were required. As a result, insufficient results could be obtained to really evaluate or refine an appropriate correlation or design tool.

In terms of flashback, a lack of visual or acoustic feedback led to major shortcomings. Ultimately thermocouples were used to detect flashback, but with six injectors operating this required expensive instrumentation. Further, when temperature was elevated it was not clear if it was due to flashback or to the proximity of the flame changing relative to the injector. In the end, despite considerable effort, little reliable flashback information was obtained. It was observed that hydrogen concentrations in excess of 30 percent (+/-3%) by volume in natural gas tended to result in flashback.

With hydrogen and carbon dioxide, flashback was observed at 10 percent (+/-3%) hydrogen by volume. Thus flashback was more likely for synthesis-type gases than for mixtures of hydrogen and natural gas.

Also noteworthy were attempts to reach flashback conditions with ethane/natural gas mixtures. At no time was flashback with ethane (even up to 100 percent) achieved. Hence, in terms of the Capstone engine test platform, flashback with higher hydrocarbons does not seem to be an issue. Only when hydrogen is present does the risk of flashback become significant.

4.2.8 Summary

To evaluate criteria for operability in terms of blowoff and flashback, several test devices were used to collect data as a function of fuel composition. These devices included a jet flame, a jet-stirred reactor, a low-swirl burner, a high-swirl burner, and a commercial gas turbine engine. Blowoff was studied in the jet-stirred reactor and high-swirl burner. Flashback was studied in the jet flame, low-swirl burner, high-swirl burner, and gas turbine engine.

In terms of blowoff, in both the jet-stirred and high-swirl burner, the inclusion of fuel components with higher reactivity, such as hydrogen or higher hydrocarbons, generally enhances the general stability of the reaction. The addition of diluents tends to decrease overall system stability. In the jet-stirred reactor, it was observed that blowoff was established by the presence of the least reactive fuel in the mixture. As a example, mixtures with 50 percent hydrogen with CO were found to be more stable than 50 percent with CH_4. Results in the jet-stirred reactor were not used extensively for validation of blowoff correlations.

On the other hand, the results for the high-swirl burner were used to evaluate correlations for blowoff that are expressed in terms of a ratio-of-time scales. The comparison of a physical time scale to a chemical time scale has been shown to correlate blowoff for bluff body stabilized flames, in which a rod or bar is inserted into the flow to create a recirculation behind it in order to anchor a reaction. In the present work, the use of time scale ratios in the high-swirl burner was found to correlate well with blowoff. In particular, if a modification to the time scale is made to account for stretch resistance of the flame, improved agreement between predicted and measured values are obtained. For example, hydrogen has a high strain resistance, and if this behavior is captured through use of Lewis number, improved correlations are obtained. As a result, it is concluded that blowoff can be well correlated through use of time scale ratios. What is necessary is the determination of the scales. The physical time scale can be derived from the ratio of a length scale (e.g., the burner diameter) to a velocity (e.g., the bulk velocity through the burner). The chemical time scale can be determined using a partially stirred reactor simulation using CHEMKIN or Cantera.

In terms of flashback, comparisons of methodologies for the jet flame, low-swirl burner, high-swirl burner, and engine were carried out. Flashback is inherently more challenging to study than blowoff because there are several distinct routes that can lead to flashback, each of which has different controlling physics. Hence, if a system with two mechanisms at play is studied, it may be difficult to correlate behavior with one expression. For the jet flame, which is expected to be dominated by boundary layer flashback, an expression for boundary layer flashback was developed in terms of a critical velocity gradient. This expression is a function of the ratio of mixture thermal diffusivity and ratio of laminar flame speeds. The ratios are expressed in terms of values for methane. The mixture thermal diffusivity and flame speeds can be calculated using a methodology in Appendix C and the flame speed using CHEMKIN. Of critical importance for the jet burner is consideration of local burner tip temperature. Because previous work did not attempt to incorporate the tip temperature into the analysis, the use of these expressions are limited for practical systems. The current results, based on CHEMKIN calculations using the

tip temperature, provide insight into the relative flame back propensity of different fuel compositions.

For the low-swirl burner, where core flashback is expected to dominate, an expression based on velocity, inlet temperature, and inlet pressure was developed for a 90/10 hydrogen/methane (by volume) fuel. The results suggest the low-swirl burner could operate satisfactorily in a lean premixed mode on high levels of hydrogen at practical gas turbine conditions.

For the high-swirl burner, where combustion-induced vortex breakdown flashback is expected, existing quenching-based correlations based on time scale ratios were evaluated. It was found that, for the conditions studied, these could not collapse the data obtained. This could be a result of another flashback mode also contributing.

For the engine, the lack of optical access and consistent flashback detection resulted in limited data. Efforts to correlate the results obtained proved largely unsuccessful, although it was observed that flashback propensity of carbon monoxide was much higher than equal amounts of methane when mixed with hydrogen. Ethane added to methane was also studied and found to not lead to flashback for the cases studied.

CHAPTER 5:

Fuel Interchangeability Impacts on Emissions

5.1 Review of Key Factors

Pollutant emissions are a result of complex chemistry occurring in the combustion process. Of particular interest for gaseous fuels is emission of NOx, due to its role in ozone formation. The NOx is formed through various complex pathways, as reviewed in Appendix B, Section B.2.4. For low-emission systems, combustion temperatures are purposefully maintained at relatively low values (e.g., below 1,900 K) to avoid forming the most commonly discussed mechanism, known as Thermal NOx. As a result, the other NOx formation pathways can become significant relative to the overall NOx emission. Sometimes the relationship of the reaction structure with the aerodynamic structure can influence which pathway is dominant.

5.2 Evaluation of Emissions Predictions Preformance

As discussed in Appendix B, Section B.2.4, the ability of simple algebraic expressions to capture fuel composition impacts on emissions is highly limited. The correlations simply do not incorporate sufficient details to capture the fuel composition. Thus the emphasis here is given to more sophisticated approaches, which couple information about the flowfield (readily available from CFD) with detailed chemical kinetic calculations. This method is referred to as the chemical reactor network (CRN) approach. This section explores the ability of CRN to predict fuel composition impacts on emissions. Three different burner configurations are examined: the jet-stirred reactor, the high-swirl burner, and the Capstone C-65 commercial microturbine engine.

5.2.1 Results for Stirred Reactor

5.2.1.1 CRN Development

The overall jet-stirred reactor test bed is described in detail in Section 4.2.2.2. This section summarizes the development of an appropriate CRN for this particular device. The chemical reactor setup used in the chemical kinetic modeling is shown in Figure 65. The elements are PSRs (perfectly stirred reactors). Burning in the JSR's jet is simulated by PSR1, while burning in the recirculation zone of the JSR is simulated by PSR2. The shear layer is represented by PSR3. The 75 percent recycle of combustion products is determined from CFD modeling of the JSR. Typically, PSR1 is modeled as adiabatic; whereas, the other PSRs are assigned to measured temperature (nominally 1,800 K). This is termed partially stirred temperature (PST). A PSB is a PSR at incipient blowout. Combustion temperature is taken as the temperature of the recirculation zone.

Figure 65: Three-Element CRN Used for Chemical Kinetic Modeling of the Experimental JSR

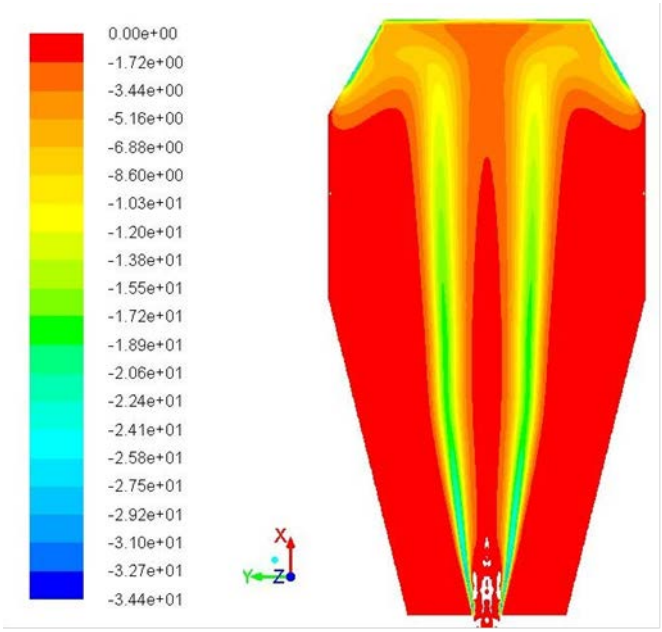

a) CH4 Reaction Rate

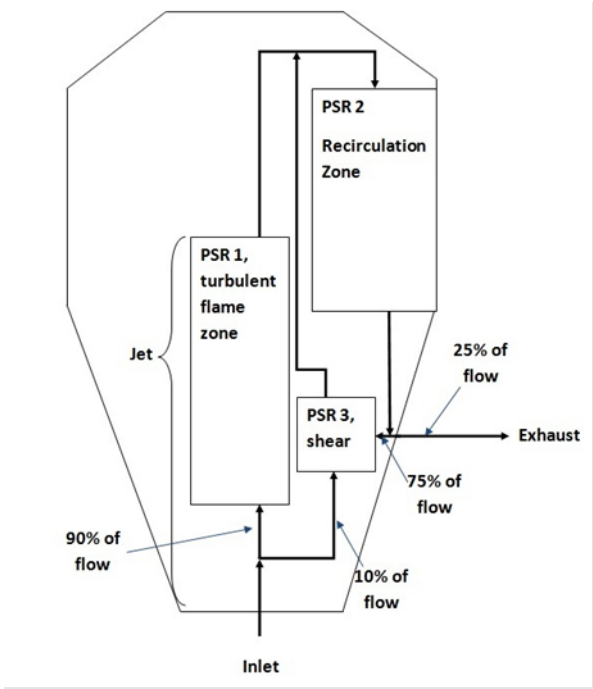

b) Corresponding Network

Beyond the development of the reactor network, an appropriate chemistry mechanism must also be selected. The prediction of NOx for the methane-fired JSR is shown in Figure 66 for five different chemical kinetic mechanisms. The baseline three-element CRN is used. The baseline mechanism is GRI-Mech 3.0 (Smith et al. 2000), which shows good agreement with the experimental data. C_2-NOx is the reaction design mechanism (Naik et al. 2011), and it also shows good agreement to the data. The Konnov (2000) and University of California, San Diego (n.d.), with NOx chemistry from Hewson and Bollig (1996) mechanisms, show somewhat less agreement to the data. However, when the Konnov et al. (2001) rate data for the Reaction NNH+O → NO+NH is substituted in GRI-Mech 3.0, best agreement to the experimental data is obtained. This mechanism is termed GRI-3.0-Konnov-4, and is typically the mechanism used for JSR modeling presented herein.

Figure 66: Comparison of NOx Prediction Obtained by the Baseline Three-Element CRN Using Five Different Chemical Kinetic Mechanisms

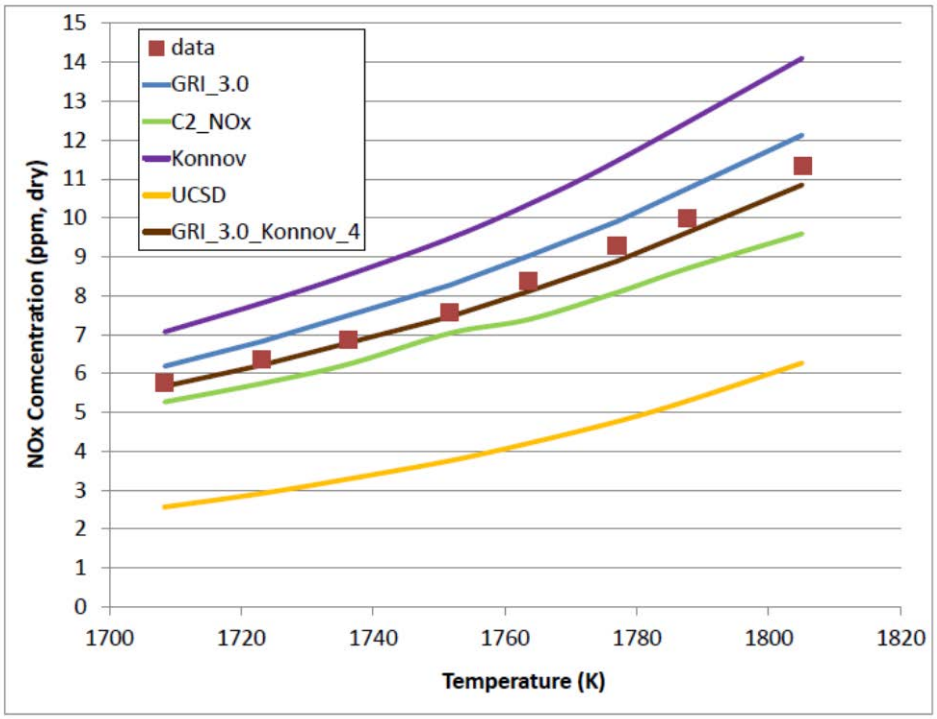

5.2.1.2 Alkane-Based Fuels

CH4 Modeling

Good agreement between the modeling results and the experimental data for lean premixed (LPM) CH_4 combustion is shown in Figure 67. Both the modeled and experimental NOX data are divided by residence time and plotted against the inverse of the combustion temperature representing an Arrhenius plot..

To gain better insight on the modeling results, each of the four NO_X production pathways presented in Section 3.2.4 is isolated using the method outlined in the next paragraph, and the model is rerun. The complete NO_X mechanism for GRI-Mech 3.0 is shown below in Table 13. It shows each reaction within the GRI-Mech 3.0 NO_X mechanism, along with the most likely direction of reaction under LPM conditions. The units are as follows: the pre-exponential factor for each reaction is equal to 10^A (mole/m^3-s), b is the temperature exponent corresponding to $(T/T_o)^b$, To is 298 K, and the activation energy, Ea, has units of kcal/mole (Novosselov 2006).

Figure 67: Net NOX Production Rate for LPM CH4 Combustion, Showing Both Experimental and Modeling Results

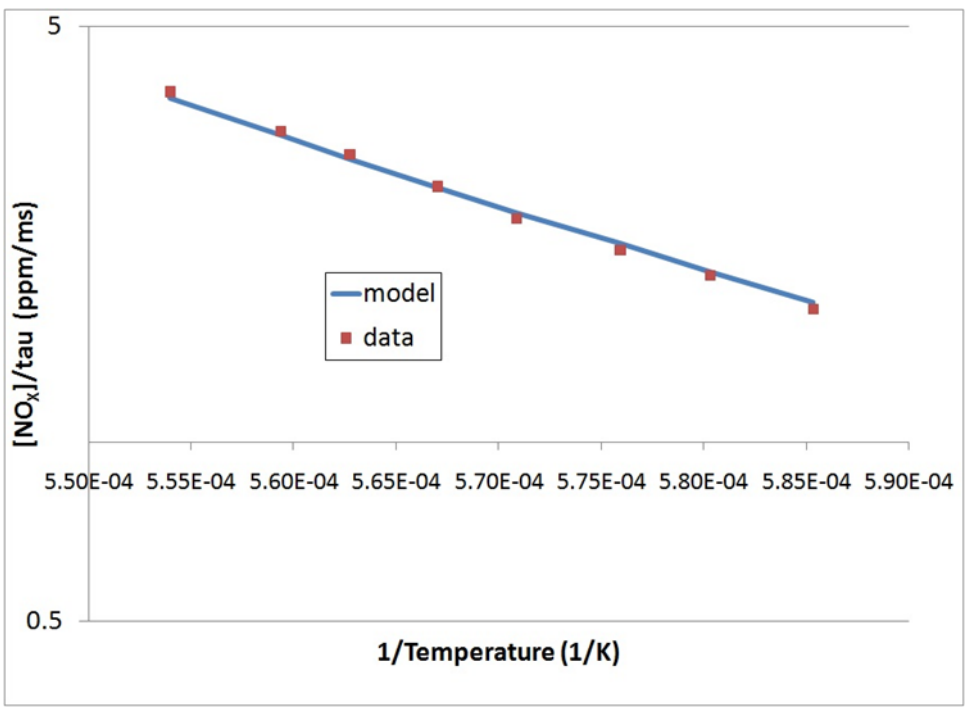

The NO_X contribution from each pathway is determined via two independent methods, in order to provide a check. The procedure for Method 1 is the following. First, all reactions are removed besides the Zeldovich pathway (Reactions 1–3). The model is run, and the computed results are the NO_X production from the Zeldovich pathway only. Next, the reactions associated with the NNH pathway (Reactions 10–22) are added. The model is run again, and the results give the contributions from the Zeldovich and NNH pathways; thus, the difference of the two is the

contribution from the NNH pathway alone. Lastly, the reactions associated with the Prompt mechanism are added (Reactions 23–34). The model is run again to determine the contributions from the Zeldovich, NNH, and Prompt pathways. The difference of this result from the previous result is the contribution from the Prompt pathway alone. The difference between the entire mechanism and the contributions from the Zeldovich, NNH, and Prompt pathways is the contribution from the N_2O pathway.

Table 13: Major Reactions of NOX Formation

Zeldovich Mechanism										
Reaction	Reactants			Direction	Products			A	b	Ea
1	N	NO		←	N2	O		13.431	0	0.355
2	N	O2		→	NO	O		9.954	1	6.5
3	N	OH		→	NO	H		13.526	0	0.385
Nitrous oxide mechanism										
	Reactants			Direction	Products			A	b	Ea
4	N2O		M	↔	N2	O	M	10.898	0	56.02
5	N2O	O		→	N2	O2		12.146	0	10.81
6	N2O	O		→	NO	NO		13.462	0	23.15
7	N2O	H		→	N2	OH		14.588	0	18.88
8	N2O	OH		→	N2	HO2		12.301	0	21.06
9	NH	NO		←	N2O	H		14.562	-0.45	0
NNH mechanism										
	Reactants			Direction	Products			A	b	Ea
10	NNH			←	N2	H		8.519	0	0
11	NNH	M		←	N2	H	M	14.114	-0.1	4.98
12	NNH	O2		←	HO2	N2		12.699	0	0
13	NNH	O		←	OH	N2		13.398	0	0
14	NNH	H		←	H2	N2		13.699	0	0
15	NNH	OH		←	H2O	N2		13.301	0	0
16	NNH	CH3		←	CH4	N2		13.398	0	0
17	NNH	O		→	NH	NO		13.845	0	0
18	NH	OH		→	N	H2O		9.301	1.2	0
19	NH	O		→	NO	H		13.602	0	0
20	NH	O2		→	NO	OH		6.107	1.5	0.1
21	N	O2		→	NO	O		9.954	1	6.5
22	N	OH		→	NO	H		13.526	0	0.385
Fenimore prompt (CH) mechanism										
	Reactants			Direction	Products			A	b	Ea
23	CH	N2		→	HCN	N		9.494	0.88	20.13
24	HCN	O		→	NCO	H		4.307	2.64	4.98
25	NCO	O		→	NO	CO		13.371	0	0
26	NCO	OH		→	NO	H	CO	12.398	0	0
27	NCO	O2		→	NO	CO2		12.301	0	20
28	HCN	O		→	NH	CO		3.705	2.64	4.98
29	NCO	H		→	NH	CO		13.732	0	0
30	NH	OH		→	N	H2O		9.301	1.2	0
31	NH	O		→	NO	H		13.602	0	0
32	NH	O2		→	NO	OH		6.107	1.5	0.1
33	N	O2		→	NO	O		9.954	1	6.5
34	N	OH		→	NO	H		13.526	0	0.385

An important question is whether the appearance of common reactions between the mechanisms lead to synergies, and thus non-additive results. Each mechanism is primarily rate-controlled by the first step that converts N_2 to a reactive species, with the subsequent reactions being relatively fast. Thus, a mechanism can be effectively disabled by removing the key initiating reaction from N_2. Instead of removing all the reactions associated with a mechanism, in Method 2 the rate-limiting reactions are the only reactions removed, and each reaction path is run separately. For example, to determine the contribution from the Zeldovich pathway only, the initial, rate-limiting reactions from the NNH, Prompt, and N_2O pathways are removed. In other words, in the Zeldovich-only model, Reactions 4, 10, 11, and 23 are removed. In the NNH-only model, Reactions 1, 4, and 23 are removed. In the N_2O-only model, Reactions 1, 10, 11, and 23 are removed. Finally, in the Prompt-only model, Reactions 1, 4, 10, and 11 are removed. As shown in Figure 68, the results between Methods 1 and 2 are nearly identical.

Figure 68: NOX Production for LPM CH4 Combustion from Each of the Four Pathways Calculated for a Series of Temperatures from two Different Methods

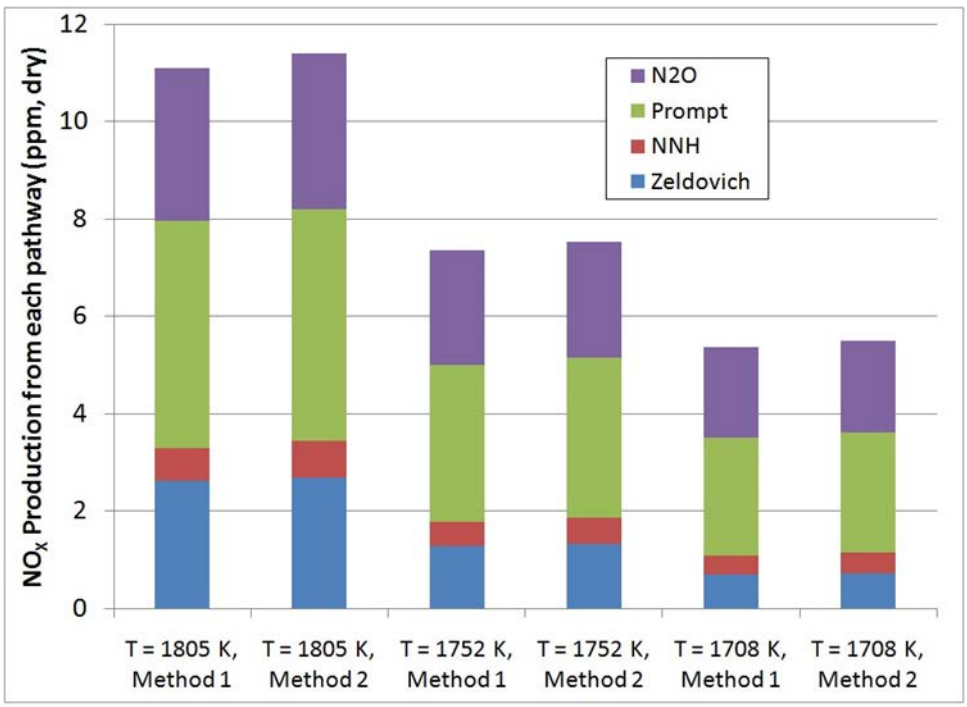

Method 2 (only removing the key reactions) to be the better of the two algorithms, since it only influences a handful of reactions rather than 20 to 30 reactions. Thus, Method 2 was used for the remainder of this study, to determine the contribution to NOX production from each of the four pathways.

The contribution from each of the four pathways is shown in Figure 69 in terms of a production rate in moles/s. This figure shows the pathway contribution at different combustion temperatures. Due to the small volume and extremely short residence time of the shear reactor (it has approximately three times more mass flow than the flame brush), it does not significantly

contribute to NO_x formation. Thus, attention is focused on the flame brush and recirculation zone.

Figure 69: NOX Rate of Production from Each of the Four Pathways in the Recirculation Zone and Turbulent Flame Brush Elements of the CRN Model

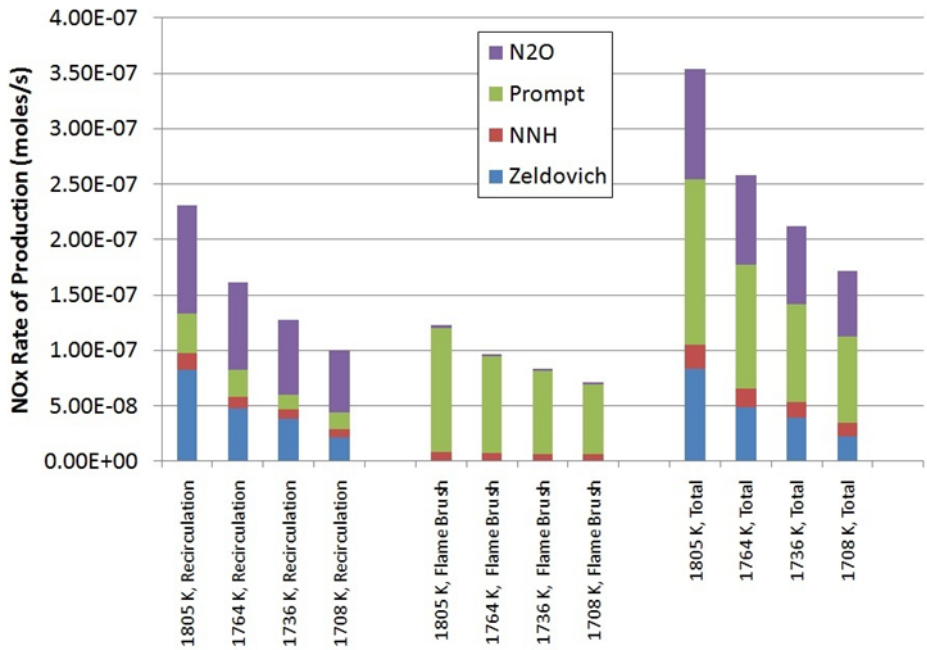

As shown in Figure 69, the total production of NO_x is of equal magnitude in both the turbulent flame brush and the recirculation zone. The majority of the Prompt NO_x is formed in the flame brush, while nearly all of the NO_x formed via the Zeldovich and N_2O pathways occurs in the recirculation zone. It is interesting to note that while the NNH and N_2O pathways have approximately equal contributions as the temperature in the recirculation zone falls, both the Zeldovich and Prompt pathways decrease in production efficiency. This can be explained by looking at the pertinent radical concentrations in the recirculation zone and flame brush, shown in the figure 70.

Figure 70: Oxygen Concentration in the Recirculation Zone and CH Concentration in the Flame Brush for the Modeling Results Shown in Figure 69

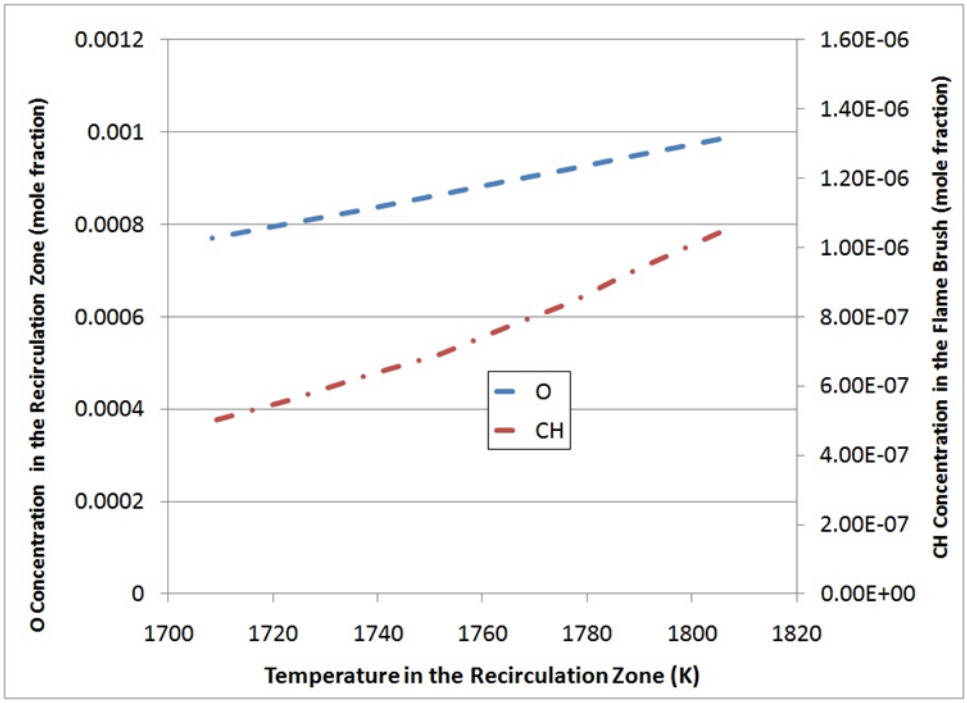

Since the air flow is fixed in the above experiments, the equivalence ratio falls from 0.71 to 0.64 as the recirculation zone temperature decreases from 1,805 to 1,708 K. The CH radical concentration in the flame brush also falls as the flame becomes leaner, which then results in a decrease in NO_X production from the Prompt pathway within the flame brush. Also shown is a decrease in O radical in the recirculation zone as the temperature falls. Although this loss of O radical can partially explain the decrease in NO_X from the Zeldovich pathway, the decrease in combustion temperature most likely has a greater effect, since the backward rate of Reaction 1 in Table 13 is strongly dependent on combustion temperature. In summary, for the experimental results displayed in Figure 68 and Figure 69, the NO_X concentration falls, mostly due to a decrease in the Prompt contribution from leaner operation and a decrease in the contribution from the Zeldovich pathway due to a decrease in combustion temperature and a loss of O atom.

Parameter Studies

As mentioned before, in addition to investigating specific fuel compositions, it is important to run experiments on a wider parameter space to determine more specifically how one or more fuels affect each other. This section describes compositional parameter studies for CH_4 mixed with varying amounts of H_2, C_2H_6, CO, CO_2, and N_2. Additionally, a syngas compositional space is studied with increasing amounts of CO mixed into a stream of H_2. The studies shown in this section simulate a broader variation in Mixtures 2, 3, 4, and 5 than those discussed above.

CH4 Mixed with CO2 and N2

The experimental results which are shown below focus on the influence of each diluent on NO_X production in LPM CH_4 combustion. The experiments are designed to hold the temperature constant for all diluent concentrations (N_2 versus CO_2). This is achieved as follows. First, the air flow is held constant. The CH_4 flow is selected to achieve a constant temperature of 1,800 K in the recirculation zone. As the diluent loading is increased, the natural tendency of the reactor to run cooler is balanced by increasing the CH_4 flow rate. Thus, as the diluent is increased, the CH_4 flow rate is also increased, and the overall fuel/oxidant ratio approaches stoichiometric.

An important question is how to best present the NO_X data. In the present experiments (1) the stoichiometry varies, and (2) the CO_2 and N_2 dilute the flow. The NO_X mole fraction (in ppm) is the normal way to present the emission data. The mole fraction is, however, influenced by dilution effects—in this case both due to stoichiometry and the added N_2 and CO_2. While the stoichiometry effect can be handled by correcting to a common O_2 value, the presence of the N_2 and CO_2 can change mole fraction without any change in chemistry. It is concluded that the most meaningful way to present the data is as a NO_X emission index, i.e., the amount of NO_X formation attributed to each CH_4 molecule entering the reactor. This avoids mole fraction changes that are due only to dilution (via variable stoichiometry, or N_2 and CO_2 addition). For the remainder of this section, the NO_X emissions are expressed as an emission index, since it is a more common method of expressing pollutant emissions.

Figure 71 shows that the NO_X emission index (grams NO_X/kg CH_4) increases for both N_2 and CO_2 dilution. The results also show that dilution with N_2 is more effective at enhancing NO_X formation than CO_2 dilution. There are, however, several ways to correlate the effect of the diluents (e.g., plotting against mass fraction of diluent, mole fraction of diluent). As mentioned above, increasing the diluent flow requires an increase in CH_4 flow to maintain the 1,800 K reactor temperature. This means that the mixture approaches a stoichiometric fuel-air ratio and the O_2 concentration decreases. In examining the various ways to correlate the effect of the diluents on NO_X formation, we selected plotting against O_2 concentration as the most fundamental approach, because the relationship between fuel, O_2, and NO_X is at the core of the chemical behavior.

Figure 72 shows the NO_X emissions index plotted against the O_2 concentration in the exhaust. As in Figure 71, the fuel stream diluted with N_2 is more effective at producing NO_X emissions than with CO_2 dilution, when compared on a common O_2 basis. Thus, there is evidence to suggest that there may be a chemical kinetic explanation for this phenomenon.

Figure 71: Measured NOX as EI versus Mass Fraction of N2 or CO2 Diluent in Fuel Stream. Temperature is maintained constant at 1,800 K.

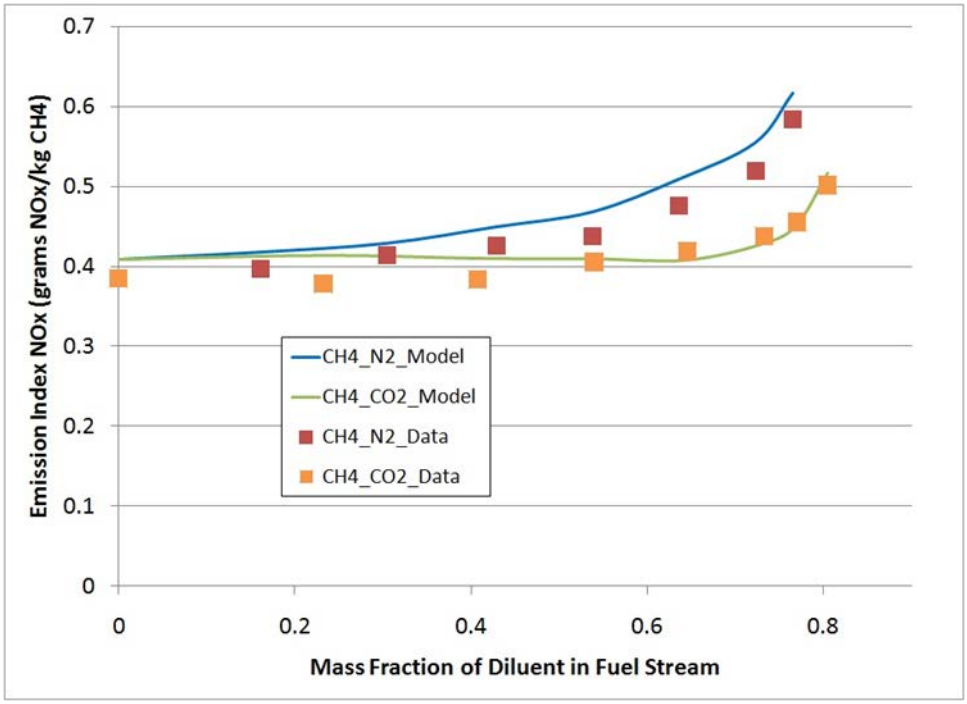

Figure 72: Measured NO_X as Emission Index (EI) versus Exit Gas O2 (mole %, dry). Temperature is maintained constant at 1,800 K

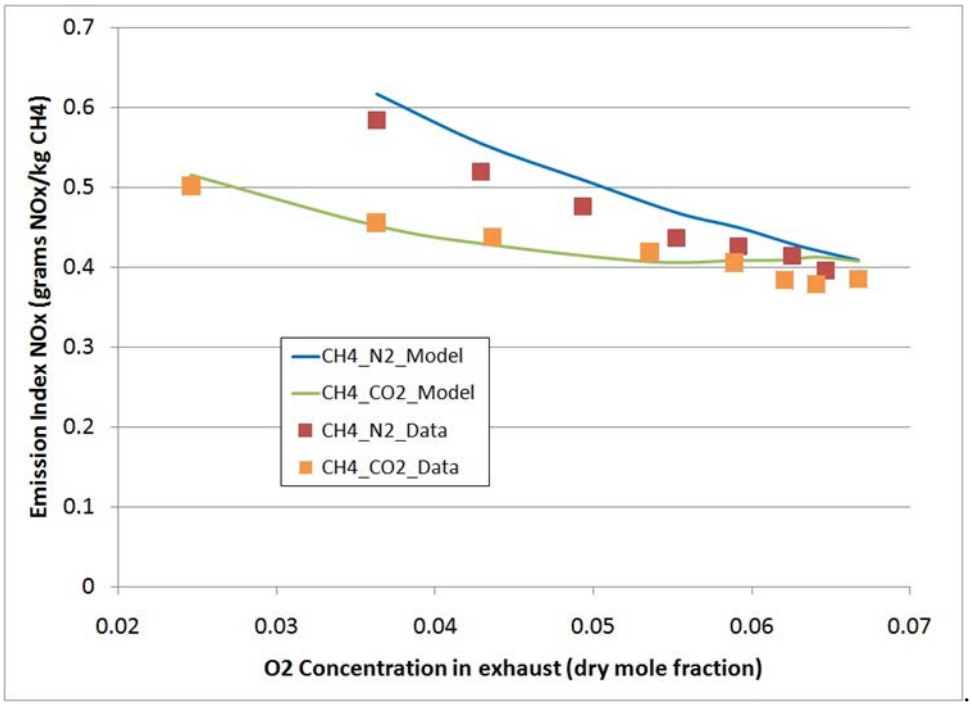

For reference, the measured NO_X (expressed as ppm) is displayed versus exhaust O2 concentration (Figure 73). Note that Figure 72 and Figure 73 show the same trend. In general, the specific heat of the two additives on a mass basis is sufficiently similar that (1) the tendency of the reactor to cool upon additive addition is nearly the same for the two, and (2) the increase in CH_4 flow needed to maintain the 1,800 K flame temperature is similar between the two. Thus, in this case the mole fraction results and the emission index results report similar trends. The other effect that can influence the data on an emission index basis is the increasingly larger molecular weight of the product gas as more CO_2 is added. For N_2 dilution, the molecular weight remains essentially constant throughout the entire range of experiments. As shown in Figure 71 through Figure 73, the model predicts the data quite well.

Figure 73: Measured NOX as (ppm, dry) versus Exit Gas O2 (mole %, dry). Temperature is maintained constant at 1,800 K.

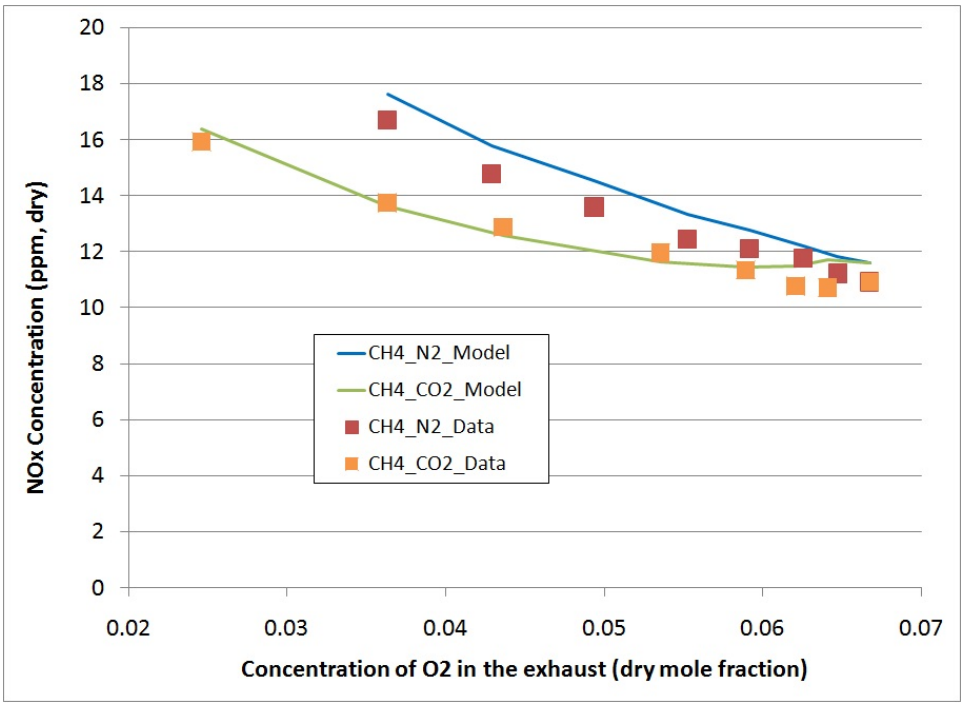

These results raise two main questions: (1) why do NO_X emissions go up when the CO_2 in the exhaust decreases/mass fraction of diluent increases? and (2) why are NO_X emissions higher for fuels diluted with N_2 rather than CO_2?

In an approach similar to the analysis done above, each of the four NO_X production pathways is isolated, and the model is rerun. The contributions of each of the four pathways as a function of dilution are shown in Figure 74 and Figure 75. Figure 76 shows the pathway contribution within each reactor of the CRN at a common O_2 concentration of 3.6 percent dry mole fraction in the exhaust. Here the emission index from each of the reactors is normalized by reactor volume and residence time.

Figure 74: NOX Emission Index Predicted by CRN Model: Total and by Four Pathways. CH4 diluted with N2.

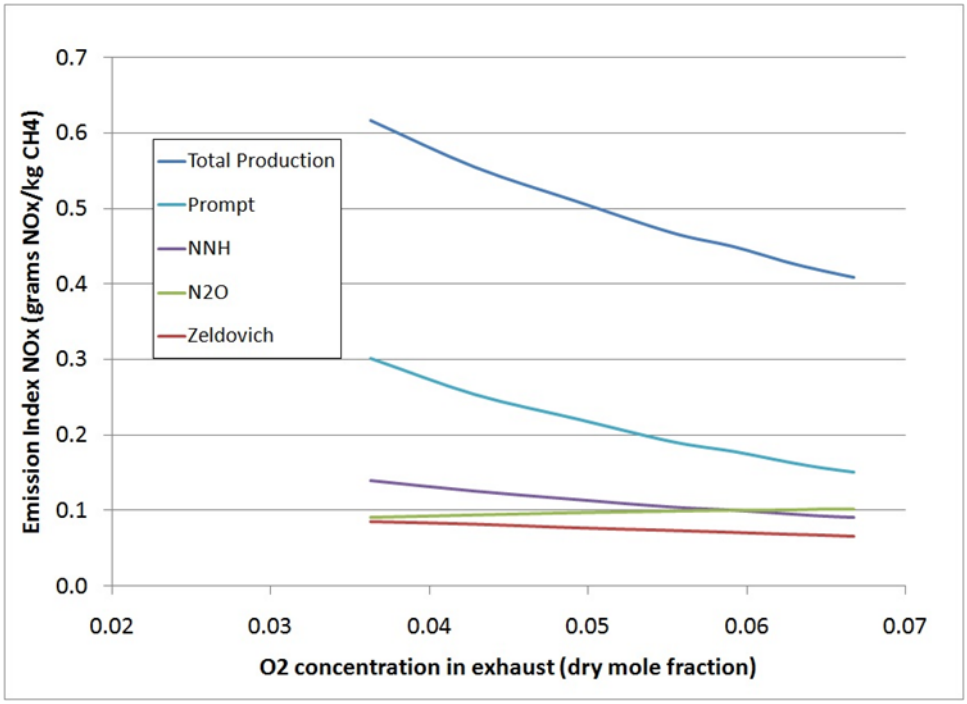

Figure 75: NOX Emission Index Predicted by CRN Model: Total and by Four Pathways. CH4 diluted with CO2.

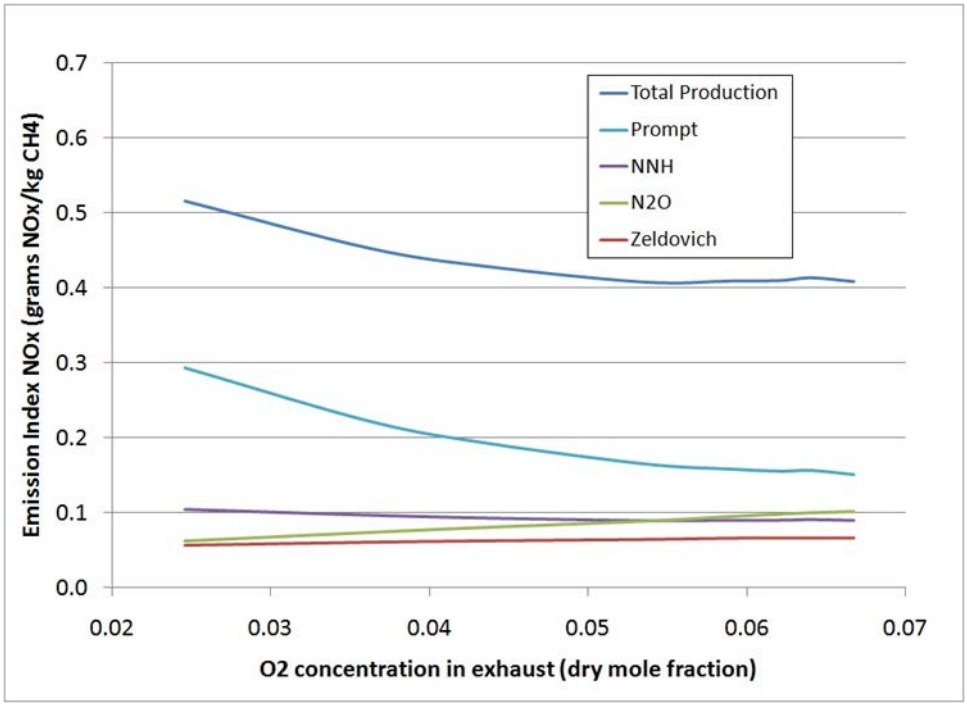

Figure 76: NOX Production Reported as Emission Index for Each of the Four Mechanisms in Each of the Three Reactor Elements of the CRN model. The O2 concentration is 3.6 percent (dry mole fraction).

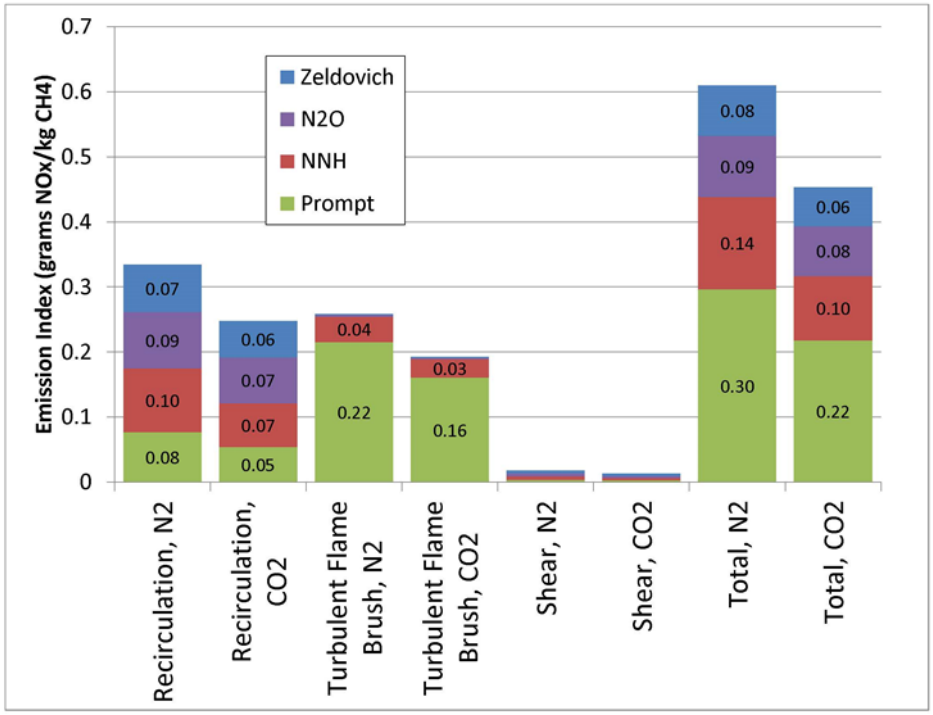

NO_x Production Reported as Emission Index for Each of the Four Mechanisms in Each of the Three Reactor Elements of the CRN model. The O_2 concentration is 3.6 percent (dry mole fraction).

Analysis of Figure 74, Figure 75, and Figure 76 show the following trends for NO_x formation in the JSR:

1. Prompt NO_x is the major source of NO_x for this experiment, and all three figures support this.

    a. This may be related to the relatively high CH_4-air equivalence ratios used: 0.71–0.86 for N_2 dilution and 0.71–0.92 for CO_2 dilution. Note that for most LPM combustion devices operating on CH_4, the equivalence ratio ranges from 0.45 to 0.65.

    b. The Prompt NO_x increases as the dilution level is increased (i.e., as the exit gas O_2 decreases). This is expected because of the increasing amounts of CH4 required as the dilution levels are increased.

    c. Much of the Prompt NO_x is formed in the turbulent flame brush (i.e., flame zone) modeled as an adiabatic PSR operating near blowout condition.

2. NNH contributes a relatively small amount of NO_x, and the N_2O and Zeldovich sources of NO_x are negligible within the flame brush, as shown in Figure 76, because of this reactor's short residence and low temperature. The computed temperature within the flame brush ranges between 1,609 and 1,612 K for both diluted fuels at all dilution levels.

3. All four sources of NO_x contribute in the recirculation zone, modeled as a PSR at measured temperature (1,800 K).

4. The sources of NO_x are greater for N_2 dilution than for CO_2 dilution in both the turbulent flame brush and the recirculation zone.

These NO_x trends are supported by the concentrations of free radicals O, H, and CH shown in Figure 77, Figure 78 and Figure 79 as calculated from the CRN modeling.

Figure 77: O Atom Concentration in the Recirculation Zone and PSB for both Diluted Fuels

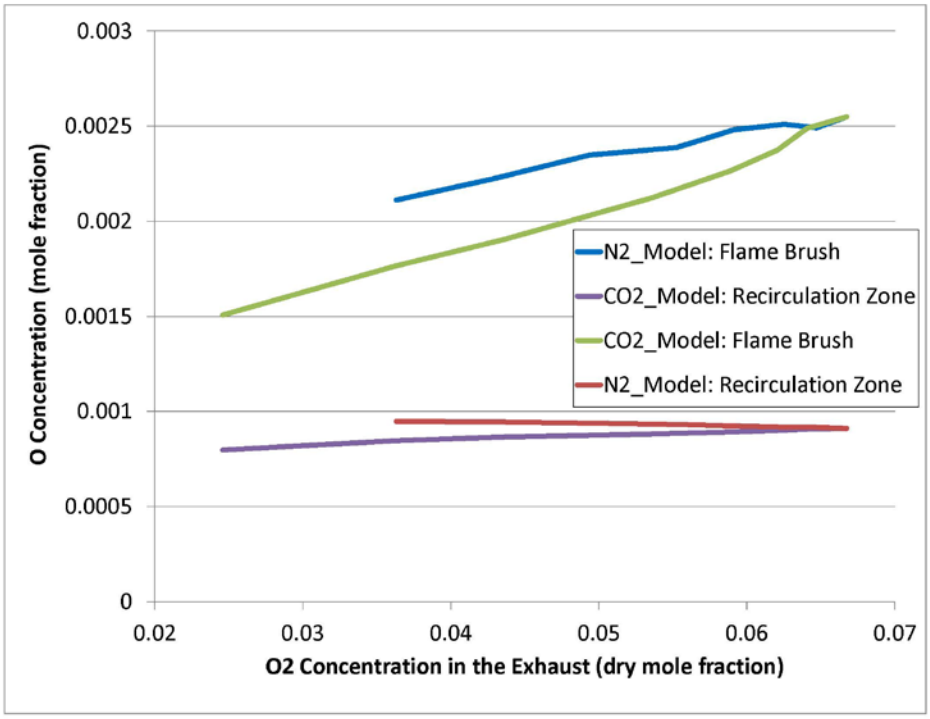

When compared to no dilution, the N_2 mole fraction is 5 percent greater for maximum N_2 dilution and 17 percent smaller for maximum CO_2 dilution. For small concentrations of NO_x at constant temperature (which is the case here) Zeldovich NO_x forms in proportion to $[N_2][O]$, where [ ] means moles/vol. Looking at the recirculation zone, for increasing N_2 dilution, O is nearly constant and N_2 increases; thus, Zeldovich NO_x increases with dilution. However, for increasing CO_2 dilution, mole fractions of both O and N_2 decrease: thus, Zeldovich NO_x decreases with dilution.

Figure 78: H-atom Concentration in the Recirculation Zone and Turbulent Flame Brush for both Diluted Fuels

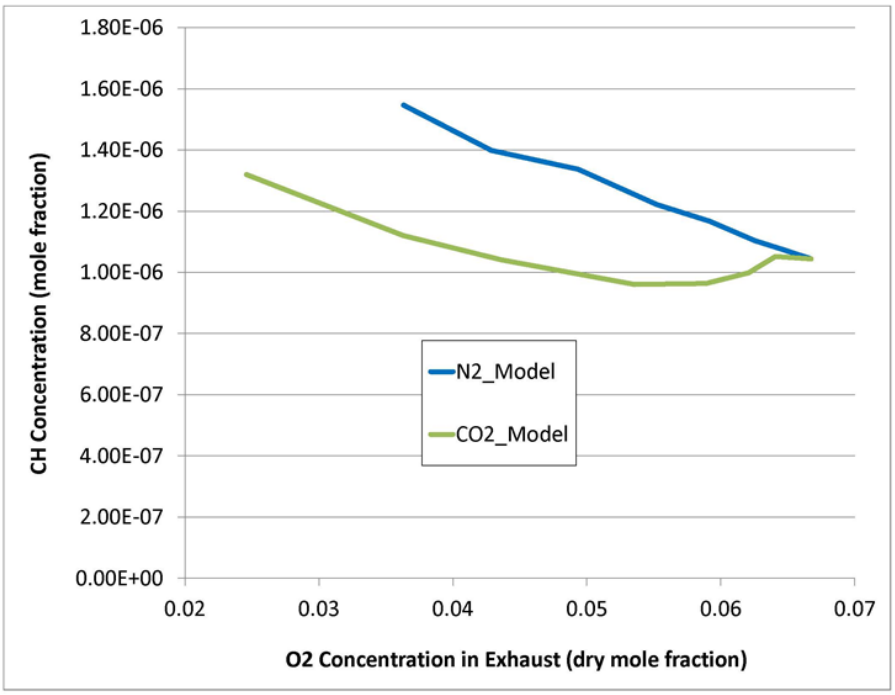

Figure 79: CH Concentration within the Flame Brush for CH4 Diluted with both N2 and CO2

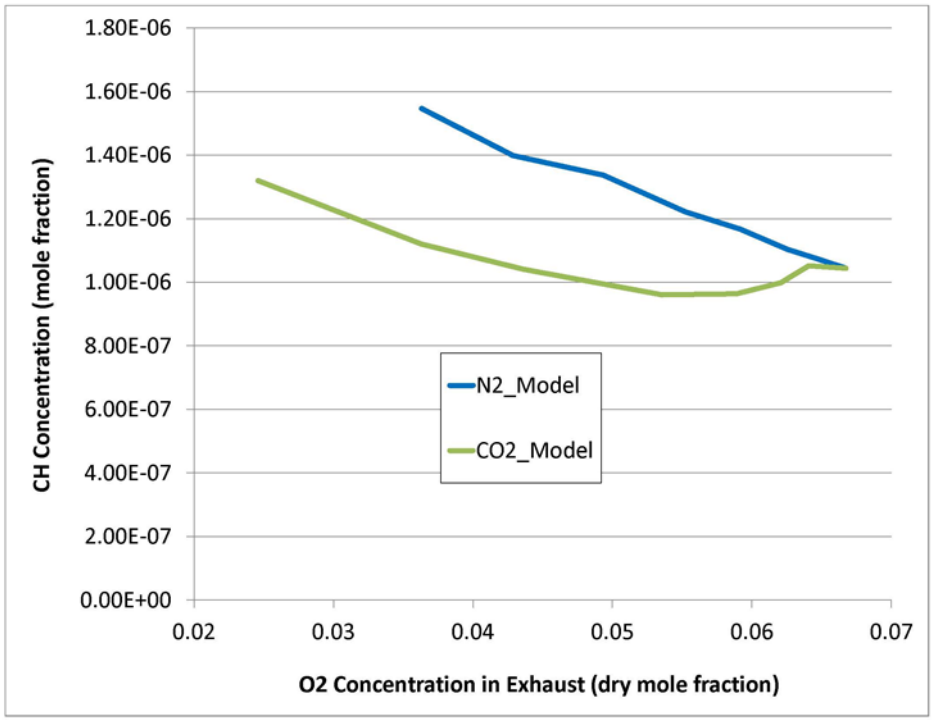

Nitrous oxide (N_2O) is formed by reaction of N_2 with O and is depleted by reaction with both O and H. As shown above in Figure 76, most of the NO_X formed through the N_2O pathway is formed in the recirculation zone. Figure 78 shows H-atom increasing as the dilution level of the JSR increases. This trend is the same for both N_2 and CO_2 dilution. Shown in Figure 77, the O concentration in the recirculation zone falls slightly for CO_2 dilution and stays flat for dilution with N_2. For N_2 dilution, N_2 and H increase, thus increasing NO. O-atom decreases, which drives NO down. These effects appear to offset each other. For CO_2 dilution, H increases, which promotes NO production; however, both N_2 and O decrease, which decreases NO production. The effects of decreased N_2 and O seem to dominate, decreasing the NO production from CO_2 dilution slightly more than for dilution with N_2.

As seen in Figure 74 and Figure 75, NO formed from NNH increases as the N_2 and CO_2 dilution levels increase. As noted from Figure 76, it forms in both reactor zones. NNH is formed by the reaction of N_2 with H, and NO is formed by reaction of NNH with O. NNH concentration follows the upward trend shown for H-atom in Figure 78, tempered by increasing N_2 concentration for N_2 dilution and decreasing N_2 concentration for CO_2 dilution. The result is a somewhat greater increase in NO with dilution level for N_2 than for CO_2.

Prompt NO forms as CH radical reacts with N_2 to form HCN and N, both of which oxidize to NO. CH has a short lifetime; thus, the Prompt N_O is produced more significantly in the flame brush than in the recirculation zone. The flame brush concentrations of CH are plotted in Figure 79, where they are seen to increase significantly as more N_2 is added to the reactor. Small amounts of CO_2 dilution appear to suppress CH, though as more CO_2 is added, the CH increases.

Large concentrations of CO_2 will compete with O_2 for H-atom via the reaction: $H + CO_2 \leftrightarrow CO + OH$. The consumption of H atom will decrease the rate of the most significant chain branching reaction: $H + O_2 \leftrightarrow OH + O$. This suppression effectively reduces the size of the O/H/OH radical pool, leading to a decrease in NOX formed by the Zeldovich, N_2O, and NNH pathways when CO_2, rather than N_2, is added to the reactor.

CH4 Mixed with C2H6

For the LPM combustion of C_2H_6 mixed with CH_4, the air flow rate is held constant, while the flow rates of both CH_4 and C_2H_6 are adjusted to maintain a combustion temperature of 1,800 K within the recirculation zone. As mentioned above, the authors of GRI-Mech 3.0 caution against using the mechanism with fuel mixtures composed of large concentrations of C_2 and C_3 hydrocarbons. Despite this caution, GRI-Mech 3.0 is used for this fuel mixture. In addition, the C_2-NOx mechanism developed by Reaction Design is used in the same CRN. It is found that the C_2-NOx mechanism shows some unstable numerical behavior near blowout. The computed blowout volumes for the first PSR in the three-element CRN from using both GRI-Mech 3.0 and C_2-NOx are shown below in Figure 80. Since the solution computed for the PSB appeared to be questionable, it was decided to test the C_2-NOx mechanism in conjunction with the PSB volumes computed by GRI-Mech 3.0. The results from all three models are shown in Figure 81.

Figure 80: The Volumes Computed for the PSB as a Function of C2H6 Concentration in the Fuel Stream for a Fuel Mixture of CH4 and C2H6 from both GRI-Mech 3.0 and C2 NOx. Temperature in the recirculation zone is kept constant at 1,800 K.

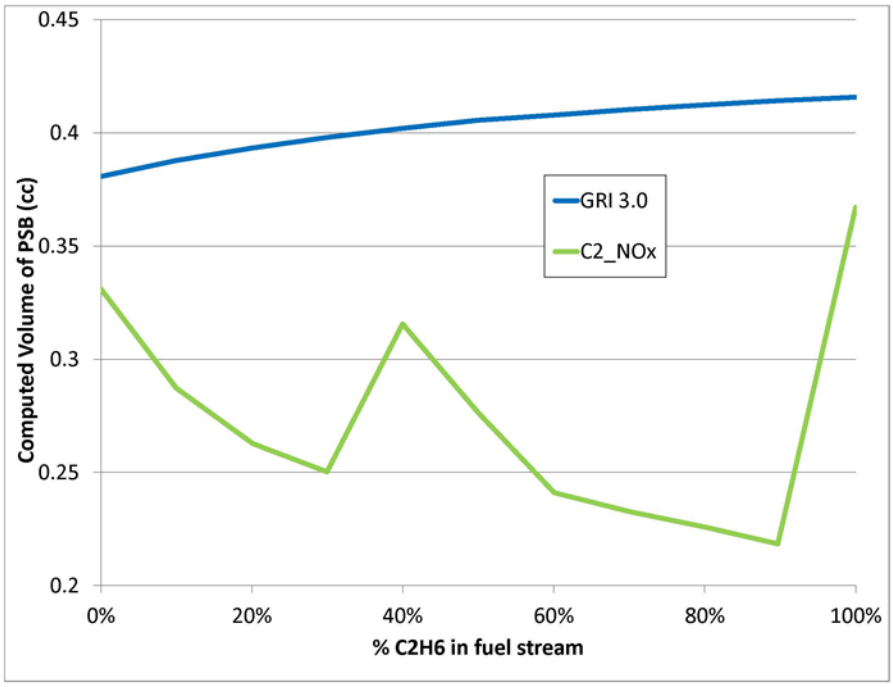

Figure 81: NOX Concentration as a Function of C2H6 Concentration in the Fuel Stream for a Fuel Mixture of CH4 and C2H6 from Experiment and the Three-Element CRN. Temperature in the recirculation zone is kept constant at 1,800 K.

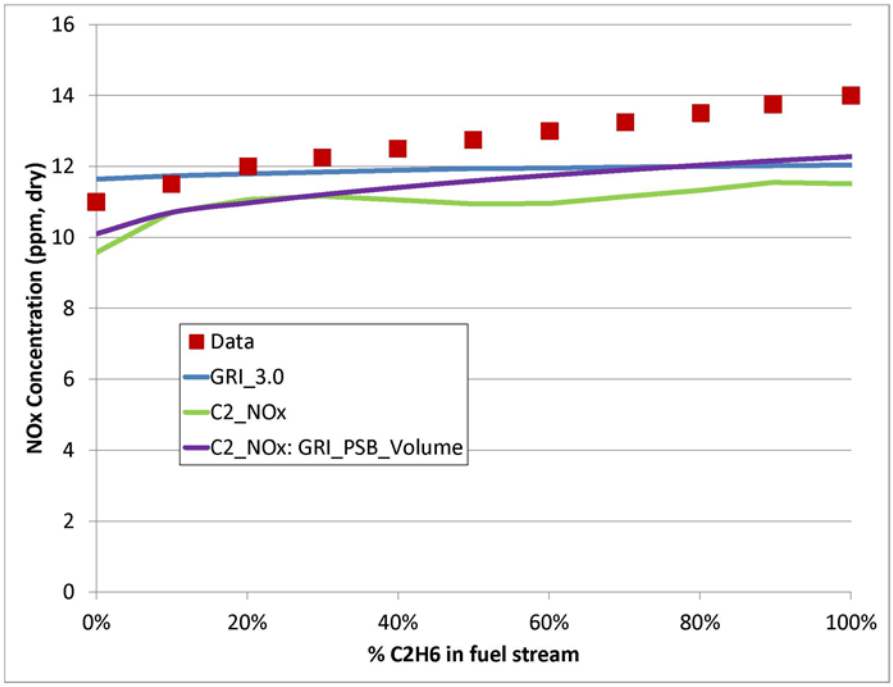

Figure 81 shows that the experimental NO_X concentration rises as the C_2H_6 concentration in the fuel increases. The results of the model with GRI-Mech 3.0 show a very slight increase in emissions with increasing C_2H_6 concentration. The model predictions from the C_2-NOx mechanism with the PSB volume computed using the C_2-NOx mechanism show a rise going from pure CH_4 to pure C_2H_6; however, the model does not show a smooth trend, which is most likely due to the unstable behavior of the model near blowout. The model predictions of the C_2 NOx mechanism using the PSB volumes computed by GRI-Mech 3.0 show the best trend with the data. The curve is smooth, which can most likely be attributed to a smooth prediction of PSB volume and the corresponding temperature that goes along with this volume. However, this model under-predicts the NO_X data by 1–2 ppm, though it does follow the proper trend with respect to C_2H_6 percentage. Since neither mechanism predict the data very well, and the C_2-NOx mechanism does not contain the same oxidation chemistry as GRI-Mech 3.0, a pathway breakdown analysis as outlined above is not performed. Further work must be put into developing a chemical mechanism that can accurately model the oxidation of C_2 and C_3 hydrocarbons with NO_X formation.

5.2.1.3 Hydrogen-Containing Fuels

CH4 Mixed with H2

In the experimental studies shown in this section, the air flow rate is held constant, while the flow rates of both CH_4 and H_2 are adjusted to maintain a combustion temperature of 1,800 K within the recirculation zone. As shown in Figure 82, for a constant recirculation zone temperature of 1,800 K, the NO_X concentration decreases with increasing H_2 concentration in the fuel stream. The model is run using the CRN with both GRI-Mech 3.0 (Smith et al. 2000) and GRI-Mech 3.0 modified by Konnov (2000). Although the NNH mechanism does not appear to affect NO_X formation from CH_4 combustion significantly, it certainly does affect NOX formation as a highly reactive, high-H radical-producing fuel such as H_2 is mixed into the fuel. Since there is clearly an issue with GRI-Mech 3.0 overpredicting the data because of the NNH mechanism, GRI-Mech 3.0 with the Konnov modification is applied from this point forward to study fuels mixed with H_2.

Figure 82: NOX Concentration as a Function of H2 Concentration in the Fuel Stream for a Fuel Mixture of CH4 and H2. Combustion temperature is kept constant at 1,800 K.

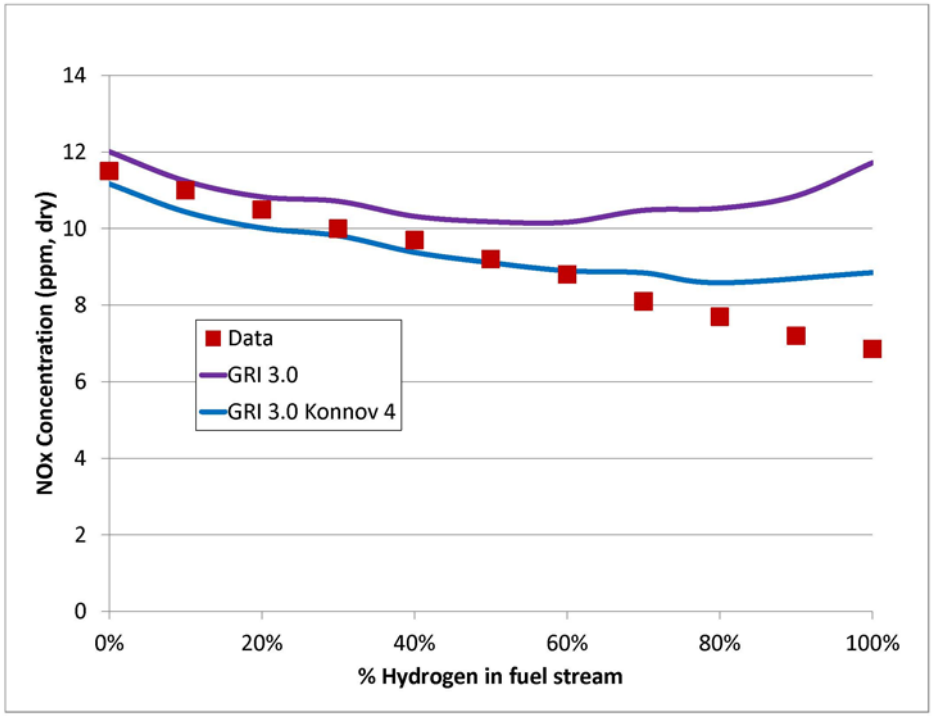

The model predicts the data fairly well up to about 80 percent H_2 and then it diverges. At this point, there is not a clear explanation for the model divergence when large levels of H_2 are added to CH_4. It is possible that the CRN configuration needs to be adjusted for fuels with large levels of H_2 since it is far more reactive than hydrocarbon fuels. The model is somewhat self-adjusting to changes in chemistry since the blowout volume of the flame brush decreases in size for more reactive chemistry (e.g., higher inlet temperature, larger % H_2). As shown in Figure 83, the computed volume of the flame brush decreases significantly moving from pure CH_4 to pure H_2.

As described in Section 5.2.1.1, the recirculation zone then occupies the rest of the volume of the JSR minus a very small volume occupied by the shear zone. It is possible that one or more elements need to be added to the current CRN in order to properly capture the physics of a flame with highly reactive chemistry like H_2. Nevertheless, a similar approach to that taken in above to quantify which pathways are responsible for NO_x formation is also performed on this set of experiments.

The NO_x contribution from each of the four pathways in the turbulent flame brush and the recirculation zone are shown in Figure 84 for five varying levels of H_2: 0, 30, 50, 70, and 100 percent, respectively. The contribution from the Prompt pathway becomes increasingly less significant as the percentage of H_2 increases in the fuel stream. Note that due to of the lack of Prompt NO_x, almost all of the NO_x produced for pure H_2 combustion is made in the

recirculation zone. Finally, the plot shows that the contributions from Zeldovich, NNH, and N_2O pathways increase as more H_2 is added to the fuel stream.

Figure 83: Volume of Turbulent Flame Brush as a Function of H2 Concentration in the Fuel Stream. Combustion temperature is kept constant at 1,800 K.

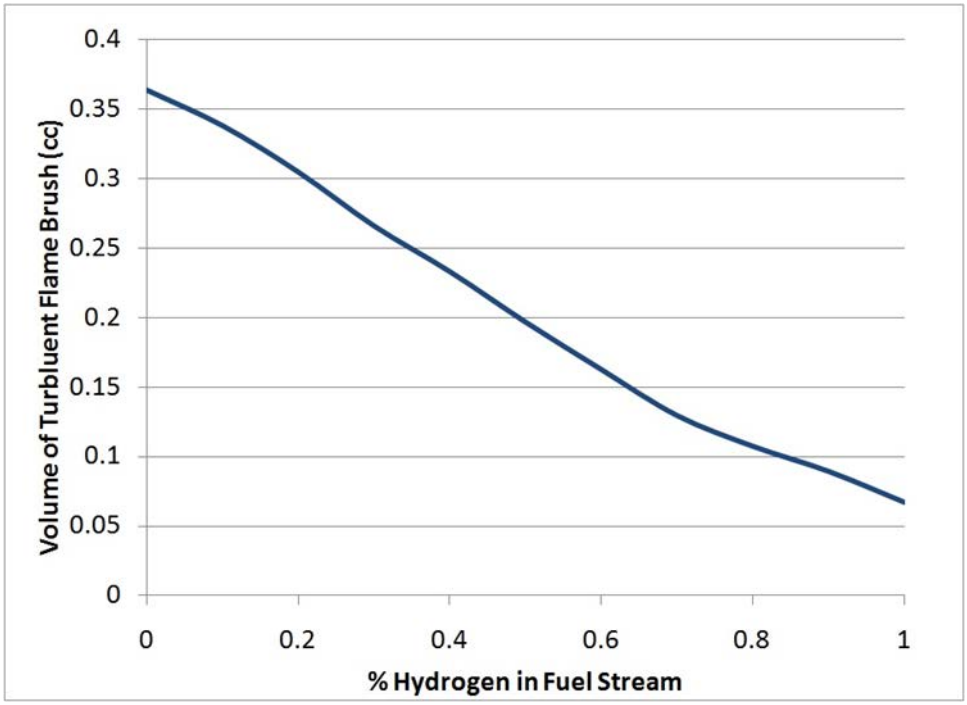

These results are supported by looking at the computed species concentrations in each reactor. The concentrations of CH and NNH in the turbulent flame brush are shown in Figure 85. The concentrations of CH, NNH, and N_2O in the recirculation zone are shown in Figure 86. The concentrations of O and H in the recirculation zone are shown in Figure 87. The CH and NNH concentrations shown in Figure 85 support the decreasing contribution of the Prompt pathway and the increasing contribution of the NNH pathway shown in Figure 84. It is interesting to note that the CH concentration is relatively flat until there is about 70 percent H_2 in the fuel stream. The decreasing Prompt contribution is due to the decreasing hydrocarbon material within the turbulent flame brush as more H_2 is added to the fuel mixture. The computed N_2O concentration in the recirculation zone remains relatively flat throughout the range of H_2 in the fuel stream and the concentration of O-atom increases, but not significantly. We speculate that the increase in contributions from both the Zeldovich and N_2O pathways within the recirculation zone is largely due to a larger volume and thus longer residence time associated with the addition of H_2.

Figure 84: NOX Rate of Production from Each of the Four Pathways in the Recirculation Zone.

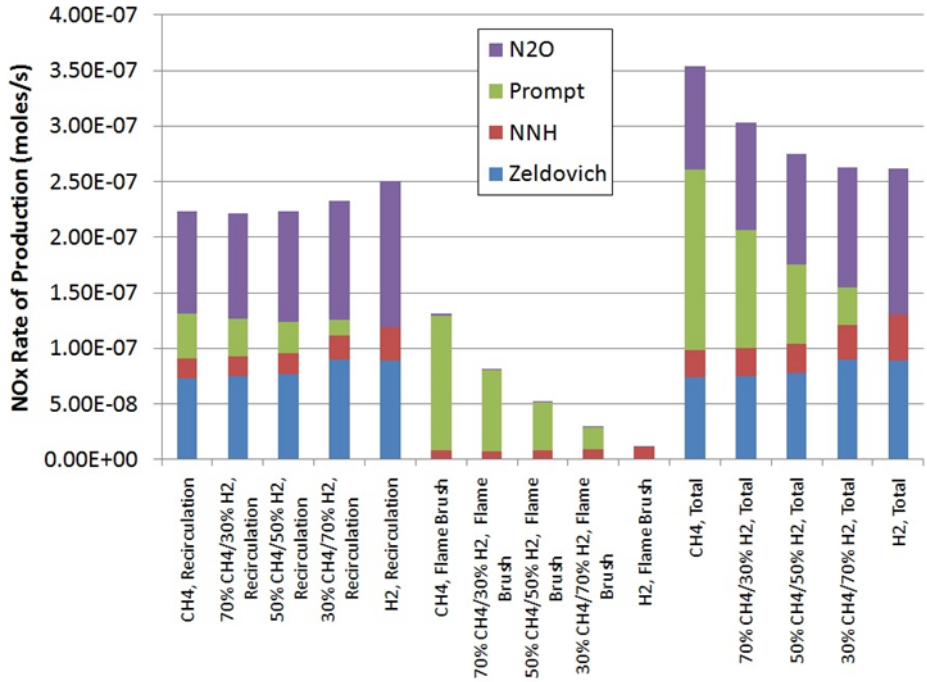

Figure 85: CH and NNH Concentration in the Turbulent Flame Brush for H2 Mixed with CH4. Combustion temperature is kept constant at 1,800 K.

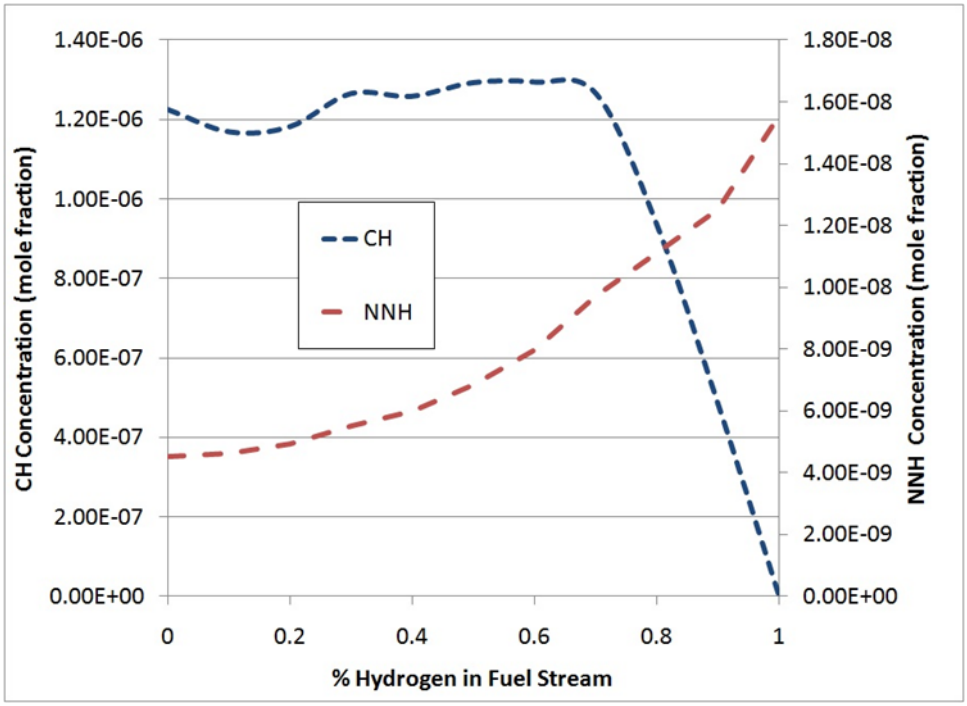

Although the CRN model developed for the JSR shows fairly good agreement with the experimental data, the configuration must most likely be modified to deal with fuels with increasing levels of H_2. Much of the disagreement is likely due to the increasingly large computed recirculation zone associated with large levels of H_2. This large recirculation zone artificially "spreads" the highly reactive H_2 chemistry over a larger volume than what is actually happening in the experiment.

Figure 86: CH, NNH, and N2O Concentration in the Recirculation Zone for H2 Mixed with CH4. Combustion temperature is kept constant at 1,800 K.

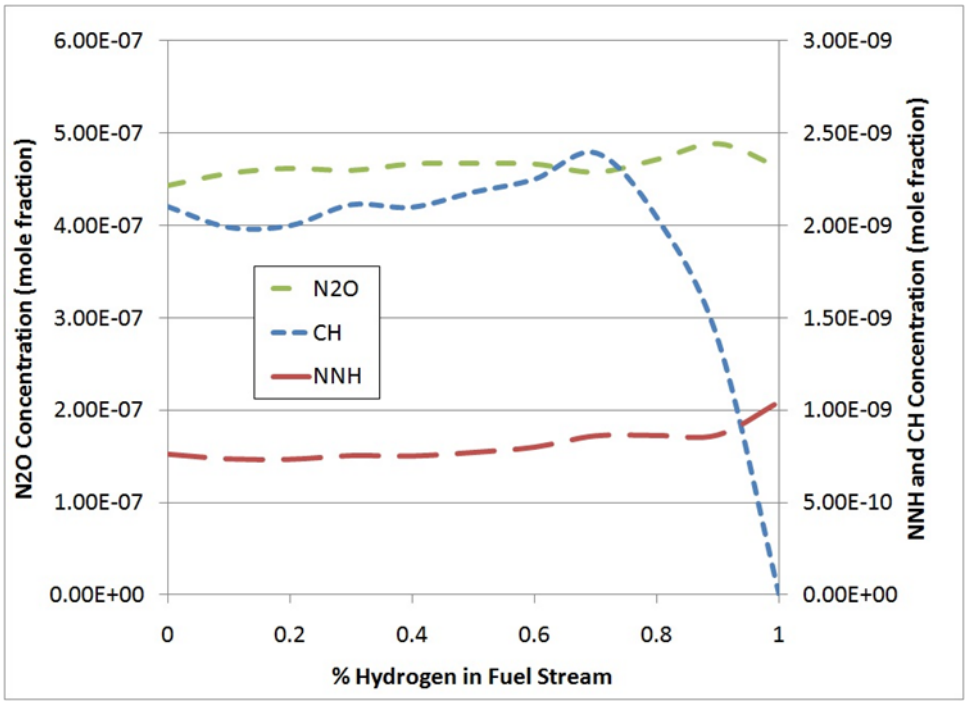

Figure 87: O and H Concentration in the Recirculation Zone for H2 Mixed with CH4. Combustion temperature is kept constant at 1,800 K.

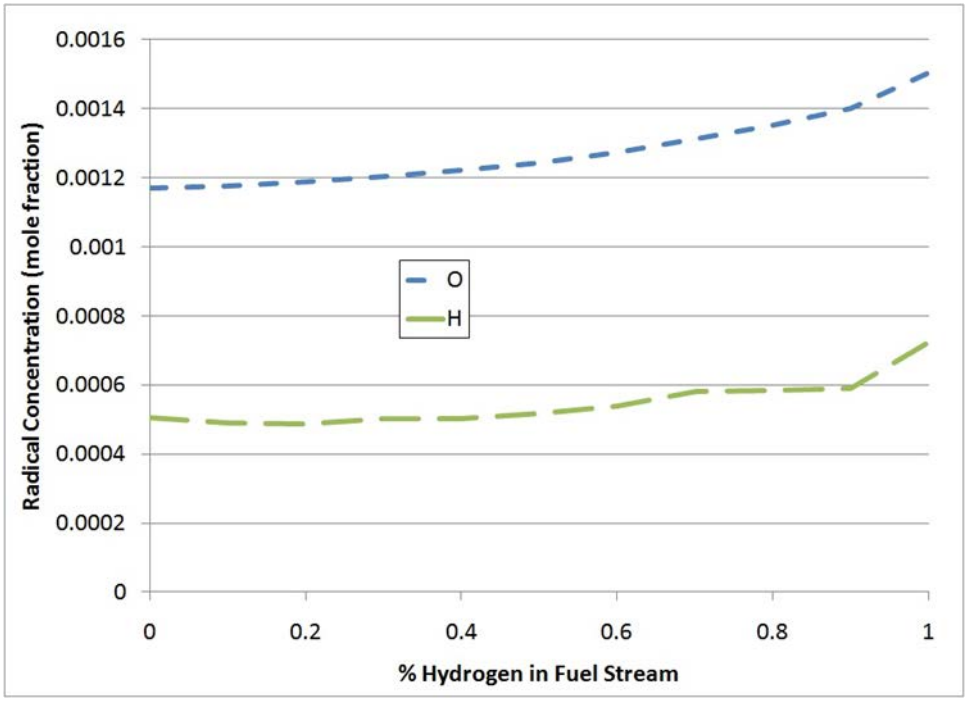

H2 Mixed with CO

Similar to the parameter studies detailed above, for the LPM combustion of H_2 mixed with CO the air flow rate is held constant, while the flow rates of both H_2 and CO are adjusted to maintain a combustion temperature of 1,800 K within the recirculation zone. Unlike the CH_4/H_2 study, the mole fraction of CO in the fuel stream is not increased past 70 percent by volume since this is thought to be the largest CO concentration that would be normally seen in any practical syngas that is produced in an O_2 blown gasification plant. As shown in Figure 88 for a constant recirculation zone temperature of 1,800 K, the NO_X concentration decreases with increasing H_2 concentration in the fuel stream.

Figure 88: NOX Concentration as a Function of H2 Concentration in the Fuel Stream for a Fuel Mixture of H2 and CO. Combustion temperature is kept constant at 1,800 K.

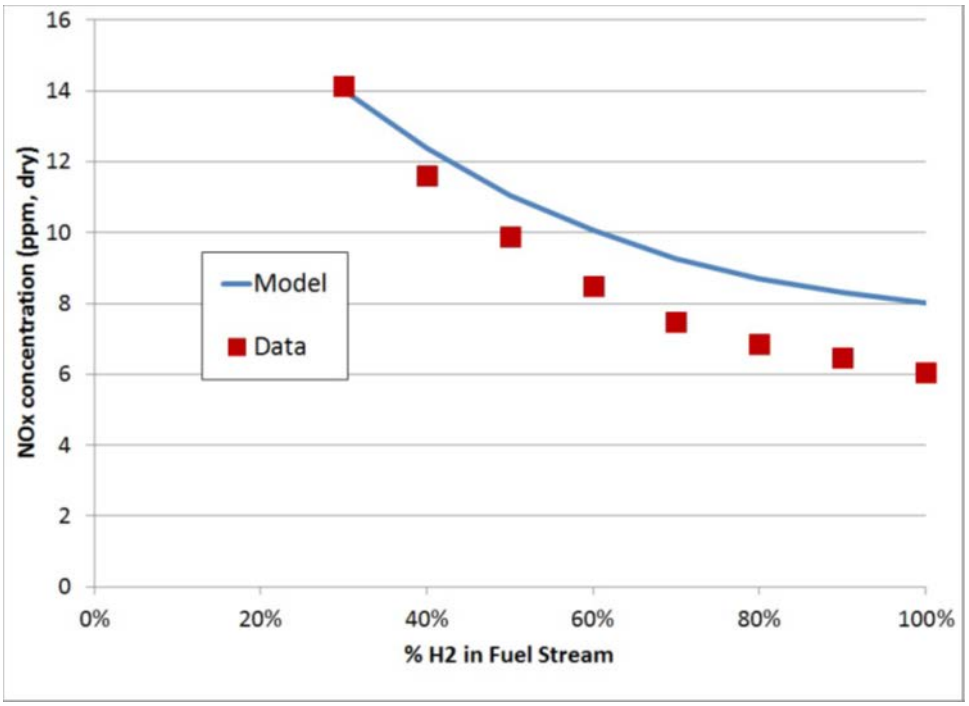

Again, the three-element CRN illustrated in Figure 65 is employed to model the data. The model follows the general trend of the data; however, for large H_2 levels the model overpredicts the data and becomes gradually better as the concentration of CO in the fuel stream increases. This discrepancy is most likely due to the same reason that the predictions diverge from the measurements for the CH_4/H_2 fuel blends.

The breakdown between NO_x produced in both the turbulent flame brush and the recirculation zone is shown below in Figure 89. The plot shows that the turbulent flame brush produces very little NO_x.

Figure 89: NOX Production Reported as a Function of H2 Concentration in the Fuel Stream.

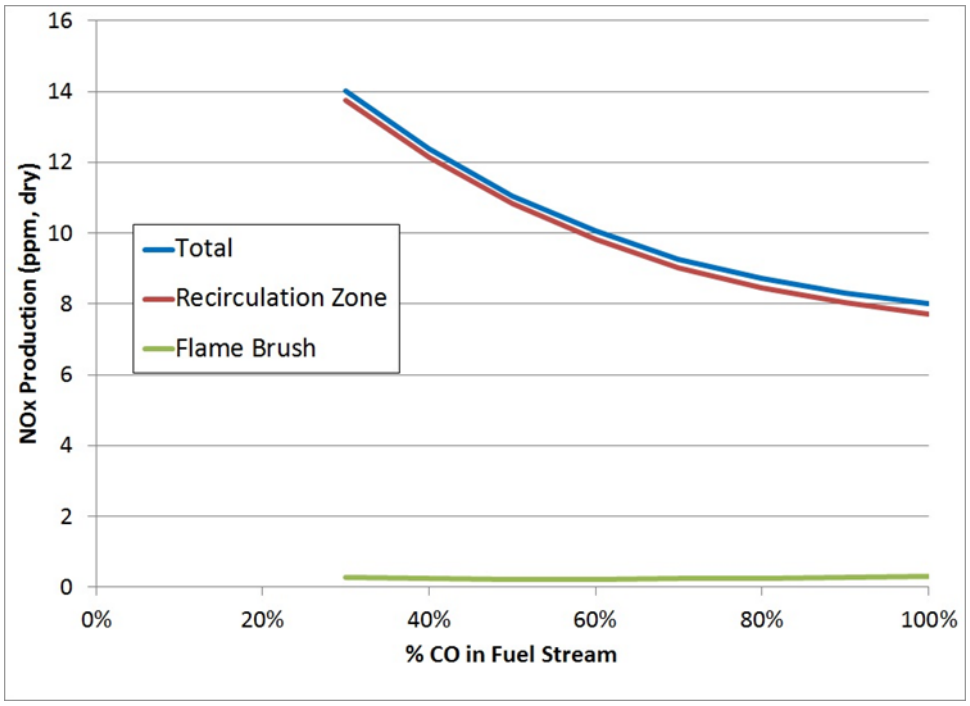

Figure 90: NOX Production Reported as a Function of H2 Concentration in the Fuel Stream for Each NOX Formation Pathway.

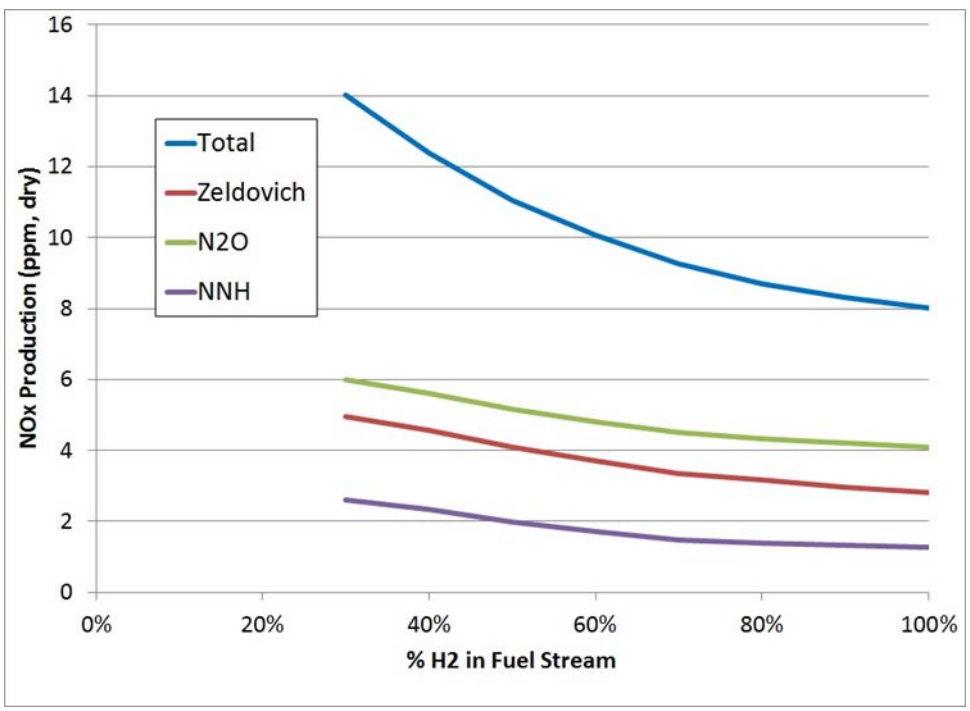

Figure 91 shows the breakdown of NO_x production as a function of H_2 concentration in the fuel stream for each of the NO_x formation pathways in the entire reactor, which in this case is essentially the formation from within the recirculation zone. It should also be noted that the Prompt pathway has been removed from consideration, since there is no hydrocarbon component of this mixture.

Figure 91: Radical Concentrations in the Recirculation Zone Reported as a Function of H2 Concentration.

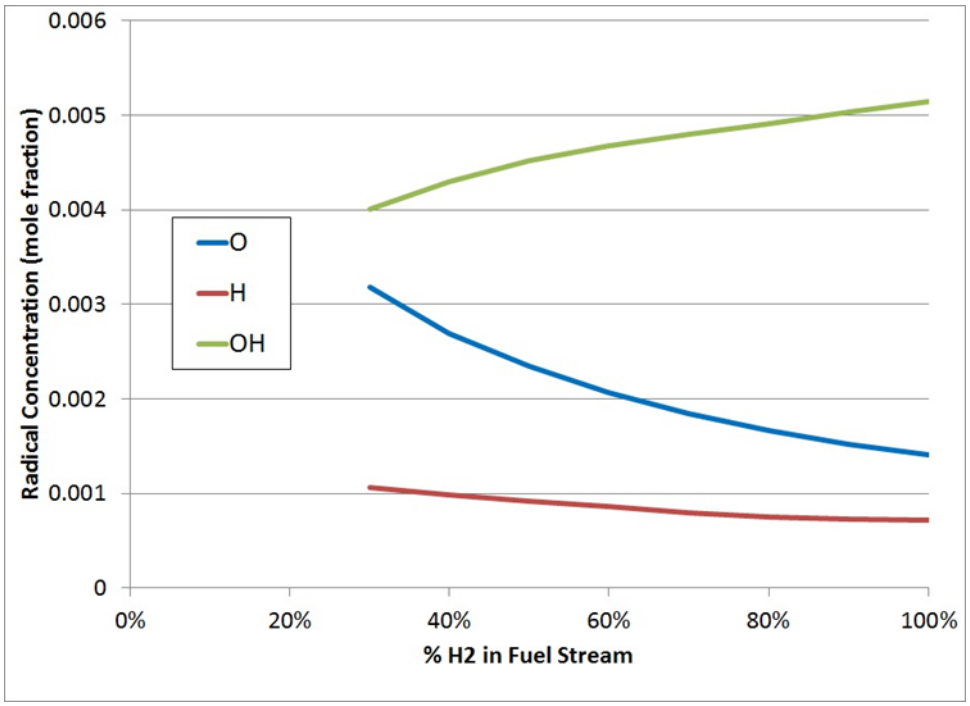

As expected, the OH concentration falls as the CO concentration in the fuel stream increases. This is an effect of the increased reactivity of the major CO oxidation step: $CO + OH \leftrightarrow CO_2 + H$. Following the same rationale, the H concentration increases as CO fuel fraction increases. An increase in H concentration increases the production of the NNH pathway and an increase in O concentration increases NOX production from both the N_2O and Zeldovich pathways.

5.2.1.4 Summary of Jet-Stirred Reactor

A high-intensity, single-jet-stirred reactor (JSR) was used to study both pollutant formation and resistance to blowout for CH_4 and the variety of gaseous fuel alternatives to CH_4. The JSR is intended to act as an idealized lean premixed combustor. NO_x measurements were taken at a nominal combustion temperature of 1,800 K, atmospheric pressure, and a reactor residence time of 3 ms. This ensured that the results focused on the effect of fuel chemistry by removing temperature, residence time, and pressure as variables. Additionally, the effects of changing temperature and residence time were investigated for selected fuels.

Experiments

At the nominal temperature and residence time, the experimental results show the following trends for NO_x emissions as a function of fuel category:

1. NO_x emissions decrease for combustion of CH_4/H_2 blends with increasing H_2 fuel fraction.
2. For category 3 (the O_2-blown gasified coal/petcoke), NO_x emissions decrease with increasing H_2 fuel fraction.
3. For category 2 (the process and refinery blend) and category 5 (the LNG, shale, and associated gases), NO_x emissions increase with the addition of C_2 and C_3 hydrocarbons.
4. For category 4 (the landfill gas) the addition of diluents such as CO_2 and N_2 at constant air flow produces more NO_x per kg of CH_4 consumed, and N_2 is more effective than CO_2 in increasing the NO_x emission index.

At temperatures and residence times other than the nominal conditions, the experimental results show the following trends:

1. The NO emissions from LPM combustion of pure CH_4, H_2, C_2H_6, and C_3H_8 are shown to be linear with residence time and exponential with temperature.
2. The addition of both H_2 and C_2H_6 to a LPM CH_4 flame is effective at extending its lean blowout limit.

Modeling

Both computational fluid dynamics (CFD) and CRN models are used to predict, illustrate, and isolate the underlying chemical kinetic reasons for differences in emissions between selected fuel blends. In general, the modeling results have correlated well with measured data.

A three-element CRN was constructed using insight from detailed spatial measurements of the reactor, the results of CFD simulations, and classical fluid dynamic correlations. Several chemical mechanisms were tested in the CRN. GRI-Mech 3.0, a modification of GRI-Mech 3.0, and the C_2-NOx mechanism proved to model the experimental data best within the CRN configuration. The CRN model performed well in predicting NO_x emissions for LPM CH4 flames at constant air flow rate and combustion temperatures between 1,700 and 1,800 K. As the combustion temperature/equivalence ratio increased, the model indicated that NO_x formation increased mainly due to an increase in the Zeldovich and Prompt pathways. The CRN was employed to predict experimental trends observed when the composition of a mixture is varied.

For an LPM CH_4 flame diluted with N_2 and CO_2 held at a constant combustion temperature of 1,800 K, the CRN model indicated that the increase in NO_x emissions with increased dilution was due to an enhancement of the Prompt NO_x pathway. This results from an increase in the CH radical concentration as the mixture moves toward stoichiometric. The model also suggested that both a smaller N_2 concentration and a preferential loss of free radicals due to CO_2-enhanced radical recombination results in decreased NO_x emissions for CO_2 dilution, compared to N_2 dilution.

The CRN model predicted NO_x emissions for a LPM CH_4/H_2 flame with reasonable accuracy. The model follows the data up to about 80 percent H_2 in the fuel stream, then it overpredicts NO_x as H_2 approaches 100 percent. The modeling suggests that a decrease in Prompt NO_x is the

main reason for the decrease in NO_X formation as the mixture moves from pure CH_4 to pure H_2. The model also predicted an increase in NO_X formation as the mixture nears 100 percent H_2 due to both the Zeldovich and N_2O pathways. As the H_2 concentration in the fuel increases above 80 percent, artificially spreading the super-equilibrium flame zone around the entire reactor appears to cause the model to increase its NO_X prediction. The CRN model should be modified to correct this problem.

The CRN also predicted NO_X emissions for an LPM H_2/CO flame reasonably well; however, as more H_2 was added to the fuel mixture, the model diverged from the data. For H_2/CO combustion there was no Prompt NO_X, due to the lack of hydrocarbon material. The model predicted that there was almost no NO_X production within the turbulent flame brush. The model predicted that as the volume fraction of CO in the fuel stream increased, the contributions of the N_2O, Zeldovich, and NNH pathways increased due to an increase in the concentration of O and H radicals. Carbon monoxide appears to produce more radicals per unit heat release than the other fuels studied.

5.2.2 Results for High-Swirl Burner

This section presents application of the CRN methodology to the high-swirl burner configuration. Fuel composition in this study included a wide range, starting from pure natural gas, as the conventional gaseous fuel, up to pure hydrogen, as a major constituent of alternative fuels with extreme combustion properties. Different adiabatic flame temperatures and residence times were considered for testing. For most cases, measured CO and NOx levels were used to verify the developed CRN, as explained in Section 4.2.2.3, and then different NOx formation pathways were calculated using chemical kinetic simulations in CHEMKIN Pro. Results for the impact of residence time and fuel composition on NOx levels for 1,800 K AFT are presented first, followed by the same results for 1,900 K AFT. Finally, important factors in NOx formation pathways will be discussed.

5.2.2.1 CRN Develpoment

The details regarding the development of the CRN for the high-swirl burner are available elsewhere, but follows the general approach discussed above for the jet-stirred reactor (Akbari 2013).

5.2.2.2 Alkane Results

The experimental measurements for three different fuel compositions with three different equivalence ratios are available in UCICL archives. For all the cases shown in Table 14, the preheating temperature is 660 K, and the air flow rate is 19.85 g/s.

Table 14: Experimental Conditions for High-Swirl Burner Emissions

Case #	$CH_4/C_2H_6/C_3H_8$ Fuel Composition	Equivalence Ratio
1	100/0/0	0.52
2	85/15/0	0.52
3	80/0/20	0.52
4	100/0/0	0.56
5	85/15/0	0.56
6	80/0/20	0.56
7	100/0/0	0.6
8	85/15/0	0.6
9	80/0/20	0.6

The NOx levels for the cases shown in Table 14 are shown in Figure 92.

Figure 92: Measured NOx Levels for Different Fuel Compositions

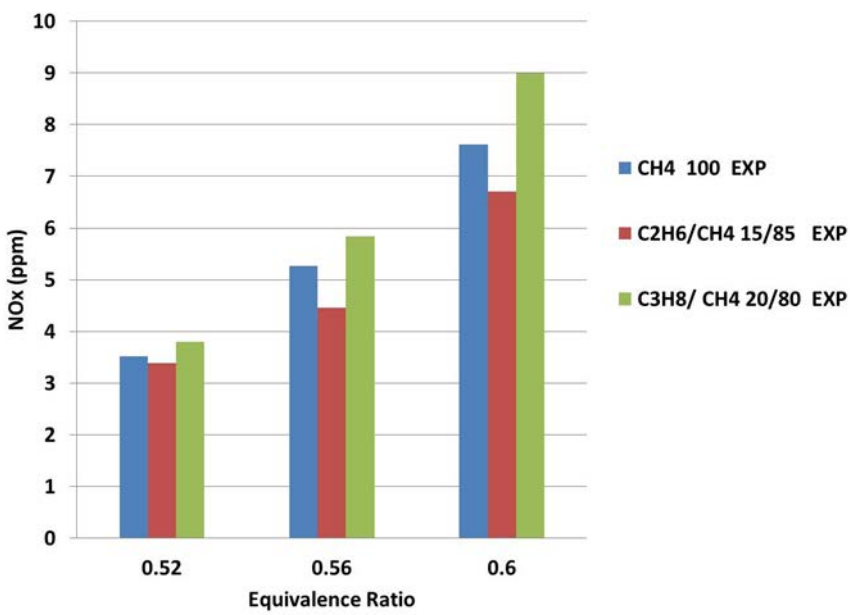

It is clear that as fuel composition changes for fixed equivalence ratios, NOx level changes. Though, as it was mentioned before, for different fuel compositions, fixed equivalence ratios result in different adiabatic flame temperature. Thus, to consider only the effect of fuel composition on NOx levels, fixed adiabatic flame temperature cases should be studied. For developing a reliable CRN, the data shown in Figure 92 can be used.

The predicted results from the CRN are shown in Figure 93.

Figure 93: CRN NOx Prediction for the Described Conditions in Table 14

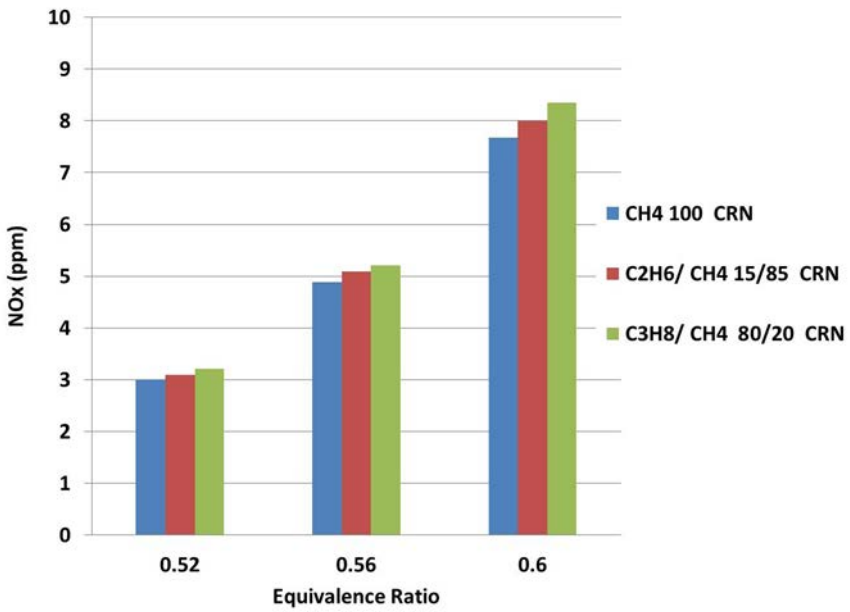

It is clear that as fuel composition changes for fixed equivalence ratios, NOx level changes. Though, as it was mentioned before, for different fuel compositions, fixed equivalence ratios result in different adiabatic flame temperature. Thus, to consider only the effect of fuel composition on NOx levels, fixed adiabatic flame temperature cases should be studied. For developing a reliable CRN, the data shown in Figure 94 can be used.

The predicted results from the CRN are shown in

Figure 94: Comparison between CRN and Measured Values for Cases in Table 14

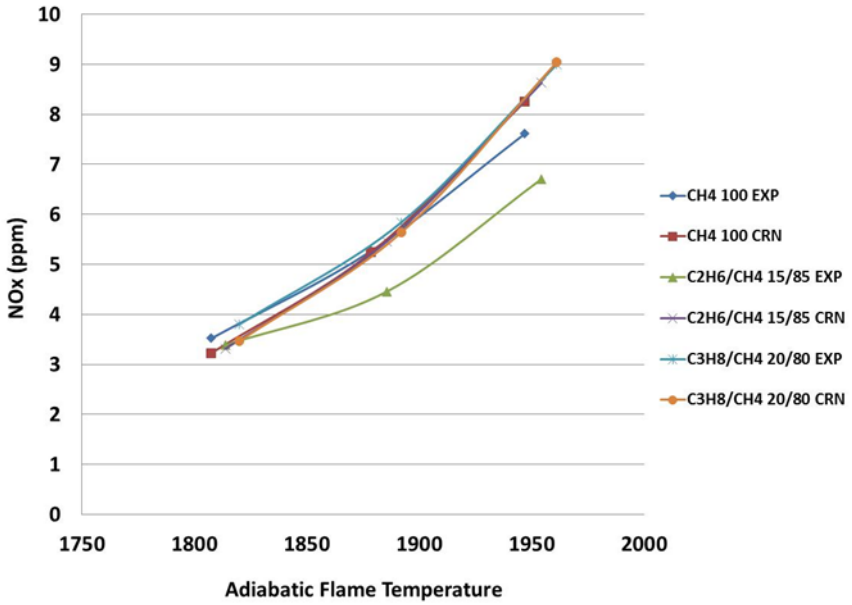

As shown inFigure 94 the overall prediction of the CRN for emission levels agrees well with the measured values. However, some discrepancy in the trends with ethane content is noted.
As mentioned before, to focus on impact of a broader range of fuel composition on NOx formation, a new set of 27 cases was defined. In the case of alkanes, seven fuel compositions for three adiabatic flame temperatures were studied. For diluted natural gas (e.g., landfill or digester gas which are mixtures of methane and carbon dioxide), two fuel compositions were studied again at three adiabate flame temperatures. For each adiabatic flame temperature, the proper equivalence ratio for each fuel composition was calculated through chemical kinetic simulations. Extreme cases were added to observe the impact of fuel composition on NOx and CO levels in different adiabatic flame temperatures. A summary of modeled cases is presented in Table 15. It should be noted that for all the cases, the preheat temperature is 660 K and the air flow rate is 19.85 g/s. A summary of NOx results from developed the CRN for the alkanes is presented in Figure 95.

Table 15: Wider Fuel Composition Range Study for High-Swirl Burner Emissions

Case #	$CH_4/C_2H_6/C_3H_8/CO_2$ Fuel Composition	AFT (K)
1	100/0/0/0	1800
2	85/15/0/0	1800
3	50/50/0/0	1800
4	0/100/0/0	1800
5	80/0/20/0	1800
6	50/0/50/0	1800
7	0/0/100/0	1800
8	80/0/0/20	1800
9	50/0/0/50	1800
10	100/0/0/0	1900
11	85/15/0/0	1900
12	50/50/0/0	1900
13	0/100/0/0	1900
14	80/0/20/0	1900
15	50/0/50/0	1900
16	0/0/100/0	1900
17	80/0/0/20	1900
18	50/0/0/50	1900
19	100/0/0/0	2000
20	85/15/0/0	2000
21	50/50/0/0	2000
22	0/100/0/0	2000
23	80/0/20/0	2000
24	50/0/50/0	2000
25	0/0/100/0	2000
26	80/0/0/20	2000
27	50/0/0/50	2000

Figure 95: CRN Prediction of NOx for Alkane Cases

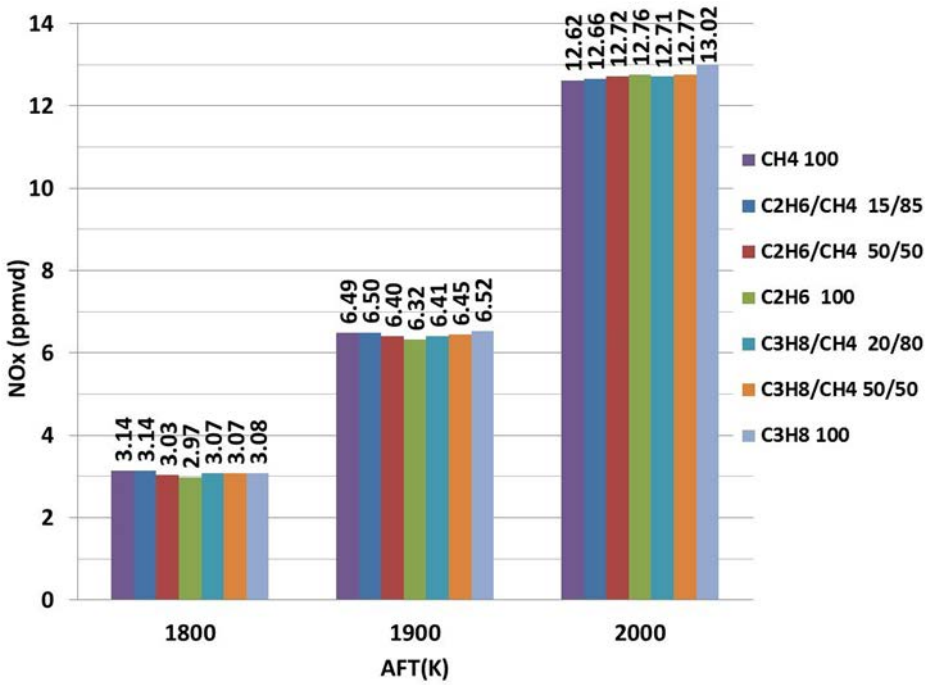

In Figure 95, it is clear that CRN predictions for NOx levels for different temperatures are approximately the same for all the fuel compositions. The difference between NOx levels for different fuel compositions for 1,800 K, 1,900 K and 2,000 K are less than 5 percent, 3 percent, and 3 percent, respectively. For 2,000 K, it is clear that as percentage of heavier alkane goes up, NOx levels slightly increase. In an effort to break down the NOx formation pathways, it is clear that the difference of each pathway contribution between different fuel compositions is minimal. On the average, the contributions for Zeldovich, N_2O, NNH, and Prompt pathways are 23, 24, 30, and 23, respectively. It is apparent that for the studied conditions and burner geometry, AFT is the key parameter in defining NOx formation levels. The difference among different alkane content fuels is not significant.

Although the change in NOx levels for different fuel compositions in alkanes is not notable, considerable change in level of CO is apparent, as shown in Figure 96.

Figure 96: CRN Prediction of CO for Alkane Cases

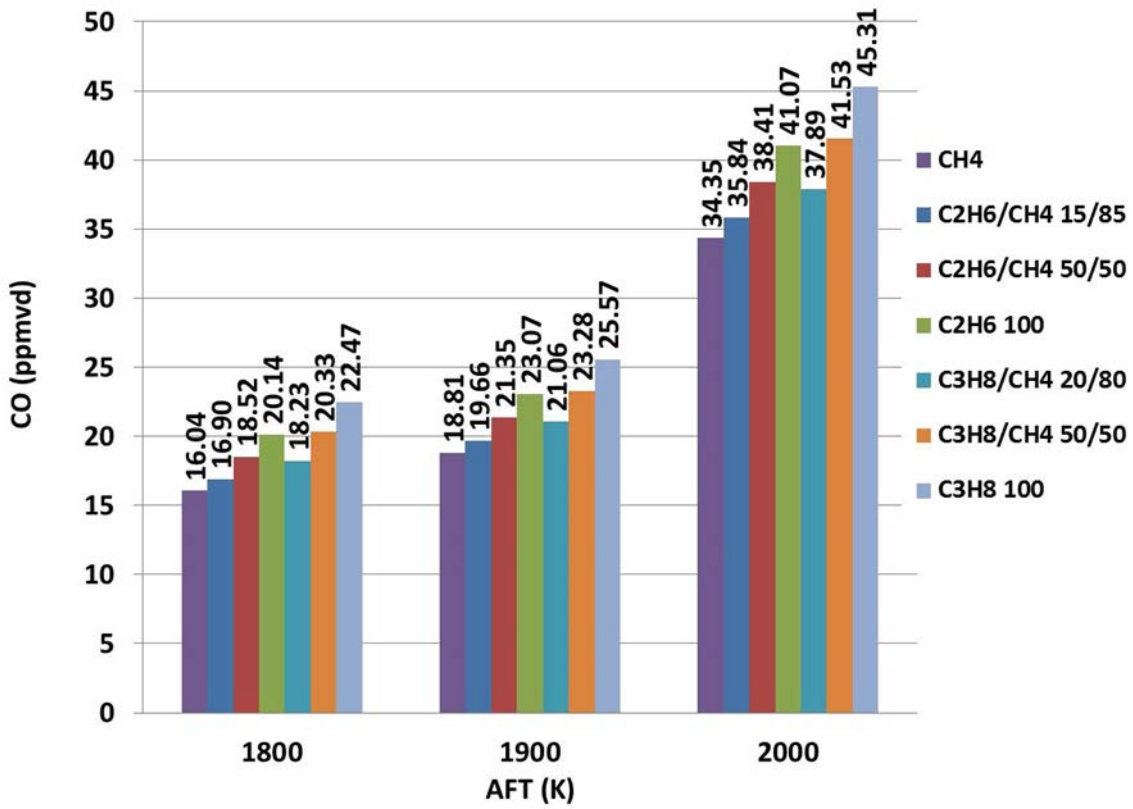

In Figure 96, it is clear that CO levels generally rise with increased concentration of heavier alkanes in fuel composition. In general, for each set of fuel composition, as concentrations of C2H6 and C3H8 increase, CO goes up. The difference between CO levels for different fuel compositions for 1,800 K, 1,900 K and 2,000 K are around 29 percent, 26 percent, and 24 percent, respectively. These changes are in contrast to the nearly negligible change in NOx emissions. Thus, considering both NOx and CO levels as pollutant emissions, care must be taken to remove the excessive CO levels for heavier hydrocarbons.

5.2.2.3 Diluted Natural Gas

In the case of landfill or digester-derived biogas, NOx formation is a function of fuel composition. In Figure 97, the general NOx levels for landfill gas compositions are added to the results previously shown for alkanes, for better comparison.

It is interesting to note that in the case of biogas, the impact of fuel composition is clear only at 2,000 K AFT. At 2,000 K, NOx decreases for the CO_2/CH_4 50/50 mixture, compared to pure natural gas. Thus, dilution of the fuel with CO2 could be effective in higher temperatures to reduce NOx. However, looking into level of CO could reveal how much impact the fuel composition would have in the case of landfill gas in overall pollution emission level.

Figure 97: CRN Prediction of NOx for Diluted Fuels along with Alkanes Cases

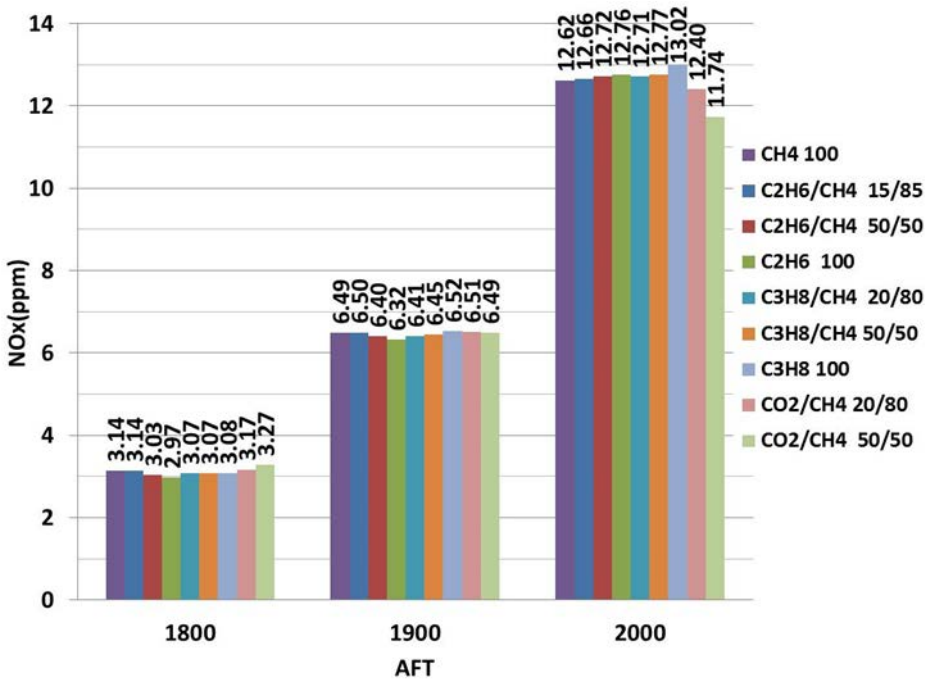

As shown in Figure 98, CO levels in landfill gas are much higher than alkanes at all the temperatures, especially for the CO_2/CH4 50/50 case. For all the temperatures, the level of CO for CO_2/CH_4 50/50 is more than twice as high as that for pure natural gas.

In the case of landfill gas, looking more closely into the NOx formation pathways indicated that the pathway contribution changes noticeably as fuel composition changes. The details of the NOx formation pathways for CH_4, CO_2/CH_4 20/80, and CO2/CH4 50/50 are shown in Figure 40, Figure 41, and Figure 42, respectively.

In general, Prompt NOx increases as CO_2 concentration in fuel composition increases, which could be due to more C atoms in the reaction. On the other side, all other pathway contributions decrease as CO_2 increases. For Zeldovich, which decreases the most as CO_2 increases, it could be that CO_2 as an inert gas in the reaction would take some heat from the reaction, which would affect the needed heat for the Zeldovich NOx reaction. The reason could be the same for the N_2O pathway, which is sensitive to heat available in the reaction. NNH NOx is reduced because of H atom decrease as CO_2 displaces CH_4.

Figure 98: CRN Prediction of CO for Landfill Gas Cases along with Alkanes Cases

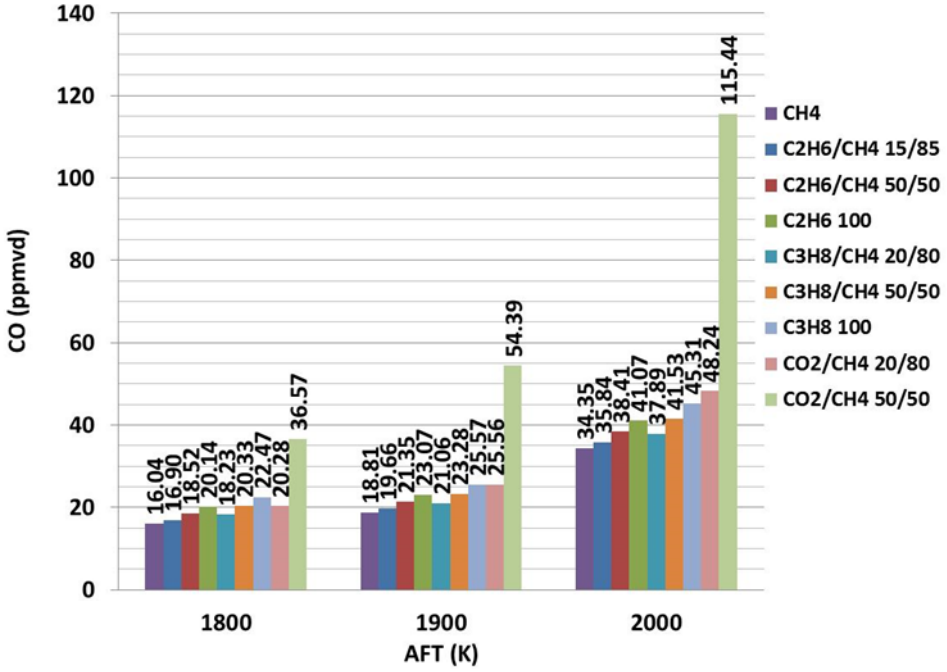

Figure 99: Details of NOx Formation Pathway for CH4

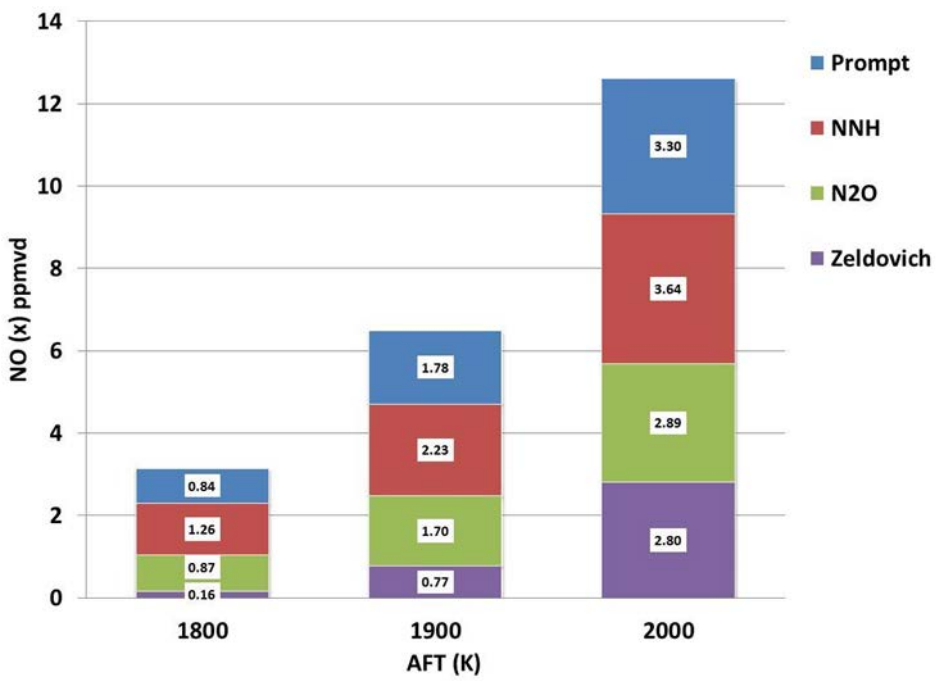

Figure 100: Details of NOx Formation Pathway for CO2/CH4 20/80

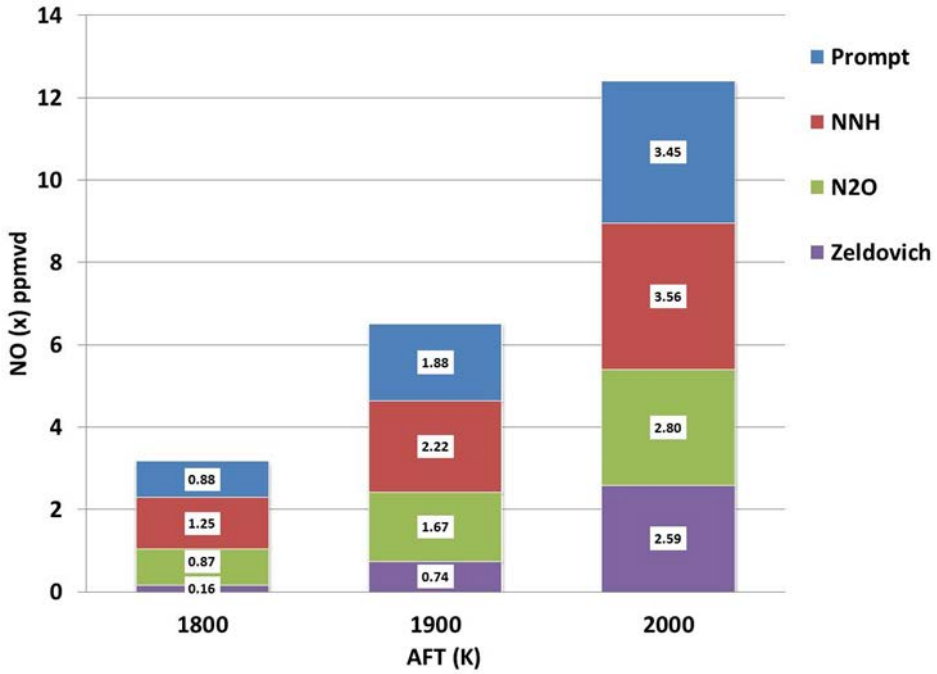

Figure 101: Details of NOx Formation Pathway for CO2/CH4 50/50

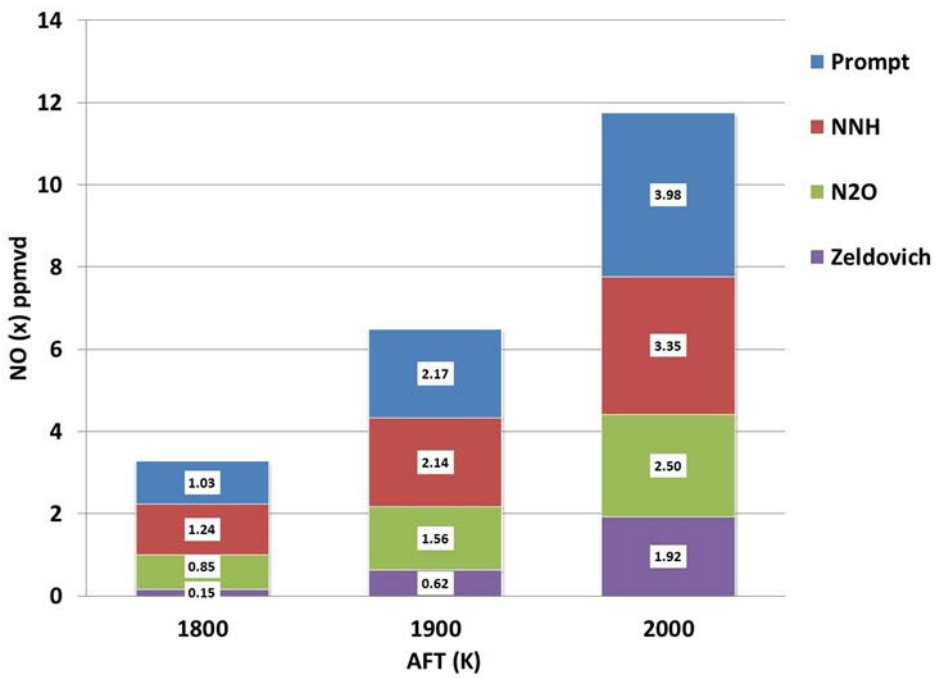

Of interest for dilute fuels (and low-temperature hydrocarbon combustion in general) is the emission of formaldehyde and NO2 from the exhaust stack. To explore these questions, the products from the CRN were analyzed. Results for formaldehyde are shown in Figure 102. The results suggest low levels in general, but dilute methane at lowest temperatures appears to have elevated levels. The lack of specific trends suggests that perhaps another chemistry mechanism might be explored. GRI-Mech 3.0 was not necessarily configured for optimal prediction of formaldehyde. In general, identifying mechanisms that have been specifically tuned to optimize prediction of aldehydes remains an open question.

Figure 103 presents the ratio of NO_2 to NOx in the exhaust. In this case, a clear dependency upon reaction temperature is evident. At 2,000 K, the NOx in the exhaust is primarily NO, but at 1,800 K, roughly 20 percent of the NOx is in the form of NO_2. No strong dependency upon fuel composition is suggested.

Figure 102: Formaldehyde Emission for Hydrocarbon Fuels at 1,800, 1,900, and 2,000 K

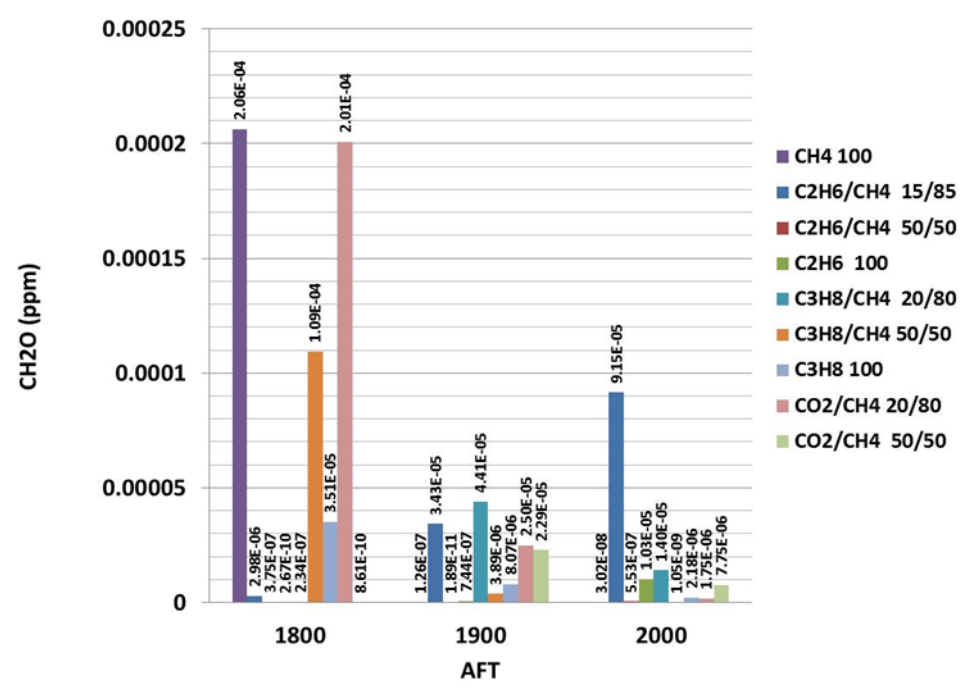

Figure 103: NO2/NOx Ratio for Hydrocarbons Fuels at 1,800, 1,900, and 2,000 K

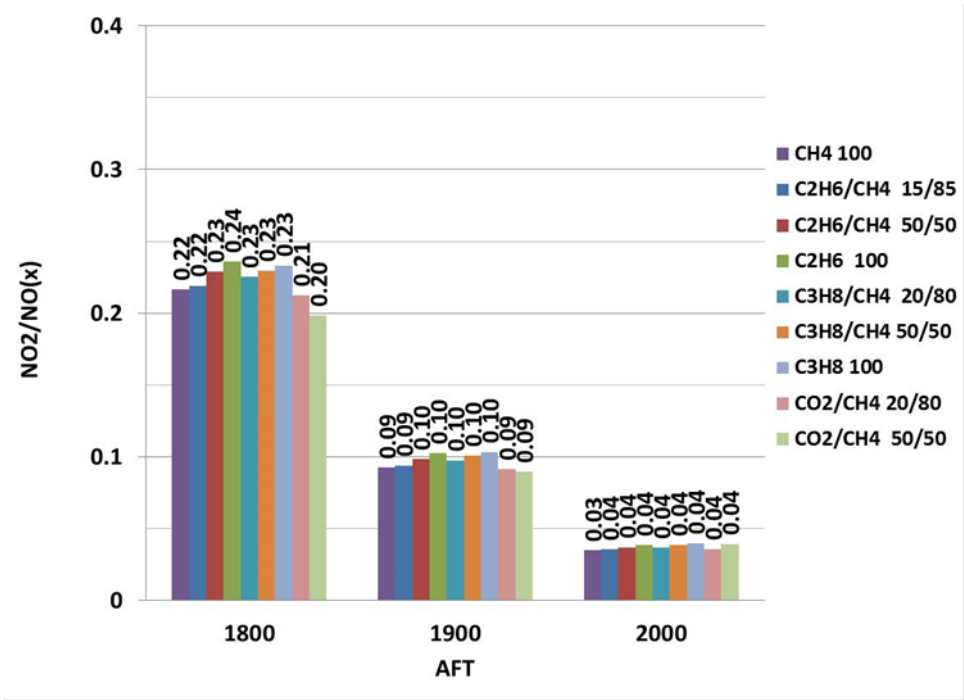

5.2.2.4 Hydrogen-Containing Fuels

1,800 K Adiabatic Flame Temperature

This section discusses NOx results for 1,800 K AFT. To keep AFT constant, a reaction equilibrium simulation was conducted to calculate appropriate equivalence ratios for combustion. Natural gas and hydrogen flow rates were then adjusted in LabView to deliver that equivalence ratio for the given air flow rates. For all the cases studied, preheating temperature was fixed at 500 K. Air flow rates were also fixed, to isolate the impact of fuel composition on NOx levels. However, to study the impact of residence time, air flow rates were changed to accommodate different flow residence times inside the combustor. In the case of fuel composition, eight different fuel compositions were studied, including: 100/0, 80/20, 60/40, 50/50, 40/60, 20/80, 10/90, and 0/100 in NG/H2 blend. For this type of study, the air flow rate was 23.6 g/s, which is equivalent to a 20 ms residence time. For the case of residence time, two different fuel compositions were chosen to represent the impact of residence time on NOx levels. One was the pure natural gas case, and the other was the 50/50 NG/H_2 case.

To begin, the impact of fuel composition on NOx levels is shown in Figure 104.

Figure 104: Impact of Fuel Composition in NG/H2 Blend on NOx, 1,800 K AFT, 500 K Tp, 20 ms Residence Time

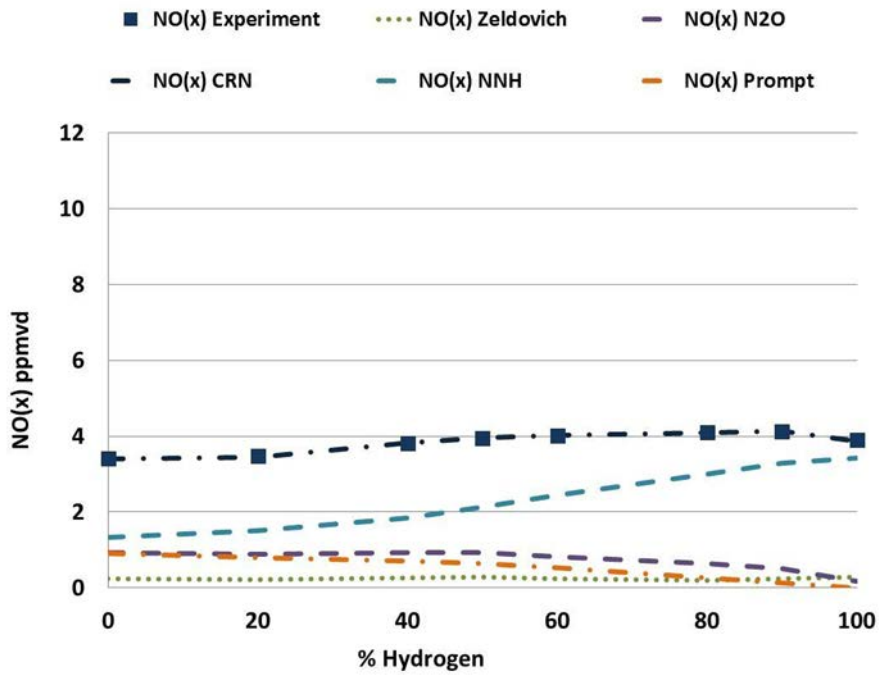

The CRN prediction compares well with the experimental measurements. Both the CRN and the measured values suggested an increase in NOx levels from pure natural gas up to the 50/50 NG/H2 blend. The NOx levels were relatively constant until the fuel was pure hydrogen; then there was a slight decrease in NOx. The results in Figure 104 are plotted in another format in Figure 105 to help elucidate the details regarding the relative contributions of the NOx emission from the various pathways. As shown, the NNH mechanism is the dominate NOx formation mechanism for the high-swirl burner configuration at 1,800 K AFT. The contribution from the thermal mechanism is relatively small and does not change with fuel composition. This might be expected for the relatively low 1,800 K AFT condition. Prompt NOx is associated with the presence of hydrocarbon fragments. As such, as the amount of methane is displaced with hydrogen, the Prompt NOx contribution decreases accordingly.

Figure 105: Details of NOx Formation Pathways, 1,800 K AFT, 500 K Tp, 20 ms Residence time

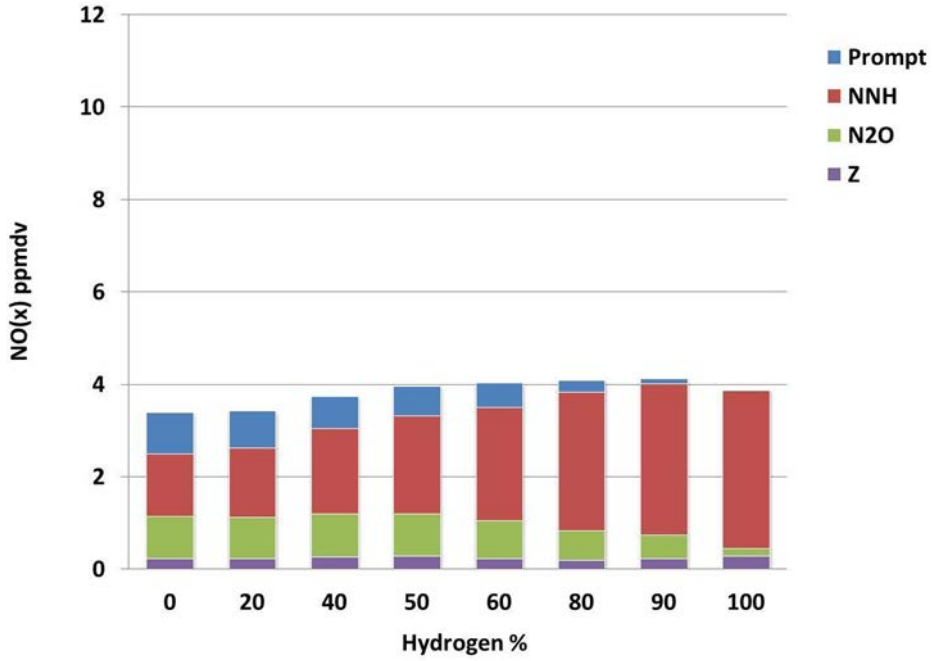

It is interesting to note that NNH NOx constantly increases as the hydrogen in the fuel increases. This observation is consistent with findings of other researchers that NNH is a major contributor to the NOx levels from combustion of NG/H_2 mixtures (Konnov et al. 2001; Bozzelli and Dean 1995; Hayhurst and Hutchinson 1998; Harrington et al. 1996; Miller et al. 1981). As hydrogen increases, H atom, which is the key element in NNH pathway, increases, and NOx goes up. In the case of NOx formed via the N_2O pathway, it is observed that it decreases as hydrogen concentrations increase. Two possible reasons for this trend are suggested. First, as hydrogen displaces methane, the number of multi-atom intermediate species goes down because hydrogen will break down into H atom. This may impact the number and type of third-body particles available for participation in the NOx formation via the N_2O mechanism. Recall from Section 3.2.4.1.3, that the N_2O NOx formation mechanism requires a collision between O atom and N_2 and a third body (M). As the concentration and/or composition of M in the mixture decreases or changes, NOx formed via the N_2O mechanism could be affected. Second, as the NNH pathway contribution increases, available O atom might be consumed in NNH+O reaction to form NOx. That might affect the availability of O atom, which is necessary in forming nitrous NOx.

Figure 106 shows the impact of residence time on NOx levels. First, the CRN predictions for both CO and NOx were good. Carbon monoxide level decreases as residence time increases. This is because with more time, the O atom concentration decreases, and less CO is formed. Also, CO has more time to react with oxygen to form CO_2. Note that here, increase of residence time is equivalent to decrease in air flow rates.

Figure 106: CRN and Measured NOx and CO, 1,800 K AFT, 500 K Tp, Natural Gas

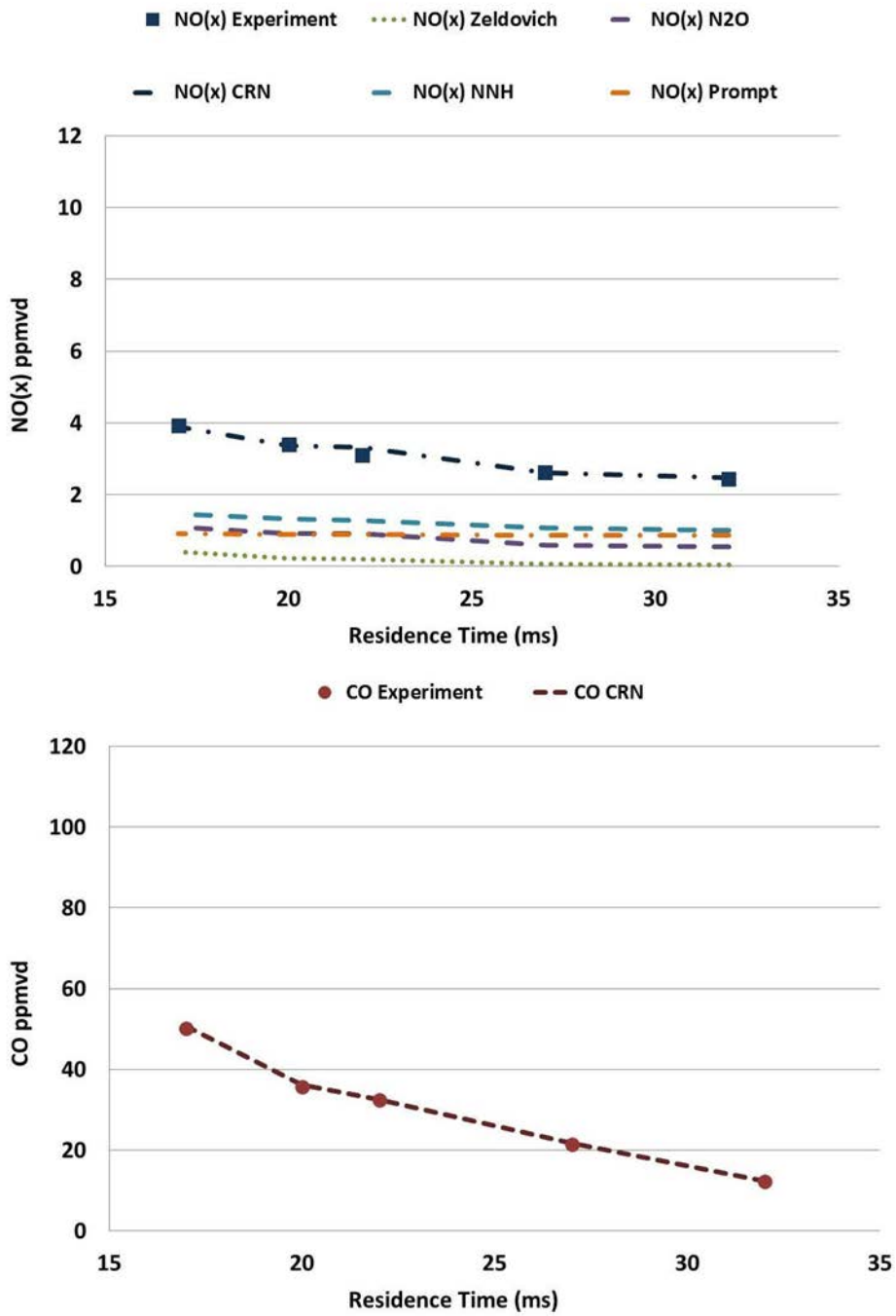

Figure 107: Details of NOx Formation Pathways, 1,800 K AFT, 500 K Tp, Natural Gas

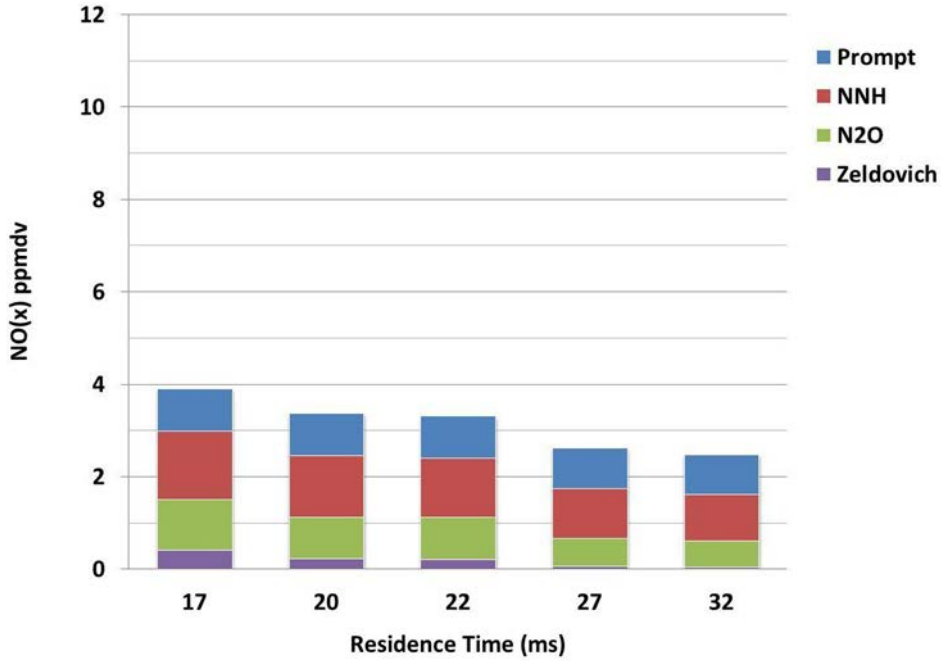

As shown in Figure 107, as residence time increases, NO formed via the Zeldovich mechanism decreases, while that from NNH, N_2O, and Prompt mechanisms all decrease slightly. For the Zeldovich mechanism, it could be that the Zeldovich NOx is due to a reaction of super equilibrium O with nitrogen. As residence time increases, super equilibrium O decreases. For nitrous NOx, decay of O atom as time increases could be the reason for a decrease. For the NNH and Prompt NOx formation mechanisms, longer residence times result in more time for radicals species needed in the reactions to decay. As a result, NOx formed from both of these mechanisms decreases as well.

To study the effect of residence time on hydrogen-containing fuels, a 50/50 NG/H_2 mixture was chosen. The CRN and measured results for NOx and CO are shown in Figure 108.

Figure 108: CRN and Measured NOx and CO, 1,800 K AFT, 500 K Tp, 50/50 NG/H2

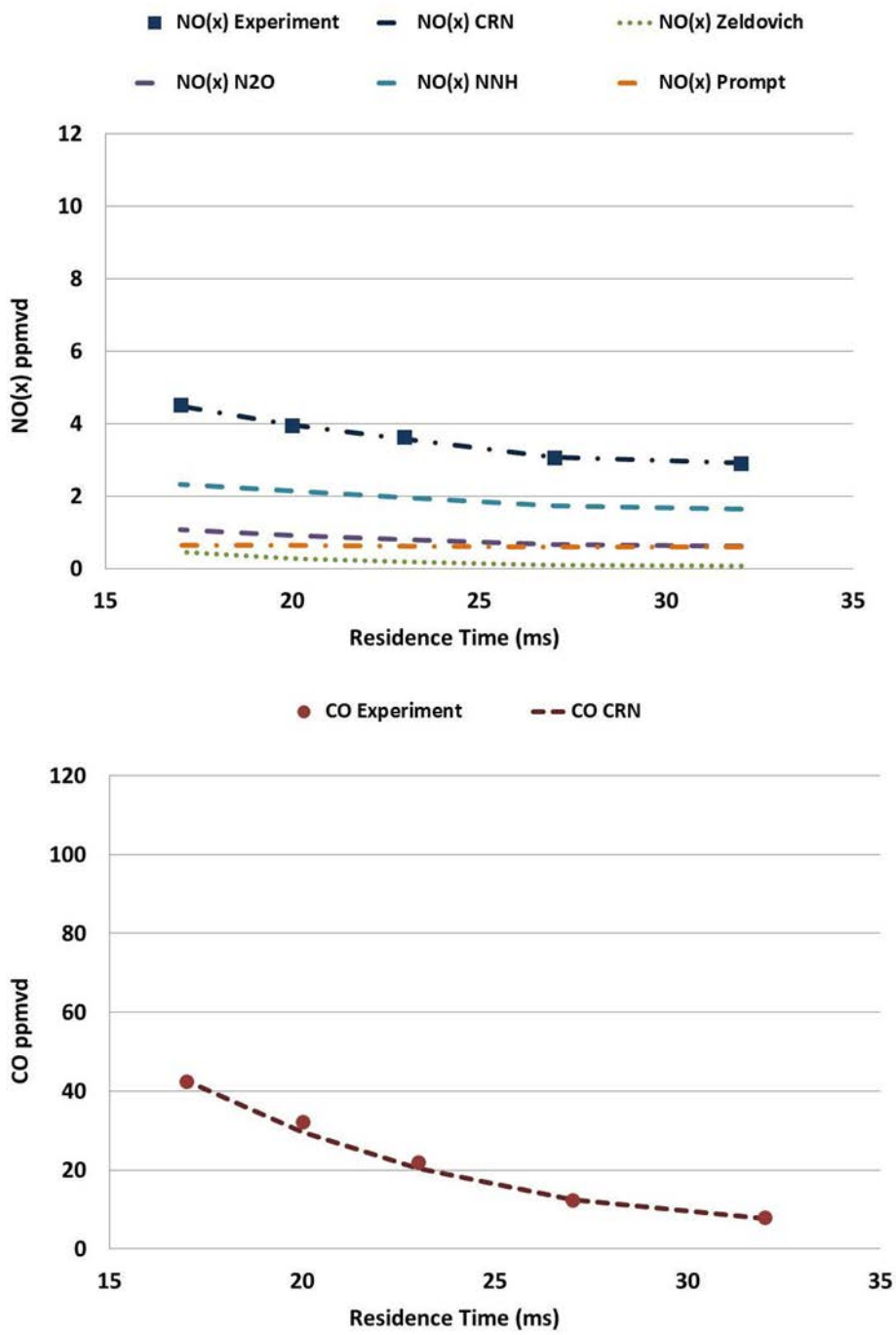

Figure 106 and Figure 108, which show results for pure natural gas and a 50/50 NG/H2 case, is that for the natural gas case, the level of CO is higher and the level of NOx is lower. For CO, it is obvious that with decreasing natural gas in fuel mixture, CO (which is an incomplete product of CxHy combustion) decreases. For NOx, as shown in Figure 106 and Figure 108, the increased level of NOx from natural gas to the 50/50 NG/H_2 case could be due to the contribution of the NNH pathway, which increases as hydrogen concentration in fuel increases. Another difference between the pure natural gas case and the 50/50 NG/H_2 case is the contribution of different pathways in formation of NOx. The details of the NOx formation pathways are shown in Figure 109

Figure 109: Details of NOx Formation Pathways, 1,800 K AFT, 500 K Tp, 50/50 NG/H2

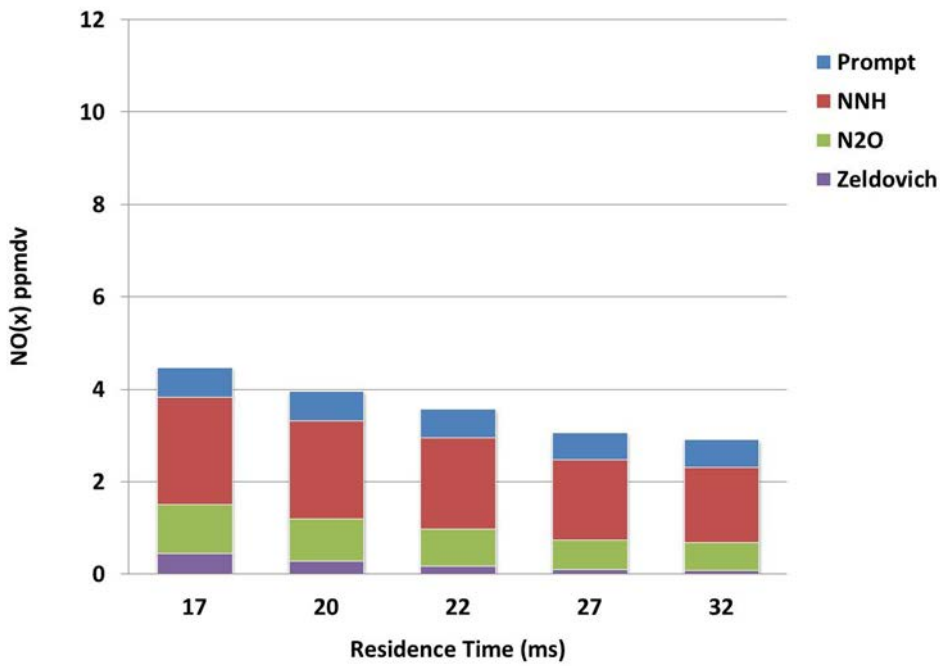

It is clear that similar to the results for natural gas shown in Figure 107, NOx decreases as residence time increases. The major differences between the natural gas case and the 50/50 case are that the Prompt pathway is generally lower, and NNH is higher in 50/50 NG/H2 case compared to natural gas. This is true for all the residence times.

To see if a change of AFT would change emissions behavior, AFT was raised to fixed 1,900 K AFT. The results are discussed in next section.

1,900 K Adiabatic Flame Temperature

This section looks at NOx level as a function of fuel composition and residence time for a fixed 1,900 K AFT. The question is how AFT will influence different NOx formation pathways for different testing conditions.

The first impact of fuel composition on NOx is shown in Figure 110.

Figure 110: Impact of Fuel Composition in NG/H2 Blend on NOx, 1,900 K AFT, 500 K Tp, 20 ms Residence Time

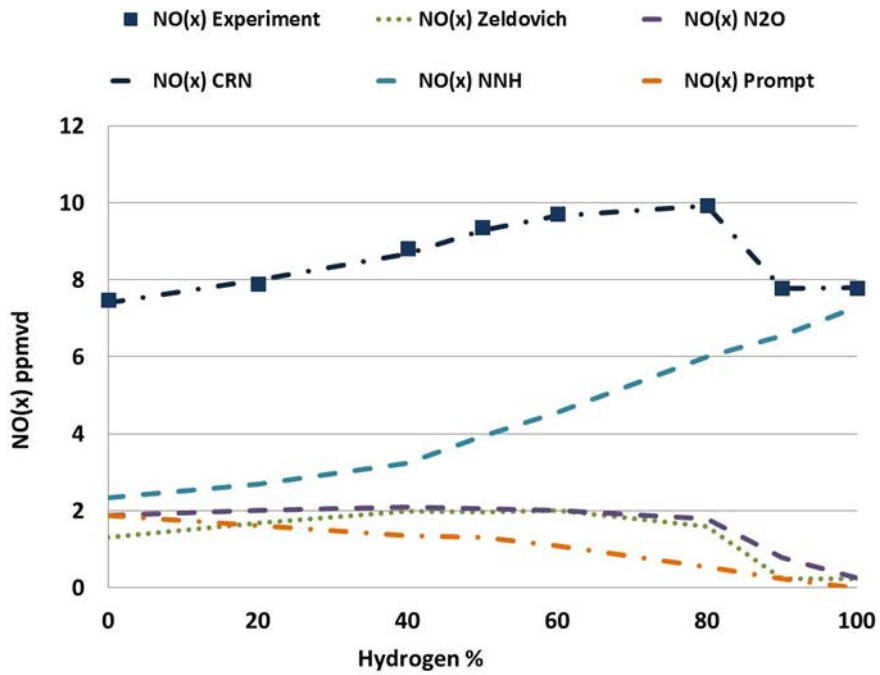

Figure 110 shows that the agreement between the CRN and measured values was good. Starting from natural gas, it is clear that by adding hydrogen percent in fuel composition, the NOx emissions increased up to 80 percent hydrogen. Then, suddenly NOx emissions decreased when using the 90 and 100 percent hydrogen fuel composition. The interesting point is that the NOx level from using pure hydrogen and pure natural gas is comparable. Another interesting point is that for the 1,800 K AFT case, the slight decrease in NOx emissions by adding hydrogen occurred after 10/90 NG/H2 mixture, but for the 1,900 K this decrease happened after 20/80 NG/H2 mixture. To investigate more, details of NOx formation pathway contributions are shown in Figure 111.

Figure 111: Details of NOx Formation Pathways, 1,900 K AFT, 500 K Tp, 20 ms Residence Time

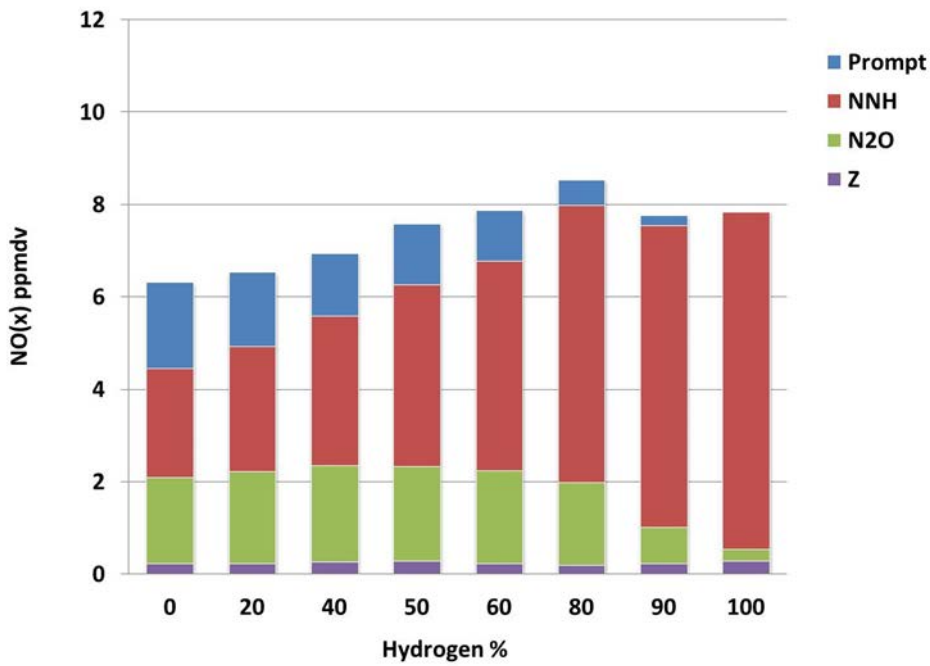

It is clear that NNH NOx is again the dominant pathway in this application. Although the total NOx decreases once hydrogen concentrations increase beyond 80 percent, the contribution from the NNH pathway continues to increase. This could be due to high concentrations of H atom in the reaction, with high levels of hydrogen in the fuel. Nitrous and Prompt NOx NO decrease rapidly once the hydrogen concentration exceeds 80 percent. For Prompt NO, it is due to lack of hydrocarbon radicals in the mixture. However, for nitrous NOx, the reason for the sharp reduction above 80 percent hydrogen is less clear. It could be due to absence of third-body collisions in those cases, or lack of O atom, which is consumed in the dominant NNH pathway. Anyhow, it is what can be seen with both experimental results and the CRN predictions.

To evaluate the impact of residence time on NOx levels, Figure 112 is shown. Decrease of Zeldovich NOx with residence time is counterintuitive because usually more residence time imposes more Zeldovich NOx. However, it is only true if the rate-limiting reaction of Zeldovich, which is $O + N_2 \square NO + N$, is triggered. If it is not triggered by the temperature, Zeldovich NOx could be due to super equilibrium O atom in the reaction which decreases as residence time increases. Note that 1,900 K AFT cannot predict the actual temperature inside the reactor. It is definitely lower than 1,900 K due to heat loss. The details of NOx formation pathways are presented in Figure 113.

Figure 112: CRN and Measured NOx and CO, 1,900 K AFT, 500 K Tp, Natural Gas/

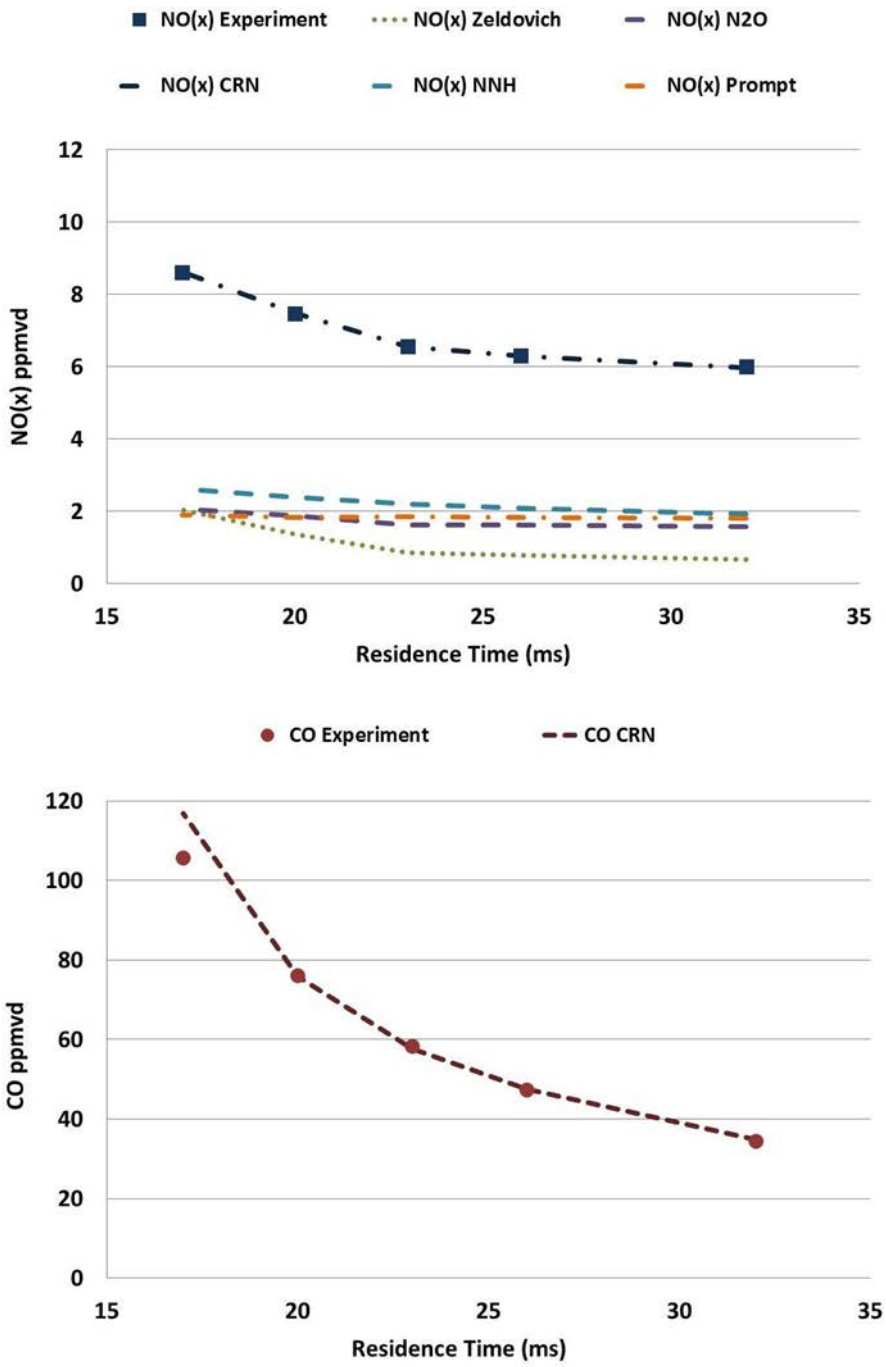

Figure 113: NOx Formation Pathways, 1,900 K AFT, 500 K Tp, Natural Gas.

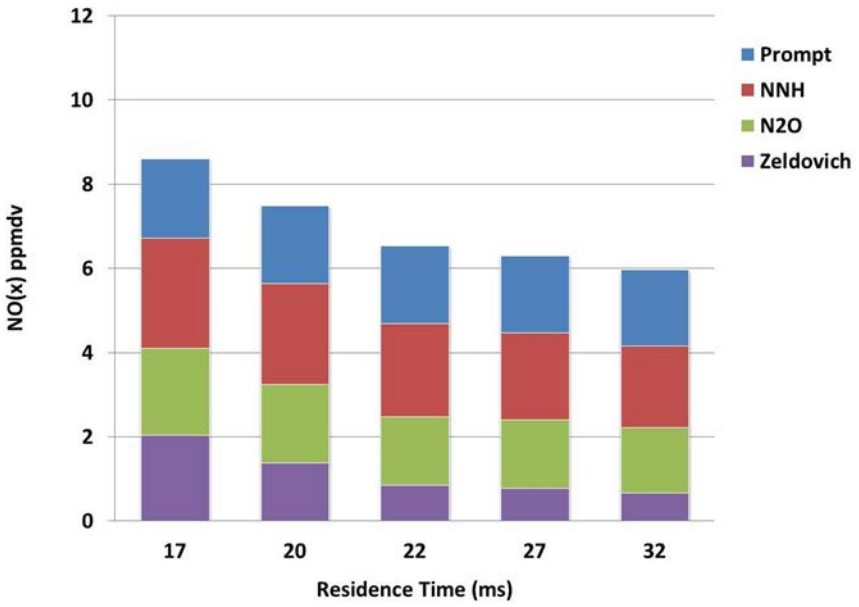

The same result is shown for the 50/50 NG/H2 mixture in Figure 114 and Figure 115.

Figure 114: NOx Formation Pathways, 1,900 K AFT, 500 K Tp, 50/50 NG/H2

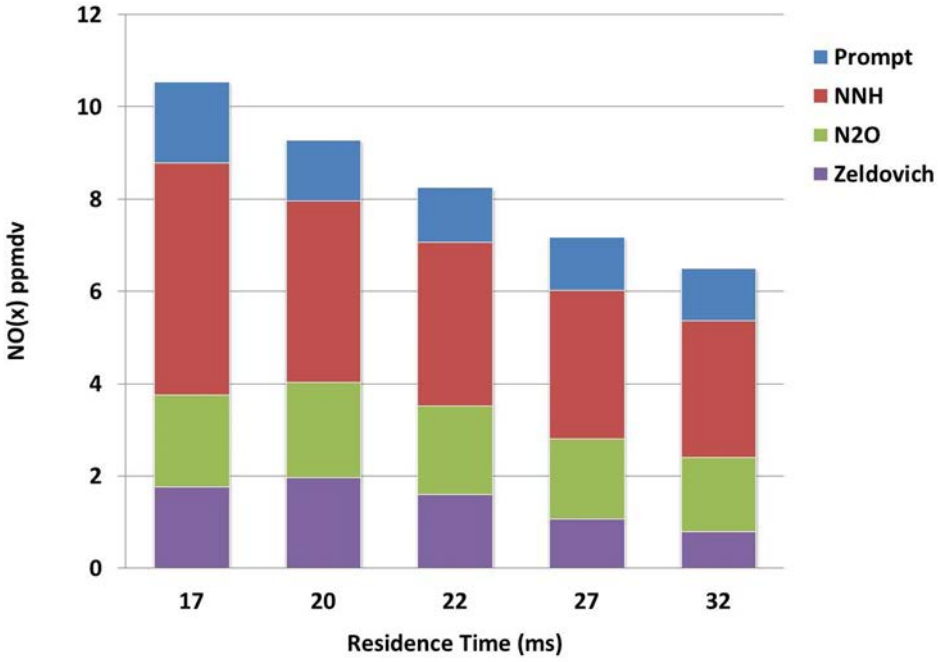

Figure 115: CRN and Measured NOx and CO, 1,900 K AFT, 500 K Tp, 50/50 NG/H2

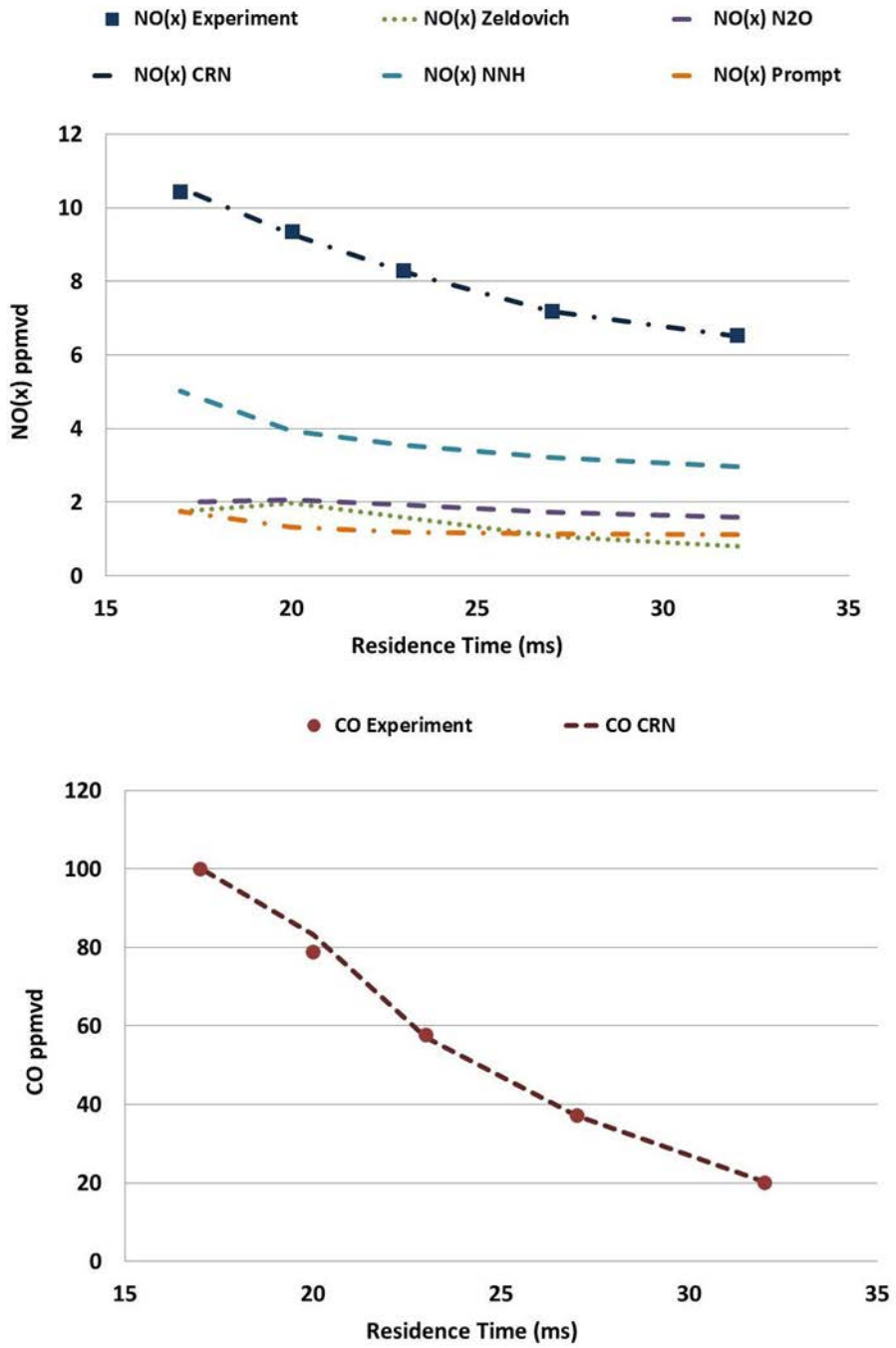

It is clear that the NOx level for all the residence times is higher for 50/50 NG/H_2, compared to natural gas. For the 50/50 NG/H_2 case, the contribution of the NNH pathway is considerably higher than other pathways.

In general, it seems that, for the conditions studied, NO formed via the NNH pathway dominates the total NO formed. The NNH pathway is enhanced as H atom increases inside the

reaction. This will occur when hydrogen increases and residence time decreases. This trend seemed promising for all the tested and modeled conditions.

Nitrogen oxide formation through different pathways could be interpreted along a map which could vary with temperatures, flow rates, fuel compositions, and burner geometry. This map could change for different applications. For this study, the combination of conditions leads to the zone in the map where the NNH reaction is the most significant pathway. Thus, an increase or decrease in NOx could be explained by specifications of this pathway. There are other reported applications, including the jet-stirred reactor work described in Section 5.2.1, where the Prompt NOx is the most important mechanism. In this case, again NOx is expected to decrease with an increase in residence time. However, increase of hydrogen in fuel will result in a decrease in NOx levels because Prompt NOx decreases as hydrogen increases in the fuel. Complications associated with the relative contributions of the different pathways to the formation of NOx could be why simple correlations cannot predict NOx behavior as fuel composition changes.

Finally, NOx formation pathways were studied over a wider range of adiabatic flame temperatures for a 50/50 NG/H_2 mixture.

Figure 116 shows the NOx and CO for various AFTs, starting from 1,500 K up to 2,000 K. The agreement between the CRN and the experimental results is good. Carbon monoxide was not shown for 1,950 K and 2, 000 K, since the levels were higher than the calibrated range for the gas analyzer. The exponential increase in level of NOx with temperature was apparent, as expected. The rate of increase was really steep after 1,900 K. It could be because around that temperature, Thermal NOx through the Zeldovich pathway kicks in. Details of the NOx formation pathways are shown in Figure 117.

Figure 116: CRN and Measured NOx and CO, 500 K Tp, 50/50 NG/H2, 20 ms residence time

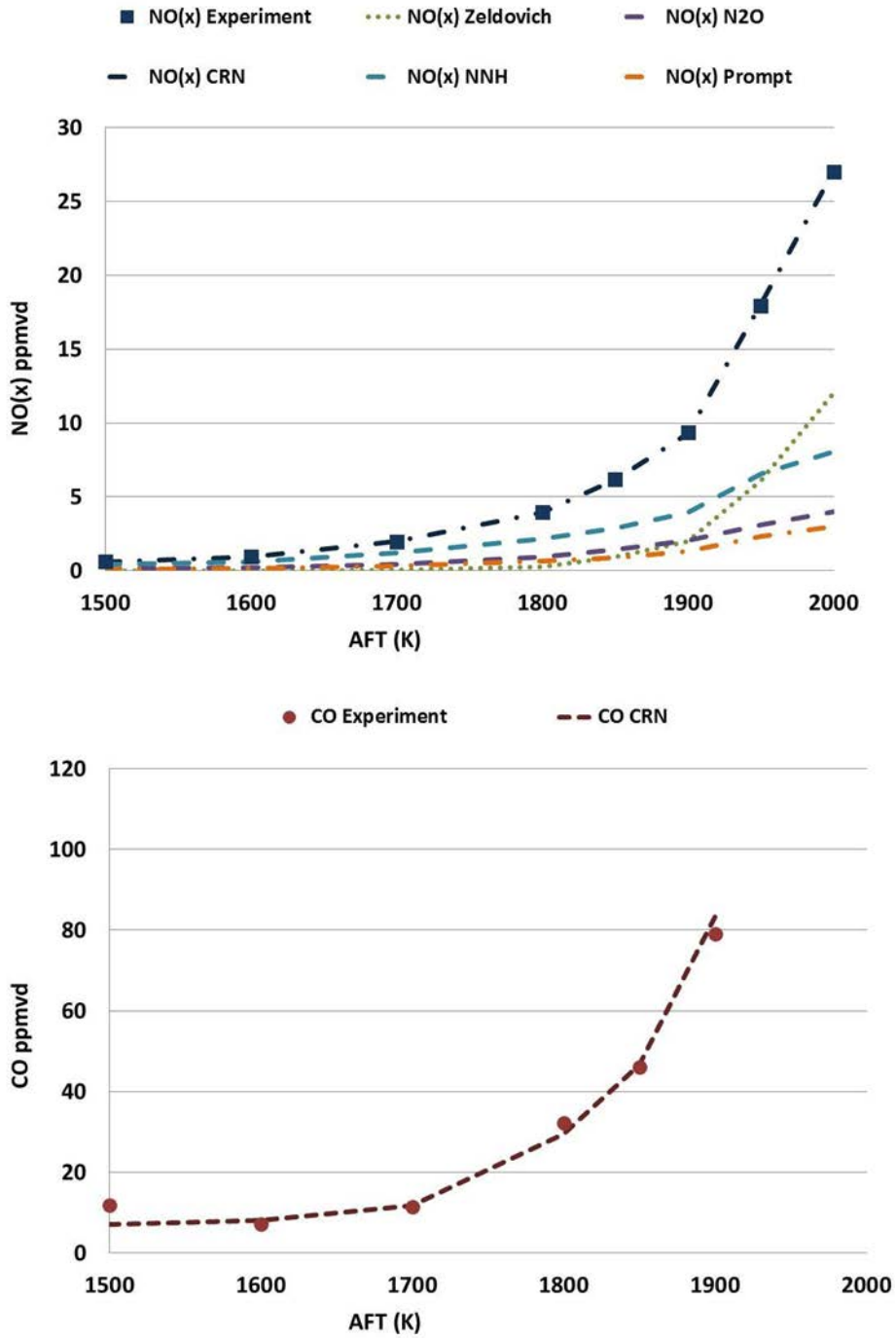

Figure 117: NOx Formation Pathways, 500 K Tp, 50/50 NG/H2, 20 ms residence time

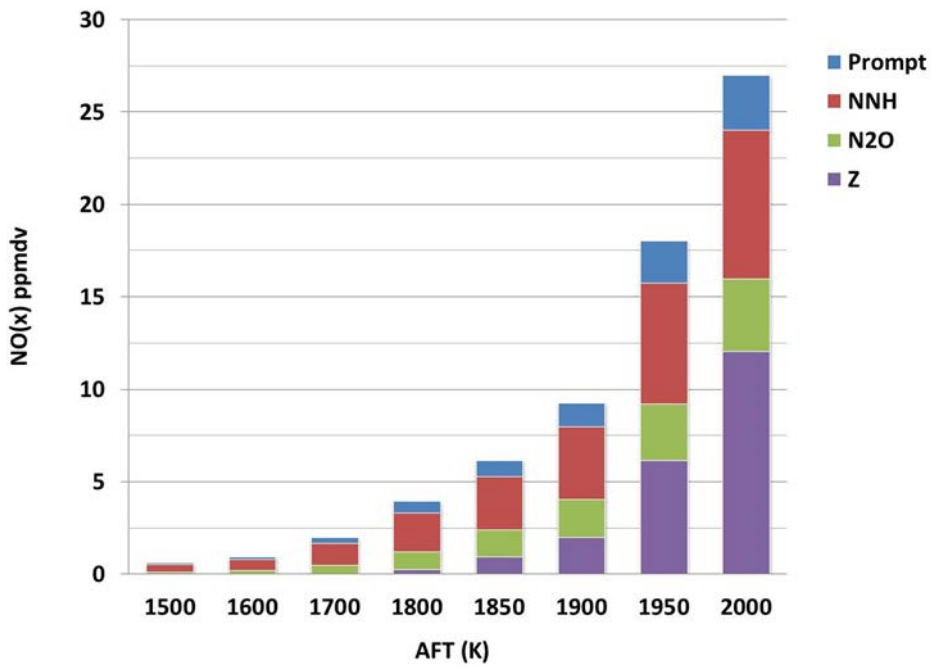

It is clear that as AFT increases, the following will take place for each pathway:

1. Prompt: This pathway increases as more radicals form in higher temperature.
2. NNH: This pathway increases because at higher temperatures the reactions are more active, and there are more H atoms in the reaction.
3. Nitrous: This pathway also increases at higher temperatures because there are more radicals, and also the collisions are more effective.
4. Zeldovich: This pathway increases, especially after 1,900 K AFT in this case. The rate of increase for this pathway is very high after 1,900 K, which makes this pathway the dominant mechanism in NOx formation.

Thermal NOx through the Zeldovich mechanism changes the NOx map after 1,900 K. It implies that for 1,950 K and 2,000 K temperatures, it is possible that the Zeldovich mechanism determines what happens to NOx if testing conditions and fuel compositions change.

5.2.2.5 Summary of High-Swirl Burner Results

Nitrogen oxide emissions from combustion of different mixtures of hydrogen and natural gas was studied for different residence times and different AFTs. The study included both experimental measurements and simulation results from the CRN. With the CRN, different NOx formation pathways are calculated. For most cases, it was shown that the NNH pathway was the dominant contributor in NOx formation at 1,800 K and 1,900 K. Increase of hydrogen concentration and decrease of residence time both enhance NNH NOx, so it was shown that as hydrogen concentration in fuel increases or residence time decreases, NOx levels generally

increase. However, there are cases in pure hydrogen or a 10/90 NG/H2 mixture where NOx decreases relative to a 20/80 NG/H2 case. Though, in these cases NNH NOx increases, but due to lack of Prompt NOx in those conditions, the total NOx decreases.

The results shown suggest that NOx emission from depends on fuel composition, adiabatic flame temperatures, residence times, and possibly burner geometry. This is illustrated for adiabatic flame temperature, where up to 1,900 K AFT, the dominant pathway in NOx formation was NNH, but after 1,900 K, the dominant pathway was the Zeldovich mechanism.

5.2.3 Results for Capstone Engine

Fuel composition in this study includes a wide range of gaseous fuels, starting from pure natural gas (assumed as pure CH_4 in the CFD and CRN models), alkane mixtures (CH_4-C_2H_6-C_3H_8), natural gas mixed with hydrogen (as hydrogen is the major constituent of alternative fuels and presents extreme combustion properties) and natural gas diluted with carbon dioxide. When varying the fuel composition, the equivalence ratio for the different mixtures was set in such a way that the adiabatic flame temperature remained constant at 1,850 K. For most fuel compositions, experimentally measured NOx results are available against which to compare the CRN results. Using the CRN presented in Figure 119 the different NOx formation pathways are calculated using CHEMKIN Pro with the GRI-Mech 3.0 mechanism. Also, in order to present the data results consistently, the emissions for the different fuel compositions are compared to those emitted when running the turbine on natural gas.

All the results are presented at the same power output, air preheating temperature, and adiabatic flame temperature (AFT). Since for a given requested power setting the turbine exit temperature remains constant, it can be expected that the global reaction temperature would remain constant regardless of the incoming fuel heat content. This control strategy is important relative to the mechanism by which fuel composition may affect NOx emissions. It has been shown that NOx is sensitive to fuel composition for the situation where the combustion temperature is held at a fixed level below the point where Thermal NOx is predominant (Hack & McDonell, 2008).

For the Capstone C65 microturbine, composition effects on the overall firing temperature are minimized due to the system control strategy, which implies that only localized effects of fuel composition (e.g., temperature changes at the reaction front, composition-based effects on Prompt, NNH, and N_2O mechanisms) play a role in NOx emissions. Also it is assumed that interchanging fuels will not have an effect on the turbine efficiency; therefore, at a given fuel power input we consider a similar power output, regardless of the fuel composition. On the other hand, the flame stability cannot be studied with this methodology and will be ignored in this section of the report. The following sections will discuss the most significant factors contributing to the NOx formation pathways when varying the fuel composition.

5.2.3.1 CRN Development

The application of the CRN methodology to the Capstone C65 microturbine engine is presented in this section. The most important characteristics of the C65 combustor were presented previously in Section 4.2.2.4. Both CFD and CRN models take into account the air/fuel splits

across the six injectors and the distribution of air jets in the dilution zone. The dilution zone includes two air streams, the inner air jets and the outer air jets, which cool the exhaust gases before they are supplied to the turbine. Information regarding air split is proprietary.

An intelligently designed chemical reactor network must be an accurate representation of the flow patterns and mixing characteristics of the device it represents. In a CRN, the flow and flame patterns in the combustion volume are divided into zones represented by a reactor. Each reactor requires several inputs, such as composition of the reactants, residence time, reactor volume, temperature, pressure, flow rate, and distribution of the recirculation patterns. That information can be obtained from previous experimental results and from CFD simulations. Since the reaction structure inside a turbine's combustion chamber is not visually accessible for the experimenter, the CFD results have shown to be particularly suitable to gain details about those reaction structures. For that reason, the flame profiles, volume of the reactors, residence time, and recirculation patterns were obtained from the CFD results.

At full load (60 kilowatts electrical, kWe) the six nozzles inject a mixture of fuel and air into the combustion chamber. The turbine operating at full load on natural gas (in this case pure CH_4) was the model base to set up the chemical reactor network. Important variable such as the residence time, volume of each reactor, and temperature after the core of the reactions, were extracted from the CFD results of the turbine at full load. Figure 118 shows the temperature contours at the first and second plane. These contours were obtained for the turbine combustor running at full load. It is possible to see in Figure 118the six injectors and the characteristic conic section of an attached premixed flame (blue region). Both the CFD and CRN simulations assume a perfect premixing of fuel and oxidant.

Figure 118: Temperature Contours of a Turbine Combustion Chamber.

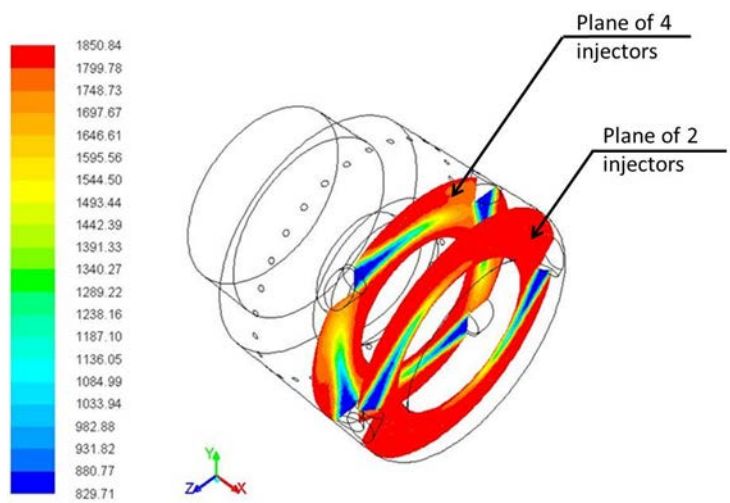

The chemical reactor network presented in Figure 119 depicts the flow distribution extracted from the CFD analysis. The first block (or Block 1) includes the total mass flow inlet of premixed gas that is necessary to achieve an electrical power output equal to 60 kWe. The flow rate of premixed gas was set using the actual thermal efficiency at full power. In the same block, the flow rate is divided into three blocks (blocks 2, 4, and 5). Since the turbine configuration displays flame symmetry, it was possible to set a block of two perfectly stirred reactors (PSR) to represent each pair symmetrical flames. Each pair of flames is grouped into blocks 2, 4, and 5, and is represented by two PSRs in series.

The first reactor of the series represents the primary reaction zone, or the core of the reactions, where the effects of the surroundings are negligible; the second reactor in each block symbolizes a post-flame zone, which is a region at high temperature where the first PSR injects its combustion products; additionally, blocks 4 and 5 account for the effect of the exhaust gases that were produced in Block 2. The splitter in the CRN divides the exhaust products from Block 2 into three flow streams; two of these portions are directed toward the two second PSRs of the fourth and fifth blocks. In that manner, the effect of the exhaust gas that comes from the plane of two injectors is accounted for with this CRN configuration. Conversely, this CRN does not consider an interaction between flames that are located within the same plane. Analysis of the CFD results indicates that, in the plane of two injectors, little interaction between the reaction zones occurs. However, the products from the combustion in the plane of two does interact with the reactions associated with the injectors in the plane of four. The exhaust recirculation effect (both from the preceding flame and from the preceding plane) is accounted for by using a portion of the exhaust gases from Block 2. Block 6 represents a post flame region where the streams of all the previous reactors are mixed again before they are diluted with air coming from Block 7 (the dilution air inlet). Finally, Block 8 accounts for the mixing process and the reactions after the dilution air is injected. Nitrogen oxide and CO emissions corrected to 15 percent O2 are analyzed in the exhaust products of Block 8.

5.2.3.2 Alkane Fuels

In 2008, Hack & McDonell conducted statistically designed experiments on a commercial natural gas-fired 60 kW gas turbine—the Capstone C60 microturbine—which is a commercial 60 kW natural-gas-fired microturbine generator. The combustor of the C60 engine is similar to the one of the C65 model, thus for the purpose of this section those results are applicable. Their study analyzed the effects of fuel composition on NOx and CO emissions; particularly the effect of blending natural gas with ethane and propane. Their results and trends indicate that the presence of higher hydrocarbons in the fuel leads to appreciably higher NOx emissions, while having less impact on CO emissions.

Figure 119: Example of a Combustion System Divided into Several Chemical Reactors

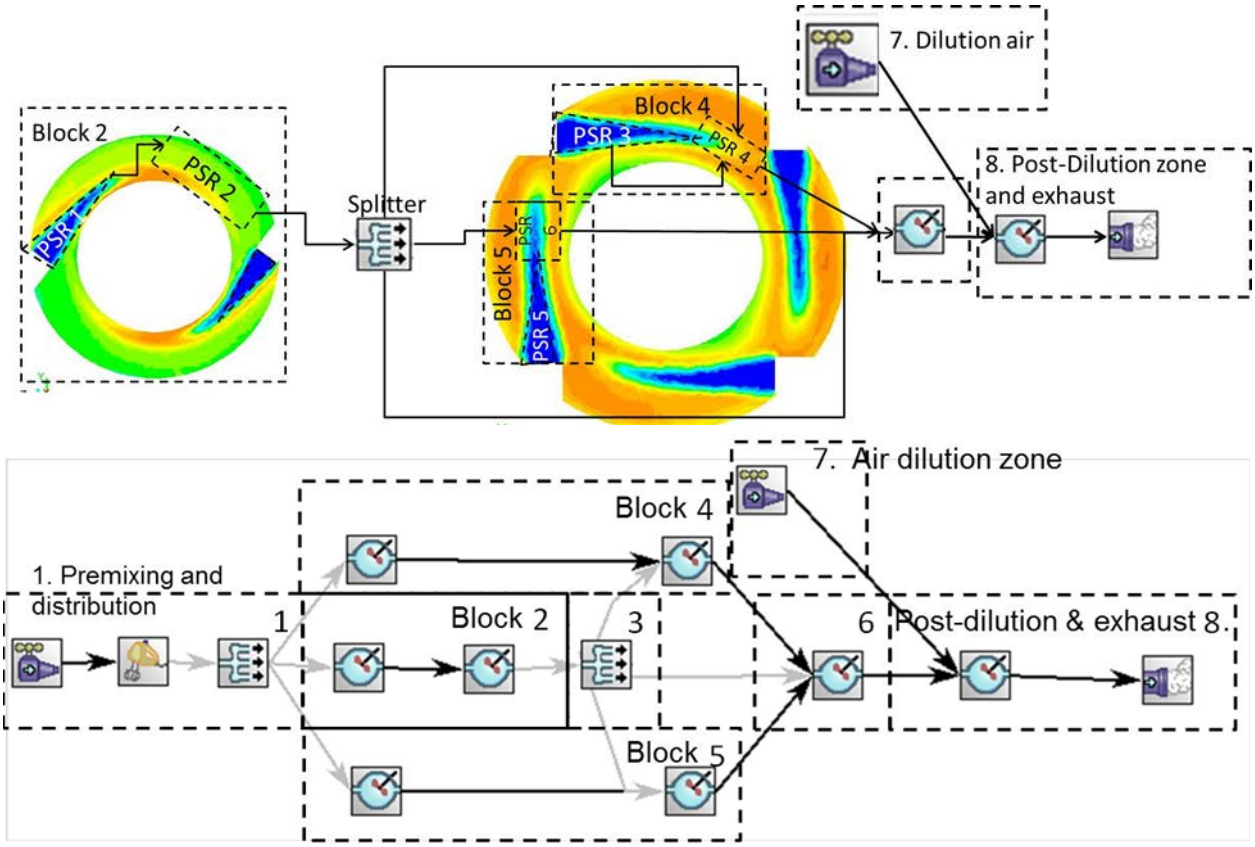

Figure 120 presents the total emissions of NOx as predicted with the CRN model and compared to the experimental results obtained by Hack & McDonell. The emissions are presented in parts per million corrected to 15 percent O2. For the CRN models, the equivalence ratio was set to guarantee a constant adiabatic flame temperature equal to 1,850 K, and the temperature of the preheated air was set at 835 K. The experimental protocol also guarantees a constant temperature at the turbine exit, while the temperature of the preheated air remains also constant, regardless of the fuel composition. Even though the NOx emissions predicted with the CRN are slightly higher than those measured during the experiments, it is clear from the figure that the CRN is capable of predicting a similar trend for different fuel compositions; besides, the CRN allows the analyst to define the NOx formation pathways.

Figure 120: Comparison of NOx Emissions (CRN and Experimental) at Constant Adiabatic Flame Temperature and Preheated Combustion Air Temperature (AFT = 1,850 K, preheated air temperature = 835 K)

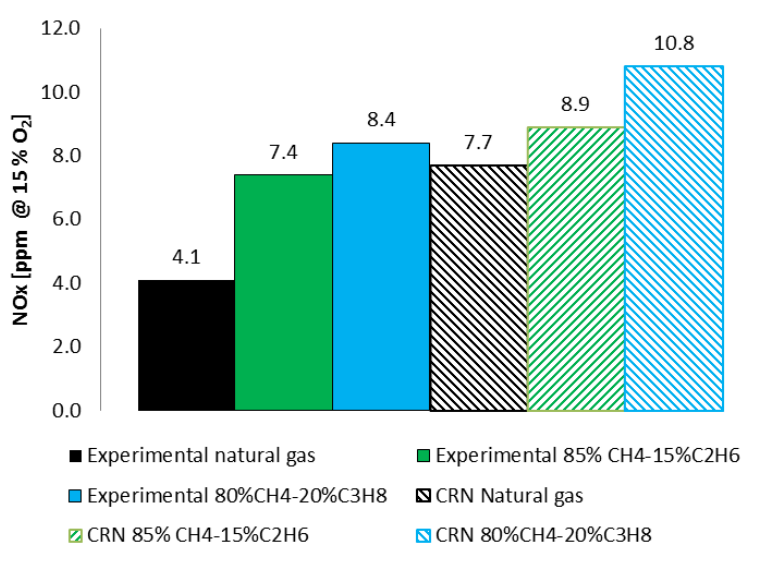

Given the relatively low equivalence ratios (~0.45–0.47) and relatively low reaction temperatures that result, it is unlikely that the Thermal NOx pathway is responsible for all of the measured NOx. The use of the CRN allows us to gain insight into the potential for non-thermal NOx pathways that contribute to a higher level of NOx emissions when burning heavier alkane fuels.

Applying CHEMKIN software in combination with the GRI-Mech 3.0, and eliminating one by one the different NOx pathways included in the full chemistry mechanism, it is possible to determine the relative production of NOx generated by each pathway (see Figure 121).

Figure 121: Influence of the Different NOx Pathways to the Total NOx Emissions

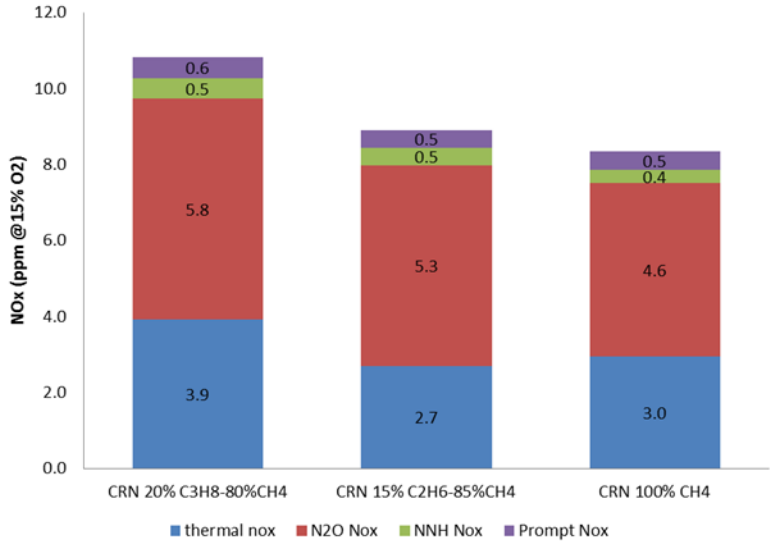

The nitrous oxide (N_2O) pathway, combined with the Thermal NOx pathway, are responsible for about ~90 percent of the total NOx emissions, with the N_2O pathway being responsible for a substantial portion—greater than 53 percent of the NOx measured. This is not surprising, considering that while Thermal NOx may be present, it requires high reaction temperatures (typically above 1,900 K) to become dominant. Below this temperature, other NOx pathways may play a significant role.

Furthermore, the percentage and amount of NOx formed from the N_2O pathway appears to increase with the addition of propane (Flores et al. 2003). This is also consistent with the fact that the MTG operates at elevated pressure (4 atm) and the N_2O mechanism is dominant at these conditions. Other pathways, such as the Prompt NOx and NNH mechanisms, are less likely to contribute to the overall emissions of NOx from the system. Prompt NOx can continue to play a role at reaction temperatures below 1,800 K; however, in lean premixed systems, it has been indicated that Prompt NOx is not a major source of NOx until the equivalence ratio exceeds values greater than approximately 0.65. The N_2O Pathway, on the other hand, has been found in other studies to play a significant role in the overall levels of NOx emitted from lean premixed reactions with equivalence ratios less the 0.80 (Flores et al. 2003). Regarding the small differences observed for the Thermal NOx pathway, they may be associated with differences in local reaction temperatures, which may give rise to different Thermal NOx levels.

5.2.3.3 Diluted Alkane Fuels

The CRN results presented in Figure 122 indicate that the addition of CO2 slightly increases the production of Prompt NOx, but reduces the formation of NOx through the thermal and N2O routes, which results in a net overall reduction. These results are consistent with measured NOx levels for diluted fuels or oxidants. The addition of CO_2 lowers the average reaction temperature in the combustor, which promotes a reduction of the Thermal NOx. Also, a higher concentration of diluting gases reduces the probability that a molecule of N_2 react with O and a third body, since the molecule of CO_2 may obstruct the collisions that promote the formation of NOx through the N_2O route.

Figure 122: Influence of the Different NOx Pathways to the Total NOx Emissions for Mixtures Methane-Carbon Dioxide

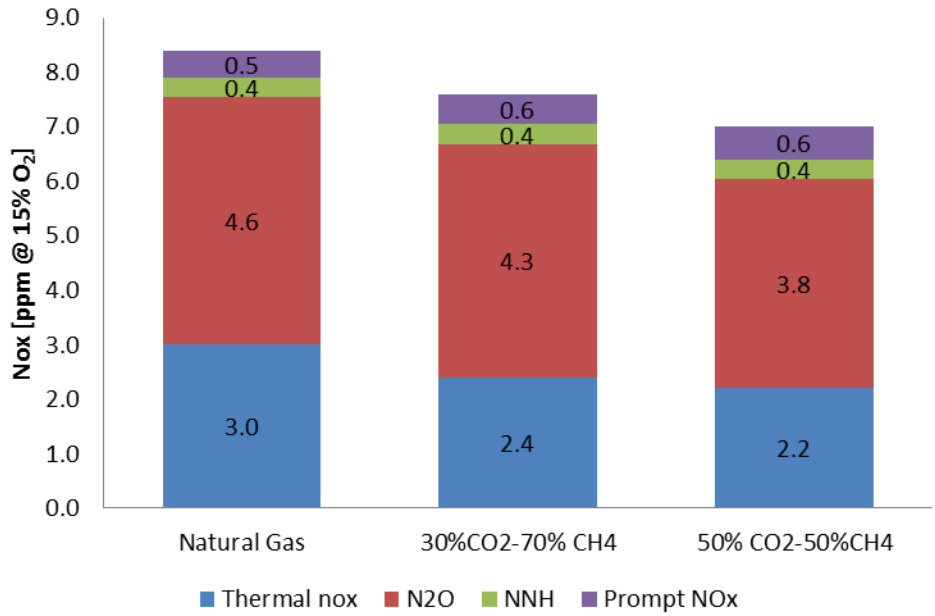

The NOx emitted from combustion systems is typically NO. However, under low-temperature combustion conditions, which may arise from operating lean or with quenching mechanisms such as cold surfaces (e.g., in reciprocating engines or continuous combustion systems under low load or startup), it has been observed that a significant fraction of the NOx generated is in the form of NO_2, which can give rise to visibility issues in the form of brown exhaust. The reason that NO_2 is generally only prevalent under low-temperature, quenching conditions is that its emission depends on the availability of hydrogen dioxide (HO_2) (Glassman, 1996). It is believed that HO_2, which is formed in low-temperature regions, can oxidize NO present in higher-temperature regions. Nitrogen dioxide is related to the HO_2 radical that can be formed by the third–body reaction $H+O_2+M \Leftrightarrow HO_2+M$. Hydrogen dioxide is very unstable and quickly breaks apart at temperatures below 1,500 K.

Figure 123 shows the predicted and measured values of NO (both presented in parts per million and corrected at 15 percent O_2). Experimental data are available from Effinger et al. (2005). Their results indicate that diluting the fuel with CO_2 can significantly reduce NO. By diluting the fuel with 8.8 percent CO_2, a 52 percent reduction in NO emissions results (from 8.4 to 4.3 ppm). The NO depletion seems to reach an asymptote as the concentration of CO_2 in the fuel increases from 36 to 44 percent. Alternatively, the CRN captures the same NO reduction trend but does not capture precisely the slope of the reduction when increasing the CO_2 concentration. At a higher CO_2 concentration, the baseline CRN becomes less accurate and may need revision to capture the trends quantitatively.

Figure 123: NO Emissions as a Function of the Concentration of CO2 in the Fuel (Experimental Results and CRN)

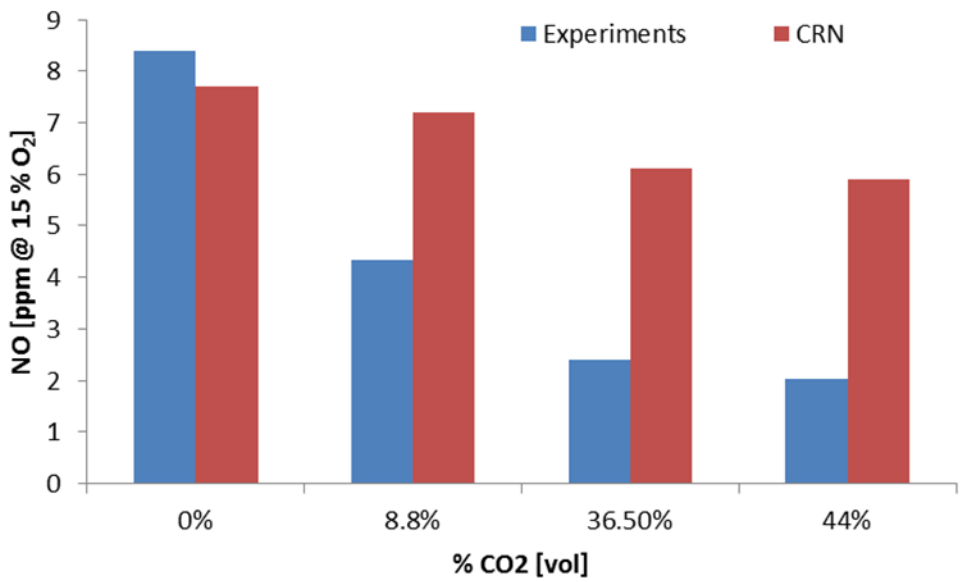

To address the question of NO_2 emissions, the CRN model was used to estimate these levels. Figure 124 shows the CRN results for NO_2 as a function of the CO_2 concentration in the fuel mixture. The CRN revealed that the presence of diluents such as CO_2 does not lead to a significant difference in the generation of NO_2. However, the presence of diluents may reduce the concentration of other radicals such as H and OH, and dilute the O_2 that is necessary in the third-body reaction that leads to NO_2. It is important to highlight that the CRN indicates that the concentration of NO_2 in the exhaust represents less than 8 percent of the total NOx emissions.

Of course, this result is for a single firing temperature and pressure. It is noted that for this system, the firing temperature is controlled. Hence, even with additional diluents, the flame temperature remains fixed, and at levels which are generally above the destruction point of HO_2; hence, for this particular system, it may not be surprising that NO_2 is not significant. If the turbine inlet temperature set point were reduced, it is likely that NO_2 emissions would increase in terms of the amount relative to NO. As shown in Section 5.2.2.3, it is likely that, at lower combustion temperatures, NO_2 would start to become more significant.

Figure 124: NO2 Emissions as a Function of the Concentration of Carbon Dioxide in the Fuel

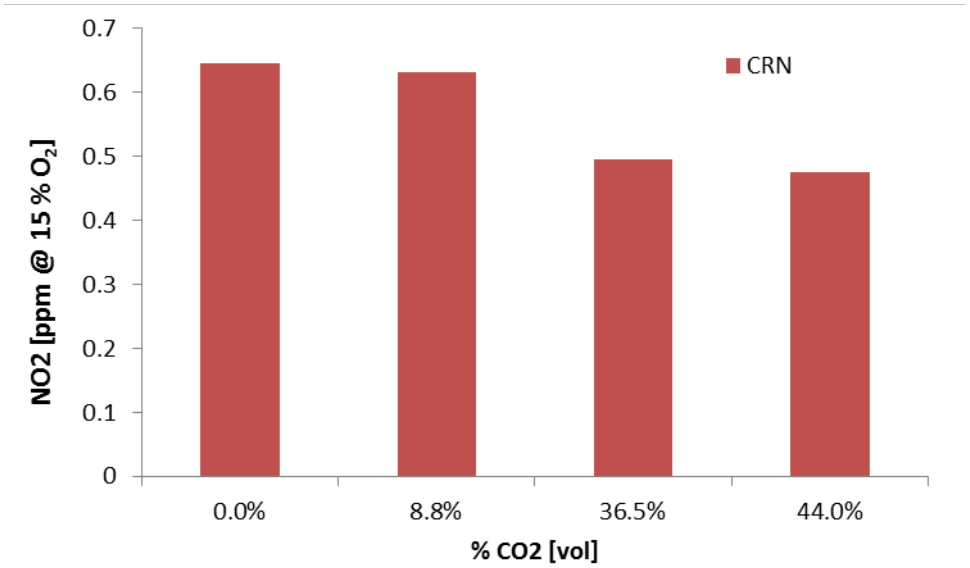

5.2.3.4 Hydrogen-Containing Fuels

Nitric Oxide (NO) emissions for the Capstone C60 turbine running on natural gas, mixtures of natural gas-hydrogen, and pure hydrogen have been previously studied experimentally by Therkelsen et al. 2009). In that study, the effect of the mixing process on the NO emissions was also analyzed. Also in that study, three injector sets were fabricated, each designed to inject the same amount of air and fuel across the power load range, but providing differing degrees of fuel/air mixing. Each design showed different grades of mixing. In one case, the fuel entered the air stream coflowing with the air. This injector type was denoted as an "axial injector," and it provided the least favorable mixing profiles. Two injectors feature two rows of six 1-mm holes on the side of the capped tube, which provide radial fuel injection. The two radial injectors differ in the mixing length afforded to the fuel/air mixture prior to injection into the combustor. The first has a mixing length of 19 mm (the same length as the axial injector) and is labeled the "radial injector." The third injector is called the "early radial injector" due to its 63.5-mm mixing length. The early radial injector produced the most uniform concentration profile of the three.

Since the CFD results and the CRN assumes a perfect mixing of fuel and air, the NO emissions obtained experimentally for the early radial injector will be the ones that match the perfect premixing conditions the best. Experimental NOx emissions at full load (60 kWe) for natural gas mixed with hydrogen are presented in Figure 125. Figure 126 presents the results of NOx emissions for the case when natural gas is mixed with hydrogen and shows the relative influence of each NOx pathway.

Figure 125: NO Emissions for Early Radial Injectors Operated on a Mixture of Hydrogen and Natural Gas

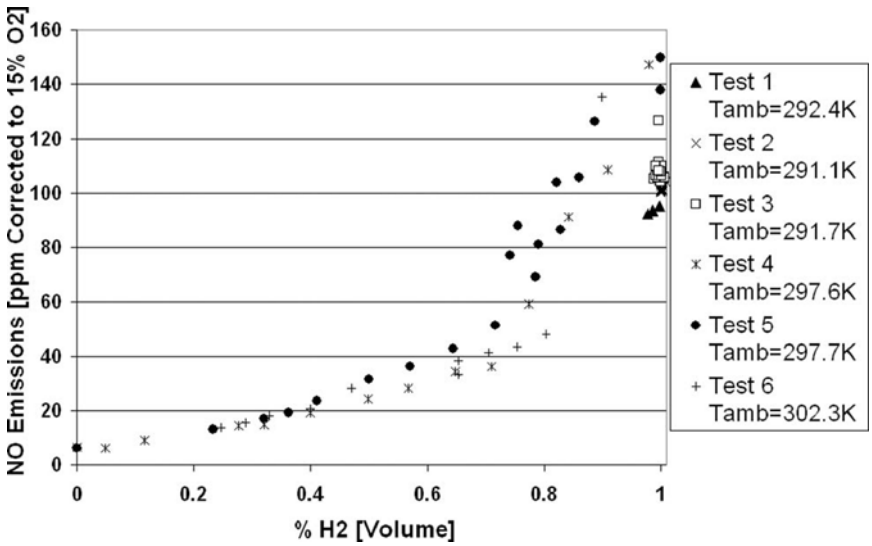

Source: Copied from Therkelsen et al 2009

Figure 126: Influence of the Different NOx Pathways to the Total NOx Emissions for Mixtures Methane-Hydrogen

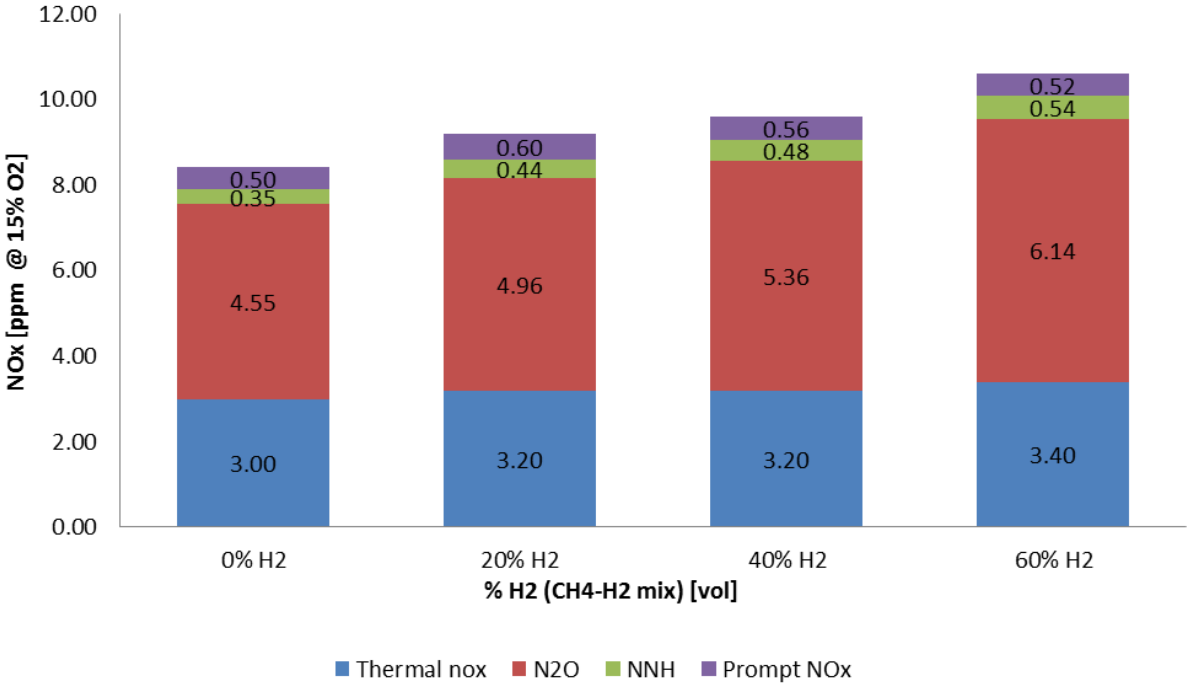

The CRN predicted an increase of NOx when the concentration of H_2 was increased (for a constant power output, preheating temperature, and adiabatic flame temperature). The CRN was in good agreement with the experimental results up to a concentration of 20 percent H2; for a higher concentration of hydrogen, the CRN was not able predict the substantial jump in NOx production that was observed in the experiments.

Figure 126. shows that the Thermal NOx pathway was not significantly affected the addition of H_2 to the fuel. This may be related to the fact that for a higher concentration of hydrogen lower equivalence ratios are used to maintain a fixed adiabatic flame temperature. The equivalence ratio was varied from 0.47 for natural gas up to 0.44 for the mixture of 60 percent H_2/40 percent CH_4. Even though the addition of H_2 leads to a higher concentration of OH radicals that certainly must increase the production of Thermal NOx, it seems that the lower equivalence ratio (higher dilution) and the low operation temperatures of the engine are able to hinder the formation of Thermal NOx regardless of the higher concentration of OH and O radicals. This is not surprising, when considering that while Thermal NOx may be present, it requires high reaction temperatures, typically above 1,900 K, to become dominant. On the other hand, the N_2O pathway is responsible for about ~54 percent of the total NOx, and the percentage and amount of NOx formed from the N_2O pathway appears to increase with the addition of hydrogen.

Similar studies report that the addition of hydrogen to methane at ultra-lean conditions increases the emission of NO in a flame due to the enhancement in the rate of the NNH or N_2O intermediate NO formation routes (Guo et al. 2005). This is consistent with the CRN results that show that Thermal NOx remains almost constant with the addition of H_2, while the Prompt NOx actually decreases. Conversely, both the N_2O and the NNH route increase with the addition of hydrogen to the fuel. Again, the effect of the high pressure in the combustor may play a significant role in the formation of NOx through the N_2O mechanism, which is dominant at these conditions. The N_2O intermediate mechanism has been shown to contribute significantly to NOx formation in diesel engines and gas turbines at low-load operation (Liu et al. 2011).

Additionally, the NO_2 emission levels were analyzed using the CRN model. Figure 127 shows the results of NO_2 as a function of the hydrogen concentration in the fuel mixture. The increase of NO_2 emissions when adding hydrogen to the fuel can be explained by the augmented concentration of the HO_2 radical that can be formed by the third–body reaction $H+O_2+M \Leftrightarrow HO_2+M$. The NO formed in the flame zone can be converted to NO_2 via reactions such as $NO+HO_2 \Leftrightarrow NO_2+OH$. For example, the HO_2 radicals could be formed in the relatively low-temperature unburned mixture region prior to the flame front. The HO_2-rich mixture reacts with the NO molecules transported from high-temperature combustion regions and enhances the formation of NO_2. When present at a suitable temperature, the unburned fuels containing hydrogen could oxidize in the presence of O_2 and form HO_2, which might enhance the formation of NO_2. This might help to explain the enhancing effect on the formation of NO_2 when H_2 is added to the fuel mixture. It is important to highlight that the CRN indicates that the concentration of NO_2 represents less than 8 percent of the total NOx emissions.

Figure 127: NO2 Emissions as a Function of the Concentration of Hydrogen in the Fuel

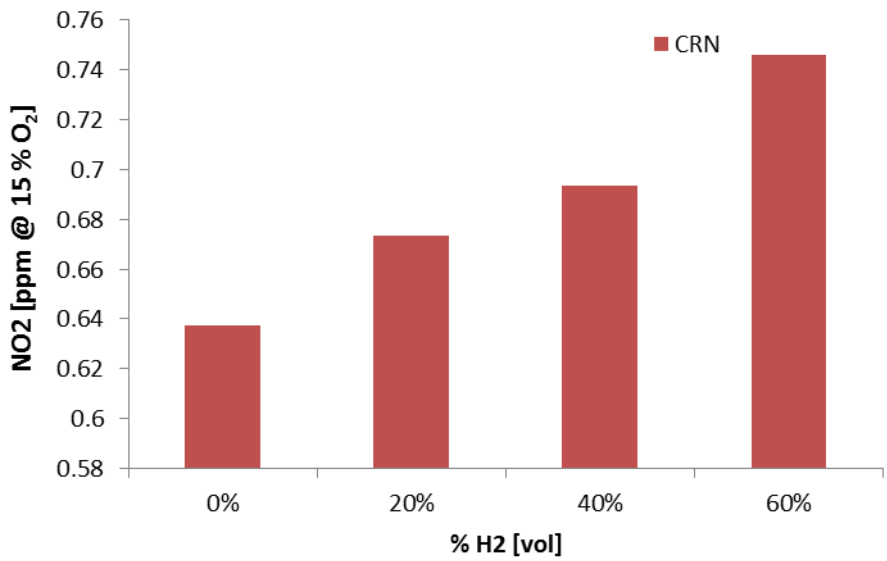

5.2.3.5 Summary of Capstone Engine Emission Results

The reactor network analysis (RNA) indicated that the addition of heavier hydrocarbons increases the production of O, H, and N_2O species. The O radical, especially, is the most significant, since it is the precursor of the N_2O intermediate formed through the triple collision of $N_2+O+M \rightarrow N_2O+M$. Even though the relative concentration of the H radical was greater when mixing the fuel with ethane, its relative importance was lower compared to the role that the O radical played in the N_2O pathway; consequently, the higher concentration of the O radical that was found when the fuel was mixed with propane led to a higher concentration of N_2O, which increased the production of NOx through this mechanism.

The addition of CO_2 lowered the average reaction temperature in the combustor, which promoted a reduction of the Thermal NOx. Also, a higher concentration of diluting gases reduces the probability that a molecule of N2 reacts with O and a third body, since the molecule of CO_2 may obstruct the collisions that promote the formation of NOx through the N_2O route. Additionally, the RNA indicated that the radicals O and H involved in the intermediate N_2O route were depleted with the addition of CO_2, which hindered the production of the intermediate N_2O molecule that is the principal molecule in the formation of NOx through the N_2O route.

For hydrogen-containing fuels, the N2O formation mechanism dominates the NOx emissions.

5.3 Comments Regarding NOx "Entitlement" Levels

As discussed in in Appendix B, Section B.2.4.1.6, a very useful concept regarding development of low-emission combustion systems is the notion of entitlement. In this case, entitlement means the lowest reasonable NOx emission level that might be expected for a given condition. Given that there are at least four major NOx formation mechanisms (see Appendix B, Section B.2.4.1), the details underlying this concept may need updating. Nonetheless, in the industrial gas

turbine community, for example, the work of Leonard and Stegmaier (1994) is often referred to in the context of comparing a new development or combustion system advancement relative to the attained NOx. For context, Figure 128 presents NOx emission data for a number of burners. As shown, some of the burners approach the "entitlement" lines, indicating they are approaching the lowest expected limits.

Figure 128: Natural Gas NOx Emission Results Compared with "Entitlement" Levels

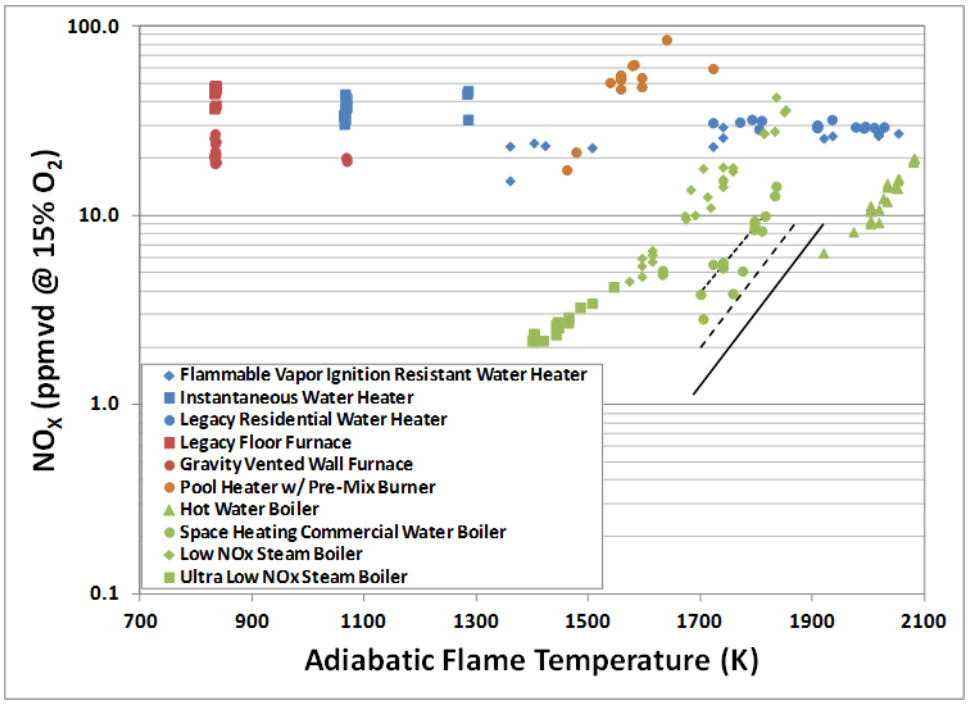

However, further examination of this entitlement concept suggests that there are a few issues to keep in mind. First, the results are always presented in terms of an adiabatic flame temperature, which is taken to represent the actual combustion temperatures. This implies no heat loss in the system, which may be applicable for some systems, especially large, well insulated ones. But for smaller systems or those with less insulation, it is likely that the actual combustion temperatures may be lower than the AFT, which would "shift" the points on the plot in Figure 128 to the left. Hence, care must be taken to estimate uncertainty in the actual temperature. This is why, for example, extensive evaluation of this is carried out for the jet-stirred reactor, which was the primary test bed for evaluating fuel composition effects on emissions, as discussed in Section 5.2.1.

The other issue, as pointed out in Appendix B, Section B.2.4.1.6, is that this concept does not account for fuel compositional effects. For alkanes, strong evidence exists that the C/H ratio will influence the NOx emissions (Lee 2000). Hence, having a single line Figure 128 to represent even all natural gas fuels is not appropriate.

The fuel compositional issue is further exacerbated by the use of the corrected NOx levels. Note that the NOx is reported on a volume percent basis for dry exhaust. To illustrate this, consider two cases where a fixed firing temperature is desired, nominally 1,850 K for combustion of fuel and air at room temperature. In one case, methane is used, and in the other, hydrogen. Because of the chemical differences in the fuels, to achieve this temperature, the equivalence ratio for methane/air is 0.71, but it is 0.61 for hydrogen/air. Based on an equilibrium calculation, Table 16 presents the major species of combustion.

Table 16: Equilibrium Products of Combustion (Volume Fraction) for 1,850 K Flame Temperature for Room Temperature Reactants

Species	H_2/Air	CH_4/Air
CO_2	0	0.069
O_2	0.071	0.055
H_2O	0.226	0.138
N_2	0.699	0.734

Assume that 10 ppm NOx is also contained in the combustion products for both cases. How this level is reported must also be examined. First, due to U.S. EPA protocols, water is dropped out of the system. Then the NOx emissions are corrected for 15 percent O2. These two steps modify the 10 ppm actual NOx to 5.58 ppmvd for H2/air and 4.49 ppmvd for CH4/air. Hence, the entitlement line for H2 should be higher than it is for CH4 when reported on a dry, volumetric basis. As an alternative, it is suggested to use mass emissions or an emissions index (e.g., mass of pollutant/mass of fuel used).

Recent data for H_2/air reactions reported by GE suggest substantially lower NOx emission than the entitlement line for CH4/air (York et al. 2012). This is consistent with the results from the current effort, as shown in Section 5.2.1.3. However, as shown above, the emissions trends with increasing H_2 levels are not consistent for the three test beds examined in the present study, and they depend on which NOx formation pathways are active. As a result, it appears that the entitlement concept as generally applied for various fuels may require further effort to establish.

5.4 Summary

In summary, it has been shown that the CRN approach can successfully predict the influence of fuel composition on emissions behavior for three test beds studied. In reviewing the behavior of the three validation test beds used in this project, it is interesting to observe that each has a different dominant NOx formation pathway, which further illustrates the utility of the CRN methodology in offering a detailed explanation for the observed NOx behavior.

For the jet-stirred reactor, NO formed via the Prompt mechanism dominates. For the high-swirl burner, the NNH pathway dominates. For the gas turbine engine, the NO_2 formation pathway dominates. How the different pathways contribute to the NO behavior as hydrogen is added to

the fuel is especially interesting. In light of these observations, some clarity is provided relative to how some systems produce more NOx as hydrogen is added (e.g., when NNH or N_2O mechanisms dominate), whereas others produce less (when the Prompt mechanism dominates). This can perhaps help explain in part the mixed effect of how fuel composition affects emissions. This result is somewhat disappointing, in that it makes generalizations relative to the impact of fuel composition on emissions difficult. The results for alkanes do indicate a consistent dependency upon higher hydrocarbons, with low-emission systems indicating an increase in NOx with addition of higher hydrocarbons. Thus, fuels with high amounts of these species will nearly certainly increase NOx emissions.

The message for hydrogen-containing fuels is not so clear. With ability of hydrogen fuels to operate at lower reaction temperatures, the relative contribution of NOx from the four formation pathways becomes more complex. At higher temperatures, the contribution from the Zeldovich (or thermal) mechanism dominates, and the results become more general. But with hydrogen, the other three pathways can contribute significantly and, as a result, additional details regarding the combustion/aerodynamic interaction are required to fully explain the observed results. The results in this section for the different test beds illustrate the insight generated by using chemical reactor networks based on measured or simulated flowfields.

CHAPTER 6: Summary of Recommended Interchangeability Methodologies

Various methods of predicting the impact of fuel composition on operability and emissions of combustion devices have been evaluated using existing data or data gathered as part of this project. This chapter summarizes the key findings.

6.1 Autoignition

The prediction of the impact of fuel composition on possible autoignition for lean premixed combustion has been successfully demonstrated. However, distinctions in what can be expected to work for different fuel classes is apparent. For alkanes, several options are available and work to varying degrees. It appears possible to determine trends based on the fuel. Lower values of methane number correspond to shorter delay times. Existing simple correlations are not recommended in the low-temperature (i.e., T < 1,000 K), high-pressure regimes that occur in gas turbine premixers. Instead, correlations based on flow reactor data obtained in the present program are recommended. Recommended correlations are provided in Appendix C of this report in the form of:

$$\tau = \mathcal{A}\, exp\left(\frac{E}{RT}\right) P^b \phi^{\,e} \qquad \text{Equation 46}$$

Also, it has been shown that detailed kinetic calculations can predict autoignition of alkanes for a wide range of conditions. The key is to use an appropriate chemistry mechanism that is valid for the conditions of interest. Examples include that from Galway University. It is noted that GRI Mech 3.0, while the most common mechanism used in kinetic calculations, does not provide accurate results in the lower temperature regimes (nor was it intended to be applied at these conditions). With an appropriate mechanism, it is possible to run a set of calculations using detailed chemistry that could then be used to generate simpler Excel-type expressions or a look-up table that could be used for predicting how alkane composition, temperature, and pressure impact autoignition.

For prediction of autoignition of hydrogen-containing fuels, detailed chemistry calculations appear to be problematic. The reason is that hydrogen, unlike the alkanes, tends to ignite at low temperature in a non-homogeneous mode. It has been observed that the ignition is highly erratic and "localized" rather than a homogeneous volume ignition. The detailed chemistry calculations rely upon the assumption of homogeneous ignition. As a result, it is recommended that correlations based on measured data be utilized for the low-temperature regimes. Equation 47 (Peschke and Spadaccini 1985) is recommended for hydrogen-containing fuel in the low-temperature regime based on validation with recent data:

$$\tau(s) \times [O_2]^{0.5} \times [F]^{0.25} = 1.29 \times 10^{-7}\, exp\left(\frac{3985}{T}\right) \qquad \text{Equation 47}$$

At high temperatures, detailed kinetic calculations are recommended. The correlations from Donato and Petersen (2008), generated from detailed calculations, can also be used reliably, but only in the high-temperature regimes.

6.2 Blowoff

For prediction of blowoff, concepts based on the Damköhler number (Da) (such as Equation 48):

$$Da = \frac{\tau_{physical}}{\tau_{chemical}} \qquad \text{Equation 48}$$

are generally recommended and have been demonstrated to be able to predict how fuel composition impacts blowoff. The numerator can be determined from an appropriate length scale and representative velocity. Essentially it will remain fixed for a given combustor geometry and operating condition. Thus to assess fuel composition impact, the primary challenge is associated with determining the chemical time scale (denominator in Equation 48). One option is to calculate this value using the thermal diffusivity of the mixture and the laminar flame speed using $\tau_{chem} = \alpha / S_L^2$ This information may be found in the literature for some cases. Alternatively, the thermal diffusivity at the conditions of interest can be calculated using a code developed for this project and available for use (see Appendix F). The laminar flame speed can be calculated using a chemical kinetics solver such as Cantera or CHEMKIN. Alternatively, the kinetic solver can be used to establish the minimum time needed to maintain the reaction, which can serve as the denominator. Once this time has been established for a given fuel, the equivalence ratio for other fuels at which the reaction blows off can be established.

A key aspect for hydrogen-containing fuels is to modify the approach by accounting for the strain resistance of the hydrogen reaction. Conceptually, including the Lewis number allows for this. For premixed systems, this Lewis number is the ratio of the thermal diffusivity of the mixture to the mass diffusivity of the fuel. As a result, the equivalence ratio at blowoff for high-hydrogen-content fuels (i.e., low Lewis number cases) will be further reduced from a baseline case, assuming unity Lewis numbers, as would be the case for alkane air mixtures.

These concepts were evaluated mainly using the high-swirl burner configuration. For blowoff, excellent predictions can be obtained using Equation 49, a kinetic calculation of the residence time at blowoff for 100 percent methane, and the use of an adjustment for fuel diffusivity per the concepts of Nobel et al. (2006) (Equation 49):

$$\varphi_{adjusted} = \varphi_{Local} = \varphi_{measured} + \Delta\varphi \qquad \text{Equation 49}$$

It was also observed that differences in the actual nature of blowoff influence the predictability. If blowoff was taken to mean a change in the initial flame-holding mode, then the correlation worked very well. This indicates that care must be taken when defining blowoff. For many combustion systems, complete blowoff may follow a partial blowoff event. The partial event was what was found to correlate well with this approach.

6.3 Flashback

For flashback, the configurations studied allowed evaluation of three flashback modes: (1) into the core flow, (2) along the wall, and (3) that induced by combustion vortex breakdown at the centerline of the burner.

For core flow flashback, the low-swirl injector configuration was studied extensively over a range of conditions for a 90/10 hydrogen-to-methane-ratio fuel. An expression for core flow flashback was developed, as shown in Equation 50, which relates the equivalence ratio, Φ at flashback, as function of $U_o T_o / P_o$:

$$\phi_{flashback} = 6.51 \cdot 10^{-5} \cdot \left(\frac{U_O^{[m/s]} T_O^{[K]}}{P_O^{[atm]}} \right) + 0.336 \qquad \text{Equation 50}$$

This expression is limited to the low-swirl injector, but provides important information on the dependency of pressure on the process, which has not been previously quantified.

The high-swirl burner configuration was evaluated for combustion-induced vortex breakdown using observed flashback measurements. For this particular burner, CIVB was not indicated as the key flashback mechanism based on the inability of correlations using the quench criteria to capture the role of fuel composition. This suggests that the mode of flashback for the high-swirl burner may not be CIVB but rather a combination of multiple mechanisms. This illustrates the need for very careful experimental configurations which isolate each mechanism for flashback. That said, in practice, devices may have multiple mechanisms at play so expressions that can integrate the mechanisms would be very useful.

For wall flashback, the contribution of flame propagation rates and wall "quenching" must be considered. Concepts dating to the 1940s have set the framework for this approach. In subsequent work, no systematic work was done examining the role of fuel composition on wall flashback. In the present work, systematic measurements were made for a wide range of fuel compositions along with injector materials an inlet conditions. Not surprisingly, the temperature of the injector wall was found to play a significant role. Ultimately, correlations for flashback were obtained based on readily available quantities, as shown in Equation 51, with reference values in Table 17:

$$g_{c_tip} = 92.28\left(\frac{\alpha_{tip}}{\alpha_0}\right)^{2.04}\left(\frac{S_{L_tip} d_{q0}}{S_{L0} d_{q_tip}}\right)^{0.328} \qquad \text{Equation 51}$$

Table 17: Definition of Reference Values for Equation 51

	Definition	Value
S_{L0}	Maximum laminar flame speed of Methane	44.8 cm/s Glassman(1996)
d_{q0}	Quenching distance of CH_4/Air at EQ=1	0.25 cm (Barnett and Hibbard (1957)
α_0	Thermal diffusivity of air at 1 atm and 300 K	22.5E-6 m^2/s (Incropera and DeWitt (2007)
T_0	Ambient temperature	300 K

6.4 Emission

Relative to emissions, the concept of "entitlement" as a performance target is important, as it can help establish a basis for technology improvement. Two concepts are worth noting: (1) that by Leonard and Stegmaier (1994), who used extensive measurements with very well mixed systems to establish an idealized NOx versus flame temperature correlation, and (2) the use of C/H. The first provides experimental basis for expected NOx levels as a function of adiabatic flame temperature.

To predict emissions, it appears that some concepts based on simple correlations can capture some of the trends within a given fuel class. For example, it appears that Wobbe Index, for alkanes, does capture the general trend for NOx emissions, with higher Wobbe Index values giving rise to higher NOx. This is true for very-low-emission systems that are approaching "entitlement" levels of NOx. Likewise, the C/H ratio also appears to capture trends for very well-mixed alkane-fueled systems.

When examining hydrogen-containing fuels, concepts like Wobbe Index and C/H ratio cannot be applied. As a result, an alternative strategy is required.

The methodology recommended from the present work is the use of chemical reactor networks (CRNs). With this approach, advanced computational tools are used to predict emission behavior. To develop the network, experimental measurements of the reaction zone or computational fluid dynamic simulation of the reaction zone are needed. In the present work, examples of both are provided. This method is able to elucidate key pathways associated with NOx formation, which can help explain different trends for fuel composition effects. For example, in one case adding higher hydrocarbons increases NOx, but in another it has little effect. The reason is due to the role of specific NOx formation pathways, which are different for these two systems.

GLOSSARY

Terms	Definition
AD	Anaerobic Digester
AFT	Adiabatic flame temperature
AGA	American Gas Association
ANOVA	Analysis of variance
ASBR	Anaerobic Sequencing Batch Reactor
ASU	Air separation unit
BTU	British Thermal Unit
CA	California
CCD	Charge-coupled device
CEC	California Energy Commission
CFD	Computational fluid dynamics
CIVB	Combustion Induced Vortex Breakdown
CO	Carbon Monoxide
CO_2	Carbon Dioxide
CPOX	Catalytic partial oxidation
CRN	Chemical reactor network
CSTR	Completely Stirred Tank Reactor
C2+	Hydrocarbons with 2 or more carbon atoms
C3+	Hydrocarbons with 3 or more carbon atoms
C4+	Hydrocarbons with 4 or more carbon atoms
C65	Capstone C65 microturbine
EQ	Equivalence Ratio
FB	Flashback
GE	General Electric
GHG	Greenhouse Gas

GW	Gigawatt
HC	Hydrocarbon
HeNe	Helium Neon
HHV	Higher heating value
HV	Fuel heating value
IGCC	Integrated Gasification Combined Cycle
JSR	Jet-stirred reactor
LHV	Lower heating value
LFG	Landfill Gas
LFGTE	Landfill Gas to Electricity
LNG	Liquefied natural gas
LPG	Liquefied petroleum gas
LPM	Lean premixed
LSB	Low-swirl burner
LSI	Low-swirl injector
MFC	Mass flow controllers
MGT	Micro turbine generator
Msec	millisecond
MN	methane number
MON	Motor octane number
MSW	Municipal Solid Waste
MTBE	Methyl-tertiary butyl ether
MW	Megawatt
MWI	Modified Wobbe Index
NDIR	Non-dispersive infrared
NOx	Nitrogen oxides
NRCS	Natural Resource Conservation Service

OEM	Original equipment manufacturer
PID	Proportional-integral-derivative
PIV	Particle image velocimetry
PMT	Photomultiplier Tube
POX	Partial oxidation
Ppm	Parts per million
PSR	Perfectly stirred reactor
PSB	PSR at incipient blowout
RANS	Reynolds-Averaged-Navier-Stokes
RCM	Rapid Compression Machine
r.m.s.	Root mean square
RNA	Reactor network analysis
RR	Reactions rates
RSM	Reynolds Stress Model
SCR	Silicone Controlled Rectifiers
SG	Specific gravity
SLPM	Standard liter per minute
TC	Thermocouple
UW	University of Washington
WI	Wobbe Index
WSR	Well-stirred reactor
UCICL	University California Irvine Combustion Laboratory
UCSD	University of California, San Diego
U.S.	United States
U.S. EPA	U.S. Environmental Protection Agency
UV: t	Ultraviole

Symbols andSubscripts	Definition
a	Stoichiometric air-to-fuel ratio (volume)
a	Hydrodynamic pressure gradient
A	Stoichiometric air-to-fuel ratio (volume)
$\mathcal{A}$	Pre-exponential factor
a_i:	Mol fraction of the component *i*
a_x	Represents a slope
a_0	Angle of the vanes
b	Constant
$\mathcal{B}$	Pre-exponential Factor
B_i	Empirical constant called the *flame factor*. The flame factor is assigned to each component in the fuel mixture.
C	Constant (function of fuel type and geometry)
C_{quench}	Variable introduced to predict flashback
d	Specific gravity
Da	Damköhler number
d_{bl}	penetration depth
D	Diameter
D_F	Fuel mass diffusivity
Do	Drop size (not relevant for gaseous fuels)
D_{OX}	Oxygen diffusivity
d_q	Quench distance
e	Exponent constant
E	Total fraction of inert gases/ activation energy
F	Fuel
f	Primary Air Factor

F_M	Position of the peak of the flashback
f_{pz}	Fraction of total burner flow involved in combustion
F	Lifting Constant
G	Fuel Mol Fraction
g	Velocity Gradient
g_c	Critical gradient
I_Y	Yellow-Tipping Index-AGA
I_L	Flame-Lifting Index-AGA
I_F	Flashback Index-AGA.
J_A	Weaver index for air supply
J_F	Weaver index for flashback
J_H	Weaver index for burner load
J_I	Weaver index for incomplete combustion
J_L	Weaver index for flame lifting
J_Y	Weaver index for yellow tipping
h	Higher heating value (AGA
h	Enthalpy
h_f°	Enthalpy of formation
H	Higher heating value (Weaver Indices
K	Lifting Limit Constant
k	Reaction rate constant
k	Thermal conductivity
L	Length
Le	Lewis number
m:	Constant
$\dot{m}$	Mass flow
$\dot{m}_A$	Air mass flow rate

$\dot{m}_{mix}$	Mixture mass flow rate
n	constant
N	Number of "readily liberated atoms" of carbon per hundred molecules of gas
N_r	Mole numbers of each species for reactants
N_p	Mole numbers of each species in the products
O_2	Oxygen
P	Pressure
P_o	Inlet pressure
P_3	Combustor inlet pressure
Q	Molar fraction of oxygen in the mixture
Q_{cond}	Conduction heat transfer
Q_{conv}	Convection heat transfer
Q_{out}	heat loss from the reactor
Q_{rad}	Radiation heat transfer
q_{LBO}	Fuel-to-air ratio at blowoff
R	Ratio of number of atoms of hydrogen in all forms of combination in the fuel gas to the number of carbon atoms in the hydrocarbons/Universal gas constant
R	Radius of the tube
$R_{Conduction}$	Conduction resistance
R_h	Radius of the hub
R_{mix}	Gas Constant of mixture
RR	Reaction Rate
r_1	Inside radii
r_2	Outside radii
S	Weaver's flame speed factor

S'	Swirl number
Sc	*Schuster index*
S_l	Laminar flame speed
S_L	Laminar Flame Speed
S_T	Turbulent flame speed
t	Time
$t_{ignition}$	Time when the mixture ignites
T	Temperature/Yellow tip constant
T_{gas}	Fuel temperature
T_{ign}	Autoignition Temperature
T_{inlet}	Inlet temperature
T_{mix}	Temperature of the mixed gases
T_{PZ}	Primary zone temperature
T_{tip}	Tip temperature
T_o	Inlet temperature/ambient temperature
T_3	Combustor inlet temperature
T_∞	Ambient temperature
Y	Yellow Tip Limit
U	Velocity at a distance at a distance r from the axis
U_{avg}	Average velocity
U_{flow}	Bulk flow velocity
U_{ax}	Freestream velocity
$\bar{u}$	Mean velocity
u'	Fluctuation velocity component
U_o	Premixer inlet velocity
V	Velocity
$\bar{V}$	Bulk Velocity

V_c	Characteristics reaction volume
W	Wobbe Index
W	Molecular weight
X_i	Volumetric fraction of the *i* component
Z	Molar fraction of inert components
E_A	Activation energy
α	Thermal diffusivity
Δ_{PL}	Liner pressure drop
λ_{eff}:	Effective evaporation constant
$\emptyset_{blowoff}$	Fuel-to-air ratio at blowoff
ϕ -	Equivalence ratio/ reduction factor
μ	Viscosity
ρ	Density
ρ_{pz}	Primary zone density
τ	Time
τ_o	Shear stress at wall
$\tau_{chemical}$	Reaction time
$\tau_{physical}$	Residence time
τ_{ign}	Ignition time
τ_{res}	Residence time
ψ	Block factor of the modules
a	Adjustment gas
c	characteristic
cond	when conduction is occurring
f	fuel
s	Substitute gas
m	mixture

mix	Associated with mixture of fuel and air
o	Unburned conditions
o	oxidant
std:	Standard
_tip:	Using tip temperature
_inlet:	Using inlet temperature
$-_{flashback}$:	at flashback conditions

REFERENCES

Akbari, A. 2013. Combustion behavior associated with alternative fuels in lean premixed, high-swirl stabilized distributed reactions. Ph.D. Dissertation, University of California, Irvine.

Anon. No date. San Diego Mechanism web page. University of California, San Diego. Available at: http://web.eng.ucsd.edu/mae/groups/combustion/mechanism.html. Accessed March 2013.

Barnett, H., and R. Hibbard. 1957. *Basic Considerations in the Combustion of Hydrocarbon Fuels and Air*. NACA.

Beerer, D. 2013. Combustion Characteristics and Performance of Low-Swirl Injectors with Natural Gas and Alternative Fuels at Elevated Pressures and Temperatures. Ph.D. Dissertation, University of California, Irvine.

Beerer, D., and V. McDonell. 2008. "Autoignition of Hydrogen and Air in a Continuous Flow Reactor with Application to Lean Premixed Combustion." *Journal of Engineering for Gas Turbines and Power* 130: 051505-1-9.

Beerer, D., V. McDonell, P. Therkelsen, and R. Cheng. 2014. "Flashback and Turbulent Flame Speed Measurements in Hydrogen/Methane Reactions Stabilized by a Low-Swirl Injector at Elevated Pressures and Temperatures." *Journal of Engineering for Gas Turbines and Power* 136: 031502-1–031502-9.

Bhaskaran, K., M. Gupta, and T. Just. 1973. "Shock Tube Study of the Effect of Unsymmetrical Dimethyl Hydrazine on the Ignition Characteristics of Hydrogen-Air Mixtures." *Combustion and Flame* 21: 45–48.

Blumenthal, R., K. Fieweger, K. Komp, and G. Adomeit. 1996. "Gas Dynamic Features of Self Ignition of Non-Diluted Fuel/Air Mixtures at High Pressure." *Combustion Science and Technology* 113–114: 137–166.

Bollinger, L., and R. Edse. 1956. "Effect of Burner-Tip Temperature on Flash Back of Turbulent Hydrogen-Oxygen Flames." *Industrial & Chemical Engineering* 48(4): 802–807.

Bozzelli, J., and A. Dean. 1995. O + NNH: A Possible New Route for NOx Formation in Flames. *International Journal of Chemical Kinetics* 27: 1090–1109.

Burcat, A., K. Scheller, and A. Liftshitz. 1971. "Shock-Tube Investigation of Comparative Ignition Delay Times for C1-C5 Alkanes." *Combustion and Flame* 16: 29–33.

Chan, C., K. Lau, W. Chin, and R. Cheng. 1992. "Freely Propagating Open Premixed Turbulent Flames Stabilized by Swirl." *Twenty Fourth Symposium (International) on Combustion* 24: 511–518.

Cheng, R., D. Littlejohn, W. Nazeer, and K. Smith. 2008. "Laboratory Studies of the Flow Field Characteristics of Low-Swirl Injectors for Adaptation to Fuel Flexible Turbines." *Journal of Engineering for Gas Turbines and Power* 130: 021501-1-9.

Cowell, L., and A. Lefebvre. 1986. *Influence of Pressure on Autoignition Characteristics of Gaseous Hydrocarbon-Air Mixtures.* SAE.

Daniele, S., P. Jansohn, and K. Boulouchos. 2010. *Flashback Propensity of Syngas Flames at High Pressure: Diagnostics and Control*. Glasgow: American Society of Mechanical Engineers.

de Vries, J., and E. Petersen. 2007. "Autoignition of Methane Based Fuel Blends under Gas Turbine Conditions." *Proceedings of the Combustion Institute* 31: 3163–3171.

Donato, N., and E. Petersen. 2008. "Simplified Correlation Models for CO/H2 Chemical Reaction Times." *International Journal of Hydrogen Energy* 33: 7565–7579.

Dryer, F., and M. Chaos. 2008. "Ignition of Syngas/Air and Hydrogen/Air Mixtures at Low Temperatures and High Pressures." *Combustion and Flame* 152: 293–299.

Dunn-Rankin, D. 2008. Lean Combustion—Technology and Control. Dunn-Rankin, D., editor. San Diego: Elsevier.

Effinger, M., J. Mauzey, and V. McDonell. 2005. *Characterization and Reduction of Pollutant Emissions from Landfill and Digester Gas Fired Microturbine Generator.* New York: American Society of Mechanical Engineers.

Flores, R.M., McDonell, V.G., and Samuelsen, G.S. (2003). "Impact of Ethane and Propane Variation in Natural Gas on the Performance of a Model Gas Turbine Combustor." *Journal of Engineering for Gas Turbines and Power* 125: 701-708.

Glassman, I., 1996. *Combustion*. 3rd ed. San Diego: Academic Press.

Goy, C., A. Moran, and G. Thomas. 2001. *Paper 2001-GT-0051: Autoignition Characteristics of Gaseous Fuels at Representative Turbine Conditions.* New Orleans: American Society of Mechanical Engineers.

Guo, H., et al. 2005. "The Effect of Hydrogen Addition on Flammability Limits and NOx Emissions in Ultra-Lean Counterflow CH4/Air Premixed Flames." *In Proceedings of the Combustion Institute* 30(1): 303–311.

Gupta, A., D. Lilley, and N. Syred. 1984. *Swirl Flows*. Kent: Abacus Press.

Hack, R., and V. McDonell. 2008. "Impact of Ethane, Propane, and Diluent Content in Natural Gas on the Performance of a Commercial Microturbine Generator." *ASME Journal of Engineering for Gas Turbines and Power* 011509-1:7.

Harrington, J., et al. 1996. Evidence for a New NO Production Mechanism in Flames. *26th Symposium (International) on Combustion*. 26: 2133–1238.

Hayhurst, A., and E. Hutchinson. 1998. "Evidence for a New Way of Producing NO via NNH in Fuel-Rich Flames at Atmospheric Pressures." *Combustion and Flame* 114(1): 274–279.

Hewson, J., and M. Bollig. 1996. Reduced Mechanisms for NOx Emission from Hydrocarbon Diffusion Flames. *26th Symposium (International) on Combustion*. 26: 2171–2179.

Holton, M. 2008. Autoignition Delay Time Measurements for Natural Gas Fuel Components and Their Mixtures. M.S. Thesis. University of Maryland.

Huang, J., P. Hills, K. Bushe, and S. Munshi. 2004. "Shock-Tube Study of Methane Ignition Under Engine Relevant Conditions: Experiments and Modeling." *Combustion and Flame*

136: 25–42.

Johnson, M., et al. 2005. "A Comparison of the Flowfields and Emissions of High Swirl Injectors and Low-Swirl Injectors for Lean Premixed Gas Turbines." *Proceedings of the Combustion Institute* 30: 2867–2874.

Kedia, K., and A. Ghoniem. 2012. "Mechanisms of Stabilization and Blowoff of a Premixed Flame Downstream of a Heat-Conducting Perforated Plate." *Combustion and Flame* 159(3): 1055–1069.

Konnov, A. 2000. "Development and Validation of a Detailed Reaction Mechanism for the Combustion of Small Hydrocarbons." *Proceedings of the Combustion Institute* 30: 317.

Konnov, A., G. Colson, and J. De Ruyck. 2001. "NO formation Rates for Hydrogen Combustion in Stirred Reactors." *Fuel* 80: 49–65.

Kroner, M., J. Fritz, and T. Sattelmayer. 2003. "Flashback Limits for Combustion Induced Vortex Breakdown." *Journal of Engineering for Gas Turbines and Power* 125: 693–700.

Lee, J. 2000. *Reduction of NOx Emission for Lean Prevaporized-Premixed Combustors.* Seattle: University of Washington.

Lefebvre, A., and D. Ballal. 2010. *Gas Turbine Combustion: Alternative Fuels and Emissions*. 3rd ed. Boca Raton: CRC Press.

Leonard, G., and J. Stegmaier. 1994. "Development of Aeroderivative Gas Turbine Dry Low Emissions Combustion System." *Journal of Engineering for Gas Turbines and Power* 116: 542–550.

Lieuwen, T., V. G. McDonell, D. Santavicca, and T. Sattelmayer. 2008. "Burner Development and Operability Issues Associated with Steading Flowing Syngas Fired Combustors." *Combustion Science and Technology* 180: 1169–1192.

Liu, S., et al. 2011. "An Experimental Investigation of NO2 Emission Characteristics of a Heavy-Duty H2-Diesel Dual Fuel Engine." *International Journal of Hydrogen Energy* 36(18): 12015–12024.

Meyer, J., and A. Oppenheim. 1971. "On the Shock-Induced Ignition of Explosive Gases." *Thirteenth Symposium (International) on Combustion* 13: 1153–1164.

Miller, J., M. Branch, and R. Kee. 1981. "A Chemical Kinetic Model for the Selective Reduction of Nitric Oxide by Ammonia." *Combustion and Flame* 43: 81–98.

Mueller, M. 2000. Experimental Study of the Modeling of Hydrogen and Carbon Monoxide Perturbed by Nitrogen and Sulfur Oxides. Ph.D. Thesis. Princeton University.

Naik, C. et al. 2011. "Detailed Chemical Kinetic Mechanism for Surrogates of Alternative Jet Fuels." *Combustion and Flame* 158: 434–445.

Nazeer, W., et al. 2006. *Full Scale Testing of a Low Swirl Fuel Injector Concept for Ultra-Low NOx Gas Turbine Combustion Systems*. New York: American Society of Mechanical Engineers.

Noble, D., et al. 2006. *Syngas Mixture Composition Effects upon Flashback and Blowoff*. Atlanta: American Society of Mechanical Engineers.

Novosselov, I. 2006. *Chemical Reactor Networks for Combustion Systems Modeling.* Seattle: University of Washington.

Pang, G., D. Davidson, and R. Hanson. 2009. "Experimental Study and Modeling of Shock Tube Ignition Delay Times for Hydrogen-Oxygen-Argon Mixtures at Low Temperatures." *Proceedings of the Combustion Institute* 32: 181–188.

Peschke, W., and L. Spadaccini. 1985. *Determination of Autoigntion and Flame Speed Characteristics of Coal Gases Having Medium Heating Value.* Palo Alto: EPRI.

Petersen, E., et al. 2007b. "Methane/Propane Oxidation at High Pressures: Experimental and Detailed Chemical Kinetic Modeling." *Proceedings of the Combustion Institute* 31: 447–454.

Ribacour, M., et al. 2000. "Ignition of Isomers of Pentane: An Experimental and Kinetics Modeling Study." *Proceedings of the Combustion Institute* 28: 1671–1678.

Richards, G., et al. 2001. "Issues for Low-Emission, Fuel-Flexible Power Systems." *Progress in Energy and Combustion Science* 27: 141–169.

Sabia, P., E. Schiesswohl, M. de Joannon, and A. Cavaliere. 2006. "Numerical Analysis of Hydrogen Mild Combustion," *Turkish Journal of Engineering for Environmental Science* 30: 127–134.

Santoro, R. 2009. *Autoignition Studies of Syngas and Hydrogen* (SGH) Fuels. Report for UTSR Project 05-01-SR117. U.S. Department of Energy.

Shanbhogue, S., S. Husain, and T. Lieuwen. 2010. "Lean Blowoff of Bluff Body Stabilized Flames: Scaling and Dynamics." *Progress in Energy and Combustion Science* 35: 98–120.

Singh, S. 1978. *A Study of Methanol Combustion and Oxides of Nitrogen Formation in a Jet-Stirred Reactor*. Spokane: Washington State University.

Slack, M. 1977. Rate Coefficients for the H+O2 + M = HO2 + M Evaluated from Shock Tube Measurements of Induction Time. *Combustion and Flame* 28: 241–249.

Smith, G., et al. 2000. GRI Mech 3.0. http://www.me.berkeley.edu/gri_mech.

Snyder, A., J. Robertson, D. Zanders, and G. Skinner. 1965. *Shock Tube Studies of Fuel/Air Ignition Characteristics, Report AFAPL-TR-65-93-1985*. U.S. Air Force.

Spadaccini, L., and M. Colket. 1994. "Ignition Delay Characteristics of Methane Fuels." *Progress in Energy and Combustion Science* 20: 431–460.

Steele, R. 1995. NOx and *N2O Formation in Lean-Premixed Jet-Stirred Reactors Operated from 1 to 7 atm.* Seattle: University of Washington.

Strakey, P., T. Sidwell, and J. Ontko. 2007. "Investigation of the Effects of Hydrogen Addition on Lean Extinction in a Swirl Stabilized Combustor." *Proceedings of the Combustion Institute* 31(2): 3173–3180.

Therkelsen, P., T. Werts, V. McDonell, and G. Samuelsen. 2009. Analysis of NOx Formation in a Hydrogen Fuel Gas Turbine Engine. *Journal of Engineering for Gas Turbines and Power* 131: 031507-1:10.

Turns, S. 2012. *An Introduction to Combustion*. 3rd ed. New York: McGraw Hill.

Voevodski, V., and R. Soloukhin. 1965. *Tenth Symposium (International) on Combustion* 279–283.

Wagner, T. 1990. Task 200—*Ignition Delay Characterization, Report R90-252099-1*. East Hartford: United Technologies Research Center.

Wang, B., H. Olivier, and H. Groenig. 2003. "Ignition of Shock Heated H2/Air Stream Mixtures." *Combustion and Flame* 133: 93–106.

Westbrook, C. 1979. "An Analytical Study of the Shock Tube Ignition of Mixtures of Methane and Ethane." *Proceedings of the Combustion Institute* 20: 5–17.

Westbrook, C., and F. Dryer. 1984. "Chemical Kinetic Modeling of Hydrocarbon Combustion." *Progress in Energy and Combustion Science* 10: 1–57.

Yetter, R., F. Dryer, and D. Golden. 1992. "Pressure Effects on the Kinetics of High Speed Chemically Reacting Flow." In: M. Hussaini, A. Kumar, and R. Voigt, eds. *Major Research Topics in Combustion*. Springer-Verlag. 309–338.

Yetter, R., H. Rabitz, and R. Hedges. 1991. "A Combined Stability-Sensitivity Analysis of Weak and Strong Reactions of Hydrogen/Oxygen Mixtures." *International Journal of Chemical Kinetics* 23: 251–278.

York, W., W. Ziminsky, and E. Yilmaz. 2012. *Development and Testing of a Low NOx Hydrogen Combustion System for Heavy Duty Gas Turbines.* New York: American Society of Mechanical Engineers.

APPENDICES

Appendix A: Review of Fuel Composition

Appendix B: Review of Existing Interchange Parameters and Methodologies

Appendix C: Alkane Ignition Delay Correlations

Appendix D: Details and Heat Transfer Analysis of JSR

Appendix E: Topical Report – Flame Speed Test Results and Analysis

Appendix F: Topical Report – Diffusion Transport Porperty Calculator

Appendix G: Topical Report – Flame Structure Tests and Interpretation

Appendix H: Topical Report – Reduced Order Kinetic Mechanisms for Alternative Fuels

These appendices are available as a separate volume, publication number CEC-500-2015-063-AP.